Cosmic rays from the supernova remnants HESS J1731-347 and W28

Dissertation

der Mathematisch-Naturwissenschaftlichen Fakultät
der Eberhard Karls Universität Tübingen
zur Erlangung des Grades eines
Doktors der Naturwissenschaften
(Dr. rer. nat.)

vorgelegt von
Yudong Cui
aus Luohe, China

Tübingen
2016

Tag der mündlichen Qualifikation: 10.02.2017

Dekan:	Prof. Wolfgang Rosenstiel
1. Berichterstatter:	Prof. Dr. Andrea Santangelo
2. Berichterstatter:	Prof. Dr. Klaus Werner

Abstract

The supernova remnant (SNR) HESS J1731-347 displays strong TeV γ-ray and nonthermal X-ray emission, thus the object is presently accelerating particles to very high energies. A distinctive feature of this young SNR is the nearby ($\sim 30\,\mathrm{pc}$ in projection) extended source HESS J1729-345, which is currently unidentified but is in sky projection coinciding with known molecular clouds (MC). Using a new analysis tool and the new data sets from 2013, we have delivered TeV morphological and spectral results at the SNR region similar to those of the previous work in 2011. However, a different TeV morphological result at the HESS J1729-345 region, in particular, a bridge structure connecting HESS J1729-345 and the SNR is found in our TeV analysis. This morphological difference is considered within the statistical fluctuations.

The main goal in my thesis is to explore whether the TeV emission from HESS J1729-345 can be explained as emission from runaway hadronic cosmic rays (CRs) that are illuminating these MCs. The observational data of HESS J1729-345 and HESS J1731-347 can be reproduced using core-collapse SN models for HESS J1731-347. Starting with different progenitor stars and their pre-supernova environment, we model potential SNR evolution histories along with the CR acceleration in the SNR and the diffusion of the CRs. A simplified three-dimensional structure of the MCs is introduced based on ^{12}CO data of that region, adopting a distance of 3.2 kpc to the source. A Monte Carlo based diffusion model for the escaping CRs is developed to deal with the inhomogeneous environment. The fast SNR forward shock velocity, as implied from the X-ray data, can easily be explained when employing scenarios with progenitor star masses between $20\,\mathrm{M}_\odot$ and $25\,\mathrm{M}_\odot$, where the SNR shock is still expanding inside the main-sequence (MS) bubble at present time. The TeV spectrum of HESS J1729-345 is satisfactorily fitted by the emission from the highest energy CRs that have escaped the SNR, using a standard Galactic CR diffusion coefficient in the interclump medium (the relative low density space where those dense MC clumps are embedded within). The TeV image of HESS J1729-345 can be explained with a reasonable three-dimensional structure of MCs. The TeV emission from the SNR itself is dominated by leptonic emission in this model. We also explore scenarios where the shock is starting to encounter the dense MS progenitor wind bubble shell. The escaping hadronic CR hypothesis for the γ-ray emission of HESS J1729-345 can still hold, but even in this case our model cannot easily account for the TeV emission from HESS J1731-347 in a hadronic scenario.

Under realistic conditions, the CRs often exhibit strong ballistically propagation behaviors rather than a purely diffusive one in relatively small environments, e.g. the MCs near the SNR HESS J1731-347 or SNR W28. This is due to that the size of the diffusion environments is often smaller than the wavelength of some Galactic magnetic eddies and/or the Gyro-radius of the very high energy CRs. Therefore, we build a purely numerical code to simulate the CR propagation inside a given magnetic turbulence. The results of our code has shown consistency with previous works. Through comparing the numerical simulation results of our code with the GeV-TeV observational data, we would like to constrain the magnetic structures near SNRs in the future studies.

Our searching for stars near/behind SNR HESS J1731-347 within the SIMBAD catalog and WISE catalog are driven by two motivations. First, SNR HESS J1731-347 may be associated with an OB star cluster. Second, ionized MCs near the SNR (an evidence for MCs being swept by the shock) could be observed through the H_3^+ absorption features with the help of

background stars. Using the extinctions derived from the ^{12}CO and HI data, we find 41 (125) potential star candidates near HESS J1731-347 on the sky map with distances to Earth as about 3–5 kpc (> 5 kpc).

The SNR W28 is an old SNR which exhibits thermal X-ray. The most intriguing finding near this SNR is the good match between the TeV features – HESS J1801-233 (HESS J1800-240 A,B,C) and the cold gas features – MCs located at the Northeast (to the South) of the SNR. The GeV-TeV emissions of HESS J1801-233, HESS J1800-240 A, and HESS J1800-240 B are successfully explained in our hadronic W28 model. Same CR acceleration/diffusion model used for HESS J1731-347 is adopted in our W28 model as well. The TeV emissions inside/around W28 are well reproduced by the early released runaway super-TeV CRs. Assuming the GeV CRs are only released when the shock has encountered the MC clumps (high-density clumps in the molecular clouds $n_{\rm ISM} \gtrsim 10^2\,{\rm cm}^{-3}$) and dissipated into the local medium, we have reproduced the GeV emission inside/around W28 through introducing two instantaneous GeV CR sources (two MC clumps being swept by the shock at ~ 40 kyr).

Zusammenfassung

Der Supernovaüberrest (SNR) HESS J1731-347 zeigt starke TeV γ- und nichtthermische Röntgenemission. Diese Daten zeigen, dass das Objekt gegenwärtig Teilchen zu sehr hohen Energien beschleunigt. Eine besondere Eigenschaft dieses jungen Supernovaüberrests ist die benachbarte (30 pc in Projektion) ausgedehnte Quelle HESS J1729-345, die zur Zeit nicht identifiziert ist, aber in Himmelsprojektion mit einer bekannten Molekülwolke zusammenfällt. Unter Benutzung einer neuen Analysemethode und zusätzlicher Daten aus dem Jahr 2013 haben wir eine ähnliche TeV-Quellmorphologie und ein ähnliches TeV-Energiespektrum zu den Ergebnissen aus dem Jahr 2011 gewonnen. Darüberhinaus wurde, für die HESS J1729-345 Region, ein verbessertes Ergebnis gefunden, im speziellen eine Brückenstruktur, die HESS J1729-345 mit dem SNR verbindet. Das Ergebnis ist im Rahmen der statistischen Fehler verträglich mit den vorhergehenden Ergebnissen.

Das Hauptziel meiner Arbeit ist es zu untersuchen, ob die TeV-Emission von HESS J1729-345 mit der Emission von entweichender hadronischer kosmischer Strahlungsteilchen erklärt werden kann, die die Molekülwolke beleuchtet. Die gewonnen Daten von HESS J1729-345 und HESS J1731-347 können durch ein Kernkollaps-Supernova-Modell reproduziert werden. Beginnend mit unterschiedlichen Vorläufersternen und ihren Umgebungen vor der Supernova entwickeln wir potentielle SNR-Entwicklungsgeschichten, zusammen mit der Beschleunigung kosmischer Strahlungsteilchen in dem SNR und der Diffusion der kosmischen Strahlungsteilchen. Eine vereinfachte dreidimensionale Struktur der Molekülwolke, basierend auf ^{12}CO Daten der Region mit einer angenommenen Distanz von 3,2 kpc, wird in die Simulation eingebracht. Ein auf der Monte-Carlo-Methode basierendes Diffusionsmodell für entweichende kosmische Strahlung wurde entwickelt, um die inhomogenen Umgebung berücksichtigen zu können. Die hohe Geschwindigkeit der fortschreitenden Stoßwelle des Supernovaüberrest, welche durch die Röntgendaten impliziert wird, kann einfach erklärt werden, wenn man ein Szenario mit einem Vorläuferstern mit einer Anfangsmasse von 20 $M_\odot$ bis 25 $M_\odot$ verwendet. In diesem Fall expandiert die Stoßwelle des Supernovaüberest noch innerhalb der stellaren Blase, die von dem Vorläufersternen in seiner Hauptreihenphase gebildet wurde. Das TeV-Energiespektrum von HESS J1729-345 wird zufriedenstellend mit einem Standardwert für die Diffusion galaktischer kosmischer Strahlung in einem Medium zwischen dichten Molekülwolken beschrieben (dichte Molekülwolken sind normalerweise von einem Medium geringer Dichte umgeben). Das Aussehen von HESS J1729-345 kann durch eine angemessene dreidimensionale Struktur einer Molekülwoke erklärt werden. In diesem Modell wird die TeV-Emission des Supernovaüberest selber durch leptonische Emissionsprozesse beschrieben. Wir testen auch ein Szenario, in dem die Stoßwelle mit der stellaren Blase des Hauptreihensterns interagiert. Die Hypothese der entweichenden kosmischen Strahlung, die die γ-Strahlung von HESS J1729-345 hervorruft, ist damit verträglich, aber selbst in diesem Fall kann unser Model die TeV-Emission von HESS J1731-347 nicht einfach mit einem hadronischen Szenario erklären.

Unter realistischen Bedingungen in einem relativ kleinen Volumen zeigt kosmische Strahlung oft eine dominant ballistische Ausbreitung statt einer rein diffusen Ausbreitung. Beispiele sind die Molekülwolken in der Nähe von HESS J1731-347 oder dem Supernovaüberrest W28. Das liegt daran, dass die Größe des Volumens, in dem Diffusion stattfindet oft kleiner ist, als die Wellenlänge typischer galaktischer Magnetfeldturbulenzen und/oder kleiner als der Gyroradius von kosmischer Strahlung mit sehr hoher Energie. Daher haben wir ein rein numerisches

Programm geschrieben, um die Ausbreitung kosmischen Strahlungsteilchen innerhalb einer gegebenen magnetischen Turbulenz zu simulieren. Das Ergebnis unserer Simulation ist konsistent mit den Ergebnissen früherer Arbeiten. Durch Vergleich der Ergebnisse der numerischen Simulation mit den GeV-TeV-Beobachtungen ergibt sich die Möglichkeit, in Zukunft die Struktur des magnetischen Felds in der Umgebung von Supernovaüberresten einzuschränken.

Aus zwei Gründen suchen wir nach Sternen in der Nähe von HESS J1731-347 in dem SIMBAD- und WISE-Katalogen: Erstens, HESS J1731-347 könnte mit einem OB Sternhaufen assoziiert sein. Zweitens, ionisierte Molekülwolken nahe dem Supernovaüberrest (ein Hinweis, dass Molekülwolken durch die Stroßwelle getroffen wurde) können durch die Absorptionslinie von H_3^+ unter Zuhilfenahme von Hintergrundsternen beobachtet werden. Durch Verwendung der Extinktion, abgeleitet von ^{12}CO und HI Daten, finden wir 41 (125) Kandidaten in der Nähe von HESS J1731-347 mit einer Distanz von 3 bis 5 kpc (>5 kpc)zur Erde.

Der Supernovaüberrest W28 ist an alter Überrest, der thermische Röntgenstrahlung zeigt. Ein interessantes Ergebnis ist, dass die TeV Quellen HESS J1801-223 und HESS J1800-240 A,B,C gut mit dem kalten Gas nordöstlich und südlich des SNRs zusammenpassen. Die GeV-TeV-Emission von HESS J1801-223, HESS J1800-240 A und HESS J1800-240 B kann erfolgreich mit einem hadronischem Modell für W28 erklärt werden. Das gleiche Modell für die Beschleunigung und Diffusion der kosmischen Strahlung, das auch für HESS J1731-347 verwendet wurde, werden nun für W28 angepasst. Die TeV-Emission innerhalb und um W28 herum wird, mit dem Modell, durch frühe Freisetzung von TeV kosmischer Strahlung mit supra-TeV-Energien, erklärt. Unter der Annahme, dass die kosmischen Strahlungsteilchen mit GeV-Energien erst dadurch freigesetzt werden, dass die Stoßwelle mit einer dichten Molekülwolke interagiert ($n_{\rm ISM} \gtrsim 10^2\,{\rm cm}^{-3}$) und unter der Annahme, dass die kosmische Strahlung anschließend im lokalen Medium dissipiert, können wir die GeV-Emission innerhalb und um W28 herum reproduzieren, indem wir zwei instantane Quellen für kosmische Strahlungsteilchen mit GeV-Energie einbringen (zwei Molekülwolken, die von der Stoßwelle ungefähr 40 Kilojahre nach der Explosion getroffen wurden).

Contents

1

Introduction

1.1 Cosmic rays and Cherenkov telescopes

The sources of the Cosmic rays (CRs) have always been a mystery since the discovery of CRs in the early 20th century. The CRs, composed primarily of high-energy protons (90%) and atomic nuclei, are mainly from outside our solar system. After a long distance propagating in the Galactic magnetic field, the CRs become isotropically distributed when detected on Earth. Hence, it is difficult to trace the CRs back to their sources. The spectrum of the CRs basically follows two power-law profiles: The first one with a power-law index $\sim$2.7 covers an energy range from $\sim 10^9$eV to $\sim 10^{15}$eV (the "knee"); the second one with a power-law index $\sim$3.0 covers an energy range from the "knee" to $\sim 10^{18}$eV (the "ankle").

Figure 1.1: Picture of H.E.S.S., which is located in Namibia. (Credit H.E.S.S. Collaboration, Arnim Balzer)

One of the best ways to reveal the CR accelerating sources is through observing tera-electronvolts (TeV) photons with Cherenkov telescopes. These very high energy (VHE) photons, which travel in straight lines, can be produced either by the Inverse Compton (IC) scattering of leptons off the ambient photon field or in interactions of hadrons with ambient matter (Hinton & Hofmann, 2009). Unlike the TeV leptons, which often show both X-ray synchrotron emission and IC γ-ray emission, the TeV hadrons only exhibit γ-rays in the GeV-TeV band via the decay of neutral pions resulting from hadronic interaction.

When a VHE hadron or photon arrives on Earth, it can hardly ever hit the ground but will collide (interact) with an atom of the air, usually several ten kilometers high. Following the collision, the Cherenkov light from the shower of secondary particles can leave a pattern (blue to UV light) on Imaging Atmospheric Cherenkov Telescopes (IACT) on ground (see e.g. the showers in Fig. 1.2). This IACT technique was first attempted via the Whipple telescope

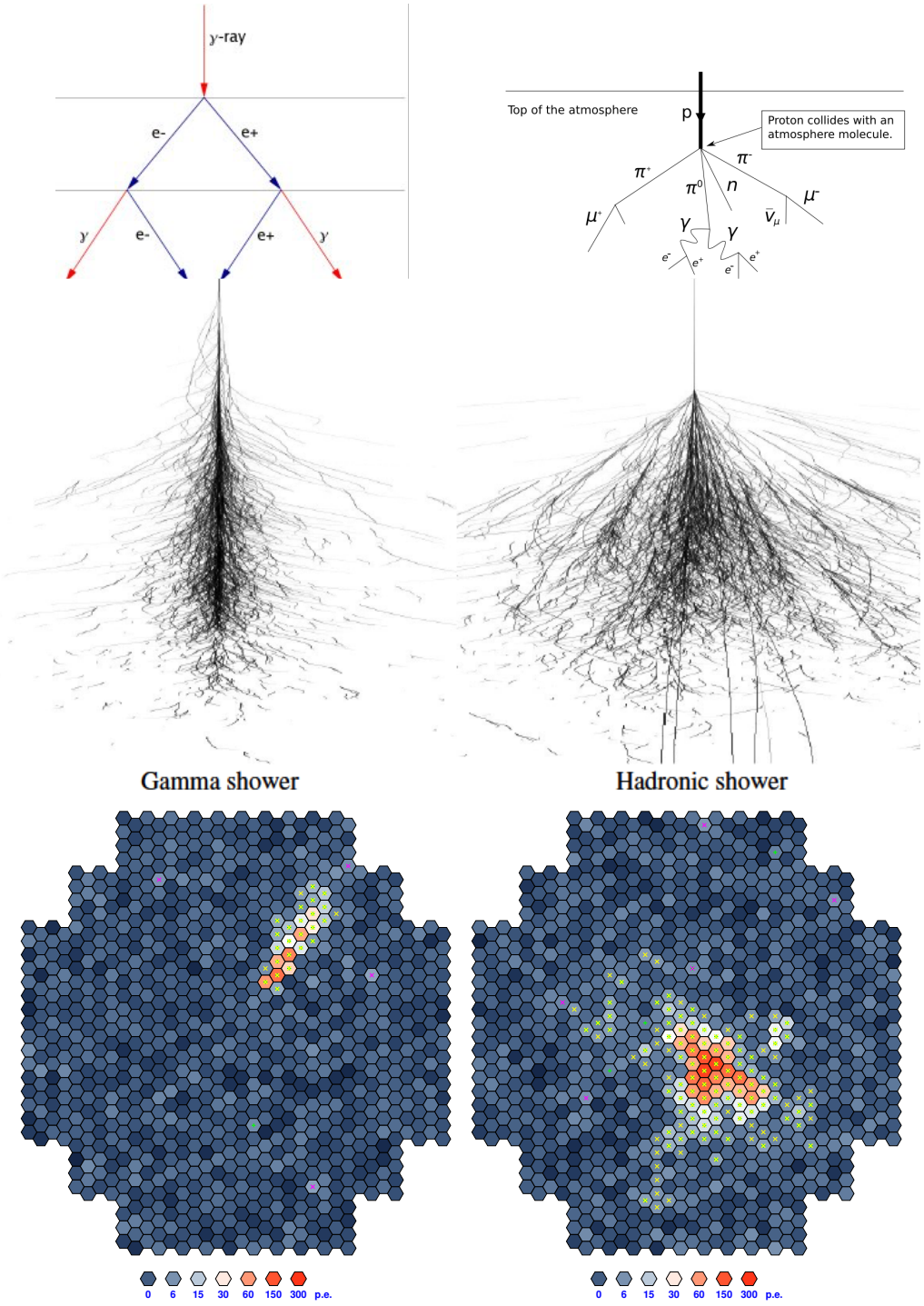

Figure 1.2: A comparison between the gamma shower(left) and hadronic shower(right) is shown. Top two figures explain the physics of the cascade processes, mid two figures show structures of cascade shower in the air, the bottom figures show the observed Cherenkov light of the cascade showers by the telescopes. The top left figure is from `http://community.dur.ac.uk/~dph0www4/whyare.php`. The top right figure is from Wikipedia. Mid and bottom pictures are from Völk & Bernlöhr (2009).

(Weekes et al., 1989). Significant improvement in sensitivity and energy resolution of the IACT technique was achieved later by the High-Energy-Gamma-Ray Astronomy telescope (HEGRA) through the introduction of stereoscopy, where showers are imaged simultaneously by multiple Cherenkov telescopes (Daum et al., 1997). Currently major operating IACTs include the Very Energetic Radiation Imaging Telescope Array System (VERITAS) (Weekes et al., 2002), the Major Atmospheric Gamma Imaging Cherenkov Telescopes (MAGIC) (Lorenz & The MAGIC Collaboration, 2004), and the High Energy Stereoscopic System (H.E.S.S.) (Aharonian et al., 2008c). Each of these currently operating IACTs has 2-5 telescopes. The next generation IACT – the Cherenkov Telescope Array (CTA) which is currently under construction will consist of tens of telescopes.

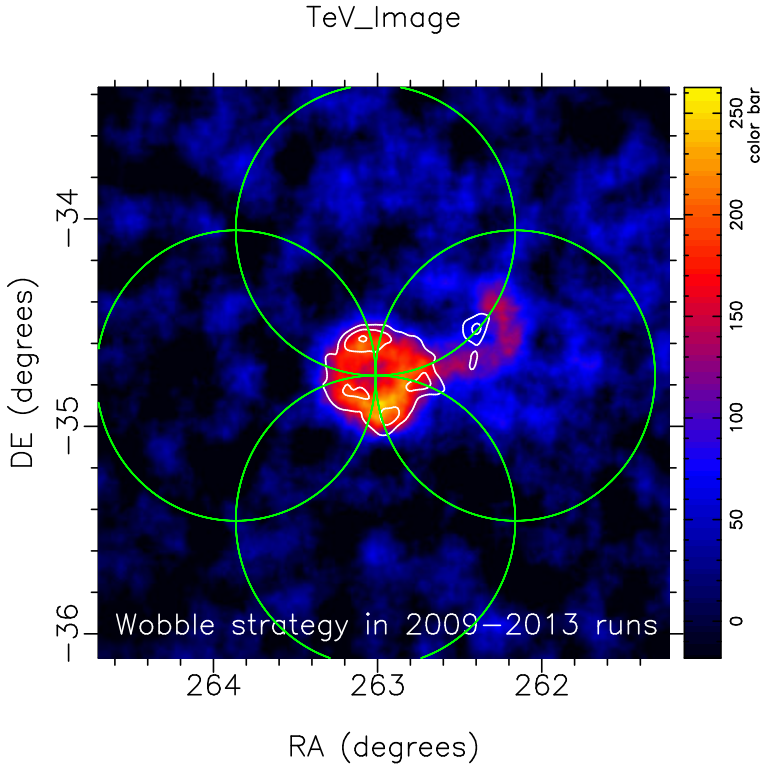

Figure 1.3: The wobble strategy used in the runs from 2009 to 2013 of Supernova remnant HESS J1731-347. The four green circles represent the viewing directions of H.E.S.S. with a wobble radius of 0.7°. The TeV image is obtained using the ImPACT analysis tool and runs in 2004-2013. The white contours represent the TeV morphology derived by H.E.S.S. Collaboration et al. (2011). The x and y coordinates represent the Right ascension and the Declination, respectively. More detailed information about this TeV image can be found in Chapt. 2.

Our studies in the following chapters mainly focus on the H.E.S.S. data of Supernova remnants in the southern sky. The H.E.S.S. located in Namibia is one of the most sensitive operating IACT at present time. As seen in Fig. 1.1, H.E.S.S. consists of four 12 meter telescopes (CT1-4) and one 28 meter telescope (CT5). In the H.E.S.S. system, once a certain number of pixels exhibit a signal larger than a given threshold (typically a few photoelectrons) simultaneously, an event is recorded (see e.g. Funk et al. 2004 for more details about the triggering system of H.E.S.S.). Currently events are split into two classes within the H.E.S.S.

system, mono-events which are seen only by CT5 and stereo events which are seen by at least 2 telescopes, these two classes can be analysed separately or joined into a single combined analysis (Parsons et al., 2015). By studying the Cherenkov shower patterns of each event (the raw data), the energies, the incoming directions, and the species of the VHE particles can be reconstructed. The available analysis tools for H.E.S.S. include Hillas, Model++, and ImPACT. While Hillas is based on the width and length of the shower pattern (Hillas, 1985), both Model++ and ImPACT are based on the Monte Carlo template of shower patterns (de Naurois & Rolland, 2009; Parsons & Hinton, 2014). The energy range of H.E.S.S. (CT1-5) is from 10s of GeV to 10s of TeV.

One of the most important tasks of these analysis tools is to separate the VHE photons – γ-rays from the majority of hadrons. As shown in Fig. 1.2, the gamma shower is slender and to a good approximation axially symmetric about the direction of the primary; the hadronic shower is irregular and may contain electromagnetic sub-showers as a result of the large transverse momenta generated in hadronic interactions (Völk & Bernlöhr, 2009). Through the analysis of shower patterns, most of the hadronic events can be removed. However, some hadronic events (mostly low energy events with weak showers), leptonic events (events with showers similar to those of the γ-rays), and other false events are difficult to be identified, therefore, further background reductions are required. To build the background, the simplest observation strategy which is barely used in H.E.S.S. operation is the on/off-observations of an astronomical target. The H.E.S.S. observational time is divided into many runs, each run has $\sim$ 30min time to track a given target. Runs with H.E.S.S pointing at the target (on-runs) and runs with H.E.S.S. pointing at an off-region (off-runs) are performed alternatively. The off-runs which are then used to derive a background estimate should use the same elevation of H.E.S.S. as used in the on-runs. If the target is smaller than the homogeneous field of view of H.E.S.S (beyond which the acceptance drops significantly, see also Sect. 2.1), then the wobble-observation becomes a more appropriate observational strategy with the pointing direction of H.E.S.S. offset from the target by roughly 0.5°–1.0° alternating in different directions in consecutive runs (see e.g. the wobble strategies of HESS J1731-347 in Fig. 1.3). The advantage of the wobble-observation is that each run can provide both the on-observation and off-observation and therefore a doubling of the observation time becomes available for target observations (see more details of observational strategies in Funk 2005).

1.2 The TeV sources

With the help of the Cherenkov telescopes, as seen in Fig. 1.4, many TeV sources have been unveiled. The well studied TeV sources can be classified mainly into Supernova remnants(SNRs), Pulsar wind nebulae(PWNe), and Active galactic nuclei(AGNs). Inside these TeV sources the shock acceleration or other acceleration mechanisms are able to accelerate charged particles up to from several to hundreds of TeV. There will be further discussions about shock acceleration in Sect. 3.1.

Most of the identified extragalactic TeV sources harbor an active galactic nuclei (AGN), where a supermassive black hole at galaxy center with mass $\sim 10^{6-9}\,\mathrm{M}_{\odot}$ accretes matter and powers jets – collimated highly relativistic outflows. The fundamental concepts concerning

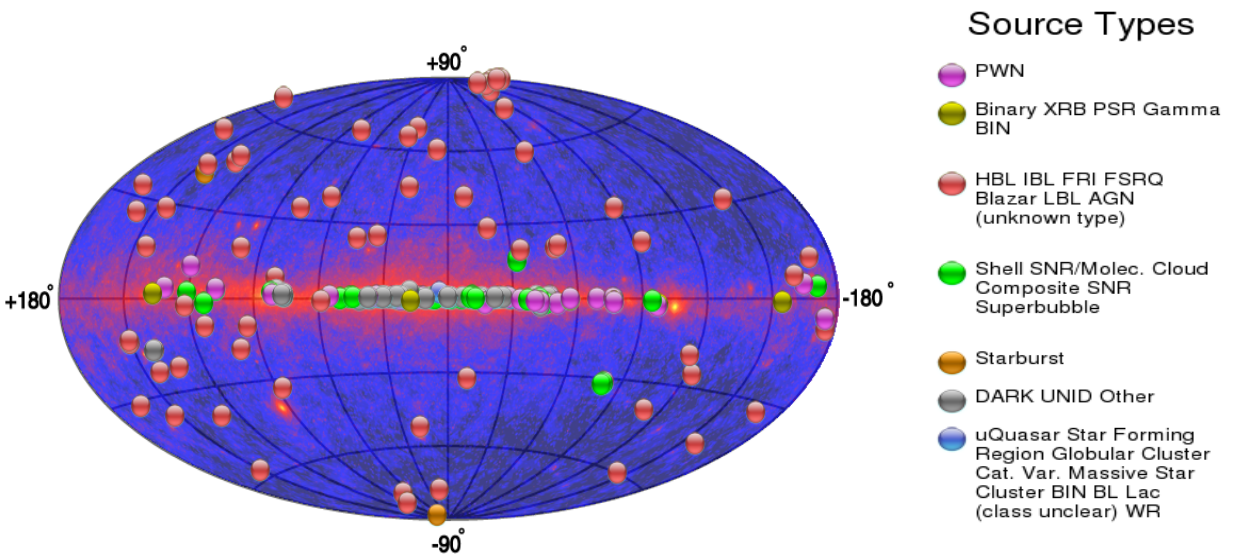

Figure 1.4: Known VHE sources as of August/2015 from the TeVCat catalog are plotted in Galactic coordinates. The colored background map show the sky map from the Fermi telescope. The color of each source identifies its source type as described in the right panel.

the AGN TeV sources can be found in the review paper by Hinton & Hofmann (2009). Except for M87 and Centaurus A, all of the AGN TeV sources belong to the blazar class where a jet is pointing toward the observer. These AGNs often show fast TeV variation within a time scale ranging from days to minutes, which may be the result of the acceleration sources being located in the vicinity of the black hole and/or beaming towards Earth (e.g. Narayan & Piran, 2012; Cui et al., 2012). The TeV photons from AGNs normally have to pass through the bright background from the host galaxies (including the accretion disks) as well as the extragalactic background (including the CMB) during their long journeys to Earth. Hence, the $\gamma\gamma$ absorption (TeV photons collide with soft photons – mainly the infrared photons, and become pairs of electrons and positrons) often plays an important role in reshaping the TeV spectra of AGNs. This absorption is clearly shown as the steepening with increasing energy in the TeV spectra of blazars, see e.g. the spectral energy distribution (SED) of Mrk 501 in Fig. 1.5. Additionally, the spectral indices also tend to increase with source distance, at least partly due to absorption of high-energy γ-rays on infrared intergalactic photon fields, but perhaps also related to the fact that distant AGN must be intrinsically brighter to be detectable.

Most of the identified Galactic TeV sources are PWNe and SNRs. The basic concepts about PWNe are summarized by Rees & Gunn (1974), Kennel & Coroniti (1984), and Gaensler & Slane (2006). The radiation from a PWN is mainly powered by a central pulsar, which generates a magnetized wind containing relativistic electrons and positrons. The wind collides with its surroundings and terminates in a shock, where the leptons can be further accelerated. Ultimately, these relativistic leptons, confined inside the SNR with energies up to PeV dominate the X-ray and IC γ-ray emissions, see e.g. the SED of Crab Nebula in Fig. 1.5. The pulsar in a PWN steadily released its total reservoir of rotational energy into its surrounding nebula during thousands of years. In contrast to the pulsar in a PWN, the dominant energy source for the nonthermal radiation of a SNR is the $\sim 10^{51}$ erg of kinetic

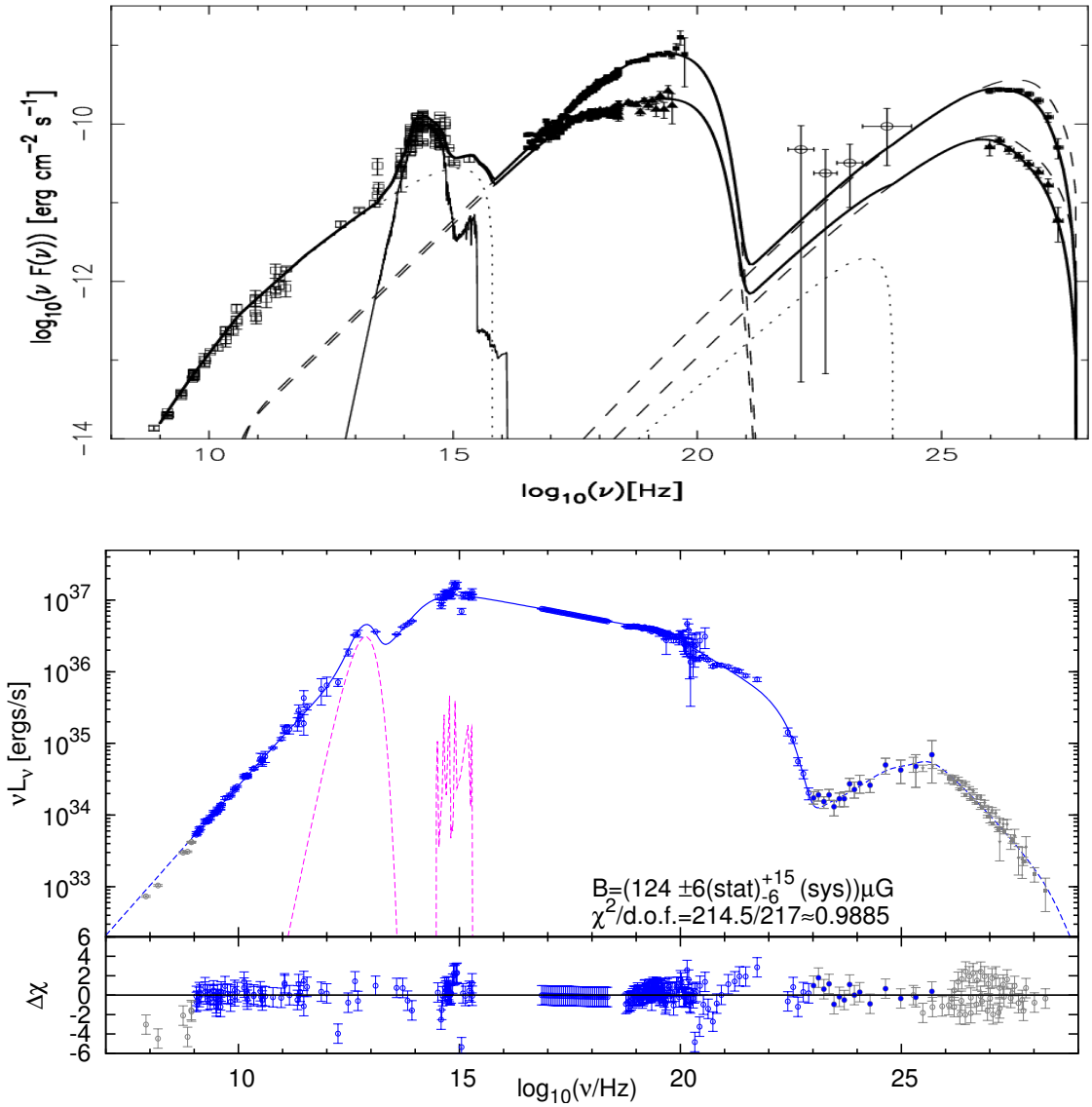

Figure 1.5: *The top panel* shows the spectral energy distribution (SED) of Mrk 501 in two different states from Katarzyński et al. (2001). The two dominant peaks are interpreted as synchrotron and synchrotron-self-Compton (SSC) emission of electrons (dashed lines). Modeling of the SED at lower frequencies adds contributions where external photons are Compton-scattered (dotted lines) and emission by the host galaxy (thin line at optical band). *The bottom panel* shows the SED of Crab Nebula from Meyer et al. (2010). The synchrotron emission fitted to the data is shown by the blue solid line while the remaining components (low energy part and inverse Compton emission) naturally result from the model in Meyer et al. (2010). In addition to the nonthermal continuum emission, the contribution of dust and line emission from the filaments is indicated with a magenta dashed line. The lower part show the residuals of the fit.

energy released at the moment of the original SN explosion. The SNRs are considered as good study platforms of shock acceleration, particularly in cases clearly showing nonthermal X-ray/γ-ray shells. The spectra of young SNRs are sometimes similar to those of PWNe, mostly due to that the nonthermal electrons are dominating the X-ray and γ-ray emissions.

In the following chapters we mainly focus on the TeV data of SNR HESS J1731-347 and SNR W28, considering their interesting TeV features and good multi-wavelength observational data.

1.3 Supernovae and Supernova remnants

Based on the explosion mechanism, supernovae (SNe) can be classified into type Ia or core collapse(CC) SNe. In the case of the type Ia SN, a white dwarf (Carbon Oxygen) has accreted enough mass ($1.38\,M_\odot$) from its companion star and is ready to re-ignite the carbon fusion process. This mechanism naturally leads to a very constant total explosion energy of $\mathcal{E}_{\rm ej} \approx 10^{51}$ erg (e.g. Mazzali et al., 2007). The core collapse SN has a massive progenitor star (about $8 - 50\,M_\odot$), the inner core of the progenitor at the end of the star life is already made of the most stable nuclear atoms (Iron Nickel) and supported by degeneracy pressure of electrons. When the mass of the inner core exceeds the Chandrasekhar limit of about $1.44\,M_\odot$, electron captures on nuclei (and some free protons) speed up and accelerate the implosion. The inner core then collapses into a neutron star (or a black hole) and releases neutrinos. The collapse of the inner core is halted by neutron degeneracy, causing the implosion to rebound and bounce outward. At the end of the CC SN stage, the gravitational energy in the progenitor is transformed into the SN explosion energy, where 99% of the total energy ($\sim 10^{53}$ erg) is released through neutrinos. The lowest-mass progenitors ($\sim 9\,M_\odot$) of CC SNe develop oxygen-neon-magnesium (O-Ne-Mg) cores through carbon (C) burning but reach electron degeneracy before hydrostatic Ne burning can be ignited. Due to the low reaction thresholds of Ne and Mg, the increasing electron Fermi energy enables electron captures, triggering gravitational collapse and resulting in an electron-capture SN (ECSN). The ECSNe could account for 20-30% of all SNe. More details of CC SN explosion can be found in Janka (2012).

In contrast to the quiet progenitor star of a type Ia SN, the massive progenitor star of a CC SN is able to blow out very strong stellar winds, which eventually form a very complex pre-SN environment. The pre-SN environment and the material left in the star before the SN determine the observational properties of a CC SN (e.g. the light curve and the metal lines), based on which core collapse SNe can further be classified into several subclasses. There will be further discussions about these subclasses in Sect. 4.1.

Unlike the significant bright SNe which can be seen tens of Mpc away, the relative dim SNRs can only be detected inside/near our Galaxy. During the thousands of years post-SN era, the evolution history of the SNRs can roughly be divided into three stages: ejecta-dominated stage, Sedov-Taylor stage, and radiation-loss-dominated stage (e.g. Truelove & McKee, 1999). The ejecta-dominated stage normally takes place in the first few hundred years after the SN, while the SNR expands with relativistic speed into the circumstellar medium. Once the shock sweeps enough material (roughly the ejecta mass), the SNR starts to slow down and enters the adiabatic-expansion or Sedov-Taylor stage. When the shock is further slowed and the radiation cooling becomes the dominating factor of energy loss, the SNR enters the radiation-loss-dominated stage. At the end of the SNR evolution history, when the SNR expanding speed is lower than the sound speed of the circumstellar medium, the shock can

no longer be formed and all the kinetic energy left is dissipated into local turbulence. During the first two stages, the SNR is considered as an excellent CR accelerating source because of the high velocity ($v_{\rm SNR} \approx 10^3 - 10^4\,{\rm km\,s^{-1}}$), large size ($r_{\rm SNR} \approx 1 - 10\,{\rm pc}$), and long surviving ($t_{\rm SNR} \approx 10^3 - 10^4\,{\rm years}$) time of its shock (e.g. Ptuskin & Zirakashvili, 2005).

1.4 Leptonic and hadronic models for TeV SNRs

In observational studies the SNRs are often the favored TeV sources because of their sharp shock morphologies in X-ray and sometimes in TeV band. At the shock front the Fermi acceleration is believed to be able to accelerate charged particles – mainly electrons and protons at least until the "knee". The synchrotron emission of the VHE electrons in the shock downstream can easily dominate the nonthermal X-ray emission of the SNR, see e.g. the nonthermal X-ray filaments of SNR Tycho and SNR Kepler in Vink (2006). The studies on these X-ray filaments can bring crucial constraints on the physical parameters of the shock, e.g. the velocity of the shock, the magnetic field and electron population at the shock. Unlike the X-ray emission, the TeV emission of the SNR could be either leptonic dominated or hadronic dominated. In this section, we present some key observational arguments to identify the origin of the TeV emission (leptonic or hadronic).

In the leptonic model a group of VHE electrons via the IC process can boost the energies of background soft photons from ν_0 to $\nu_{\rm p} = \gamma_{\rm e}^2 \nu_0$ (when $\nu_{\rm p} \ll \gamma_{\rm e} m_{\rm e} c^2$), where $\gamma_{\rm e}$ is the Lorentz factor of electrons. The background soft photons (Infrared - UV - X) can either come from outside sources in the external inverse Compton (EIC) model or from the same group of electrons in the synchrotron self Compton scattering (SIC) model. The SIC model has successfully explained the Broadband SEDs of many AGNs, e.g. the SED of Mrk 501 (Katarzyński et al., 2001) (Both the quiet and flaring states are shown in Fig. 1.5) and the SED of PKS 2155-304 (Kusunose & Takahara, 2008). The densities of both the VHE leptons and the magnetic energy in the SNRs are much lower in contrast to those in the AGNs, therefore, the synchrotron emissions in the SNRs are too weak for the SIC model to reproduce the TeV spectra. In the EIC model, local Galactic background of soft photons are normally adopted unless there are some stars or dust clouds in the vicinity of the SNRs (see e.g. Acero et al. 2015; H.E.S.S. Collaboration et al. 2011).

In the hadronic model some of the CRs are expected to have hadronic interactions with atoms/ions in the surrounding medium, e.g. the downstream plasma of the shock, molecular clouds (MC). In most cases the hadronic interactions are proton-proton (pp) collisions. When the total kinetic energy of the two protons exceed the rest mass of a pion (in the reference where the total momentum $P_{\rm pp} = 0$), the pions can be generated through $p + p \rightarrow p + p + \pi^0$ or $p + p \rightarrow p + n + \pi^+$, where the decay time of $\pi^0 \rightarrow \gamma + \gamma$ is only $\sim 10^{-16}$s. In the hadronic process the VHE photons are mostly attributed to CRs with $\gtrsim$10 times higher energy than that of photons (see the cross section profile of pp collision in Fig. 1.6). Hence, in order to reproduce a TeV spectrum with a given high-energy cutoff, the cutoff energy of the CRs in the hadronic model is about 10 times higher than that of the electrons in the leptonic model (see e.g. the typical SEDs of leptonic and hadronic model in Fig. 1.7).

Through studying some observational features of the SNR, the γ-ray production mechanism

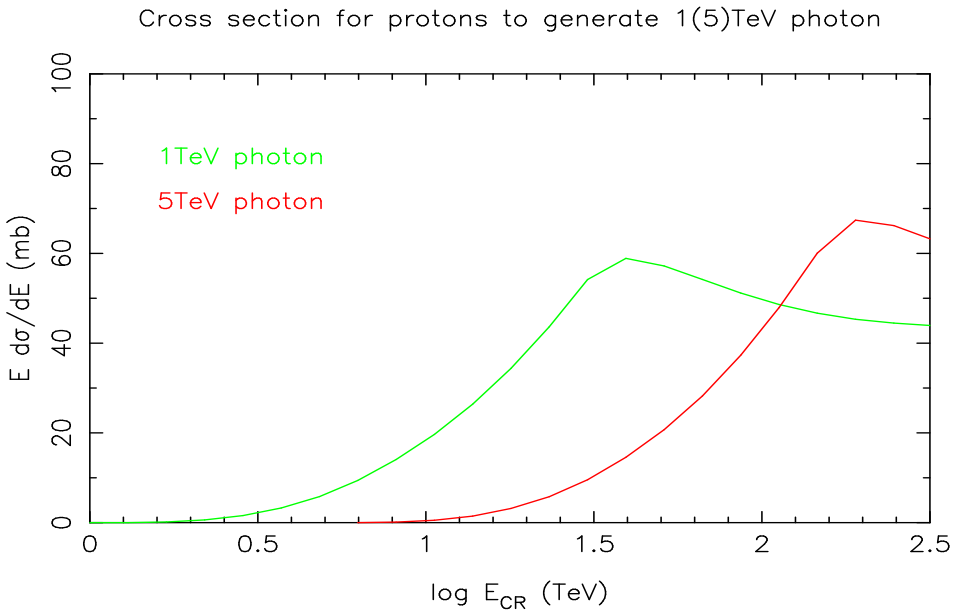

Figure 1.6: The cross section $E_{\rm CR}d\sigma/dE_{\rm CR}$ of proton-proton collision for generating 1 TeV(green line) and 5 TeV(red line) photons are shown. Cross section table used in this work are from Kachelrieß & Ostapchenko (2012).

(leptonic or hadronic) can be identified. The expected morphological features of the SNR in a leptonic/hadronic dominated scenario is presented in the following list.

- In the leptonic dominated scenario, the same group of electrons which emit the IC γ-ray are also responsible for the X-ray synchrotron emission, therefore, the nonthermal X-ray morphology could match well with the TeV morphology (see e.g. several young SNRs shown in Fig. 1.8). However, the inhomogeneity of the magnetic field at the shock should be taken into account for the synchrotron process if necessary, while the soft photon background is normally considered to be homogeneous.

- In the hadronic dominated scenario, the TeV emission is proportional to the CR density and the target gas density. In the case of an old SNR, the released CRs are homogeneously filling the space near the SNR after a long diffusion time ($\gtrsim 10$ kyr), and a good match between TeV morphology and gas density morphology can be expected (see e.g. the two old SNRs in Fig. 1.9). In the case of a young SNR, most of the accelerated CRs are still confined at/near the shock region, thus a TeV shell may be expected, and it is likely to be more extended (in both the upstream and downstream directions) than the X-ray synchrotron shell resulting from the much less energy loss of CRs via synchrotron radiation than that of electrons.

The expected spectral features of the SNR in a leptonic/hadronic dominated scenario is also presented in the following list.

- In the leptonic dominated scenario, the same group of electrons are used to fit both the TeV spectrum and the X-ray spectrum. The main parameters of the spectrum fitting include the magnetic field, the electron spectrum, and the spectrum of soft photon background. The magnetic field at the downstream of the shock can often

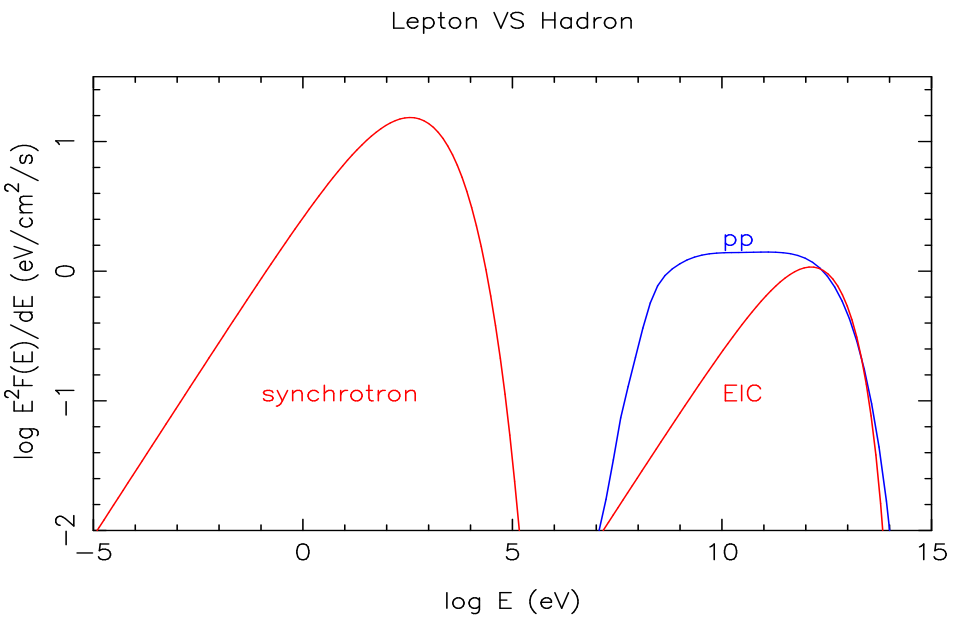

Figure 1.7: The example spectra of leptonic model(red) and hadronic model(blue) are shown. Both electrons and protons follow the power-law distribution $dN/dE \propto E^{-2}\exp(-E/E_c)$. The cutoff energy E_c for electrons/protons are 18/100 TeV. A magnetic field 25 μG is used in this synchrotron process. A blackbody spectrum with temperature 40K and density 1 eVcm^{-3} are used to represent the soft photon background.

be constrained through observational evidences, e.g. the X-ray filaments, while the soft photon background normally adopt the local Galactic background of soft photons. Therefore, the electron spectrum is sometimes the only free parameter in leptonic models. The high-energy cutoff of the IC spectrum is roughly as same as the cutoff energy of electrons. In the energy band right below the high-energy cutoff, the leptonic spectrum normally follows a relative hard power-law ($\Gamma \sim 1.5$), see the reproduced EIC spectrum in Fig. 1.7.

- In the hadronic dominated scenario, the TeV spectrum and the X-ray spectrum can be reproduced by the hadronic collisions of CRs and the synchrotron emission of electrons, respectively. This naturally leads to more free parameters in the hadronic dominated scenario. One of the most important parameters in the hadronic model is the target gas density. The density of cold gas – mostly molecular clouds (MCs) can be measured via ^{12}CO or CS emission lines, while the density of hot gas is normally measured through thermal X-ray emission. The hadronic model normally displays a relative softer power-law spectrum in the energy band lower than $\sim 10\%$ of the cutoff energy of CRs. See the reproduced hadronic spectrum (blue line with power-law index $\Gamma \sim 2.0$) in Fig. 1.7. Since the SNRs mentioned in our study are all Galactic sources, we ignore the Klein-Nishina effect in both the leptonic and hadronic models.

Overall, due to that the old SNRs can no longer accelerate fresh electrons, their γ-ray emissions display hadronic observational features. The γ-ray spectra of many young SNRs have shown a high-energy cutoff of ~ 1 TeV, therefore, the GeV observation (with the Fermi telescope) often becomes the key argument of choosing leptonic/hadronic model. More

observational properties of young/old SNRs are summarized in the following section.

1.5 Young and old SNRs

Young SNRs are considered to be still inside the ejecta-dominated stage or the Sedov-Taylor stage, while old SNRs are considered to be in the post Sedov-Taylor stage (more details about SNR evolution can be found in Sect. 4.1). There is no clear line to classify the SNRs into young or old, however, some direct and indirect observational evidences for a rough classification are discussed in the following list (see also the eight well studied SNRs listed in Table 1.1).

- Some young SNR detected today have been associated with SNe found in astronomy records, e.g. SN185 (RCW86), SN1006, SN1572 (Tycho), SN1604 (Kepler), SN1987A. These records provide us not just the ages of the SNRs, sometimes they also bring informations about the SNe and the progenitors.

- The shock velocity of a young SNR is much higher $v_{\rm SNR} \gtrsim 1000\,{\rm km\,s^{-1}}$ than that of an old SNR. The shock velocity can directly be measured through observing the filaments expansion (from radio to X-ray band) over years or through observing the emission/absorption lines (mainly in the optical band; mostly used in old SNRs) from the post-shock gas.

- Young SNRs with high shock velocity are likely to display X-ray synchrotron shells (see e.g. the young SNRs in Fig. 1.8). Vink (2012) found that the SNRs with high shock velocity ($v_{\rm SNR} \approx 2000 - 6000\,{\rm km\,s^{-1}}$) are always accompanied with X-ray synchrotron emission ($\sim$1 keV) and sometimes with clearly detected X-ray filaments at the shock front. This finding is also supported by the theory that the synchrotron peak energy does not depend on magnetic field strength but only on the shock velocity (e.g. Aharonian & Atoyan, 1999; Vink, 2013): The mean diffusion distance of electrons during time t is $r_{\rm dif} \approx \sqrt{Dt}$, where $D \approx \eta cE/3eB$ and η is the length of mean free path in unit of gyro-radius, then the typical acceleration time scale can be written as $\tau_{\rm acc} = D/v_{\rm SNR}^2$ assuming that the acceleration stops when the shock sweeps the plasmas further than the mean diffusion distance. The typical synchrotron loss time of the electrons is $\tau_{\rm sun} = 636/B^2E\,{\rm s}$. When $\tau_{\rm acc} < \tau_{\rm sun}$, we can derive the maximum electron energy as $E_{\rm max}^2 \propto v_{\rm SNR}^2/(\eta ceB)$. Ultimately, the peak photon energy is obtained as $h\nu \propto E_{\rm max}^2 B \propto v_{\rm SNR}^2$ (Vink, 2013).

- Young SNRs also tend to show shell structure in TeV morphology (see the four young SNRs in Fig. 1.8). In the leptonic dominated scenario, high velocity shock is the key factor in generating fresh VHE electrons. In the hadronic dominated scenario, high velocity shock can maintain strong magnetic turbulence at the shock which helps confining the VHE CRs there, see e.g. the hadronic model for SNR RX J1713 with the assumption that the SNR has just encountered with the main-sequence bubble shell (Berezhko Völk, 2006).

Table 1.1: The properties of some well studied SNRs

SNR	Type	$t_{\rm SNR}$ (year)[a]	$r_{\rm SNR}$ (pc)[b]	$v_{\rm SNR}$ ($\rm km\,s^{-1}$)[c]	$n_{\rm H}$ ($\rm cm^{-3}$)[d]	TeV[e]	Match-X[f]	GeV[g]
Tycho[r1,r5]	Ia	440	2	4500	0.3	low-res(V)	-	1.97
Kepler[r1,r3,r6]	Ia	410	2	4200	0.35	no(H)	-	-
SN1006[r1,r10,r11]	Ia	1000	10	4300	0.1	shell(H)	yes	$\lesssim$1.7
Cas A[r1,r4]	CC	300 - 400	2.5	5200	3	low-res(V)	-	2.0
RX J1713[r2,r12,r13]	CC	1600	10	4500	$\lesssim 0.02$	shell(H)	yes	1.5
Vela Jr.[r2,r14,r15]	CC	2k - 4k	12	1500	$\lesssim 0.03$	shell(H)	yes	1.85
HESS J1731[r2,r16,r17]	CC	2k - 6k	$\gtrsim$15	2000	$\lesssim 0.01$	shell(H)	roughly	<1.5
W28[r7,r8,r9]	?	40k	12	80	5	diffuse(H)	no	2.74

[a] The age of the SNR at present time. Here only Tycho, Kepler, SN 1006 and RX J1713 are associated with corresponding guest stars on the ancient astronomy records. The ages of other SNRs are derived from SNR evolution models.
[b] The radius of the SNR at present time. The radius is based on the distance of the SNR which is normally obtained through X-ray absorption or association with nearby objects (e.g. Molecular clouds).
[c] The velocity of the forward shock at present time. Here only the shock velocities of Tycho, Kepler, SN 1006, Cas A and W28 are obtained with direct observational evidences. The others are derived from SNR evolution models.
[d] The density of the medium where the SNR is expanding into. Here only the density of the surrounding medium of Tycho, Kepler, SN 1006, Cas A and W28 are obtained with direct observational evidences. The upper-limits of the medium densities surrounding other SNRs are given based on the lack of thermal X-ray emission.
[e] The TeV morphology which is observed by H.E.S.S. (H) or Vertitas (V). The "low-res" represents that the resolution in the TeV band is too low to identify a shell structure in the SNR. The "no" represents no detection in the TeV band at all. The "diffuse" indicates that an extended TeV structure is found but it is not shell shaped.
[f] Whether the X-ray morphology matches with the TeV one.
[g] The spectrum index detected with Fermi telescope. W28 has displayed two diffuse sources in Fermi sky map – source N (the main source at the SNR region) and source S(a weaker source to the South of the SNR). Photon index 2.74 is for source N and 2.19 is for source S.

References: r1 (Vink, 2006, and references therein); r2 (Acero et al., 2015, and references therein); r3 (Vink, 2008); r4 (Ghiotto & for The VERITAS Collaboration, 2015); r5 (Park & for the VERITAS Collaboration, 2015); r6 (Aharonian et al., 2008d); r7 (Aharonian et al., 2008a); r8 (Rho & Borkowski, 2002); r9 (Gabici et al., 2010); r10 (Acero et al., 2010); r11 (Acero et al., 2015); r12 (Acero et al., 2009); r13 (Abdo et al., 2011); r14 (Aharonian et al., 2007); r15 (Tanaka et al., 2011); r16 (H.E.S.S. Collaboration et al., 2011); r17 (Cui et al., 2016)

- Due to the lack of fresh accelerated VHE electrons, the old SNRs show neither the nonthermal X-ray emission nor the IC γ-ray emission. Sometimes the diffuse thermal X-ray emission which is caused by the hot gas left inside the old SNRs can be seen (see e.g. the X-ray emission from SNR W28 Rho & Borkowski 2002 and from SNR IC443 Asaoka & Aschenbach 1994).

- The old SNRs often show diffuse TeV morphologies instead of TeV shell structures, this is due to that the hadronic TeV emission is mainly attributed to the CRs released from the SNR tens of kyr ago. As a result of the old age of the SNR, the CRs have enough

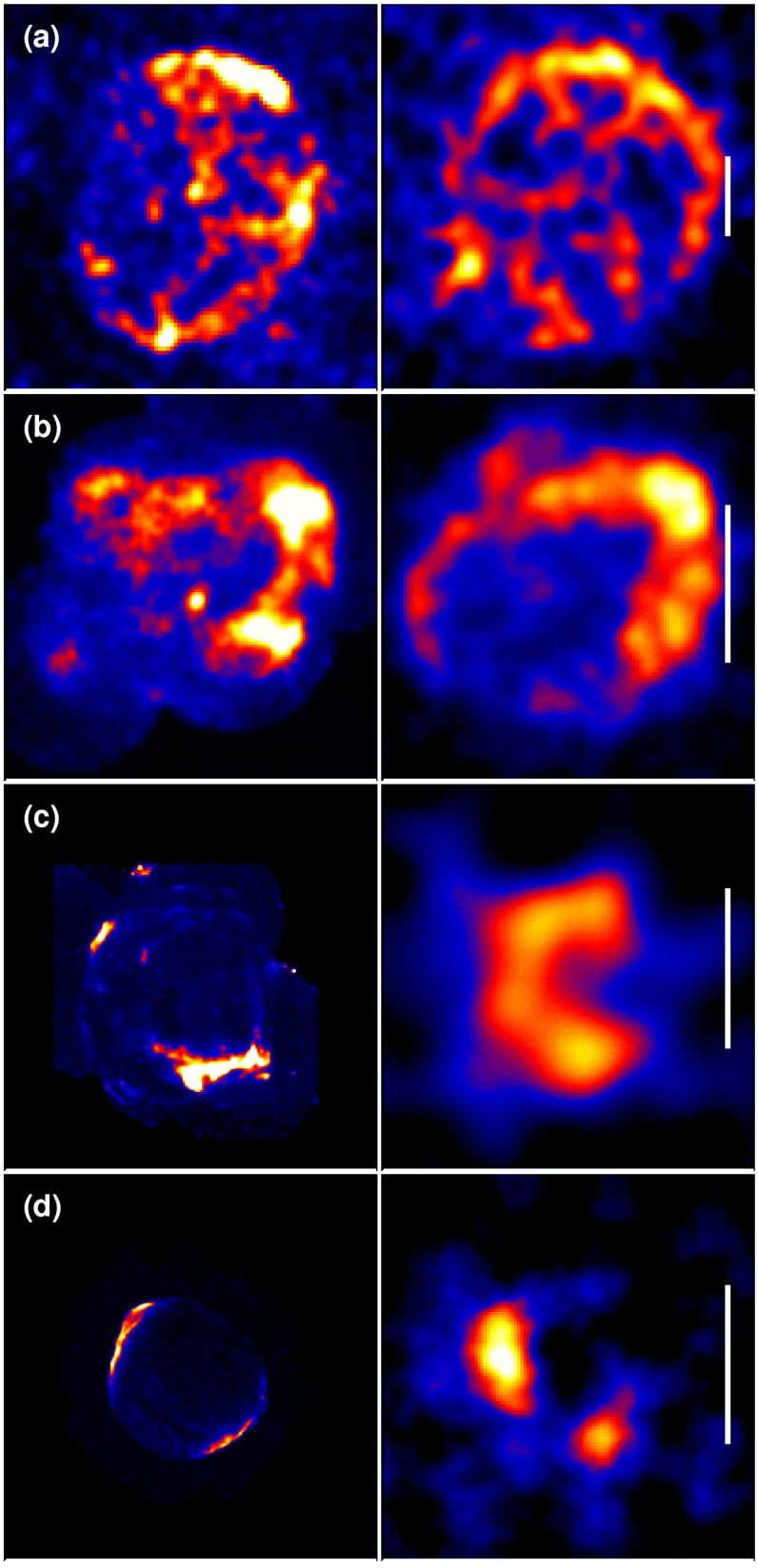

Figure 1.8: Four SNRs imaged in (dominantly) nonthermal X-rays (left) and resolved in VHE γ-rays with H.E.S.S. (right). a) RX J0852.0-4622 with ROSAT (1.3–2.4 keV) , b) RX J1713.7-3946 with 1–3 keV data from ASCA , c) RCW 86 with 2–4 keV data from XMM-Newton, d) SN 1006 with Chandra archive data (0.5–10 keV). The white scale bars are 0.5° long. All figures are taken from Hinton & Hofmann (2009).

time to diffuse and become more homogeneously distributed near the SNR. As seen in Fig. 1.9, inside and around both the SNR W28 and SNR IC443 the gas morphologies match well with the TeV morphologies. Meanwhile, the GeV emission of SNR W28 is mostly from regions very close to the SNR (Abdo et al., 2010), this situation is well explained with the shock accelerating theory that only the super-TeV CRs are released at the early stage of SNR, while the GeV CRs are trapped behind the shock for relative longer time until the shock is slowed and disassembled eventually. More detailed study of SNR W28 can be found in Chapt. 7.

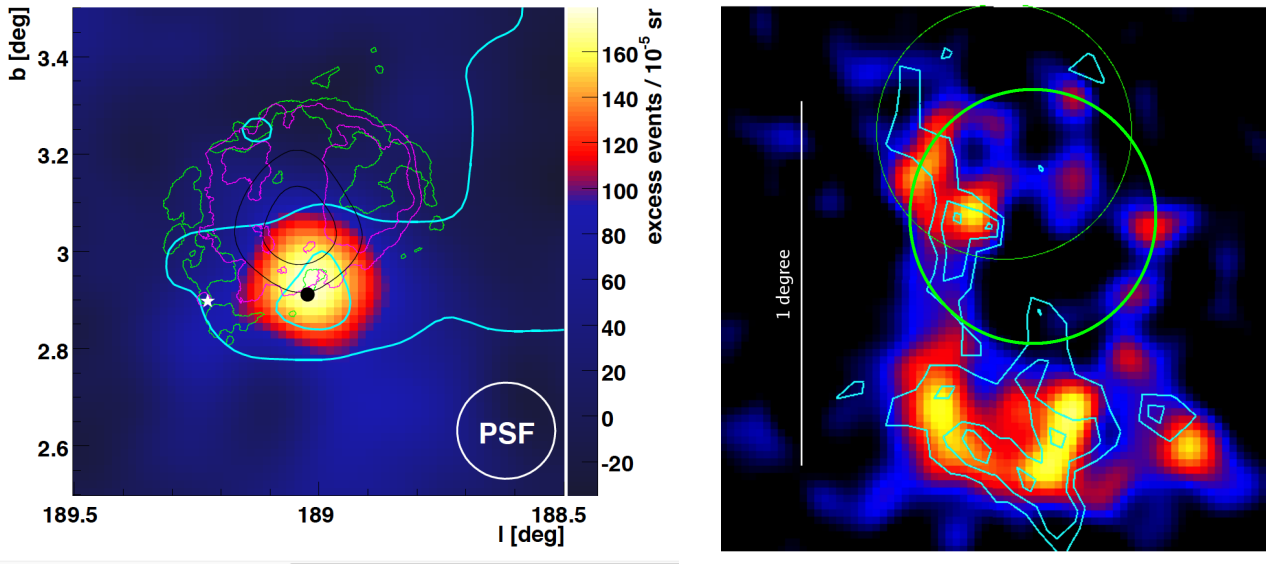

Figure 1.9: Multiwavelength views of IC443 (left) and W28 (right). Molecular tracer ^{12}CO (J=2→1) is shown (cyan contours) in comparison to TeV data (color scale) from H.E.S.S.(right) and MAGIC(left). For IC443, green contours are 20 cm VLA radio data, X-ray contours from ROSAT are shown in purple, γ-ray contours from EGRET are shown in black. For W28, the thick green circle represents the radio boundary. Figures are taken from Hinton & Hofmann (2009), Albert et al. (2007) and Aharonian et al. (2008a).

As seen in Table 1.1 and Fig. 1.8, all the three SNRs – RX J1713.7-3946, Vela Jr, and HESS J1731-347 share similar physical features including large size, young age, high shock velocity, low density of the circumstellar medium, clear shell structures in both the X-ray and TeV band, and hard GeV spectrum. These three SNRs together with RCW86 are known as siblings in Yang et al. (2014) and may be still expanding inside the pre-SN wind bubbles. Their hard GeV spectra and low densities of the circumstellar medium can be well explained with leptonic models, but the hadronic models are not excluded as well, considering that in certain localized regions of these SNRs the shock probably encounters enhanced densities and that locally the hadronic contribution might become important. The next generation of Cherenkov telescopes such as CTA will provide the necessary angular resolution to carry out detailed spatially resolved spectroscopy, which might unveil different emission mechanisms depending on the regions (Acero et al., 2015).

2

Motivation to study HESS J1731-347

HESS J1731-347 was first discovered as an unidentified TeV source presented in Aharonian et al. (2008b). This TeV source is in spatial coincidence with a new discovered radio SNR (G353.6-0.7) by Tian et al. (2008). The following X-ray and TeV observations of this SNR (H.E.S.S. Collaboration et al., 2011) have shown a clear shell structure with nonthermal radiation. Additionally, at the center of the SNR (RA=17h32m03s, Dec = −34°45'18"), the thermal X-ray emission from a compact centre object (CCO) has been discovered. Upper limits of the GeV emission from the SNR region are given by Yang et al. (2014); Acero et al. (2015). According to the classification of the SNRs discussed in the last chapter, SNR HESS J1731-347 is likely to be a young SNR with TeV emission of leptonic origin. The most unique and interesting feature of HESS J1731-347 is the discovery of a bright TeV structure – HESS J1729-345 (RA=17h29m35s, Dec = −34°32'22") to the Northwest of the SNR. In the following work, we refer to HESS J1731&J1729 as the sum of SNR HESS J1731-347 and HESS J1729-345.

The TeV data and the multi-wavelength data of HESS J1731&J1729 are presented in Sect. 2.1 and Sect. 2.2, respectively. Several arguments about the distance of the SNR HESS J1731-347 are described in Sect. 2.3. We also discussed the possible hadronic/leptonic explanations for the TeV emission of HESS J1731&J1729 in Sect. 2.4. At the end, our motivations behind studying HESS J1731-347 are given in Sect. 2.5.

2.1 TeV data

With 59 hours good quality data from H.E.S.S. during 2004-2009 and a sensitive analysis tool – Model++, H.E.S.S. Collaboration et al. (2011) has delivered a clear TeV shell – SNR HESS J1731-347 (detection significance 22σ) and an extended TeV source – HESS J1729-345 (8σ), see the left panel in Fig. 2.4. In 2013 another 27.1 hours of H.E.S.S. observation were obtained on HESS J1731&J1729. The data from 2013 have been preselected in our following data analysis according to spectral selection criteria (e.g. each run must have ≥ 2 telescopes working and must last ≥ 10 minutes). After the selection, the 2013 data set include only 6.8 hours data of HESS II configuration (HESS II hybrid data are taken by telescopes including CT5 from Jun-2-2013 to Jun-16-2013) and 19.4 hours data of HESS I configuration. The HESS II hybrid data have not been analyzed in our study, due to CT5 data quality issues in the period when the data have been taken.

There are three data lists adopted in our analysis.

1. *The old list* is the data set used in H.E.S.S. Collaboration et al. (2011), it consists of 59 hours good quality runs during 2004-2009.

2. *The new list* is the sum of the old list and the selected data from 2013, it consists of totally 59 + 19 hours runs.

3. *The reduced new list* is based on the new list, but without the runs which are not supported by ImPACT yet. In the reduced new list, we still have 54 (2004-2009)+13 (2013) hours available data.

In this section, the analysis tools – TMVA (a Hillas based analysis tool using the multivariate training machinery tool-kit, see `http://tmva.sourceforge.net/`) and ImPACT are used in our TeV analysis. The analysis results with Model++ (H.E.S.S. Collaboration et al., 2011) are also shown for comparison.

2.1.1 The morphological analysis of the TeV data

Following Berge et al. (2007), we adopt the ring background method in our morphological analysis and the reflected background method in our spectral analysis. As discussed in Sect. 1.1, a wobble strategy is used in the runs of HESS J1731&J1729 during 2009-2013, and the viewing positions of the wobble strategy are marked as white crosses in Fig. 2.1 and 2.3. The goal of the background reduction is to find the appropriate off-events (background events) for the on-events (the events collected in the target region). In both the ring and reflected background methods, the background estimate is derived from the same run as the on-events. Thus a good wobble strategy should contain runs with good observations on both the target region and the background regions.

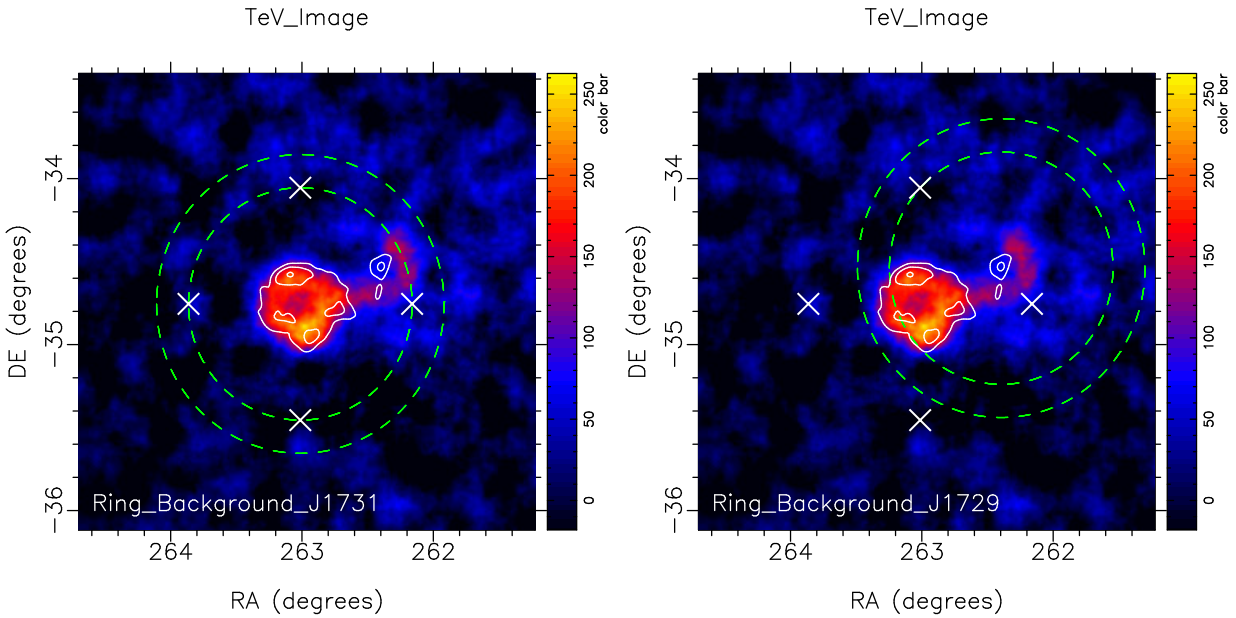

Figure 2.1: Ring backgrounds of the pixels located at the center of SNR HESS J1731-347 (left panel) and the center of HESS J1729-345 (right panel) are shown in dashed rings. The radius of the rings is $0.7° - 0.9°$. The TeV image is obtained through ImPACT analysis tool and runs from 2004-2013. The white contours represent the TeV morphology of HESS J1731&J1729 from H.E.S.S. Collaboration et al. (2011). The viewing position in 2009-2013 runs are marked in white crosses.

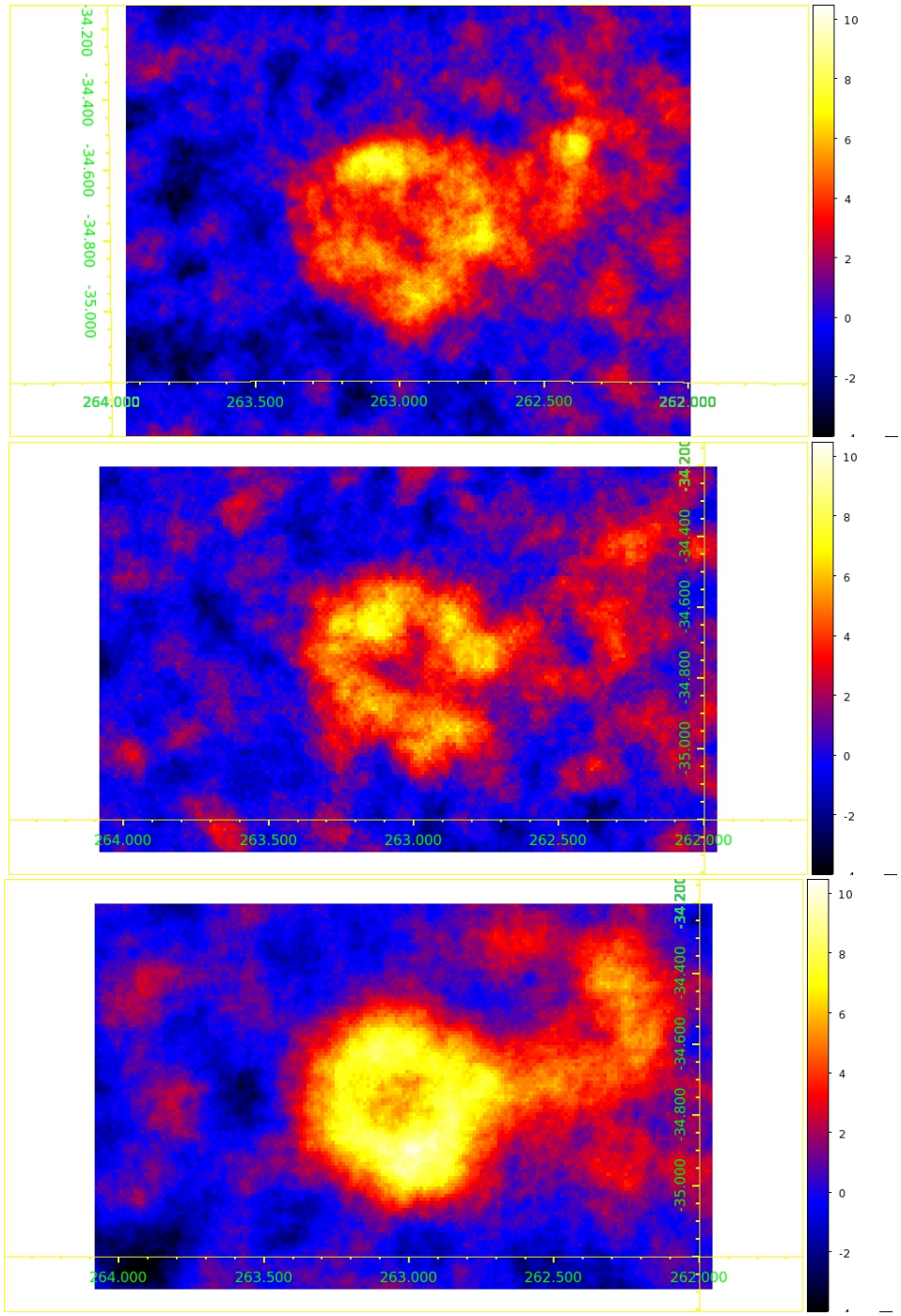

Figure 2.2: The TeV image (significance map) of HESS J1731&J1729 derived through different analysis tools & data sets, including Model++ & old data (top panel; the data is taken from H.E.S.S. Collaboration et al. 2011), TMVA & old data (middle panel), and ImPACT & reduced new data (bottom panel), are shown. See more details about data sets in the text. X axis is the Right ascension(RA) and Y axis is the Declination(Dec). All three images use the same color bar, the same correlation radius of 0.06° and the same bin size of 0.01°. The bottom panel which uses the new list (more hours of data) naturally shows higher significance at the on-region.

In the ring background method, each pixel on the image is associated with a ring-shaped

(torus-shaped) background which is centered at the pixel itself. In Fig. 2.1, the ring background method used in our analysis is shown. The exclusion region of the background which is not shown here is mainly made of the SNR HESS J1731-347 region and the northwest region (roughly centered at the HESS J1729-345 region).

Obviously, the wobble strategy during 2009-2013 works well for SNR HESS J1731-347, but not well for HESS J1729-345. For most of the pixels at the SNR HESS J1731-347 region, the angular offsets of the ring backgrounds from the viewing positions are only $\lesssim 1.6^\circ$ (see the left panel in Fig. 2.1). In HESS J1729-345 region, both the on-events and their backgrounds suffer from the large angular offset from the east and south viewing positions (see the right panel in Fig. 2.1). The acceptance of H.E.S.S. drops significantly when the angular offset of an event from the viewing position is above $\sim 1.0^\circ$.

In Fig. 2.2, we list three TeV images of HESS J1731&J1729 under different analysis scenarios (different analysis tools and data sets). Despite some minor differences among these three images, a clear shell structure at SNR HESS J1731-347 and an extended TeV source at HESS J1729-345 are shown in each image. The SNR HESS J1731-347 has displayed a quite low TeV flux ($F_{\rm J1731} \sim 9\%$ of that from Crab Nebula or 9% crab) and a quite small TeV shell ($R_{\rm J1731} \sim 0.3^\circ$), in contrast to its sibling – SNR RX J1713.7-3946 ($F_{\rm J1713} \sim 66\%$ crab and $R_{\rm J1713} \sim 0.65^\circ$). Higher flux naturally leads to better statistics for both the morphological and spectral analysis. Larger size of the TeV source leads to higher ratio between the source size and the average PSF, resulting in a better TeV morphology, where the PSF (point source function) represents the uncertainty in the direction reconstruction of each event. Therefore, it is not surprising to find differences among the TeV images of HESS J1731&J1729 when different analysis tools are used (see Table 2.1 and Fig. 2.2). Especially in the even fainter region – HESS J1729-345, a bridge structure connecting the SNR and HESS J1729-345 is found in our ImPACT analysis. Overall, these differences are most likely to reside in the statistical fluctuations.

2.1.2 The spectral analysis of the TeV data

As seen in Fig. 2.1, the reflected background method is used in our spectral analysis. In the reflected background method, the on-region (target region) tries to get as many reflected backgrounds as possible on a ring around the viewing position. Under the assumption of rotational symmetry in the acceptance of H.E.S.S., the reflected background method is independent of the exact shape of the acceptance function. For the simplicity of Fig. 2.1, only the reflected backgrounds surrounding the north and south viewing positions are shown. Here the exclusion region of the background is the same one mentioned in the ring background method. The reflected backgrounds which overlap with the exclusion region are not shown.

The angular offset of the reflected backgrounds of HESS J1729-345 from the north, south and east viewing position are $\sim 0.7^\circ, \sim 1.0^\circ$, and $\sim 1.2^\circ$, respectively. In the runs with the west viewing position, due to the too small angular offset of HESS J1729-345, there are hardly any reflected backgrounds.

In the spectral analysis of SNR HESS J1731-347, results of four different analysis scenarios with different analysis tools and/or data sets are listed in Table 2.1. Same on-region (see the big white dashed circle in the left panel of Fig. 2.4) is used in each analysis scenario, since

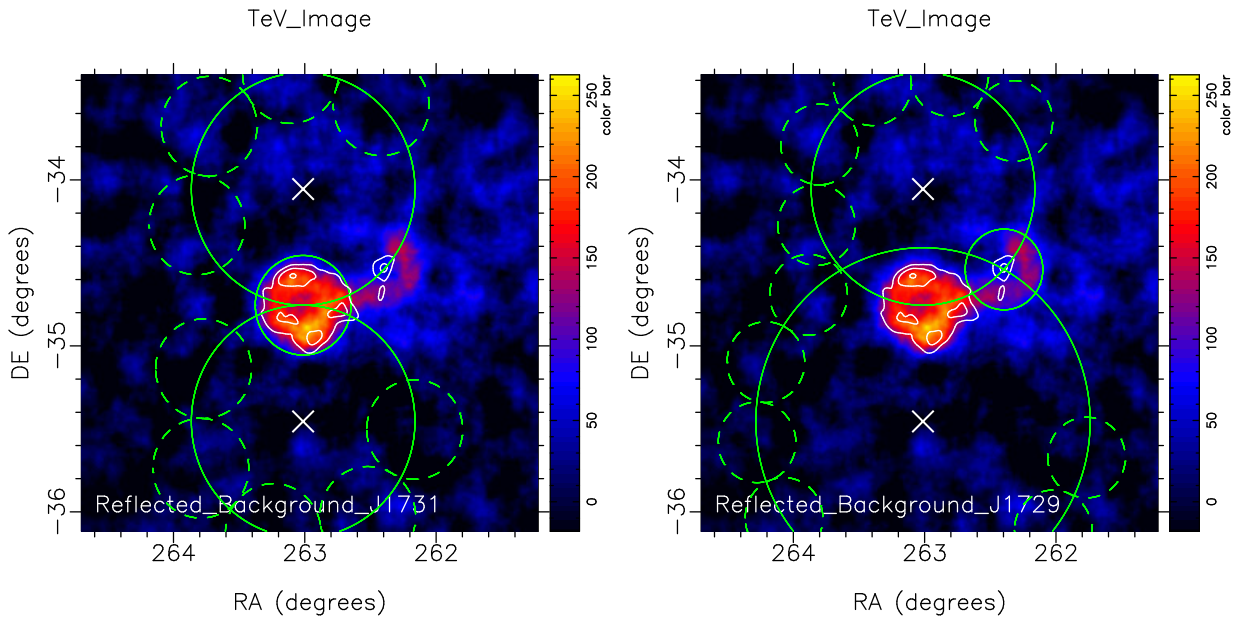

Figure 2.3: Reflected backgrounds (dashed green circles) of SNR HESS J1731-347 (left panel) and HESS J1729-345 (right panel) are shown. The on-regions are marked in small solid circles. The radius of the big green circles (0.7° and 0.9°) represent the angular offset of the on-regions from the viewing positions. The TeV image and the white contours use the same setup in Fig. 2.1.

Table 2.1: Spectrum analysis with different analysis tools and data sets

Region	data sets	analysis tools	power-law index
HESS J1731-347[a]	old list	Model++	2.32 ± 0.06[e]
HESS J1731-347	old list	TMVA	2.31 ± 0.05
HESS J1731-347	new list	TMVA	2.31 ± 0.04
HESS J1731-347	reduced new list	ImPACT	2.32 ± 0.05
HESS J1729-345[b]	old list	Model++	2.24 ± 0.15
HESS J1729-345 full circle[c]	reduced new list	ImPACT	2.45 ± 0.17
HESS J1729-345 partial circle[d]	reduced new list	ImPACT	2.44 ± 0.12

[a] The circle region centered at the CCO with a radius of 0.3° is shown as the big white dashed circle in the left panel in Fig. 2.4.
[b] The circle region centered at HESS J1729-345 with a radius of 0.14° is shown as the small white dashed circle in the left panel in Fig. 2.4.
[c] The circle region centered at HESS J1729-345 with a radius of 0.24° is shown as the red circle in the right panel in Fig. 2.4.
[d] The partial ring region centered at HESS J1729-345 with a radius of $0.07 - 0.24°$ is shown as the green partial region in the right panel in Fig. 2.4.
[e] Analysis results with old list & Model++ are taken from H.E.S.S. Collaboration et al. (2011). All spectra are obtained through forward folding method. The errors shown here are only statistical errors, while systematic errors are $\sim \pm 0.2$.

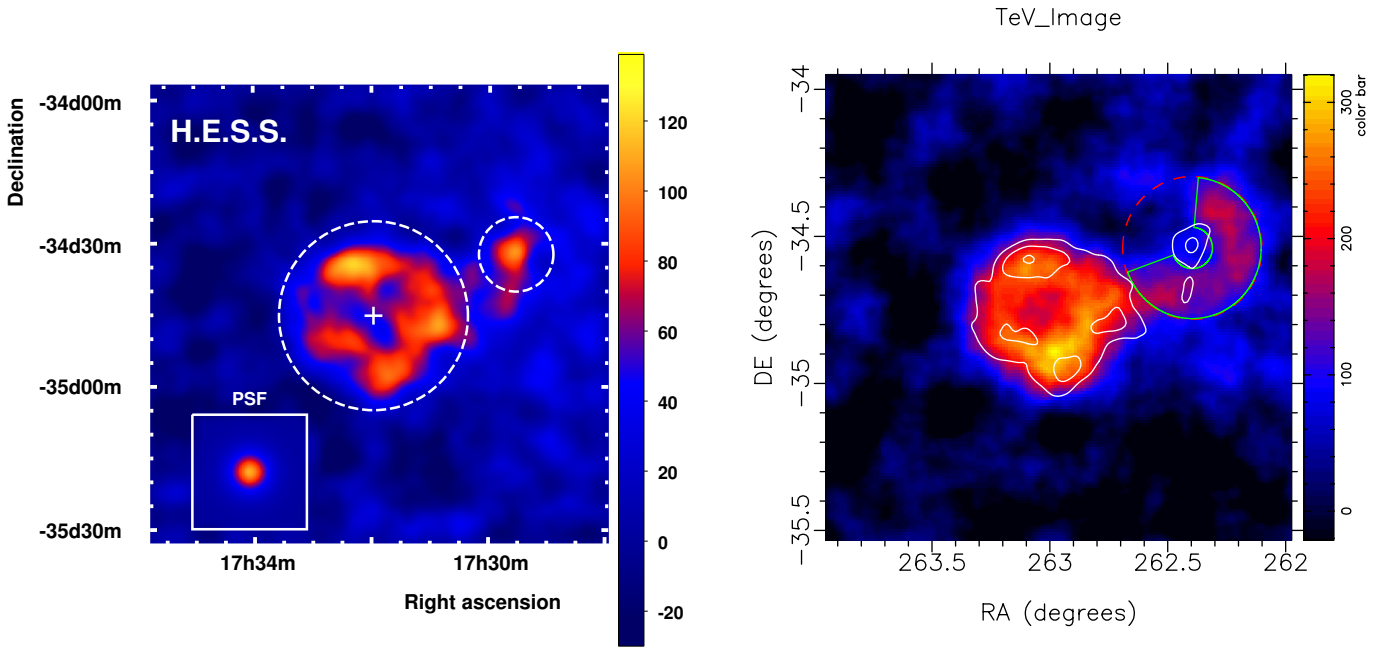

Figure 2.4: *Left panel*: The TeV image (excess map) using Model++ and old list is smoothed with Gaussian width 0.04° (H.E.S.S. Collaboration et al., 2011). The big dashed circle is centered at the CCO with a radius of 0.3°, the small dashed circle is centered at HESS J1729-345 with a radius of 0.14°. *Right panel*: The TeV image (excess map) using ImPACT and reduced new list is smoothed with Gaussian width 0.03°. The white contour represents the TeV morphology from the left panel. Special areas marked with red dashed lines and green lines at the HESS J1729-345 region are used for further spectrum analysis, whose results are shown in Table 2.1 and Fig. 2.5.

the SNR morphology of each analysis scenario can match well with this on-region (see e.g. the three SNR morphologies in Fig. 2.2). These four analysis scenarios have delieved almost identical spectral results – a power-law spectrum with index $\Gamma \approx 2.32$, thus we only display one spectrum of SNR HESS J1731-347 in Fig. 2.5.

Although different morphological results of HESS J1729-345 are found in different analysis scenarios, the existence of HESS J1729-345 to the Northwest of the SNR is unquestionable. As seen in Fig. 2.4, three different on-regions (small white dashed circle, green contour, red dashed circle) of HESS J1729-345 are chosen in three different spectral analysis scenarios (list in Table 2.1). As seen in Fig. 2.5, the results of the spectral analysis of HESS J1729-345 with different on-regions are shown.

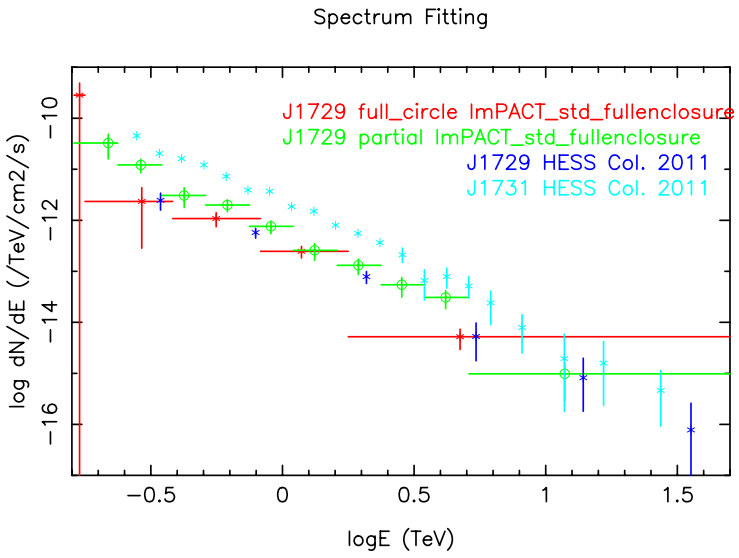

Figure 2.5: The reduced spectra of HESS J1731&J1729 under different analysis scenarios are shown. More details about the setup in each analysis scenario can be found in Table 2.1 and Fig. 2.4. Blue(HESS J1729-345) and light blue(HESS J1731-347) stars are from H.E.S.S. Collaboration et al. (2011) (Model++ & old run list). Since the spectrum analysis of HESS J1731-347 show almost same result in different analysis scenarios, we only show one of them(light blue) here.

2.2 Radio, X-ray and GeV data

In this section, we present a detailed discussion about the multi-wavelength counterparts of HESS J1731&J1729 (see the multi-wavelength morphologies in Fig. 2.6 and Fig. 2.7). Non-thermal emission is clearly identified in radio, X-rays and TeV band at SNR HESS J1731-347. Due to the limited statistics in the TeV data, H.E.S.S. Collaboration et al. (2011); Bamba et al. (2012) used the radial profile to compare the TeV morphology with morphologies in other energy bands. The rough match among radio, X-ray and TeV radial profiles can be seen in Fig. 2.8. More details of the multi-wavelength observations of HESS J1731&J1729 are presented in the following list.

- *The radio data.* The radio shell (GHz) as shown in Fig. 2.6 (top left) is spatially coincident with the TeV shell and has a similar extent (see also the radial profiles in Fig. 2.8). The total radio flux of the SNR measured by Tian et al. (2008) is 2.2 ± 0.9 Jy. Together with the X-ray emission, the radio emission can be explained by the synchrotron emission from the shock region (H.E.S.S. Collaboration et al., 2011). The compact HII region (G353.42-0.37) located to the West of the SNR at a distance of 3.2 ± 0.8 kpc (Tian et al., 2008) is indicated in Fig. 2.6 (top left).

- *The X-ray data.* The X-ray emission as shown in Fig. 2.6 (top right) is concentrated in many arc-like features, similar to broken shell seen from many shell-type SNRs.

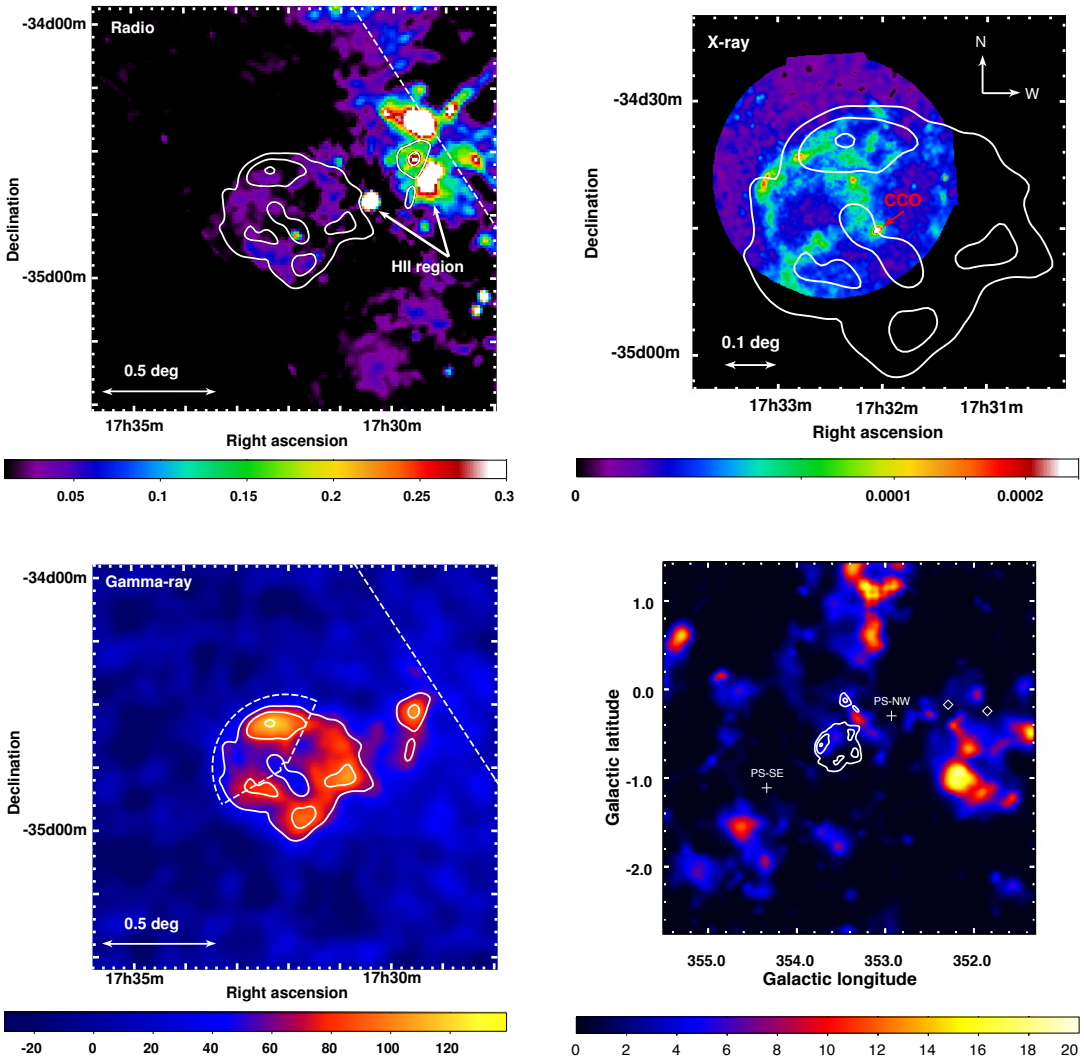

Figure 2.6: *Top left:* Radio 1.4 GHz map with two obvious bright HII region G353.42-0.37 (left) and G353.381-0.114 (right) which are marked with arrows. *Top right:* X-ray map from XMM-Newton in 0.5-4.5 keV energy band. *Bottom left:* TeV excess map with a dashed contour marking the counterpart region of XMM-Newton. *Bottom right:* Residual test statistical maps from Fermi telescope for $E > 3$ GeV. The TeV significance contours(white) at 4,6, and 8σ obtained with an integration radius of 0.06° are represented in each panel. Pictures are taken from H.E.S.S. Collaboration et al. (2011) and Acero et al. (2015).

Some of the arcs partly coincide with the radio and TeV shell. Some of the structures could hint at an additional, smaller shell, but might also come from irregular SNR expansion in an inhomogeneous and/or dense medium (H.E.S.S. Collaboration et al., 2011). The X-ray image in Fig. 2.6 only cover partial of the whole SNR. A fully covered X-ray image from the X-ray Multi-Mirror Mission (XMM-Newton) can be seen in Fig. 2.7, which has clearly shown that the X-ray emission from the west part of the SNR is dimmed due to absorption. The diffuse X-ray emission is fitted by an absorbed power-law model and no emission lines were found. This clear shell structure of purely nonthermal X-ray emission indicates that SNR HESS J1731-347

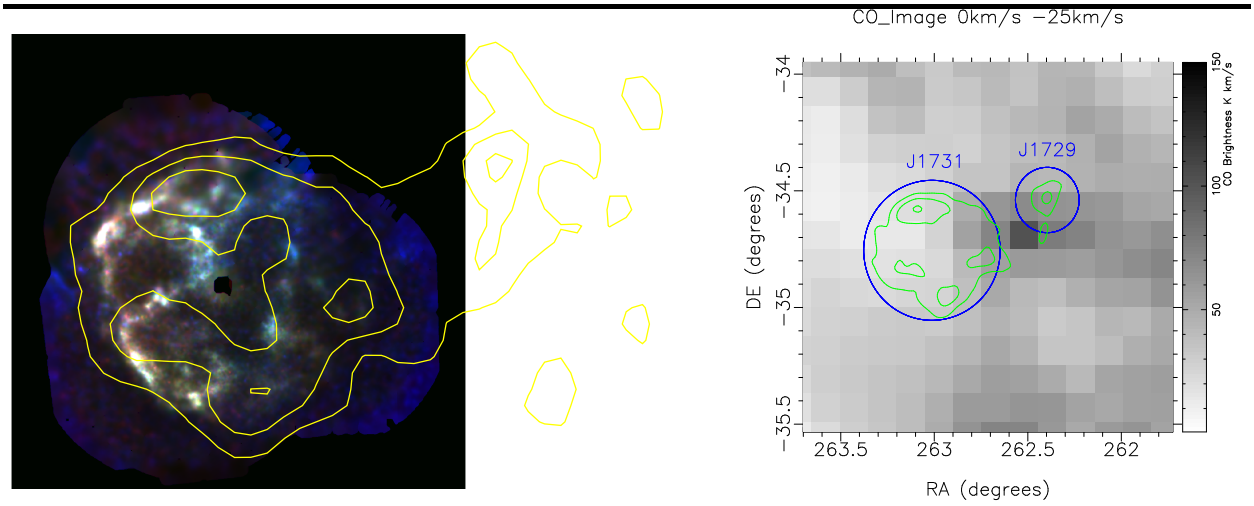

Figure 2.7: *The left panel:* The X-ray image of SNR HESS J1731-347 are shown. Data are taken from XMM-Newton in wave band 1-2 keV(red), 2-4.5 keV(green), 4.5-6 keV(blue). The CCO region in the centre is removed. The TeV morphology from H.E.S.S. Collaboration et al. (2011) are shown in contours. Figure is taken from Victor Doroshenko through private conversation. *The right panel:* The ^{12}CO image from the CfA ^{12}CO survey, which is integrated from $0\,\mathrm{km\,s^{-1}}$ to $-25\,\mathrm{km\,s^{-1}}$. The blue circles indicate the locations of SNR HESS J1731-347 and HESS J1729-345. The TeV significance image from H.E.S.S. Collaboration et al. (2011) is also shown in green contours.

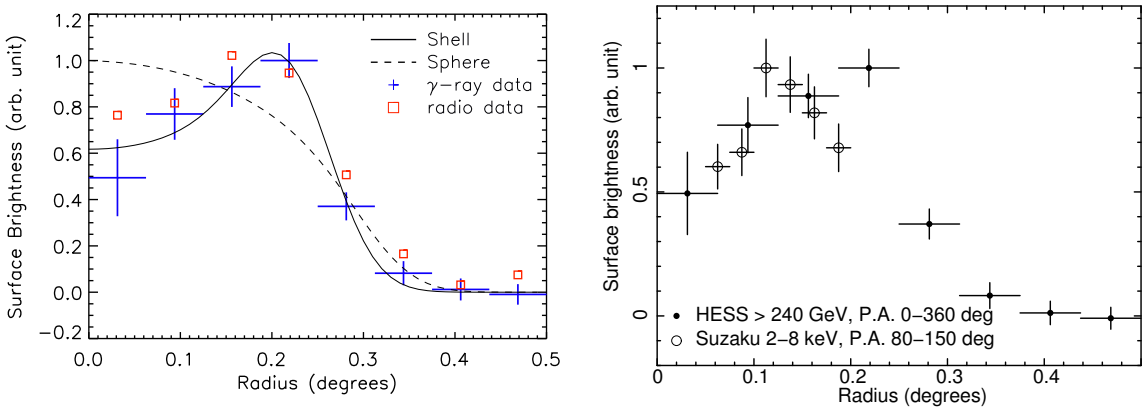

Figure 2.8: *On the left panel*: The black cross and the squires separately represented the TeV-radial profile and the radio-radial profile, the solid line(Shell structure source) and dashed lines(Homogeneously Sphere structure source) are models to fit the radial profile. Figure is taken from (H.E.S.S. Collaboration et al., 2011).
On the right panel: VHE γ-ray (filled circle) and 2–8 keV using Suzaku data (open circle) radial profiles are shown. The central part was cut in the X-ray data due to the contamination from the central source. Note that the VHE γ-ray profile is taken from the entire remnant, whereas the X-ray one is from the Western part of the shell, using position angle (P.A.) 80°–150° (counted clockwise starting from North). Figure is taken from (Bamba et al., 2012). *Radius* $= 0°$ is the CCO's location in both panels.

should be still a young SNR with high shock velocity $v_{\mathrm{SNR}} > 1000$km/s. Owing to the lack of thermal X-ray emission detected at/near the SNR, an upper-limit (90% confidence level) on the ambient medium density $\sim 0.01\,\mathrm{cm^{-3}}$ of the SNR is derived by H.E.S.S. Collaboration et al. (2011) using a shocked medium model along with some

strong assumptions, e.g. an electron temperature $kT_e = 1\,\mathrm{keV}$, an ionization timescale parameter $\tau = 10^9\,\mathrm{cm}^{-3}\,\mathrm{s}$. The bright point source XMMU J173203.3-344518 which lies at the geometrical center of the radio and TeV shell is a good candidate of the CCO of the SNR (H.E.S.S. Collaboration et al., 2011). In a detailed study on this CCO by (Klochkov et al., 2015), the thermal X-ray spectrum of this CCO is explained well by a NS model with carbon atmosphere. The finding of this CCO indicates a massive progenitor star ($M > 8\,\mathrm{M}_\odot$) of SNR HESS J1731-347. So far there is no deep X-ray observation of HESS J1729-345 yet, since its location happens to be coinciding with some star forming region (HII region), at least some point X-ray sources may be expected from this region.

- *The ^{12}CO data.* A good match between the ^{12}CO image integrated from $0\,\mathrm{km\,s}^{-1}$ to $-25\,\mathrm{km\,s}^{-1}$ (see Fig. 2.7) and the X-ray absorption image was found in H.E.S.S. Collaboration et al. (2011). This finding suggests that MCs at $\sim 3.2\,\mathrm{kpc}$ are lying in front of the SNR. More detailed discussions about these MCs are presented in the following section.

- *The GeV data.* No detection with Fermi telescope is found at the SNR region, upper-limits are given by Yang et al. (2014) and Acero et al. (2015). As discussed in Sect. 1.4, the lack of GeV emission slightly favors the leptonic model and is consistent with the low density of ambient medium surrounding the SNR. At the HESS J1729-345 region no detection with Fermi telescope is found either. However a GeV feature is found to the West of the SNR and to the South of HESS J1729-345, and it may be the result of Galactic CR background interacting with dense MCs there.

2.3 The distance of SNR HESS J1731-347

Distance is one of the most important parameter of an astronomical object, since it can also confine other parameters, e.g. the size and the absolute luminosity. Due to the complex and violent evolution history of the SNRs, it is impossible to setup a standard model that can provide accurate explanations for the observational data of each SNR at different evolution stages. Therefore, with only the observational data from the SNR itself, its distance is very model dependent and difficult to be derived. Nonetheless, the distance of a SNR can often be estimated through associating it with some nearby objects, e.g. nearby molecular clouds, companion stars. In this section, four well studied methods of finding the distance of SNR HESS J1731-347 are presented.

1. *Comparing the ^{12}CO data with the X-ray absorption data.* The ^{12}CO(J=1-0) emission line is known as a good tracer of dense gas ($n \sim 10^2\,\mathrm{cm}^{-3}$). Following the standard Galaxy rotation model, the MCs shown in Fig. 2.9 with velocity range $-13 \sim -25\,\mathrm{km\,s}^{-1}$ should be inside the Scutum-Crux arm which is about 3.2 kpc away. Through modelling the nonthermal X-ray spectra in different sub regions of the SNR, as shown in Fig. 2.10, H.E.S.S. Collaboration et al. (2011) had found that the X-ray absorption image can very well be explained when the SNR is put behind these $\sim 3.2\,\mathrm{kpc}$ MCs.

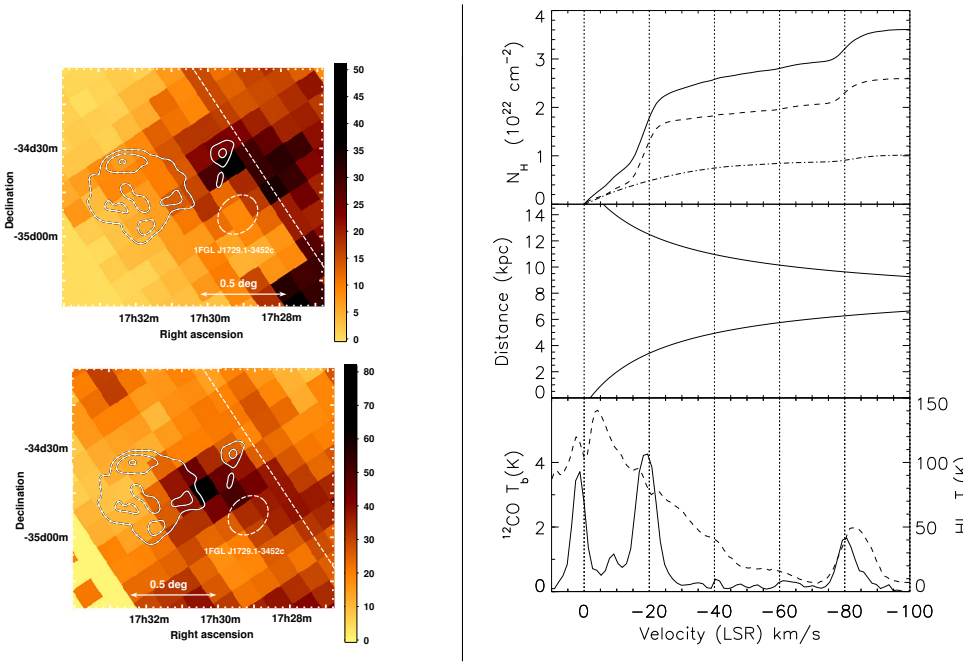

Figure 2.9: *Left:* The ^{12}CO images integrated from -13km/s to -25km/s(left bottom) and -75km/s to -87km/s (left top). *Right top:* Cumulative absorbing column density (solid line) as a function of radial velocity at the position of highest X-ray absorption. The relative contributions from the atomic and molecular hydrogen are represented by the dashed and dash-dotted lines respectively. *Right middle:* Rotation curve towards the same direction as derived from the model of Galactic rotation of Hou et al. (2009). *Right bottom:* ^{12}CO (dashed line) and HI (dash-dotted line) spectra obtained the region highest X-ray absorption. Figures are from H.E.S.S. Collaboration et al. (2011).

2. *The HII region.* Tian et al. (2008) suggested a distance of 3.2 ± 0.8 kpc assuming that the SNR is at the same distance as the HII region G353.42-0.37 (see Fig. 2.6). Based on the HI absorption spectrum features, the distance of this HII region is found similar to that of the MCs mentioned above (also inside the Scutum-Crux arm). Although CC SNe are very likely to be born in clusters of OB stars which can create huge HII region, since the SNR is located in line with the Galactic plane, one can not draw any strong connections between HESS J1731&J1729 and this HII region.

3. *Modelling the CCO spectrum.* In Klochkov et al. (2015) the thermal X-ray emission from the neutron star at HESS J1731-347 is explained well using a carbon atmosphere model with certain absorption density. At the most likely distance ~ 3.2 kpc (see Fig. 2.11), the model gives corresponding column density $n_{\rm H} = 2.00 \times 10^{22}\,{\rm H\,cm^{-2}}$, NS mass $M_{\rm NS} = 1.55\,{\rm M_\odot}$, NS radius $R_{\rm NS} = 12.4$ km and NS lab temperature $T_{\rm NS} = 1.78$ keV. Clearly the $n_{\rm H}$ in this model matches well with the ^{12}CO data integrated from 0 to 3.2 kpc as well (see Fig. 2.10). The relative high temperature of this neutron star indicates a quite young age of the SNR $t_{\rm SNR} < 10$ kyr according to current cooling theory.

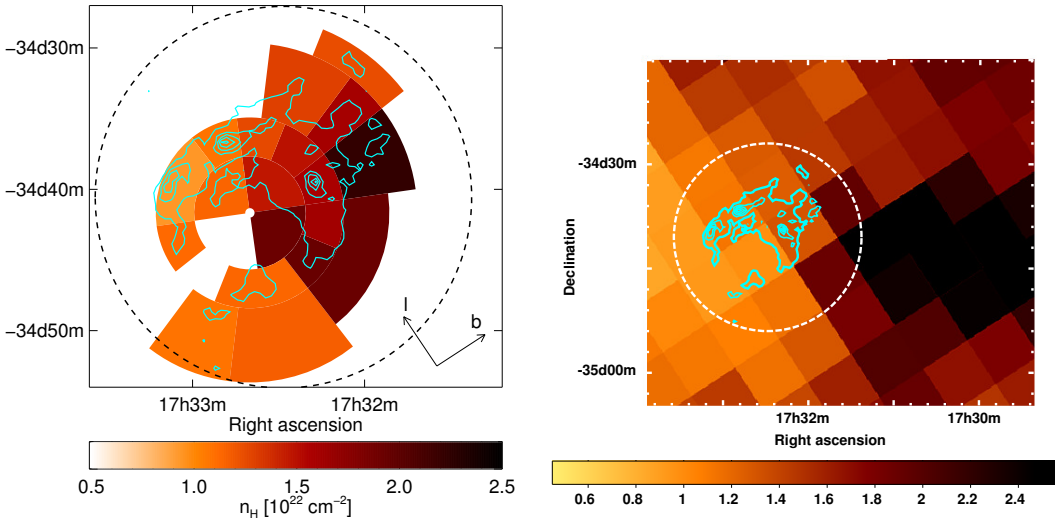

Figure 2.10: *Left* : X-ray absorption map derived from a spectral fit to XMM-Newton data assuming an absorbed power-law model. A significant increase of NH towards the Galactic plane is observed. *Right* : Absorption column map derived from atomic and molecular hydrogen when integrating over radial velocities from 0 km/s to -25 km/s (see also Fig. 2.9). The Galactic plane is represented by the white dashed line. In both panels, the XMM-Newton field of view is represented by a dashed circle and the X-ray contours obtained from Fig. 2.6 are overlaid. Figures are taken from H.E.S.S. Collaboration et al. (2011).

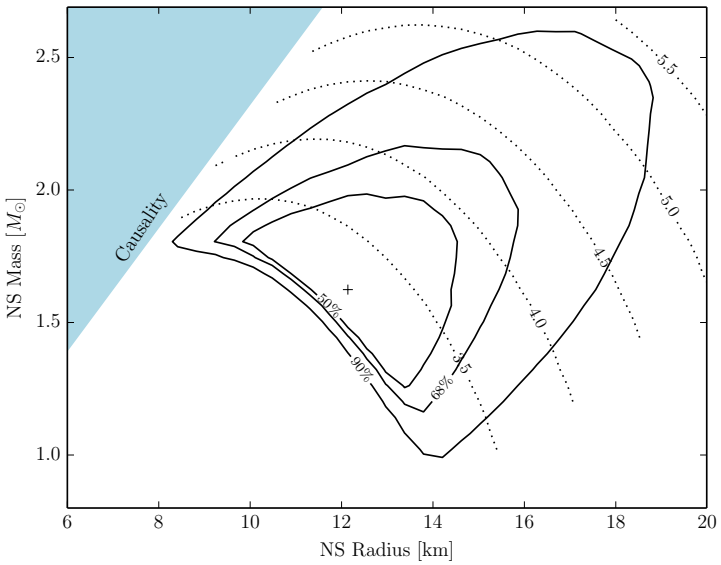

Figure 2.11: χ^2 confidence regions in the mass-radius plane for the CCO in HESS J1731-347 obtained with the carbon atmosphere models. Distance is a free parameter with lower limit of 3.2 kpc. The shaded area in the top left indicates the region excluded by the causality. The dotted contours indicate best-fit distance in kpc computed for each point of the mass-radius grid. Figure is taken from Klochkov et al. (2015).

4. *Comparing the* ^{12}*CO data with the TeV data.* We note that in a recent work by Fukuda et al. (2014), a distance of ~ 5.2 kpc was derived by matching the TeV image with the

interstellar gas density profile (using the ^{12}CO data from NANTEN and the HI data). They argued the hadronic explanation for the TeV emission from the SNR and linked the SNR to MCs at ~ 5.2 kpc.

In conclusion, we are almost certain that SNR HESS J1731-347 is behind the MCs located in the Scutum-Crux arm ($D_{\rm J1731} \gtrsim 3.2$ kpc), however, there is no indication of an interaction between the SNR and the 3.2 kpc MCs. Combining the observational evidence from the CCO, SNR HESS J1731-347 is most likely to be inside the Scutum-Crux arm as well ($D_{\rm J1731} \sim 3.2$ kpc).

2.4 TeV emission from HESS J1731&J1729, Lepton or Hadron?

In this section, we discuss the leptonic/hadronic origin of the TeV emissions from SNR HESS J1731-347 and HESS J1729-345 through the methods mentioned in Sect. 1.4.

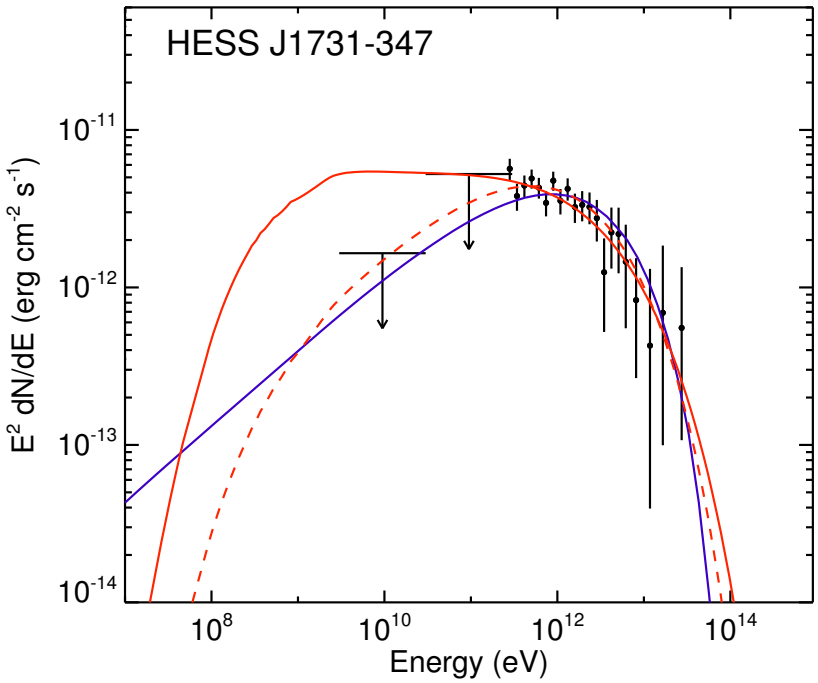

Figure 2.12: The reproduced SEDs of SNR HESS J1731-347. A purely leptonic (blue solid) scenario and a hadronic (red solid) scenario are shown in the test particle case (power-law index 2.0). The red dashed line shows the steep hadronic spectral (power-law index 1.5) slope compatible with the data. The HESS data points are extracted from H.E.S.S. Collaboration et al. (2011) and the Fermi 95% confidence level upper-limits are derived assuming a spectral index of 2.0. Figure is taken from Acero et al. (2015).

In the study of the morphology of SNR HESS J1731-347, no clear match between X-ray and TeV morphologies is found so far, however, it could be due to the low statistics of the TeV image. When comparing the radial profiles of the radio, X-ray and TeV data,

H.E.S.S. Collaboration et al. (2011); Bamba et al. (2012) found a rough match, as seen in Fig. 2.8. To argue the hadronic origin, Fukuda et al. (2014) presented a rough match between the TeV image and the interstellar gas density at 5.2 kpc (using the ^{12}CO data from NANTEN and the HI data). From the morphological study, so far it is hard to determine either leptonic model or hadronic model being responsible for the TeV emission from the SNR.

In the study of the SED of SNR HESS J1731-347, due to the low flux in GeV band, the leptonic model is slightly favored (Acero et al., 2015). As seen in Fig. 2.12, to reproduce the γ-ray spectrum with hadronic model, one need to introduce a very hard CR spectrum $\Gamma_p \lesssim 1.5$, see also e.g. Gabici & Aharonian (2014). This hadronic model is a possible explanation but not well supported by current shock acceleration theory: CR spectrum at shock with power-law index $\Gamma_p \sim 1.7 - 1.8$ is typical for the moderately modified shocks (Zirakashvili & Ptuskin, 2008).

No counterpart of HESS J1729-345 has been confirmed yet. In the argument of leptonic origin, if HESS J1729-345 has its own active TeV engine (e.g. a PWN, a young SNR), the fresh accelerated TeV electrons will emit comparable X-rays as well. In the argument of hadronic origin, if HESS J1729-345 is illuminated by the CRs generated from itself (e.g. an old SNR) or from outside sources (e.g. SNR HESS J1731-347), we would expect some dense MCs there. Considering the scenario that HESS J1729-345 is illuminated by the CRs originated from SNR HESS J1731-347, the ^{12}CO data at ~ 3.2 kpc (see Fig. 2.9) has indeed shown some MC clumps or filaments (high-density features in the molecular clouds $n_{\rm ISM} \gtrsim 10^2\,{\rm cm}^{-3}$) to the West of the SNR. Adopting the TeV analysis results derived by H.E.S.S. Collaboration et al. (2011), the gas morphology at 3.2 kpc does not match perfectly with the TeV morphology outside the SNR. This may be the results of the unknown of the three-dimensional structure of the MCs (see Sect. 4.4) and/or the young age of the SNR (see Sect. 1.5).

2.5 Motivation and thesis outline

In our study we focus on the TeV-emitting SNR HESS J1731-347. This SNR is very similar to the well-known TeV SNRs – RX J1713.7-3946 and Vela Jr., regarding their physical size and TeV luminosity, in displaying low surface brightness radio emission (Tian et al., 2008) and exhibiting essentially purely nonthermal X-ray emission (H.E.S.S. Collaboration et al., 2011; Bamba et al., 2012). The high forward shock velocity ($\gtrsim 1000\,{\rm km\,s}^{-1}$) inferred from the nonthermal X-ray emission indicates that the remnant is still in an early evolutionary stage with super-TeV particle acceleration ongoing in the shocks. A distinctive feature of the SNR HESS J1731-347 environment is another resolved TeV source, HESS J1729-345, located just outside of the SNR (H.E.S.S. Collaboration et al., 2011). This source is in apparent spatial coincidence, at least in projection, with molecular clouds seen through sub-mm molecular line emission (H.E.S.S. Collaboration et al., 2011). Since no other local particle accelerators are known so far, a scenario is conceivable in which particles that have escaped the SNR HESS J1731-347 are presently penetrating molecular clouds coincident with HESS J1729-345 and thus lead to enhanced γ-ray emission, above the emission induced by the sea of cosmic rays that are homogeneously filling the Galaxy.

In fact, a similar scenario has been successfully invoked to explain the γ-ray emission region HESS J1800-240 to the South of the SNR W28 (Aharonian et al., 2008a; Abdo et al., 2010; Li & Chen, 2010). HESS J1800-240 displays a very good morphological match to the molecular gas measured through CO emission from that region. Unlike the old SNR W28, SNR HESS J1731-347 is however much younger and is presently still accelerating super-TeV particles. This region offers the opportunity to model the evolution of the SNR and its associated particle acceleration history, simulating the particle acceleration and escape history up to the present time with good precision. For this purpose, we adopt the particle acceleration and escape formalism developed by Zirakashvili & Ptuskin (2008) and couple it to simulated SNR evolution histories.

Some physical parameters adopted in our model are listed here.

- So far there is no evidence to tell which analysis tool (ImPACT or Model++) is better in the case of HESS J1731&J1729. Hence we adopt the published TeV analysis results of SNR HESS J1731-347 and HESS J1729-345 by H.E.S.S. Collaboration et al. (2011) in the following chapters.
- The nonthermal X-ray shell found at the SNR indicates a high shock velocity $v_{\rm SNR} > 1000\,{\rm km\,s^{-1}}$.
- The discovery of the CCO leads to a CC SN with a massive progenitor $M \gtrsim 8\,{\rm M_\odot}$.
- Under certain assumptions mentioned above, the lacking of thermal X-ray at the SNR seems to favor a density of circumstellar medium $\lesssim 10^{-2}\,{\rm cm^2}$. There will be further discussions about this density in the modelling of SNR history below.
- We adopt the distance of the SNR as 3.2 kpc in the following chapters. The size of the SNR is then $\sim$ 15pc.

The main goal in our study is to explore whether the observational constraints are compatible with a scenario in which CRs that have been accelerated in SNR HESS J1731-347 and are now diffusing outward could indeed explain the γ-ray emission seen from HESS J1729-345. To this extent, we explored SNR evolution models (Sect. 4.1) that are consistent with the known properties of SNR HESS J1731-347 (Chapt. 2). Using these models, CR acceleration in the forward shock and the escape of the highest energy particles was simulated, adopting the recipes developed by Zirakashvili & Ptuskin (2008) (Sect. 3.1). Over the history of the SNR, we simulated the diffusion of the escaping CR particles (Sect. 3.2) into an environmental molecular cloud setup (Sect. 4.4), which we constructed to match the known observational constraints. In Chapt. 5, we discuss two possible scenarios: one in which the SNR still resides in the main-sequence wind bubble of the progenitor star (Sect. 5.1), and a second scenario in which the SNR has started to enter the surrounding wind bubble shell (Sect. 5.2). Additionally, in Chapt. 6, we present the search results of stars behind or near the SNR HESS J1731-347. And in Chapt. 7, the GeV-TeV emission around another TeV SNR – W28 is explained using the models builded for HESS J1731&J1729. At the end, the summary for the whole thesis is in Chapt. 8.

3

Cosmic ray acceleration and diffusion

Diffusive shock acceleration theory (first-order Fermi mechanism) has been studied extensively and naturally explains the commonly observed power-law dependence of the energy distribution of cosmic rays, see e.g. Krymskii (1977) and Bell (1978). In Sect. 3.1.1, we introduce the basic concepts of the first-order Fermi mechanism. In order to accelerate the CRs to the "knee" energy, a fast amplification mechanism of the magnetic turbulence in the upstream is discussed in Sect. 3.1.2.

Once the CRs are released from the accelerators, CR diffusion become the key factor in modifying the spacial distribution and the energy distribution of the CRs. In Sect. 3.2, we study the diffusion process of the CRs in our TeV source HESS J1731&J1729. Starting from the introduction of diffusion equation and Galactic diffusion coefficient (Sect. 3.2.1), we further deliver a Monte Carlo diffusion method (Sect. 3.2.2) which is based on the diffusion equation. In Sect. 3.2.3 and Sect. 3.2.4, we provide the code of calculating the propagation of a particle inside a turbulent magnetic field. Based on this code, the statistical behavior of the particles is also obtained in Sect. 3.2.5 through analysing the trajectories of hundreds of thousands of particles with energy 10^{12} eV $\sim 10^{16}$ eV. In Sect. 3.2.6, we discuss the "magnetic tube" scenario which leads to a fast CR propagation along the background magnetic field .

3.1 Cosmic ray acceleration at the shock

3.1.1 Fermi acceleration - Bouncing between "Walls"

When charged particles are diffusing around the shock front (see the concept of diffusion in Sect. 3.2), they are constantly interacting with the plasma from the upstream or the downstream. At the collisionless shock, the charged particles are more likely to scatter off the magnetic turbulence rather than to scatter off other particles in the plasma, e.g. the proton-proton total cross section of a 1 TeV proton is $\sim$ 45mb (TOTEM Collaboration et al., 2011), and the corresponding mean free path is $\sim 10^7$ lightyears. The magnetic turbulence (static) can change only the direction rather than the energy of a particle, thus the collisions between the accelerated particles and the plasmas can be considered to be elastic and the particles are simply bounced back by the plasma without energy loss.

As seen in Fig. 3.1, once the particles cross the shock front forward and back, they can be considered to have an elastic collision with the plasma from the upstream or downstream.

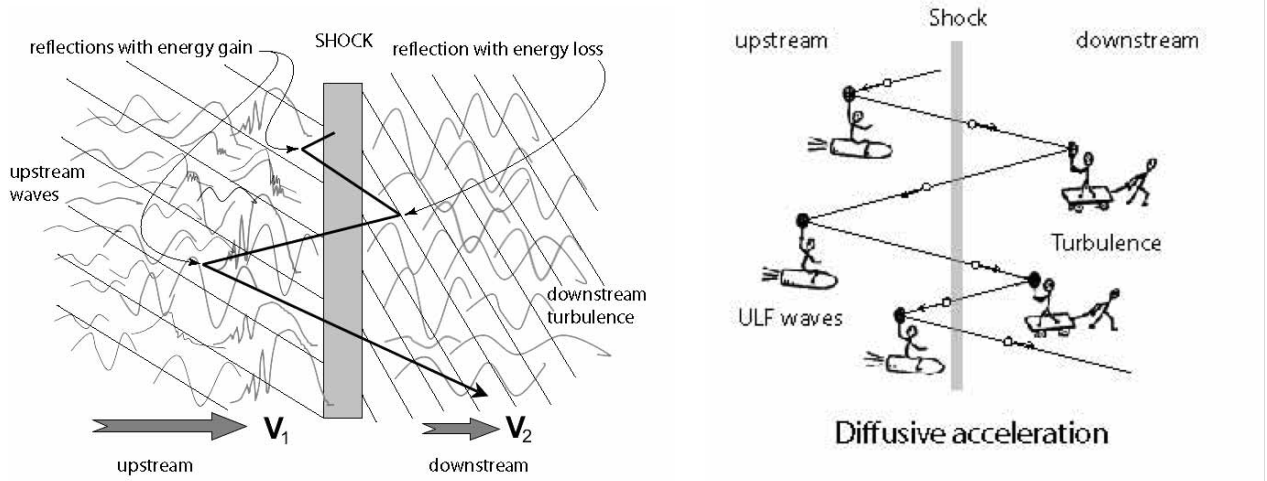

Figure 3.1: *The left figure*: The schematic representation of the acceleration mechanism of a charged particle in reflection at a quasi-parallel supercritical shock. on the left of the shock is the upstream plasma flow of velocity $V_1 \gg V_2$ much larger than the downstream velocity. It contains the various upstream plasma modes: upstream waves, shocklets, whistler, and pulsations. The average magnetic field is inclined at small $< 45°$ angle against the shock normal. On the downstream side the plasma is flowing slowly and contains the downstream turbulence. *The right figure*: Cartoon of the diffusive shock acceleration . Figures are taken from Treumann & Jaroschek (2008).

In the reference systems at rest of the shock front, the upstream plasma is moving towards the shock with speed $V_1 = v_{\rm SNR}$, while the downstream plasma is moving away with speed V_2 ($V_2 = v_{\rm SNR}/4$ for strong shocks in monatomic gas). Assuming shock velocity $V_1 \ll c$, the average energy gain of a particle after integrating the incline angle during a round trip (crossing the shock front twice) is

$$\Delta E \approx \frac{4(V_1 - V_2)}{3v_0} E_0 \approx \frac{V_1}{c} E_0 \tag{3.1}$$

The flux of VHE particles crossing the shock front from upstream to downstream is $f_{\rm in} = 1/4\ n_0 v_0$ and the flux of drifted away VHE particles in the downstream is simply $f_{\rm out} = n_0 V_2$, where n_0 and $v_0 \approx c$ are the density and velocity of the VHE particles, respectively. Therefore, during a round trip, the chances of this particle remaining at the shock region instead of being carried away by the downstream plasma are $P = 1 - f_{\rm out}/f_{\rm in} = 1 - V_1/c$. If we set $\beta = E/E_0 = 1 + V_1/c$ as the fractional change in kinetic energy, then after n round trips, particle number will drop from N_0 to $N = N_0 P^n$, and the particle energy will increase from E_0 to $E = E_0 \beta^n$, which gives

$$\frac{N}{N_0} = \left(\frac{E}{E_0}\right)^{\frac{\ln P}{\ln \beta}}. \tag{3.2}$$

In non relativistic approximation where $U \ll c$, one can find $\frac{\ln P}{\ln \beta} \approx -1$, thus we obtain the power-law spectrum $N(E)dE \propto E^{-2}dE$ in differential form. More details about the Fermi acceleration at shock front can also be found in the review papers by Jones & Ellison (1991) and Drury (1983).

3.1.2 Cosmic ray driven instabilities in the upstream of the shock

In diffusive shock acceleration, the maximum energy a particle can achieve ($E_{\rm max}$) depends on how many times it can be bounced between the upstream and downstream plasma before it can no longer be confined inside the shock region. In other words, the particle can escape the shock either through being carried away by the downstream plasma, or through running away from the shock by itself (mostly from the upstream) when its energy is higher than the escape energy $E_{\rm max}$. The latter escaping mechanism leaves an exponential cutoff ($E_{\rm max}$) on the particle spectrum at the shock. In the downstream of the shock, the shocked gas generates a quite strong B-turbulence (up to $10^{2-3}\,\mu$G) which is observationally confirmed through the nonthermal X-ray filaments in many SNRs. Therefore, increasing the B-turbulence or the waves in the upstream becomes the key factor in confining the CRs at the shock and accelerating them longer.

Substantial theoretical improvement has been achieved to support the idea that SNR shocks can indeed accelerate particles up to "knee" energies, i.e. up to $\sim 10^{15}$ eV, employing the concept of fast amplification of magnetic fields upstream of SNR shocks through non-resonant streaming instability (Bell, 2004; Zirakashvili & Ptuskin, 2008). CRs streaming through background plasma faster than Alfvén speed will excite instabilities. The energy and momentum transferred from CRs to gas via Alfvén waves will quickly amplify the magnetic turbulence in the upstream, and eventually the escape energy $E_{\rm max}$ is increased.

A fast shock scenario ($v_{\rm SNR} = 3300\,{\rm km\,s^{-1}}$) and a slow shock scenario ($v_{\rm SNR} = 660\,{\rm km\,s^{-1}}$) of numerically modelling the non-resonant instability are shown in Fig. 3.2 (Zirakashvili & Ptuskin, 2012). In the fast shock scenario, the size of the upstream acceleration region where the magnetic turbulence is amplified by CRs is about $5-10\%R_{\rm SNR}$, while the size of the downstream acceleration region where most CRs are confined is about $10\%R_{\rm SNR}$, and the swept gas by the shock are mostly confined inside the downstream acceleration region as well. Different from the fast shock scenario, the slow shock scenario has shown CRs filling the centre region of the SNR, owing to the old age of the SNR ($\sim 10^4$ years).

In the following paragraphs, we apply the analytical solution of the non-resonant streaming instability acceleration derived by Zirakashvili & Ptuskin (2008). In Zirakashvili & Ptuskin (2008) and the presented work, the momentum distribution of CRs is used, and it can be transformed to the energy distribution through

$$f(E)dE = 4\pi p^2 f(p)dp,\ \ E = pc. \tag{3.3}$$

The momentum distribution of CRs at the shock front can be written as

$$N_0(p) = \frac{\eta_{\rm esc}\rho u_1^2}{8\pi c I} p^{-\gamma_{\rm s}} p_{\rm m}^{\gamma_{\rm s}-4} n_0(\frac{p}{p_{\rm m}}), \tag{3.4}$$

with

$$n_0(s) = \exp[-\gamma_{\rm s}\int_0^s \frac{ds_1/s_1}{\exp(s_1^{-2})-1}], \tag{3.5}$$

where $u_1 = v_{\rm SNR}$ is the shock velocity, ρ is the density of the ambient gas, and p ($p_{\rm m}$) is the momentum (maximum momentum) of the CRs. The parameter I is the normalization factor, when $\gamma_{\rm s} = 4$ we obtain $I = 1/4$ (as used in Sect. 5.1). The acceleration coefficient

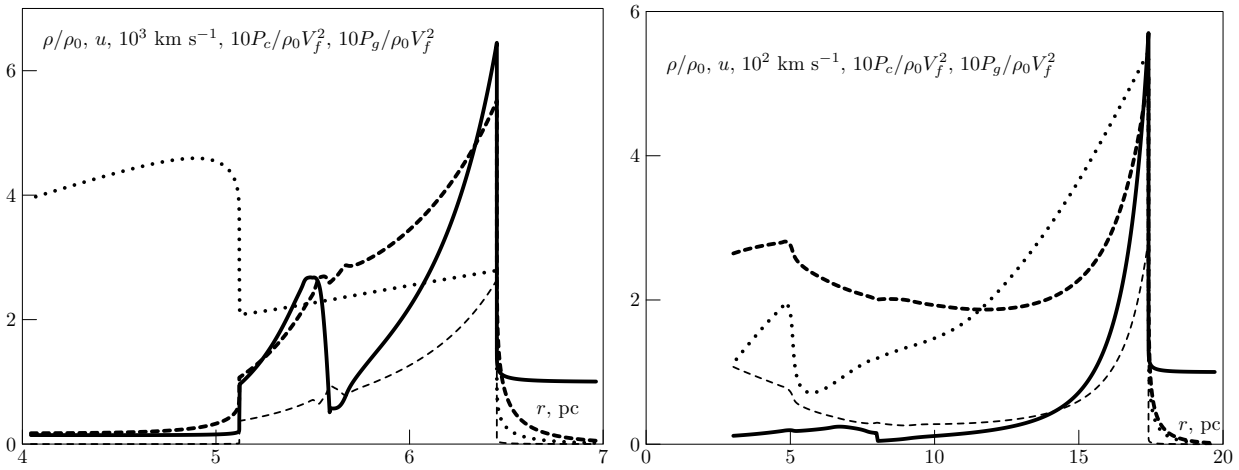

Figure 3.2: Radial dependencies of the gas density (thick solid line, $\rho \sim \rho_0$ at the upstream), the gas velocity (dotted line), CR pressure (thick dashed line) and the gas pressure (dashed line) at $t = 10^3$ years(left panel) and $t = 10^4$ years(right panel). In left (right) panel, at this epoch the forward shock velocity is $V_{\rm SNR} = 3300(660)\,{\rm kms}^{-1}$, its radius is 6.5 (17) pc, the reverse shock velocity is 1650 km s^{-1}, its radius is 5.1 pc, the magnetic field strength downstream of the forward shock is 160 (40) μG while the magnetic field strength downstream the reverse shock is 56 μG. Figures are taken from Zirakashvili & Ptuskin (2012)

$\eta_{\rm esc} = (F_{\rm esc})/(1/2\rho u_1^3)$ is the ratio between the energy flux of escaping CRs and the kinetic energy flux of the upstream medium that is approaching the shock.

The absorption boundary $R_{\rm Abs} = R_{\rm SNR} + L$ represents the box size of the MHD simulation in Zirakashvili & Ptuskin (2008). The parameter $L = v_{\rm SNR}t$ is measured from the shock position $R_{\rm SNR}$ in radial direction outwards and is set to the scale that CRs at the high-energy cutoff $E_{\rm max} = p_{\rm m}c$ cross the boundary and escape into the surrounding medium with a flux $J(E)$. The parameter L is of similar order as $R_{\rm SNR}$. The acceleration region in the upstream, as shown in Fig. 3.2, only covers a region from the shock front $R_{\rm SNR}$ to $\sim 0.1\,R_{\rm SNR}$, beyond the acceleration region the diffusion coefficient increases significantly. From the acceleration region $R \sim 1.1\,R_{\rm SNR}$ to the absorption boundary $R = R_{\rm Abs}$ is the region where the escaping CRs are driving streaming instabilities before the shock arrives, however, the magnetic turbulence in this region has not been significantly amplified. The flux of escaping particles at the absorption boundary can be written as

$$J(p) = u_1 N_0(p)/(e^{p_{\rm m}^2/p^2} - 1). \tag{3.6}$$

In Fig. 3.3, an example spectrum of the CRs at shock front and the corresponding spectrum of the runaway CRs are shown. Obviously, the runaway particles which are peaked at the escape energy $p_{\rm m}c$ are responsible for the exponential cutoff in the spectrum of CRs at shock front.

To obtain the escape energy $p_{\rm m}c$, one needs to know the size of the absorption boundary, the shock velocity u_1, the density of the incoming gas from upstream $n_{\rm H}$, and the amplified magnetic field $B_{\rm r}$. An approximated analytical solution derived from the MHD simulation

results is also provided in Zirakashvili & Ptuskin (2008):

$$p_{\rm m}c = \frac{\eta_{\rm esc} q u_1^2 B_0 L}{4cV_{\rm A}} \begin{cases} \ln^{-1}\left(\frac{2B_0 u_1^2}{B_{\rm b} u_*^2}\right), u_1 < u_* \\ \left[\ln\left(\frac{2B_0}{B_{\rm b}}\right) - 1 + \left(2\frac{u_1^4}{u_*^4} - 1\right)^{1/4}\right]^{-1}, u_1 > u_* \end{cases} \tag{3.7}$$

where the velocity

$$u_* = (24\pi c V_{\rm A}^3/\eta_{\rm esc}^2)^{1/4}, \tag{3.8}$$

and the Alfvén velocity

$$V_{\rm A} = B_0/\sqrt{4\pi\rho} = 2.18\,{\rm km\,s^{-1}}(\frac{n_{\rm H}}{1\,H\,{\rm cm^{-3}}})^{-1/2}(\frac{B}{1\,\mu{\rm G}}). \tag{3.9}$$

The value B_0 is the original unamplified magnetic field in the upstream region, and $B_{\rm b}$ is the initial value of magnetic fluctuations in the upstream region, which is set to $ln(2B_0/B_{\rm b}) = 5$ in Zirakashvili & Ptuskin (2008) and our following studies.

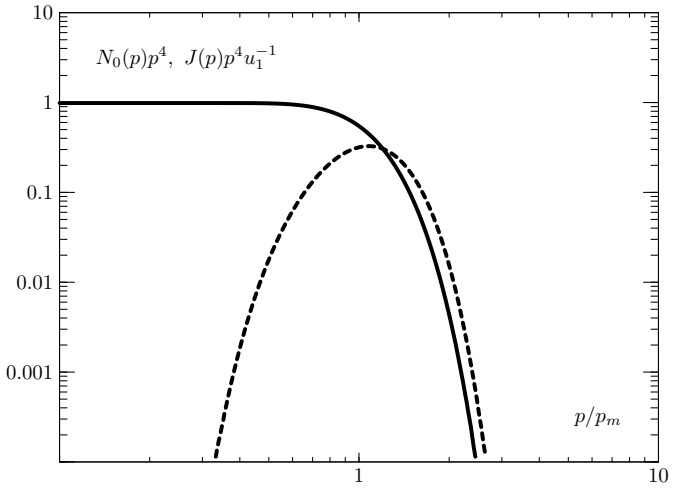

Figure 3.3: The particle spectrum at the shock front (solid line) and the spectrum of escaping particles (dashed line), the x-axis is the momentum of particles in unit of $p_{\rm max}$, the y-axis is the momentum distribution of particle density and momentum distribution of particle flux divided by shock velocity u_1. Figure is taken from Zirakashvili & Ptuskin (2008).

One important caveat is that in the CR acceleration model as elaborated in Zirakashvili & Ptuskin (2008), non-resonant instabilities only become efficient when the shock velocity is high enough, a corresponding critical shock velocity is given by

$$v_{\rm sh} > (1340\,{\rm km/s})(V_{\rm A}/10\,{\rm km/s})^{2/3}(\eta_{\rm esc}/0.05)^{-1/3}. \tag{3.10}$$

Nevertheless, the approximated analytical solution still works when the shock velocity is slower than this critical shock velocity.

Cosmic rays escape the SNR starting from the absorption boundary which is assumed to be a spherically symmetric surface surrounding the SNR. In a homogeneous environment, the analytical diffusion solution discussed in Sect. 3.2.1 can be adopted, and the final CR density at distance R from the SNR center and SNR age $t_{\rm age}$ can simply be written as

$$n_{\rm target}(E, R, t_{\rm age}) = \frac{1}{2}\int_0^{t_{\rm age}} dt \int_0^{\pi} \sin\theta J_{\rm total}(E, t) G(E, R', t_{\rm age} - t) d\theta \tag{3.11}$$

where G is the Green's function which is given in Sect. 3.2.1, R' is the distance from certain point on the absorption boundary to the diffusion target and can be written as

$$R' = \sqrt{[R - (R_{\rm Abs} - R_{\rm Abs}\cos\theta)]^2 + (R_{\rm Abs}\sin\theta)^2}, \tag{3.12}$$

$J_{\rm total} = 4\pi R_{\rm SNR}^2 J$ is the escaping CR flux at different time along the SNR evolution history. Here we use $4\pi R_{\rm SNR}^2$ instead of $4\pi R_{\rm Abs}^2$ to calculate the total escaping CR flux, because J is calculated through a plain shock approximation instead of a three-dimensional spherical shock scenario.

Furthermore, through combining the CR density at the shock N_0 with the downstream size discussed above, we can obtain a rough estimate of the total CRs trapped inside a young SNR:

$$N_{\rm total} = 4\pi R_{\rm SNR}^2 \cdot 0.1 R_{\rm SNR} \cdot N_0. \tag{3.13}$$

This estimate is later used in Sect. 5.2 to calculate the hadronic TeV emission from the SNR itself.

The main parameters in this non-resonant streaming instability acceleration theory are:

- $v_{\rm SNR}$. Faster shock velocities lead to a faster energy gain of the CR acceleration at the shock and a higher CR injection rate. Both the J and the $E_{\rm max}$ are most sensitive to the shock velocity.

- $\eta_{\rm esc}$. Higher acceleration efficient leads to higher percentage of kinetic flux of incoming medium turned into CR pressure in the upstream, and eventually results in amplifying the B-turbulence as well as boosting $E_{\rm max}$.

- L. The size of the absorption boundary defines where the unstable waves grows in the upstream, it increases with the age of the SNR. Larger L also leads to higher $E_{\rm max}$.

- ρ. Higher density of incoming gas from upstream leads to higher CR injection rate, which also boost the $E_{\rm max}$ and the J, e.g. a scenario in which the SNR is encountering with the main-sequence bubble shell as shown in Sect. 4.3.

Additionally, as mentioned in Sect. 1.3, young SNRs are considered as good CR accelerators because of their fast, large, and long surviving shocks. Under the shock acceleration theory, it can easily be explained by that the larger size of the shock leads to a better chance of the CRs returning back to the accelerator; the higher velocity of the shock leads to higher energy gain of the CRs in each crossing of the shock front and stronger magnetic turbulence in both the upstream and downstream; the longer age of the shock leads to longer acceleration time of the CRs and allows the magnetic turbulence to grow stronger.

3.2 Diffusion of cosmic rays

3.2.1 The diffusion equation

When a group of particles only show thermal movement (no bulk movement) and their mean free paths are much smaller than the diffusion space $\lambda \ll r$, their statistical behavior can be described by the diffusion equation:

$$\partial n/\partial t = -\nabla(D \cdot \nabla n) + S; \tag{3.14}$$

where D is the diffusion coefficient, n is the particle density and S is the source function.

The spherically symmetric solution of the diffusion equation can be found in e.g. Aharonian & Atoyan (1996) and Vink (2013): For each particle starting at $r = 0, t = 0$, the probability of finding it between r and $r + dr$ at time $t = \Delta t$ will be

$$p(E, r, \Delta t)dr = G4\pi r^2 dr, \tag{3.15}$$

where G is the Green's function (see the radial distribution of G in Fig. 3.4):

$$G = G(E, r, \Delta t) = 1/8(\pi \Delta t D)^{-3/2} \exp[-r^2/(4\Delta t D)]. \tag{3.16}$$

The mean diffusion distance after time Δt can then be written as

$$\bar{R} = \frac{\int_0^\infty 4\pi r^2 \cdot r \cdot G(E, r, \Delta t)dr}{\int_0^\infty 4\pi r^2 G(E, r, \Delta t)dr} = \frac{\sqrt{\frac{16}{\pi} D\Delta t}}{1} \approx 2.3\sqrt{D\Delta t}. \tag{3.17}$$

The CR propagation inside heliosphere has been well studied by Jokipii (1971) through the resonant scattering theory: a charged particle with Gyro-radius $R_{\rm Gyro}$ is mainly scattered by magnetic fluctuations of size $1/k = R_{\rm Gyro}$. Similar to that, the CR diffusion process in the Galaxy is caused by the resonant scattering off the Galactic magnetic turbulence (B-turbulence). And the Galactic B-turbulence is normally assumed to follow a power-law power spectrum with maximum length scale extending up to 100 pc. Therefore, the Galactic diffusion coefficient of CRs up to $10^5 Z$ TeV can be described as $D \sim (E/Z)^\delta$, where Ze is the electric charge of CR and $\delta = 1/3$ is normally adopted for a Kolmogorov's turbulence (Berezinskii et al., 1990). It is very difficult to get direct observational data of B-turbulence in our Galaxy, however, based on the CR spectrum observed on earth and the Galactic CR source models, the widely accepted Galactic standard diffusion coefficient $D_{\rm G}$ can be written as

$$D_{\rm G}(E) = D_{10}(\frac{E}{10\,{\rm GeV}})^\delta(\frac{B}{3\,\mu{\rm G}})^{-0.5}, \text{ with } {\rm D_{10}} = 1 \sim 3 \times 10^{28}\,{\rm cm^2/s}\ ,\ \delta = 0.3 \sim 0.6\ , \tag{3.18}$$

see e.g. Berezinskii et al. (1990) and Ptuskin (2006) for extensive discussions. Due to the lack of information about the B-turbulence near the SNR HESS J1731-347, $D_{\rm G}$ becomes an important indicator for calculating the CR diffusion in our study.

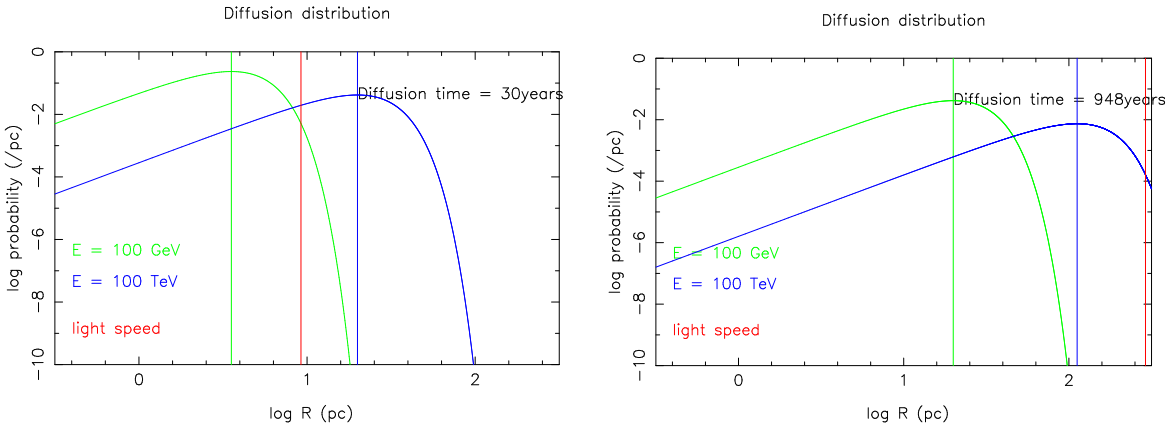

Figure 3.4: The probability distribution along radius R at $t = 30$(left), 948(right) years from an instantaneous point source injecting at $t = 0$. The diffusion coefficient is set as Galactic standard $D_{10} = 10^{28}\,\mathrm{cm^2\,s^{-1}}$, $\delta = 0.5$. In the left panel, there is $\sim 99.6\%$ chance to find the 100 GeV particles, but only $\sim 6.4\%$ chance find the 100 TeV particles inside the light speed limit (red line as $R_c = ct$). In the right panel, $\sim 100\%$ (100 GeV) and $\sim 99.6\%$ (100 TeV) of the particles are inside the light speed limit. The green and blue straight lines indicate the peaks in the distribution function.

Clearly one could notice that the Green's function G extend from $r = 0$ to $r = \infty$, but particles can not travel faster than the light speed and diffuse to infinity $\Delta r < c\Delta t$. Thus this analytical diffusion solution only works in relative long diffusion time Δt (see Fig. 3.4). In order to maintain most particles(99.6%) inside the light speed limit (the distance a particle travels with light speed in straight line), we should have

$$\Delta t > 3 \times \frac{D(E)}{10^{28} cm^2/s}\, years, \int_0^{c\Delta t} p(E, r, \Delta t) dr > 99.6\%. \tag{3.19}$$

3.2.2 Monte Carlo diffusion

As discussed above, the diffusion coefficient is usually assumed to be a power law function of energy, $D(E) = D_{10}(E/10\,\mathrm{GeV})^{\delta}$. Under realistic conditions, both D_{10} and δ vary in different environments, for example, in the MS wind bubble or in MCs. To simulate the particle diffusion inside such an inhomogeneous diffusion environment, tracking each step of the particles becomes necessary. The causality from the diffusion equation allows us to use the Monte Carlo simulation, which can divide the diffusion process of a particle into many random small steps. During each small step Δt, particles are considered to diffuse inside a homogeneous environment. At the beginning of each step, the particle scatters off B-turbulence and goes into a random direction, along which direction it travels the mean diffusion distance $\Delta\bar{R} = 2.5\sqrt{\Delta t D}$. We derived the coefficient 2.5 by matching results from the Monte Carlo method with the corresponding analytical expressions in a homogeneous environment (see Fig. 3.5); a similar result ($\Delta\bar{R} = \int_0^{\infty} dr \cdot 4\pi r^2 \cdot r \cdot G \approx 2.3\sqrt{\Delta t D}$) is discussed above when integrating the Green's function. The diffusion results of the Monte Carlo method, as seen in Fig. 3.5, are independent of the step length. However, in order to make

the Monte Carlo simulation sensitive to the irregularly shaped boundaries between different diffusion environments, each step should be much smaller than size of the MCs $\Delta r << R_{\rm MC}$ and the SNR. In the following chapters the step size is set to $\Delta r = 1\,\mathrm{pc}$ for the sake of fast computing speed.

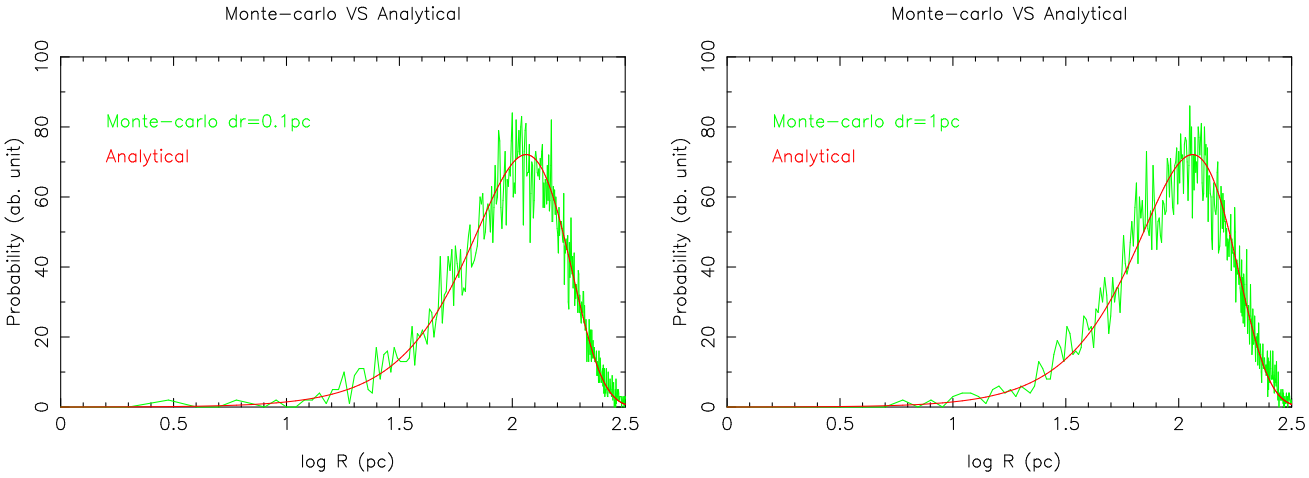

Figure 3.5: The particle distribution along radius R after 10^4 years diffusion with Galactic standard diffusion coefficient. Through injecting 10000 particles at $R = 0, t = 0$ with step length Δr=0.1 pc (left), 1 pc (right), we present the results of the Monte Carlo method in green lines. The corresponding analytical expressions are shown in red lines.

Both the analytical diffusion method and the Monte Carlo diffusion method are based on the knowledge of the diffusion coefficients in the environments, e.g. the MCs. Considering the complexity and the small scale ($10 \sim 100$pc; while the Galactic scale is $1 \sim 10$kpc) of the diffusion environment near HESS J1731-347, there will be further discussions about applying the Galactic diffusion coefficient into our study in later chapters. In the following subsections of Sect. 3.2, we explore the CR diffusion process from building the structure and the power spectrum of B-turbulence.

3.2.3 Turbulent magnetic field

In the interstellar space, the magnetic field (B-field) is the dominating force on the movement of a charged particle. Hence, the charged particles are basically bound on the B-field doing helical movement. The total magnetic field can be divided into background B-field $\vec{B}_0$ and turbulent B-field $\vec{B}$, there is no need for the turbulent part $\vec{B}$ to be small in our calculations. Increasing $\vec{B}_0$ naturally leads to higher diffusion coefficient along the direction of $\vec{B}_0$ or $-\vec{B}_0$ (see Sect. 3.2.6). In an extreme case when $|\vec{B}_0| \gg |\vec{B}|$, all the particles are propagating semi-ballistically along the $\vec{B}_0$ or $-\vec{B}_0$ direction. In the following subsections, to better describe the relation between the turbulence scales and the diffusion coefficient, we mainly focus on the scenario in which only purely turbulent and static magnetic fields (without the $\vec{B}_0$ part) are adopted.

The total energy density of the magnetic turbulence (B-turbulence) can be written as the

sum of the energy densities of many independent B-waves with different wavelengths:

$$U_{\rm B} = \int_{k_{\rm B,max}}^{k_{\rm B,min}} E_{\rm B}(k_{\rm B}) dk_{\rm B},\ k_{\rm B} = 2\pi/L_{\rm B}, \tag{3.20}$$

where $L_{\rm B}$ is the B-turbulence scale (wavelength), $U_{\rm B}$ is the total B-field energy density, and $E_{\rm B}(k_{\rm B})$ is the derivative of B-field energy density on wave number $k_{\rm B}$. Assuming an incompressible isotropic turbulence, we can adopt Kolmogorov's turbulence power spectrum which is presented as

$$E_{\rm B}(k_{\rm B}) = E_{\rm B,0} k_{\rm B}^{-\delta_{\rm B}},\ \delta_{\rm B} = 5/3, \tag{3.21}$$

Under the assumption of a homogenous and isotropic turbulence, a random B-turbulence $\vec{B}$ covering the whole space is pre-build before each particle sets foot in the space. Here the $\vec{B}$ consists of N random transverse B-waves:

$$\vec{B} = \sum_{n=1}^{N} \vec{B}_{\rm n}. \tag{3.22}$$

Each of the B-waves has its own wave number $k_{\rm B,n}$ and its own energy density

$$|\vec{B}_{\rm n}|^2/2\mu_0 = \int_{k_{\rm B,n}}^{k_{\rm B,n+1}} E_{\rm B}(k_{\rm B}) dk_{\rm B} \propto k_{\rm B}^{-\delta_{\rm B}+1} \propto L_{\rm B}^{\delta_{\rm B}-1}, \tag{3.23}$$

where $k_{\rm B,1} = k_{\rm B,min}$ and $k_{\rm B,N} = k_{\rm B,max}$. Each transverse B-wave $\vec{B}_{\rm n}$ should also satisfy $\bigtriangledown \cdot \vec{B}_{\rm n} = 0$, and in a static B-turbulence they can be written as (e.g. Fatuzzo et al., 2010; Giacalone & Jokipii, 1994)

$$\vec{B}_{\rm n} = |\vec{B}_{\rm n}|(\cos\alpha\hat{x} \pm i\sin\alpha\hat{y}) \exp(ik_{\rm B,n}\vec{z} + i\beta), \tag{3.24}$$

where $\hat{z}$ is the direction of wave propagation, α is a random angle on the $\hat{x}\hat{y}$ plane which determines the direction of $\vec{B}_{\rm n}$, β is a random phase between $0 - 2\pi$. The value of $|\vec{B}_{\rm n}|$ is normalised through the given turbulence power spectrum (e.g. Kolmogorov's turbulence) and the total energy density $U_{\rm B}$. In our following simulations, the B-waves follow Kolmogorov's turbulence power spectrum and their waves numbers are evenly chosen along the logarithm of $k_{\rm B}$.

Ultimately, to build a random B-turbulence for each particle, we create $4N$ random parameters which include N random three-dimensional directions $\hat{z}_{\rm n}$ (each of $\hat{z}_{\rm n}$ breaks into a random longitude angle and a random latitude angle), N random polarisation angles $\alpha_{\rm n}$, and N random phases $\beta_{\rm n}$. In our following simulations, the total number of B-waves is set as $N = 300$; the direction of $\vec{B}_{\rm n}$ which is given through $\alpha_{\rm n}$ is generated through the cross product of $\hat{z}_{\rm n}$ and a new random three-dimensional direction; the phase of each wave at any physical position $\vec{R}$ can be obtained through $|\vec{z}| = \vec{R} \cdot \hat{z}$.

3.2.4 Particle movement inside magnetic turbulence

When propagating inside the B-turbulence $\vec{B}$, the movement of a particle can be divided into small steps (Δt) of helical movement $\Delta\vec{R}$. Each step can be considered as the sum of a

rotational movement $\Delta\vec{R}_{\rm rot}$ by an angle $\Delta\phi$ and a rotation-center movement $\Delta\vec{R}_{\rm B}$ along the $\vec{B}$ axis. Therefore, each step can be written as

$$\Delta\vec{R} = \Delta\vec{R}_{\rm B} + \Delta\vec{R}_{\rm rot}. \tag{3.25}$$

Same like the position shifting vector $\Delta\vec{R}$, the velocity vector $\vec{V}$ can also be written as the sum of a vector along the B-line $\vec{V}_{\rm B} = (\vec{V}\cdot\vec{B})\hat{B}$ and a rotating vector around the B-line $\vec{V}_{\rm rot} = \vec{V} - \vec{V}_{\rm B}$, of which the former one determines the rotation-center movement $\Delta\vec{R}_{\rm B} = \Delta t\vec{V}_{\rm B}$ and the latter one determines the Gyro-radius $R_{\rm Gyro} = E|\vec{V}_{\rm rot}|/(c^2eB)$, where E is the energy of a relativistic particle.

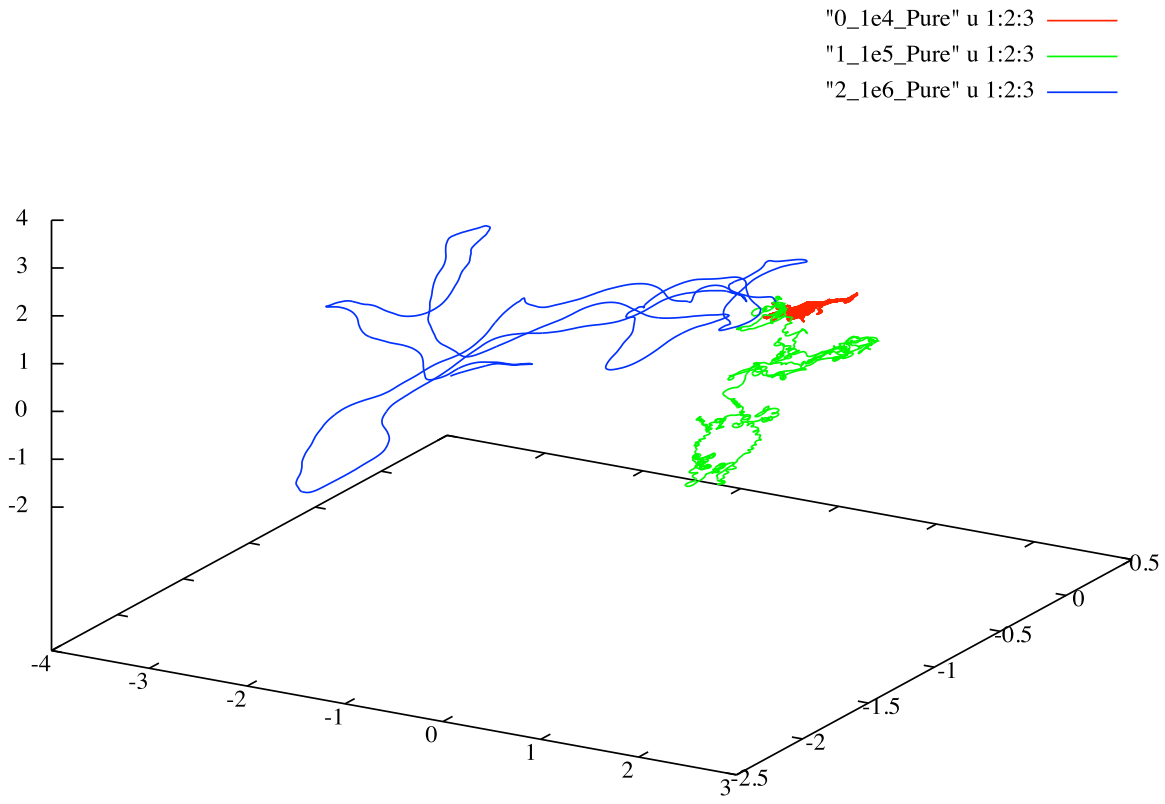

Figure 3.6: The trajectories of test particles with energy $10^4\,$GeV(red), $10^5\,$GeV(green) and $10^6\,$GeV(blue) in 100 years are shown. All coordinates(x,y,z) is in unit of pc. The magnetic turbulence are spacial homogeneous and following Kolmogorov's law, with $L_{\rm B} = 0.001\,{\rm pc} \sim 1\,{\rm pc}, {\rm U_B} = 7.8\,{\rm eVcm^{-3}}$.

At the beginning of each step, regarding to the starting position of the particle $\vec{R}$, the rotation-center is located at (for positive charge)

$$\vec{R}_{\rm o} - \vec{R} = R_{\rm Gyro}\frac{\vec{V}\times\vec{B}}{|\vec{V}\times\vec{B}|}. \tag{3.26}$$

Using the rotating matrix (see Wikipedia:Rotation Matrix), we rotate the vector $\vec{R}_{\rm o} - \vec{R}$ around $\vec{B}$ by an angle $\pi + \Delta\phi$ to obtain a new position $\vec{R}_{\rm C}$. The position shifting of the particle through this rotating is then $\Delta\vec{R}_{\rm rot} = \vec{R}_{\rm C} + \vec{R}_{\rm o}$. Once we obtain the new starting position for the next step as $\vec{R}_{\rm new} = \vec{R} + \Delta\vec{R}_{\rm rot} + \Delta\vec{R}_{\rm B}$, as described in the earlier subsection, we can also calculate the corresponding B-field for next step through summing up all the B-waves at this new position. In our simulation, the step size is set much smaller than the Gyro-radius of the particle $|\Delta\vec{R}| \ll R_{\rm Gyro}$.

The electric fluctuation in the B-turbulence can significantly accelerate charged particles given a sufficiently long time (Fraschetti & Melia, 2008). However, since magnetic fluctuations in MCs are expected to propagate at the Alfvén speed of $V_{\rm A} \approx 1 - 10\,{\rm km\,s^{-1}}$, the electric field has a negligible effect on the local motion of high energy particles, e.g. significant energy gain on TeV particles can only happen when $t > 10^5$ years (Fatuzzo et al., 2010). Thus the electric field is neglected in our simulations, and the particles do not lose or gain energy. The absolute value of the velocity $\vec{V}$ remains the same after each step and we can directly rotate $\vec{V}$ by $\Delta\phi$ around $\vec{B}$ to get the velocity for next step $\vec{V}_{\rm new}$. In our Monte Carlo simulations below, the absolute value of the velocity is simply set as light speed for particles with energy $E > 10^3\,{\rm GeV}$.

As a result of the Monte Carlo simulation, the trajectories of three particles during 100 years are shown in Fig. 3.6. These particles are set free at $t = 0, x = 0, y = 0, z = 0$ with different energies and different initial velocity directions. The B-turbulence (Kolmogorov's turbulence) of each particle is made of 300 B-waves which are evenly distributed along the logarithm of $L_{\rm B}$, ranging from 1 pc to 0.0001 pc. The energy density of the B-turbulence is set at $U_{\rm B} = 7.8\,{\rm eV\,cm^{-3}}$, corresponding to a B-field strength $|\vec{B}| = 5\,\mu{\rm G}$. As seen in Fig. 3.6, higher energy particles with larger $R_{\rm Gyro}$ are able to ignore more fluctuations and diffuse faster than lower energy particles do. This is due to that the fluctuations with wavelength much smaller than the Gyro-radius ($R_{\rm Gyro} \gg L_{\rm B,n}$) can barely impact the movement of the particles, and this is also consistent with the resonant scattering theory mentioned in Sect. 3.2.1.

3.2.5 From magnetic turbulence to the diffusion coefficient

To better show the statistical results of the Monte Carlo simulation inside a given B-turbulence, in this subsection, we present the particle radial distributions after certain propagating time frames (e.g. 10^4 years) as well as the corresponding diffusion coefficients derived from these distributions. Additionally, only the simulation results with particle energy at $10^3\,{\rm GeV} \sim 10^7\,{\rm GeV}$ are shown, considering that their hadronic emission can fall in the energy range of H.E.S.S..

In Fig. 3.7, the results of comparing the radial distributions obtained from our simulation with the analytical expressions from the diffusion equation are shown. At each energy band – 10^3GeV, 10^4GeV, 10^5GeV, 10^6GeV, and 10^7GeV, starting from $r = 0,\ t = 0$, one thousand particles are set free in a Kolmogorov's turbulence. Their final locations at $t = 1000$ years are recorded and resulting the radial distribution profiles which are shown as symbols in Fig. 3.7.

Through averaging the radial distributions of all 1000 particles along their entire propagating history, as shown in Fig. 3.8, we have derived the mean diffusion distances $\bar{R}$ in each energy band as a function of time. To better compare with the analytical expressions from the

diffusion equation ($\bar{R} = 2.3\sqrt{Dt}$), in each energy band we present the power-law fitting line ($\bar{R}(t) \propto \sqrt{t}$) which is derived from the last three symbols of each $\bar{R}(t)$ evolution profile in Fig. 3.8 (e.g. the three $\bar{R}(t)$ at time frame 5.9×10^3 years, 7.7×10^3 years, 1.0×10^4 years in the 10^3 GeV profile). The diffusion coefficients resulting from those fitting lines are shown in Fig.3.9.

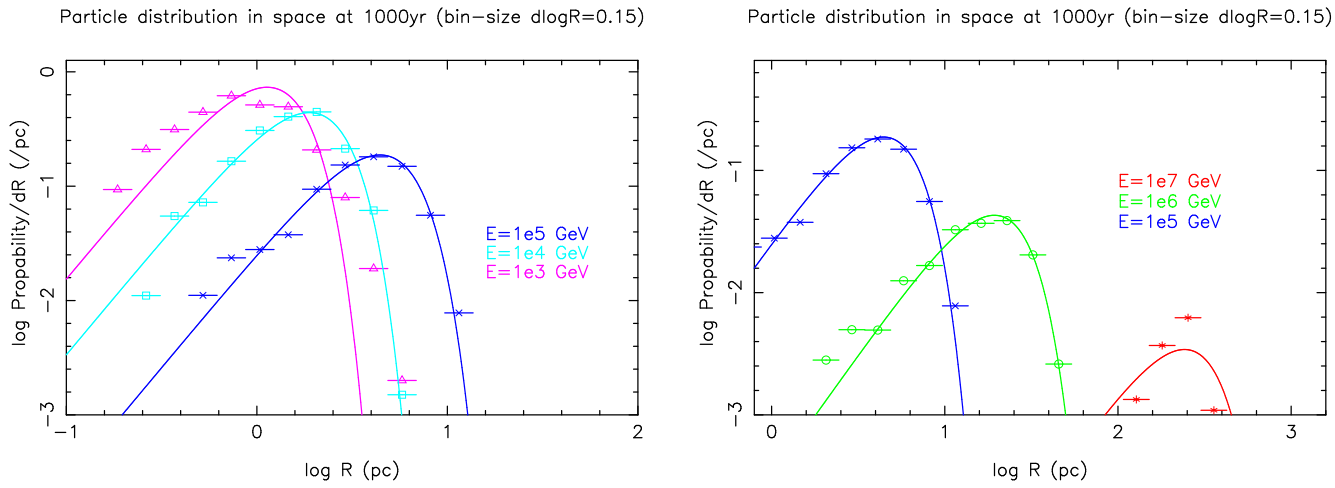

Figure 3.7: Radius distribution of CRs with energy $E = 10^3, 10^4, 10^5, 10^6, 10^7$GeV at 1000 years are shown with triangle, square, cross, circle, star symbols respectively. Corresponding best fit of distribution from the analytical diffusion solution are also shown in lines. Pure B-turbulence following Kolmogorov's law is used here, with $L_{\rm B} = 0.001\,{\rm pc} \sim 1\,{\rm pc}$, $U_{\rm B} = 7.8\,{\rm eVcm}^{-3}$.

As shown in Fig. 3.7 and Fig. 3.8, not all the particles with energy $10^3 - 10^7$GeV propagate diffusively in a limited time period (10^3 years). Three types of propagating behaviors in our simulations are discussed in the following lists:

1. *Particles with energy* $E = 2 \times 10^4\,{\rm GeV} \sim 2 \times 10^6\,{\rm GeV}$. Their $\bar{R}$ start to follow the diffusion power-law ($\bar{R} \propto \sqrt{t}$) at around $10^2 \sim 10^3$ years. Their radial distribution profile at 10^3 years also match well with the analytical expression.

2. *Particles with energy* $E = 1 \times 10^3\,{\rm GeV} \sim 2 \times 10^4\,{\rm GeV}$. Their $\bar{R}$ start to follow the diffusion power-law at around $10^3 \sim 10^4$ years. Their radial distribution profile at 10^3 years are more smeared than that of the analytical solution. To find the diffusion coefficient, one need to extend the propagating time until $\bar{R} > L_{\rm B,N} = 1\,{\rm pc}$ that the particles could fully experience the impact of fluctuations with even the maximum length scales.

3. *Particles with energy* $E = 2 \times 10^6\,{\rm GeV} \sim 1 \times 10^7\,{\rm GeV}$ *(*$R_{\rm Gyro} \gtrsim 0.4\,{\rm pc}$*).* Their $\bar{R}$ start to follow the diffusion power-law at around $10^3 \sim 10^4$ years. Their radial distribution profile at 10^3 years are more concentrated than that of the analytical solution, due to their nearly ballistic movement. To find the diffusion coefficient, one need to extend the propagating time until $\bar{R} \gtrsim 20 R_{\rm Gyro}$ that the particles could be scattered enough times (mean free path $\lambda \sim R_{\rm Gyro}$).

With the propagating time set as 10^3 and 10^4 years, we derive the diffusion coefficient of particles at each energy band, as shown in Fig. 3.9. The diffusion coefficient profile has

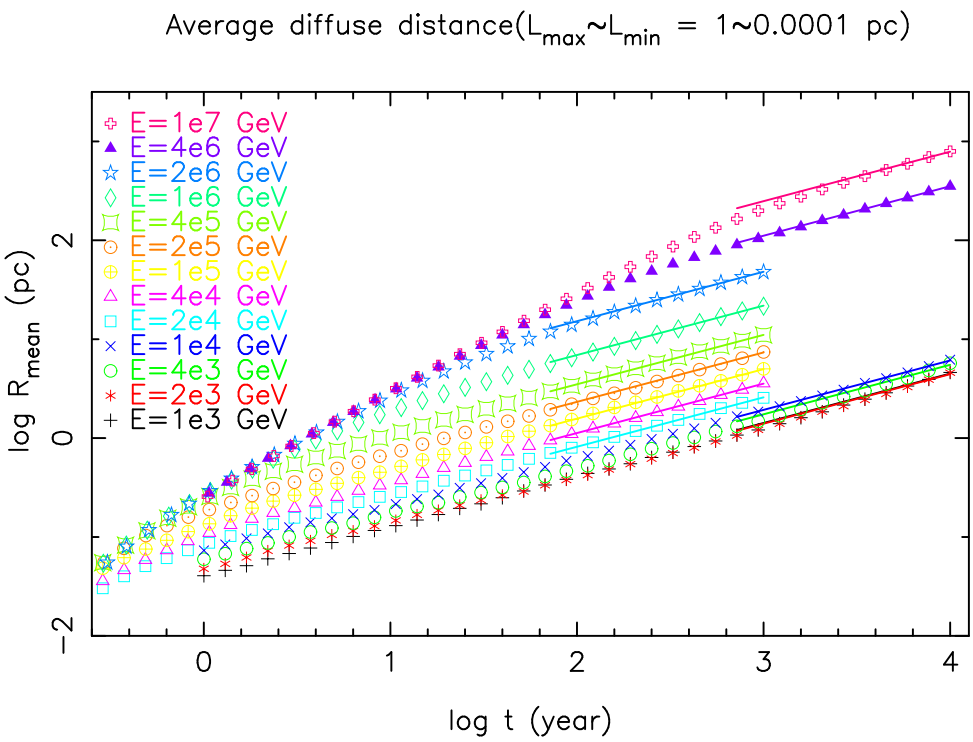

Figure 3.8: The mean diffusion distance $\bar{R}$ as a function of time t. At each energy band, the trajectories of 1000 particles are calculated. Same B-turbulence setup as in Fig. 3.6 is used here. The lines with power-law index 0.5 represent the fitting of diffusion coefficient ($\bar{R} \propto t^{0.5}$). To optimise the realization of the diffusion coefficients at infinite time with limited computing power, we choose $t_{\rm max} = 10^3(10^4)$year for energy band $E = 2 \times 10^4\,{\rm GeV} - 2 \times 10^6{\rm GeV}$ (the other energy band).

clearly shown three power-law slopes. The low-energy slope $E \lesssim 1.6 \times 10^4\,{\rm GeV}$ is consistent with the theoretical power-law profile (index $\delta = 1/3$) mentioned in Sect. 3.2.1. The mid-energy slope $1.6 \times 10^4\,{\rm GeV} \gtrsim E \lesssim 1.1 \times 10^6\,{\rm GeV}$ has shown a softer power-law profile (index $\delta \sim 0.9$) and is corresponding to the phenomenological Bohm diffusion. The high-energy slope $E \gtrsim 1.1 \times 10^6\,{\rm GeV}$ has shown a very steep power-law profile (index $\delta \sim 2.1$). More detailed theoretical explanations for these three slopes are discussed in Casse et al. (2002). Additionally, our results are sensitive to $L_{\rm max}$, but insensitive to $L_{\rm min}$. The propagating behaviors of the particles rely on their "footstep size" – Gyro-radius and the turbulence structure ($L_{\rm max}$ and $L_{\rm min}$), thus we can shift the derived diffusion coefficients to higher energy band as long as we also increase the magnetic strength and maintain a same "footstep size" (see Fig. 3.9).

Observationally, neither the diffusion coefficient in MC clumps or the one in interclump medium (the relative low density space where those dense MC clumps are embedded within) is well constrained. For example, Gabici et al. (2010) argued that to explain the TeV emission of the molecular clouds near the SNR W28, an average diffusion coefficient around 10% of the Galactic standard diffusion coefficient is required, albeit not only in the molecular clouds but everywhere around the SNR. Crutcher (2012) found that the maximum strength of the interstellar magnetic field stays constant at $\sim 10\,\mu$G up to densities $n_{\rm H} \sim 300\,{\rm cm}^{-3}$, and above $300\,{\rm cm}^{-3}$ it increases following a power-law with exponent $\approx 2/3$. If one assumes

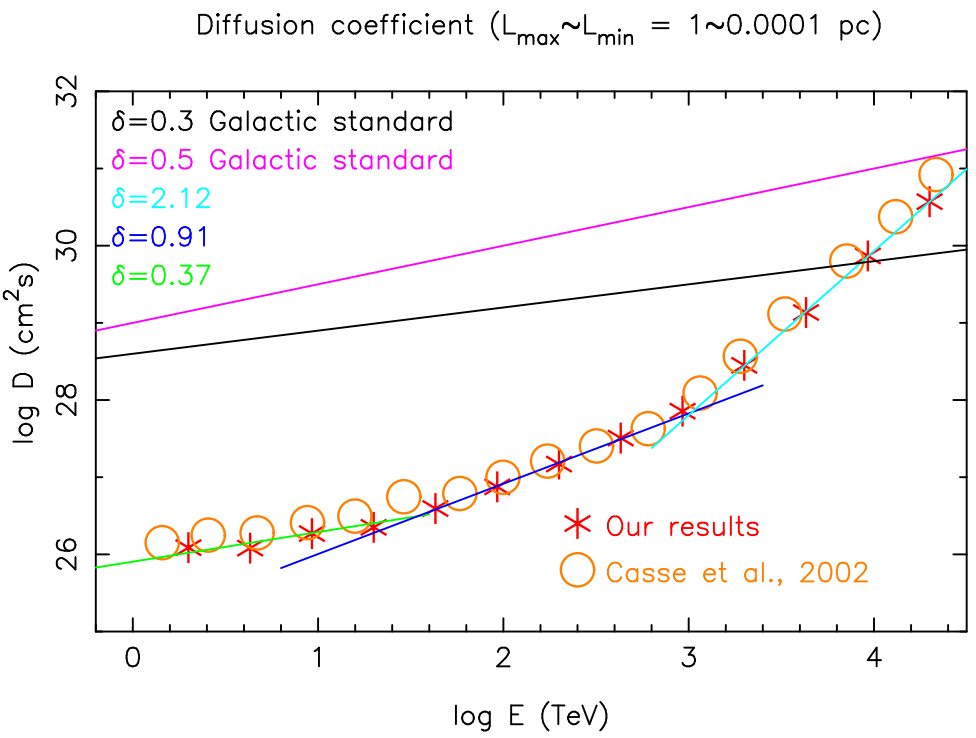

Figure 3.9: The diffusion coefficient of particles at different energy bands are shown in red stars. This results are based on the mean diffusion distances at $t_{\rm max}$, as shown in Fig. 3.8. Three power-law fitting results are presented in green line (low-energy), blue line (mid-energy), and cyan line (high-energy), respectively. Corresponding power-law index δ of these fitting results are shown as well. The results from Casse et al. (2002) are represented in yellow circles. Additionally, the Galactic standard diffusion coefficient $D_{10} = 10^{28}\,{\rm cm}^2/{\rm s}$, $\delta = 0.3(0.5)$ are shown in black (purple) line. Here we double the magnetic field strength to $U_{\rm B} = 31.2\,{\rm eVcm}^{-3}, |\tilde{\rm B}| = 10\,\mu{\rm G}$, thus the particle energies are also doubled to maintain the same $R_{\rm Gyro}$ and D.

that the magnetic turbulence strength in MC clumps is of order $\sim 10\,\mu$G as well, with a Kolmogorov-type power-law for the magnetic turbulence power spectrum and the size of the MC clumps $\sim$1 pc as maximum wavelength, one can obtain a much lower diffusion coefficient in dense clump regions, with $\lesssim 1\%$ Galactic standard for 1-1000 TeV CRs (see Fig. 3.9). Furthermore, as discussed above, the diffusion coefficients derived from this Kolmogorov-type B-turbulence fail to describe the statistical behavior of CRs with energy $E = 1 \times 10^3 \sim 2 \times 10^4\,{\rm GeV}, {\rm E} = 2 \times 10^6 \sim 1 \times 10^7\,{\rm GeV}$ until $10^3 \sim 10^4$ years, and this minimum time which is required to allow the CRs to propagate diffusively is much longer than the ages of most the young SNRs. On the other hand, diffusion in dense molecular clouds could be even much faster than Galactic standard due to damping of the turbulent magnetic field in the high density environment.

3.2.6 Diffusing in a "magnetic tube"

Following the discussion of B-turbulence structure near our SNR, we present a "magnetic tube" scenario in this subsection. Based on a set of 490 pulsars combining their observed rotation and dispersion measures with their estimated distances, Han et al. (2004) has suggest the maximum scale of magnetic fluctuation in our Galaxy as $\sim 100\,\mathrm{pc}$, which is much larger than the diffusion distance between our SNR and its nearby MCs. The magnetic wave at larger scale can function like an additional background magnetic field to the existing magnetic turbulence (smaller scale). Thus the CRs are likely to be travelling through these larger scale "magnetic tube" with bulk movement (e.g., Giacinti et al., 2013). This scenario can be clearly seen in Fig. 3.10 that once we add the background B-field $\vec{B}_0$ to the turbulent B-field $\vec{B}$, the particles diffuse much faster along the $\vec{B}_0$ direction, and meanwhile diffuse much slower along other directions which are perpendicular to the $\vec{B}_0$ direction. It is not hard to see that this background B-field indeed behaves like a "magnetic tube", inside which the particles are confined and propagating semi-ballistically.

To better describe the anisotropy of the CR diffusion, a time dependent B-turbulence is needed. The corresponding B-waves can be written as

$$\vec{B}_{\mathrm{n}}(t) = |\vec{B}_{\mathrm{n}}|(\cos\alpha\hat{x} \pm i\sin\alpha\hat{y})\exp[ik_{\mathrm{B,n}}(|\vec{z}| + V_{\mathrm{A}}t) + i\beta], \tag{3.27}$$

the turbulence fluctuation speed can be assumed as the Alfvén speed ($V_{\mathrm{A}} \approx 10\,\mathrm{km\,s^{-1}}$ in MCs). Obviously, the fluctuation time scale ($L_{\mathrm{n}}/V_{\mathrm{A}}$) of larger scale B-waves are naturally much longer. In order to present the bulk movement of CRs along the larger scale B-waves, this time dependent simulation requires all particles sharing one B-turbulence. Further exploration of such simulations will be performed in near future.

This "magnetic tube" scenario could help fast transferring the CRs to certain target positions, e.g. HESS J1729-345. However, in our following chapters we do not invoke this anisotropic diffusion (Jokipii, 1966; Nava & Gabici, 2013; Malkov et al., 2013; Giacinti et al., 2013), due to the lack of observation evidence of magnetic structure near our SNR. Additionally, a diffusive transport of CRs is necessary in order to transform an in energy space narrowly-peaked distribution (around E_{max}) of CRs at escape time into a sufficiently widened particle spectrum, that after γ-ray emission is broadly compatible with the measured TeV spectrum. Therefore, we also do not consider modifications on the γ-ray emissivity in the line of sight to the observer that result from an anisotropic CR momentum distribution, occurring initially in magnetic flux tube bulk movement as in purely ballistic particle propagation (Prosekin et al., 2015).

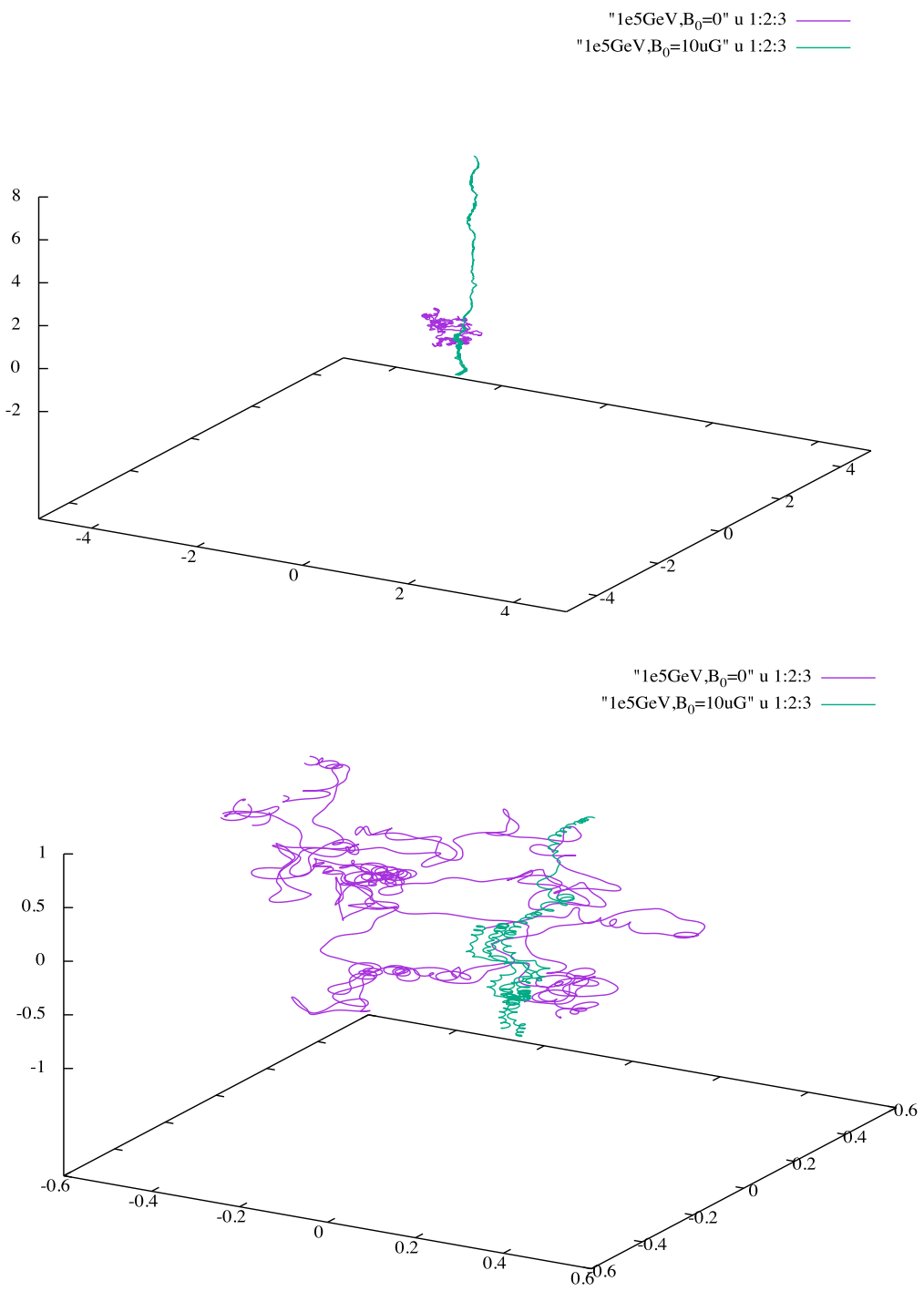

Figure 3.10: The trajectories of test particles with energy 10^5 GeV during 100 years are shown. The bottom panel is simply the zoom-in version of the top panel. The purple lines represent the particle trajectories inside a purely turbulent B-field $\vec{B}$. After adding an uniform background B-field to this purely turbulent B-field $\vec{B} + \vec{B}_0$, where $\vec{B}_{0,\mathrm{x}} = \vec{B}_{0,\mathrm{y}} = 0, \vec{B}_{0,\mathrm{z}} = 10\,\mu\mathrm{G}$, the corresponding trajectories are shown in green lines. All coordinates(x,y,z) is in unit of pc. The magnetic turbulence are spacial homogeneous and following Kolmogorov's law, with $L_{\mathrm{B}} = 0.001\,\mathrm{pc} \sim 1\,\mathrm{pc}, \mathrm{U_B} = 7.8\,\mathrm{eVcm}^{-3}$.

4

The evolution and the nearby environment of SNR HESS J1731-347

In this chapter we mainly explore the possible SNR evolution histories of SNR HESS J1731-347. In Sect. 4.1, we explore several subclasses of CC SN and their pre-SN environments, which include the red supergiant bubble, the main-sequence bubble, the Wolf-Rayet wind, the interclump medium, and the molecular cloud clumps. To study the SNR evolution history during the ejecta-dominated stage and Sedov-Taylor stage, one-dimensional (radius) solutions are adopted in our study, as seen in Sect. 4.2. The simulation results of the evolution histories of five CC SN scenarios, as shown in Sect. 4.3, indicate that SNR HESS J1731-347 is most likely still evolving inside the main-sequence bubble. Additionally, based on the ^{12}CO data at the HESS J1731&J1729 region, we provide a simplified three-dimensional structure of the molecular clouds in Sect. 4.4.

4.1 The circumstellar environment before the supernova

The presence of a CCO is suggesting a core collapse supernova (SN) scenario for HESS J1731-347, implying a progenitor star with relatively large mass, $M > 8\,\mathrm{M}_{\odot}$. Massive stars are normally formed as clusters inside MCs which can be considered MC clumps floating inside the interclump medium (ICM): clumps have densities around $10^3 \sim 10^4\,\mathrm{cm}^{-3}$, but only take $2\% - 8\%$ of the volume; the pressure in the ICM is around $10^5\,\mathrm{K\,cm}^{-3}$ and the density is around $5 - 25\,\mathrm{cm}^{-3}$ Chevalier (1999). Thus the ICM is the actual environment into which stellar wind bubble and SNR expand.

In Table 4.1, some observational properties of the progenitors of the core collapse SNe are shown. The classification of SN types based on SN light curves and elements emission lines are reviewed in Filippenko (1997), and can be roughly linked to the progenitor mass classification as well (Smartt, 2009). The type I SNe are defined by the lack of H features (either in emission or absorption). Type Ia SNe also show no He features but have a characteristic Si absorption feature. Both type Ib and Ic (Ib/c) SNe show the absence of He features but strong features of the intermediate mass elements O, Mg, and Ca, this can be explained by a strong Wolf-Rayet wind which is capable of blowing away the entire H and He-envelopes. The type II SNe are all defined by the presence of strong H lines. Most type II SNe can be further subdivided into the type IIP SNe and the type IIL SNe via their optical light curves, the former one show a plateau phase while the later one exhibit a linear decay after peak brightness. The plateau phase is probably caused by SN exploding in a low-mass H-envelope that cannot sustain a lengthy recombination phase. The type IIb SNe begin with spectra like type II but evolve rapidly to exhibit He lines and at the same time the H lines weaken and

Table 4.1: Core collaps Supernovae

SNe Type	Detection probability[a]	Progenitor mass	Stages before SN	After the SN
SNe IIP	$58.7\% \pm 8.0\%$	$8 - 25\,M_{\odot}^{b}$	RSG	NS
SNe IIL/b	$8.1\% \pm 4.4\%$	$\gtrsim 17\,M_{\odot}$?	RSG	NS
SNe Ib/c	$29.4\% \pm 7.8\%$	$\gtrsim 25\,M_{\odot}^{c}$	WR	NS
SNe IIn	$3.8\% \pm 2.0\%$	$\gtrsim 30\,M_{\odot}$?	LBV?[d] WR?	PISN?[e]

[a] The data are taken from Smartt et al. (2009) which contain 92 samples within range of 28 Mpc.
[b] The RSG problem may request smaller maximum progenitor mass for SNe IIP, e.g. with 20 SNe IIP progenitor samples, no RSGs have mass $\gtrsim 17\,M_{\odot}$ (Smartt et al., 2009).
[c] Some SNe Ib/c may come from the binary system which allows a much smaller progenitor mass without WR stage, considering that their companions could help ripping away the H-He layer (Smartt, 2009).
[d] LBV stands for Luminous Blue Variable.
[e] PISN stands for Pair Instability SN.

disappear. Both type IIb and IIL (IIL/b) progenitors may have lost most of their H-envelope but $\lesssim 1\,M_{\odot}$ before the SNe happen. If this H-envelope of type IIL/b progenitors is reduced by the wind loss, higher mass progenitors of type IIL/b than those of type IIP are expected. The type IIL/b SNe appear to be relatively infrequent, but they may be important in solving the RSG problem (the lack of high mass RSGs $\gtrsim 15\,M_{\odot}$ detected as type IIP progenitors). Finally the type IIn SNe usually have multiple components of velocity and always have a strong "narrow" profile. For more detailed classification studies, one should also take some special SNe into account, which exhibit fast rotating progenitors, close companions or low metal abundant (Smartt, 2009).

Before the SN exploded, the massive progenitor star during its main-sequence (MS) phase can blow a bubble with size up to tens of pc in the MC. As seen in Fig. 4.1, the MS bubble is filled with hot and low density gas; meanwhile, at the border of the MS bubble, swept circumstellar medium is compressed and forms a dense bubble shell. After the MS phase, the massive star will enter the red supergiant (RSG) phase. The slow, dense RSG wind expands into the structure formed by the main sequence wind and a thin, dense shell of shocked RSG material forms ahead of the freely expanding wind (see Fig. 4.2). In scenarios of SNe IIP ($M \approx 8 - 15\,M_{\odot}$), the RSG wind extends only to $\lesssim 1\,\mathrm{pc}$, while SNe IIL/b will have larger RSG wind bubbles above 5 pc with material up to the CNO layer striped up from the star and extending into the bubble (Chevalier, 2005). After the RSG phase, progenitor stars of SNe Ib/c are expected to go through the Wolf-Rayet(WR) phase. The numerical simulation result of a $60\,M_{\odot}$ WR star is shown in Fig. 4.3 (van Marle et al., 2007). During the WR stage the high speed wind blows away the dense RSG bubble and forms a very complex structure inside the MS bubble. In the following studies, we explore the evolution history of SNR HESS J1731-347 via modelling type IIP SN, type IIL/b SN, and type Ib/c SN scenarios. Thus right before the SN starts to explode, we first build the pre-SN environments in the following lists.

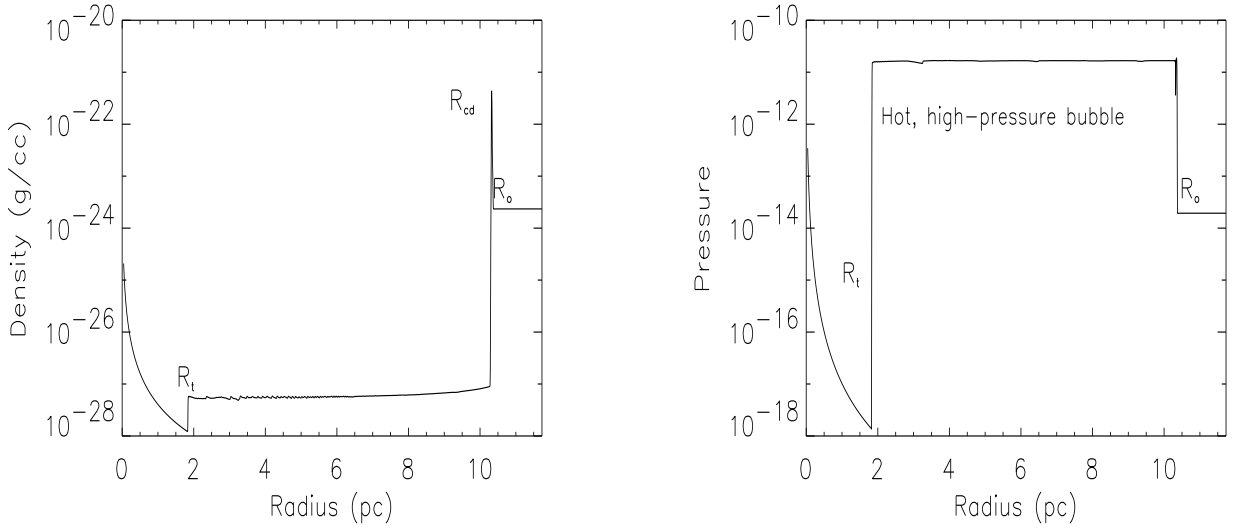

Figure 4.1: Density(left) and pressure(right) profiles from a numerical simulation of a MS wind blown bubble around a massive star. From $R = 0$ to $R = R_{\rm t}$ is the stellar wind region; from $R = R_{\rm t}$ to $R = R_{\rm cd}$ is the long shocked wind region; from $R = R_{\rm cd}$ to $R = R_0$ is the MS bubble shell; above R_0 is the outside circumstellar medium. Figures are taken from Dwarkadas (2008).

- *ICM.* The density of ICM is in range of $5 - 25\,{\rm H\,cm^{-3}}$, we adopt $n_{\rm ICM} = 5\,{\rm H\,cm^{-3}}$ for the ICM density in our work, because we would like our SNR able to keep a high shock velocity ($v_{\rm SNR} > 1000\,{\rm km\,s^{-1}}$) when it has expanded to such a large size (15 pc). We adopt the standard Galactic diffusion coefficient ($D(E) = D_{10}(E/10\,{\rm GeV})^{\delta}$, $D_{10} = 10^{28}\,{\rm cm^2/s}$, $\delta = 0.3 \sim 0.6$) in the ICM.

- *MC clumps.* High gas densities are expected inside MC clumps, and they can be deduced from the ^{12}CO data with three-dimensional structure models. Diffusion coefficients in the MC clumps are unknown, we will discuss this issue further below.

- *The MS wind bubble.* The MS wind bubble can be roughly divided into three regions, as seen in Fig. 4.1. Starting close to the star, the density in the MS bubble first follows a power law in the stellar wind region; then it remains constant inside the long shocked wind region ($n_{\rm b} \approx 0.01\,{\rm H\,cm^{-3}}$); at the border of the MS bubble, ICM swept up by the MS wind forms a MS bubble shell (Weaver et al., 1977). In our models, we ignore the power law wind region because of its small size and low density compared to the whole MS bubble. The bubble shell is assumed to have a thickness ~ 1 pc. Turbulence is strong in this shocked wind region, thus lower diffusion coefficients than inside the ICM region may be assumed in the following chapters. The magnetic field is assumed to be $B_0 = 5\,\mu$G for CR acceleration calculations, which is consistent with Berezhko Völk (2000) and Ptuskin & Zirakashvili (2005).

- *The RSG wind bubble.* Compared to the MS wind bubble, the size of the RSG bubble is smaller but its density is much higher (see Fig. 4.2). The density follows $n_{\rm RSG}(r) = \dot{M}_{\rm RSG}/4\pi r^2 v_{\rm RSG}$ (Chevalier, 2005). Here, $\dot{M}_{\rm RSG}$ and $v_{\rm RSG}$ are the mass loss rate and wind speed during RSG phase. The bubble shell between the RSG wind bubble and the

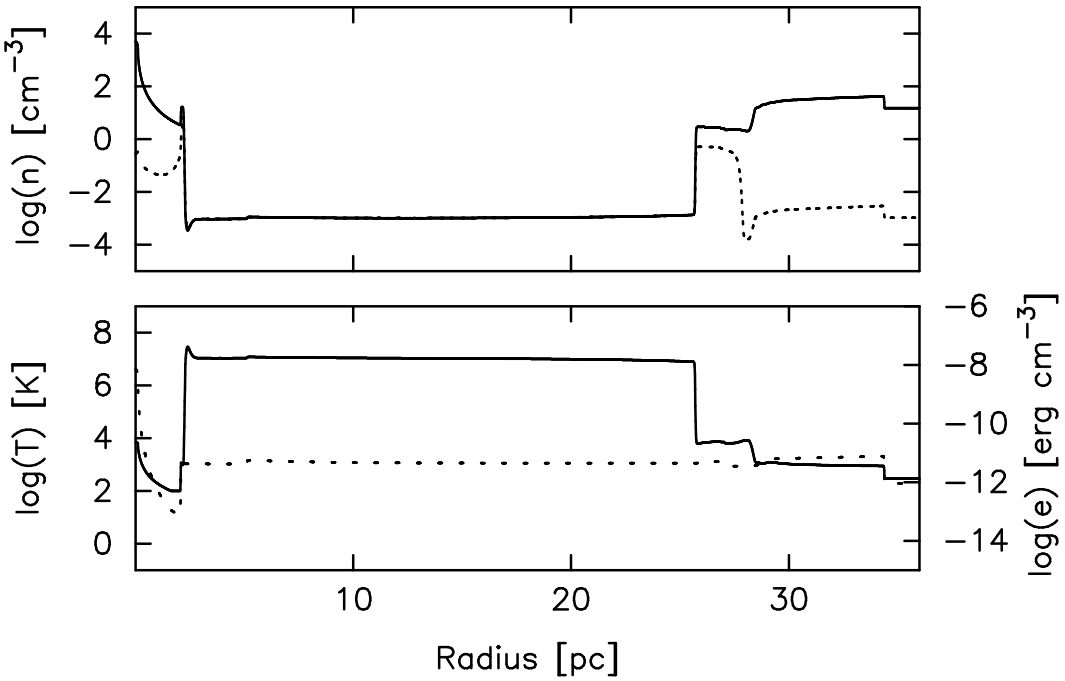

Figure 4.2: Radial structure of a stellar wind bubble around a 40 $M_\odot$ star at the end of the red supergiant stage, i.e. after 4.5×10^6 years. The results are based on one-dimensional numerical simulations, and show the RSG wind bubble, shocked wind region, and HII region. MS bubble shell in this model has spread out and its density has dropped. Top panel: total number density (solid line) and ionized number density (dotted line). Bottom panel: temperature (solid line) and internal energy (dotted line). Figures are taken from Arthur (2007).

MS bubble is ignored in our calculations because it only contains very little mass swept up from the almost empty MS bubble. The turbulence in the RSG wind is also strong. The magnetic field is assumed to be $B_0(r) = 2 \times 10^{13} (v_{\rm RSG}/10^6 cm/s)^{-1} (r/cm)^{-1}$ G (Ptuskin & Zirakashvili, 2005) which is similar to the interplanetary magnetic field (Parker, 1958).

- *The WR wind.* We also explored SNe Ib/c scenarios which imply the presence of a WR wind phase in the progenitor environment. However, we did not explore the complex inhomogeneous structures that are typical for the instabilities evolving from WR winds expanding into RSG wind bubbles. The WR wind together with the RSG wind can only inject very little material into the MS wind bubble. For example, before the SN explosion, a 25 $M_\odot$ star blows about 21 $M_\odot$ material into the MS wind bubble (with a size of ~ 21 pc) and leaves a CNO core behind. When the WR wind-driven material collides with the MS bubble shell, and if we assume that all material bounces back into the MS bubble, the maximum density contribution after dissipation in the MS bubble is about 0.02 H cm^{-3}. Thus, we adopt a homogeneous but very tenuous density for the WR wind, extending up to the inner boundary of the MS bubble. The magnetic field is assumed to be the same as in the MS bubble.

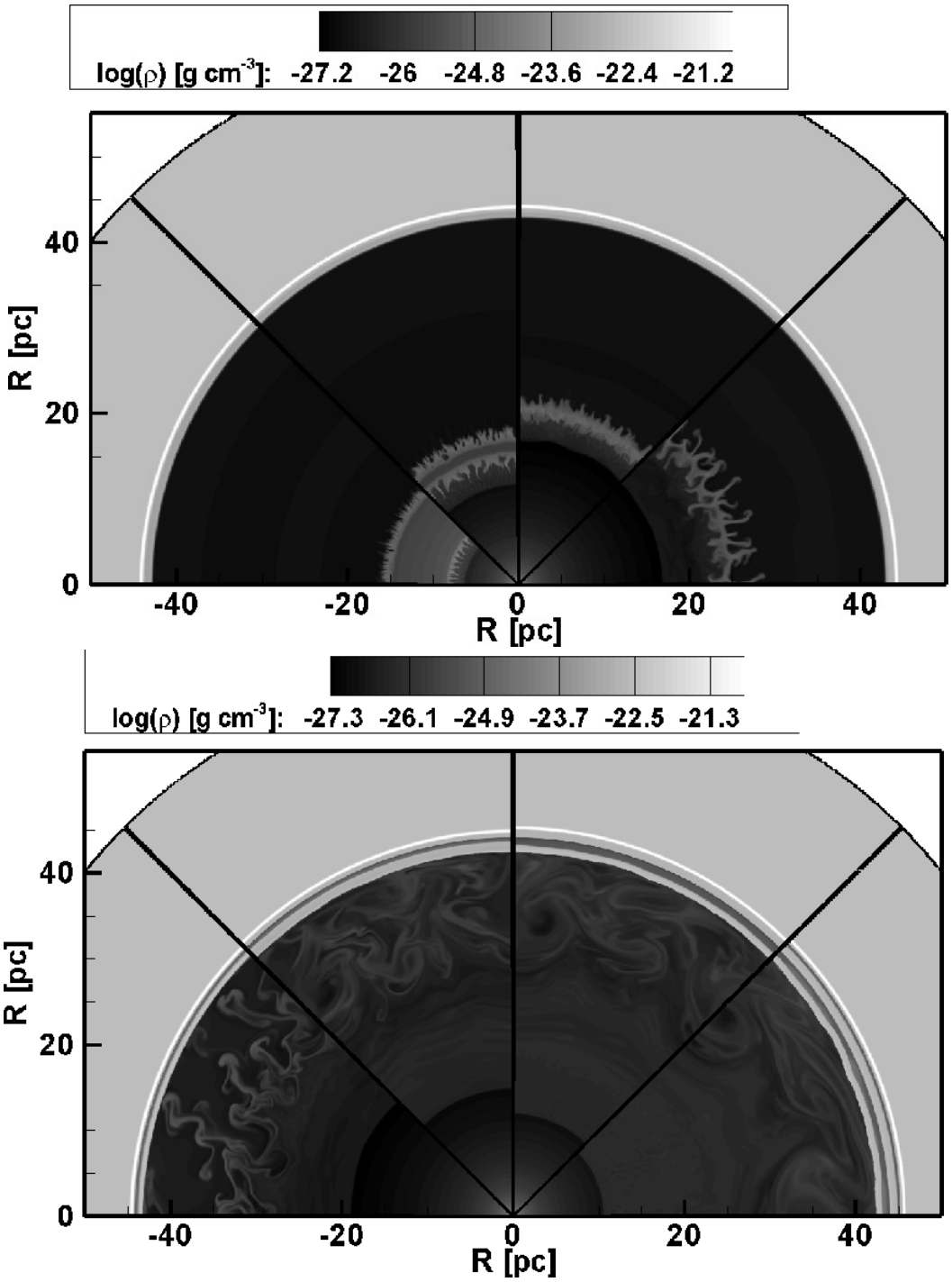

Figure 4.3: The logarithm of the density (g cm^{-3}) of the circumstellar medium of a 60 $M_{\odot}$ star at its WR phase. Each segment shows a moment in time starting on the left at t = 3.4516 Myr(left panel), 3.5436 Myr(right panel). Each following segment is taken 7927(left panel), 47565(right panel) years later. *In the top panel*, the fast WR wind sweeps up the dense Luminous Blue Variable(LBV) wind in a shell, which overtakes the earlier LBV shell. *In the bottom panel*, the shell fragments travel outwards in the bubble and collide with the outer edge. Afterwards, they dissipate into surrounding medium. Figures are taken from van Marle et al. (2007).

4.2 Ejecta-dominated and Sedov-Taylor stage

In this section, we explore the relationship among the age, the velocity and the radius of a evolving SNR. After starting the SN explosion, the SNR is likely to evolve into an environment with significant density changes, e.g. in a type IIL/b pre-SN environment, the SNR forward shock first passes the relatively dense RSG bubble, then enters the MS bubble, eventually it sweeps through the MS bubble shell and encounters the ICM. Hence, we expect a SNR evolution solution which can be used in an inhomogeneous but spherically symmetric circumstellar medium.

In our study, we focus on the CR acceleration capable phases during the SNR history which are the ejecta-dominated and the Sedov-Taylor stage. A self similar solution for the shock wave at the ejecta-dominated stage was found by Chevalier (1982) and Nadezhin (1985), it shows that the relation between SNR radius and SNR age can be approximately described by the power-law dependence, where $R_{\rm SNR} \propto t^{4/7}$ for an SNR expanding in a uniform medium and $R_{\rm SNR} \propto t^{7/8}$ for an SNR expanding in a RSG wind. Here we adopt the derived equations from Ptuskin & Zirakashvili (2005) following these power-law rules:

For the type Ia SN explosion in the uniform interstellar medium,

$$R_{\rm SNR} = 5.3 \left(\frac{\mathcal{E}_{51}^2 M_\odot}{n_0 M_{\rm ej}}\right)^{1/7} t_{\rm Kyr}^{4/7}\ {\rm pc},\ \ v_{\rm SNR} = 2.7\times10^3 \left(\frac{\mathcal{E}_{51}^2 M_\odot}{n_0 M_{\rm ej}}\right)^{1/7} t_{\rm Kyr}^{-3/7}\ {\rm km\,s^{-1}}. \tag{4.1}$$

For the type II SN explosion in the wind of a pre-supernova star,

$$R_{\rm SNR} = 7.7 \left(\frac{\mathcal{E}_{51}^{7/2} v_{\rm RSG,6} M_\odot^{5/2}}{\dot{M}_{\rm RSG,-5} M_{\rm ej}^{5/2}}\right)^{1/8} t_{\rm Kyr}^{7/8}\ {\rm pc},\ \ v_{\rm SNR} = 6.6\times10^3 \left(\frac{\mathcal{E}_{51}^{7/2} v_{\rm RSG,6} M_\odot^{5/2}}{\dot{M}_{\rm RSG,-5} M_{\rm ej}^{5/2}}\right)^{1/8} t_{\rm Kyr}^{-1/8}\ {\rm km\,s^{-1}}. \tag{4.2}$$

Here the $\dot{M}_{\rm RSG,-5}$ is the mass loss rate at RSG stage in unit of $10^{-5}\,{\rm M_\odot/year}$, $v_{\rm RSG,6}$ is the wind speed of RSG in unit of $10^6\,{\rm cm\,s^{-1}}$.

Once the shock leaves the RSG wind and enters the essentially empty MS bubble, and if, at this stage, the SNR is still in ejecta-dominated stage, we simply assume that the shock maintains its speed until it enters the Sedov-Taylor stage (swept-up mass equals the ejecta mass, $M_{\rm s} \approx M_{\rm ej}$). To smooth the transition between two SNR phases, the swept-up mass at this transition phase is adapted slightly around $1 M_{\rm ej}$.

At Sedov-Taylor stage, to solve the SNR evolution in an inhomogeneous but spherically symmetric circumstellar medium, a thin-shell approximation of a SNR evolution was derived in Ostriker & McKee (1988) and Bisnovatyi-Kogan & Silich (1995). Start from the momentum conservation, we have

$$\frac{d(Mv)}{dt} = 4\pi R_{\rm SNR}^2 \left(P_{\rm in} - P\right). \tag{4.3}$$

Here v is the gas velocity behind the shock, $P_{\rm in}$ is the pressure behind the shock, and P is the pressure of ambient gas. For the adiabatic blastwave, v is related to the shock velocity $v_{\rm SNR} = dR_{\rm SNR}/dt$ by the equation $v_{\rm SNR} = (\gamma_{\rm ad}+1)\,v/2$, where $\gamma_{\rm ad}$ is the ratio of the specific heats (adiabatic index). The energy of explosion $E = E_{\rm th} + \frac{1}{2}Mv^2$ consists of the internal energy $E_{\rm th} = \frac{4\pi}{3} R_{\rm SNR}^3 P_{\rm in}/(\gamma_{\rm ad}-1)$ and the kinetic energy. $M = M_{\rm ej} + 4\pi \int_0^{R_{\rm SNR}} dr r^2 \rho(r)$ is

the total mass confined by the shock of radius $R_{\rm SNR}$ where $M_{\rm ej}$ is the ejected mass and ρ is the density of the ambient gas. Ignoring the pressure in the circumstellar medium P, Ptuskin & Zirakashvili (2005) has derived:

$$v_{\rm SNR}(R_{\rm SNR}) = \frac{\gamma_{\rm ad}+1}{2}\left[\frac{12(\gamma_{\rm ad}-1)\mathcal{E}_{\rm ej}}{(\gamma_{\rm ad}+1)M^2(R_{\rm SNR})R_{\rm SNR}^{6(\gamma_{\rm ad}-1)/(\gamma_{\rm ad}+1)}}\cdot\int_0^{R_{\rm SNR}} drr^{6\left(\frac{\gamma_{\rm ad}-1}{\gamma_{\rm ad}+1}\right)-1}M(r)\right]^{1/2}, \tag{4.4}$$

$$t(R_{\rm SNR}) = \int_0^{R_{\rm SNR}}\frac{dr}{v_{\rm SNR}(r)},$$

where the adiabatic index is set as $\gamma_{\rm ad} = 4/3$ in our simulations, assuming that the pressure downstream of the shock is determined by the relativistic particles.

4.3 Is SNR HESS J1731-347 still inside main-sequence bubble?

To explain the large size and the high shock velocity of SNR HESS J1731-347, as mentioned in Chapt. 2, a very low density of circumstellar medium may be required in the SNR evolution model. Here we test this assumption by presenting five possible CC SN evolution scenarios following the models discussed above. The parameters and results of the five SNR evolution histories are shown in Table 4.2 and in Fig. 4.4, 4.5.

More than half of all recorded core collapse SNe are of type IIP, and their progenitor star masses range from $8\,{\rm M}_\odot$ to $\sim 25\,{\rm M}_\odot$ (Smartt, 2009). In agreement with the lack of high mass RSGs $> 15\,{\rm M}_\odot$ exploding as Type IIP SNe (Smartt, 2009), we choose progenitor stars with masses $8\,{\rm M}_\odot$ and $15\,{\rm M}_\odot$ for our first two scenarios. In the $8\,{\rm M}_\odot$ scenario, the progenitor star produces almost no MS wind bubble or RSG wind bubble, thus the SNR expands directly into the ICM. The SNR first follows $R_{\rm SNR} \propto t^{4/7}$ during ejecta-dominated stage, after sweeping $\sim 1 M_{\rm ej}$ ICM at around 800 years, it enter the Sedov-Taylor stage. At around 15.5 kyr ($\sim 10\,{\rm pc}$), the shock velocity gradually decreased to $\sim 250\,{\rm km\,s^{-1}}$ and it can no longer support an efficient CR accelerator.

In the $15\,{\rm M}_\odot$ scenario, the weak RSG wind blows away only $M_{\rm RSG} = \dot{M}_{\rm RSG}t_{\rm RSG} \approx 0.2\,{\rm M}_\odot$ material from the outer layer of the star into a $R_{\rm b,RSG} = v_{\rm RSG}t_{\rm RSG} = 1\,{\rm pc}$ size bubble. Inside this RSG bubble the SNR follows $R_{\rm SNR} \propto t^{7/8}$ during the ejecta-dominated stage, once the SNR enters the empty MS wind bubble we simply assume that the shock velocity remains constant. At ~ 2000 years, the SNR starts to encounter with the MS wind bubble shell which contains $\sim 400\,{\rm M}_\odot$ gas swept from the ICM. In the MS bubble shell, the SNR quickly sweeps $\sim 1 M_{\rm ej}$ and enters the Sedov-Taylor stage in less than 100years. As shown in Fig. 4.4, when the SNR just start to encounter with the MS bubble shell, the $E_{\rm max}$ profile shows a little bump followed by a quick drop. This is due to the coexistence of the high shock velocity and the high density gas in which the shock sweeps.

In the $17\,{\rm M}_\odot$ scenario a type IIP SN is also adopted, and the MS bubble is just large enough (15 pc) to keep a high shock velocity at present time. Except for the MS bubble shell, same gas density structure from scenario $15\,{\rm M}_\odot$ is used everywhere. At present time (15pc), the shock has swept only $\approx 4\,{\rm M}_\odot$ material and remains a high velocity ($4340\,{\rm km\,s^{-1}}$). The small bump of the $E_{\rm max}$ profile mentioned in scenario $15\,{\rm M}_\odot$ is not obvious in this scenario,

Table 4.2: SNR evolution in different scenarios

SN Type	M [a]	$R_{\rm b,MS}$ [b]	$R_{\rm b,RSG}$ [c]	$\mathcal{E}_{\rm ej}$ [d]	$M_{\rm ej}$ [e]	$R_{\rm SNR,\,end}$ [f]	$t_{\rm SNR,\,end}$ [g]	$v_{\rm SNR,\,end}$ [h]	$\eta_{\rm esc}$ [i]	$E_{\rm max,\,end}$ [j]	$\mathcal{E}_{\rm CR,end}$ [k]
SNe IIP	$8\,M_\odot$	0.5 pc	-	$1\,\mathcal{E}_{51}$	$6\,M_\odot$	10 pc	15.5 kyr	$250\,{\rm km\,s^{-1}}$	0.1	6.5 TeV	$0.23\,\mathcal{E}_{51}$
SNe IIP	$15\,M_\odot$	10 pc	1 pc	$1\,\mathcal{E}_{51}$	$12\,M_\odot$	10 pc	5.8 kyr	$150\,{\rm km\,s^{-1}}$	0.1	0.8 TeV	$0.12\,\mathcal{E}_{51}$
SNe IIP	$17\,M_\odot$	16.1 pc	1 pc	$1\,\mathcal{E}_{51}$	$14\,M_\odot$	15 pc	3.3 kyr	$4340\,{\rm km\,s^{-1}}$	0.02	81.1 TeV	$0.01\,\mathcal{E}_{51}$
SNe IIL/b	$20\,M_\odot$	18 pc	5 pc	$1\,\mathcal{E}_{51}$	$2\,M_\odot$	15 pc	6.1 kyr	$2140\,{\rm km\,s^{-1}}$	0.02	34.9 TeV	$0.05\,\mathcal{E}_{51}$
SNe Ib/c	$25\,M_\odot$	22 pc	-	$1\,\mathcal{E}_{51}$	$2\,M_\odot$	15 pc	2.9 kyr	$2470\,{\rm km\,s^{-1}}$	0.01	16.5 TeV	$0.01\,\mathcal{E}_{51}$

[a] Initial mass of progenitor star.
[b] The size of MS wind bubble, including the bubble shell (1 pc). Here we choose these numbers with a fair assumption that the pressure of circumstellar medium is $10^5\,{\rm K\,cm^{-3}}$ (Chevalier, 1999). Which is also consistent with the observational data (Chen et al., 2013)
[c] The size of RSG wind bubble. It corresponding to $\dot{M}_{\rm RSG} \approx 0.2(5) \times 10^{-5}\,M_\odot$/year and $v_{\rm RSG} \approx 10(15)\,{\rm km\,s^{-1}}$ for $15\,M_\odot$ SNe IIP ($20\,M_\odot$ SNe IIL/b) (Chevalier, 2005) .
[d] The SN total energy. Core collapse SN have observed kinetic energies of typically $\sim 10^{51}$ erg(Smartt, 2009).
[e] The ejecta mass of SN. It is consistent with the mass loss through MS wind and RSG wind. The neutron star mass is assumed $M_{\rm NS} \approx 2\,M_\odot$.
[f] For the first two SNe IIP scenarios, we stop the calculations when the Sedov-Taylor stage is about to end ($v_{\rm SNR} \ll 1000\,{\rm km\,s^{-1}}$), the corresponding SNR radius is around 10 pc. For the other scenarios, we calculate the SNR history until the forward shock reaches 15 pc which is the observed radius.
[g] Age of SNR when it expands to $R_{\rm SNR,\,end}$.
[h] The forward shock velocity of SNR when it expands to $R_{\rm SNR,\,end}$.
[i] The acceleration efficient. This parameter is one of the tuning parameters for fitting observation data in Chapt. 5.
[j] The escape energy of CRs from the shock when SNR at $R_{\rm SNR,\,end}$.
[k] The total escaped CRs flux integrated from the SN explosion to $R_{\rm SNR,\,end}$.

due to its relative larger time interval of the numerical integration. In our simulation, we evenly divided the logarithm of the SNR evolution time into many time intervals Δt. In each time interval, we use the shock velocity at $t + \Delta t$ instead of t for the calculation of $E_{\rm max}$.

Stars with progenitor masses that are above $\sim 17\,M_\odot$ can end as SNe IIL/b, which represent only $\sim 10\%$ of the total recorded core collapse SNe (Smartt, 2009). Here we choose $20\,M_\odot$ to make sure the MS-wind bubble ($\sim$17 pc) just exceeds the observed SNR radius. The RSG wind is able to blow $M_{\rm RSG} \approx 16\,M_\odot$ material into $R_{\rm b,RSG} = 5$ pc size bubble. As shown in Fig. 4.5, the SNR first follows $R_{\rm SNR} \propto t^{7/8}$ during the ejecta-dominated stage. At ~ 30 years, the SNR has swept $\sim 0.5 M_{\rm ej}$ and enters Sedov-Taylor stage while it is still inside the RSG bubble. When the SNR is expanding inside the empty MS bubble, it barely lose its speed until it enters the MS bubble shell at 17 pc.

A progenitor star with much larger mass ($\gtrsim 25\,M_\odot$) develops into a Wolf-Rayet phase after the RSG phase. The ongoing WR phase is characterized by strongly nonuniform, turbulent spatial distribution of the wind material. Indeed, the X-ray morphology of the SNR, as shown in H.E.S.S. Collaboration et al. (2011) and Bamba et al. (2012), might be indicative of such a phase. Since we only model structures in one (radial) dimension, such a turbulent configuration cannot be accommodated for in our model. Nevertheless, no matter what kind of structure the wind bubble has, the total mass confined inside the MS wind bubble mainly

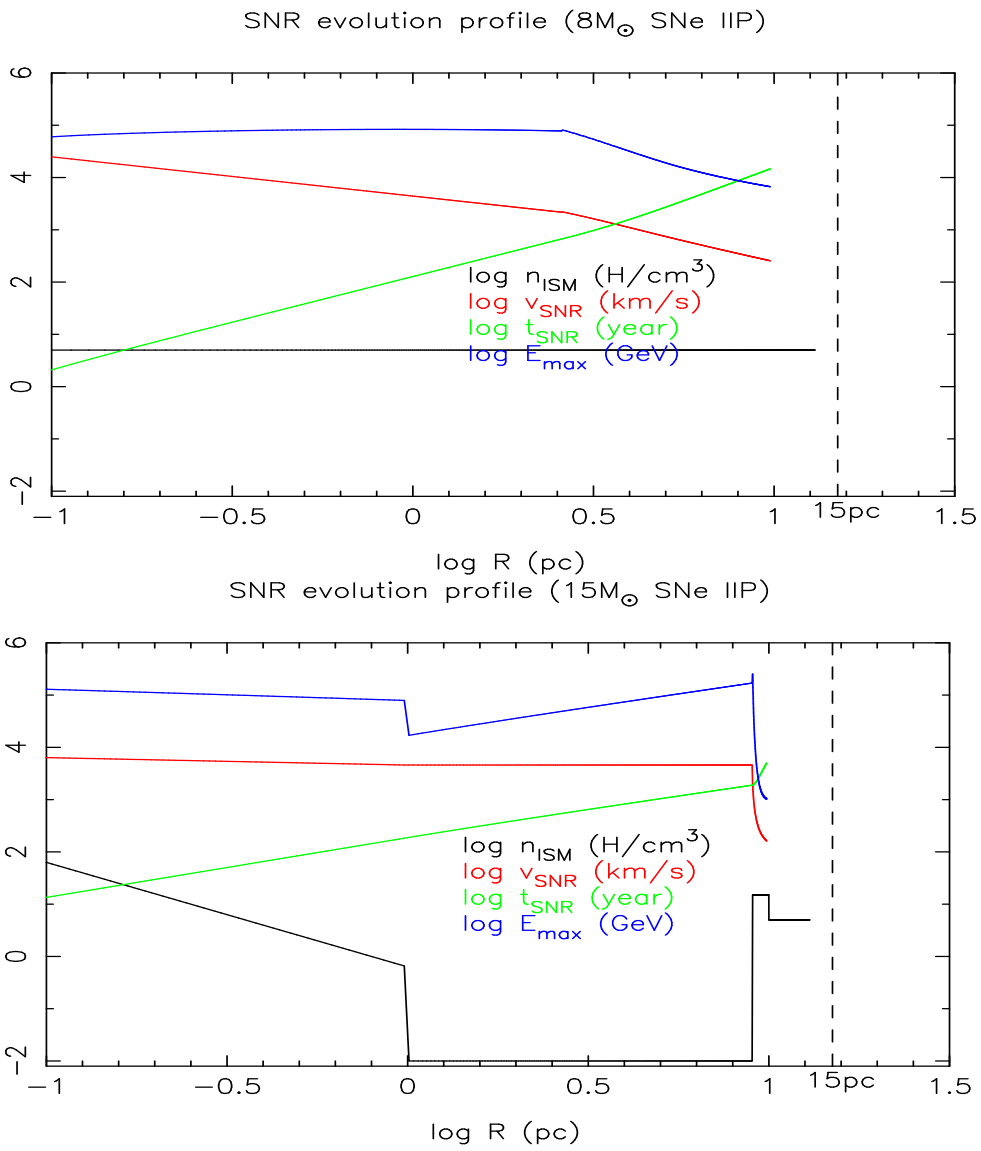

Figure 4.4: The SNR evolution profiles of the circumstellar medium density (black), the shock velocity (red), the age of SNR (green) and the escape energy (blue; see the acceleration model in Sect. 3.1) as functions of SNR radius are shown. From top to bottom, two different scenarios $8\,M_\odot$ SNe IIP, $15\,M_\odot$ SNe IIP are presented, respectively. The SNR size (15 pc) is marked in dashed line. The time, velocity and escape energy profiles are cut off at the end of Sedov-Taylor stage ~ 10 pc. Detailed parameters of these two scenarios can be found in Table 4.2. Figures are from Cui et al. (2016).

comes from the progenitor star and, therefore, is very limited. Thus, when the shock is sweeping inside the post-WR MS bubble, it can also maintain a relatively high velocity just as the shock in the $20\,M_\odot$ scenario does. Ultimately, in scenario $25\,M_\odot$, the WR wind blows away the dense RSG wind material ($\sim 21\,M_\odot$) into the MS bubble, as discussed in Sect. 4.1, leaving a bubble that is filled with a tenuous but roughly homogeneous gas ($n \approx 0.02\,\mathrm{H\,cm^{-3}}$). The SNR evolution profile first follows $R_{\rm SNR} \propto t^{4/7}$ during ejecta-dominated stage, after the SNR has swept $\sim 1.6 M_{\rm ej}$ material at around 1500 years (~ 10 pc), it enters the Sedov-Taylor stage.

Apparently, both scenario $8\,M_\odot$ and $15\,M_\odot$ fail to explain the high shock velocity of SNR HESS J1731-347, even with the lowest possible ICM density $n_{\rm ICM} = 5\,{\rm H\,cm^{-3}}$. As discussed above, despite the complexity of the progenitor history (even for WR stars), all materials injected into MS bubble later can only come from the star itself and is significantly less massive than the swept ICM material by the MS wind. Therefore, no matter what type of SN, as long as its shock is still expanding in the MS bubble, high shock velocity $v_{\rm SNR} > 1000\,{\rm km\,s^{-1}}$ can be easily obtained. Clearly, the MS bubble size become the key parameter to maintain a high velocity shock. Both the soft X-ray which is expected from the hot shocked MS wind region and the Hα emission lines which is expected from the MS bubble shell are hard to be detected, due to the heavy absorption at HESS J1731&J1729. In our study, we adopt a linear relationship between the progenitor mass and the MS bubble size, which is developed by Chen et al. (2013). This relationship is based on 15 well observed OB stars ($8-72\,M_\odot$) and can be written as

$$p_5^{1/3} R_{\rm b} = \left[\alpha \left(\frac{M}{M_\odot}\right) - \beta\right]\ {\rm pc}, \tag{4.5}$$

where $\alpha = 1.22 \pm 0.05$ and $\beta = 9.16 \pm 1.77$. If the ICM pressure is constant and $\approx 10^5\,{\rm cm^{-3}K}$ (i.e., $p_5 \approx 1$) as suggested, e.g., by (Chevalier, 1999), then $R_{\rm b}$ is linearly correlated with M. This relationship is also consistent with the theory that one can obtain the maximum $R_{\rm b}$ when the bubble pressure equilibrium with its surroundings (Chevalier, 1999):

$$R_{\rm b} = 15.8 \left(\frac{\dot{M}}{10^{-7} M_\odot\,{\rm yr^{-1}}}\right)^{1/3} \left(\frac{\tau_{\rm ms}}{10^7\,{\rm yr}}\right)^{1/3} \left(\frac{v_{\rm w}}{10^3\,{\rm km\,s^{-1}}}\right)^{2/3} \left(\frac{p/k}{10^5\,{\rm cm^{-3}K}}\right)^{-1/3}\ {\rm pc}, \tag{4.6}$$

where $\dot{M}$ and $v_{\rm w}$ are the mass-loss rate and terminal velocity of the stellar wind, respectively, $\tau_{\rm ms}$ is the main-sequence age, and p is the pressure of the surrounding interclump medium. The stellar parameters $\dot{M}$ and $v_{\rm w}$ can be estimated from theoretical or empirical studies, and are ultimately functions of stellar mass M mainly.

In our SNR models, the SNR needs to evolve inside a circumstellar medium with significantly density changes along the radial direction. During the Sedov-Taylor stage, the "thin-shell" approximation solution can naturally cover those density changes with smaller numerical integration steps. As seen in Fig. 4.4 and Fig. 4.5, the biggest changes in the density profiles are the step functions used at the MS bubble shells. The adoption of these simplified step functions is due to that the encountering between the shock and the MS bubble shell is not our main interests in this section, however, an exponential density function of the MS bubble shell is used in Sect. 5.2 to provide a hadronic explanation for the TeV emission from the SNR itself.

Overall, scenarios with larger MS bubbles $R_{\rm MS} > 15\,{\rm pc}$ (scenario $17\,M_\odot$ $20\,M_\odot$, $25\,M_\odot$) have successfully delivered high shock velocities $v_{\rm SNR} \gtrsim 1000\,{\rm km\,s^{-1}}$ and young SNR ages ($t_{\rm SNR} \lesssim 6000$years) at present time (15 pc). These results satisfy the observational constraints of HESS J1731&J1729, as discussed in Chapt. 2. The nonthermal shell observed in X-ray and TeV band requires a high shock velocity at present time; the lack of thermal X-ray inside the SNR indicates a very low density circumstellar surrounding the SNR; the high temperature of the neutron star (CCO) in a carbon atmosphere model suggests that the SNR is still a very young. Additionally, the young age of the SNR also plays an important role in explaining the TeV morphology of HESS J1729-235, which is discussed in next subsection.

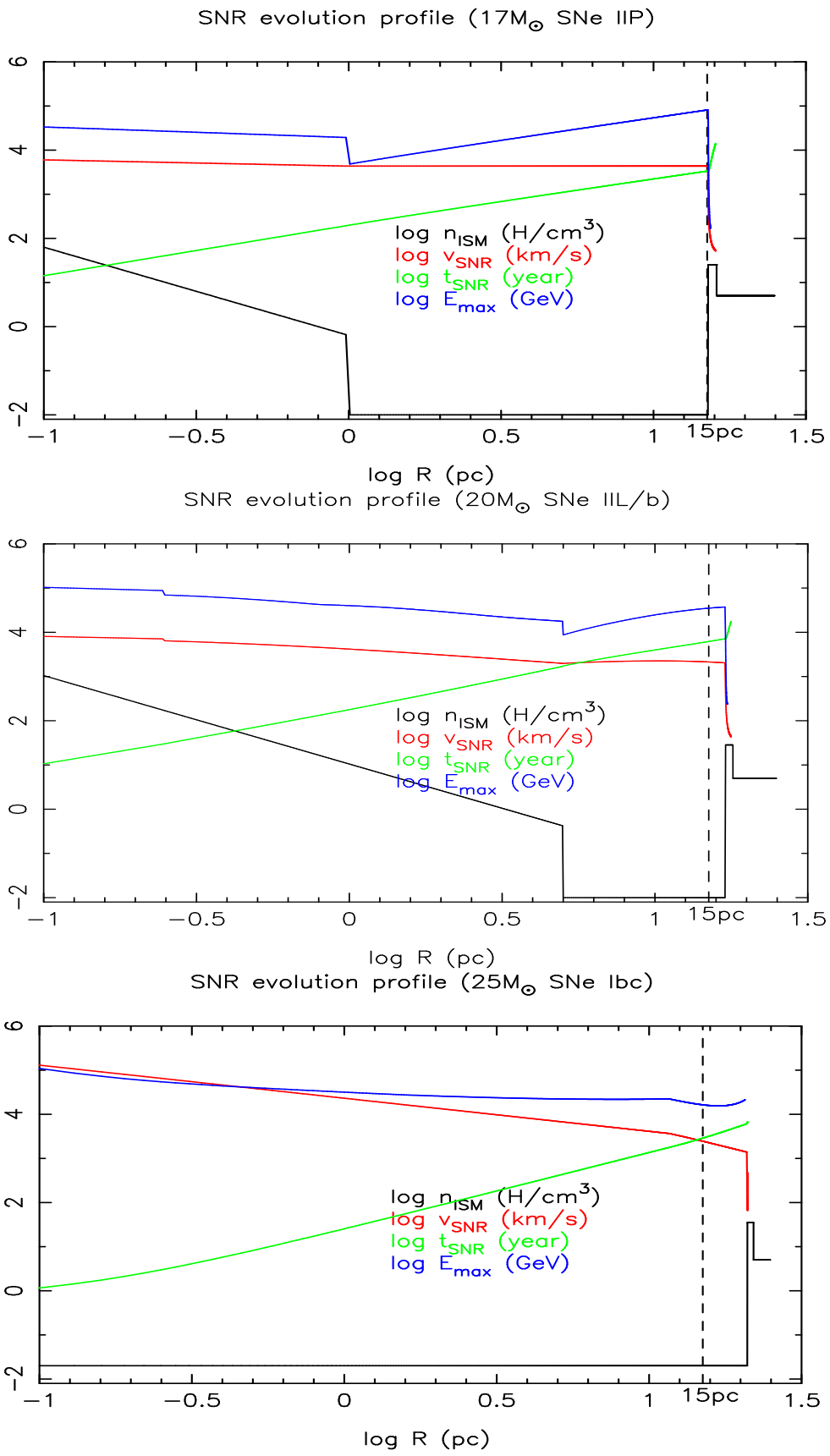

Figure 4.5: The SNR evolution profiles of three different scenarios $17\,M_\odot$ SNe IIP, $20\,M_\odot$ SNe IIL/b and $25\,M_\odot$ SNe Ib/c are shown. Same figure setup in Fig. 4.4 is used here as well. Figures are from Cui et al. (2016).

4.4 Modelling the nearby Molecular Clouds

As discussed above, the goal of this work is to explore if a scenario is feasible in which the TeV-emitting region HESS J1729-345 can be explained by CRs that escape the young SNR HESS J1731-347 and are currently diffusing away from the SNR. To that extent, we therefore constructed a simplified molecular cloud setup that is consistent with the current molecular line observations and can explain the boost of TeV emission toward HESS J1729-345 through π^0-decay of CRs interacting with the dense gas.

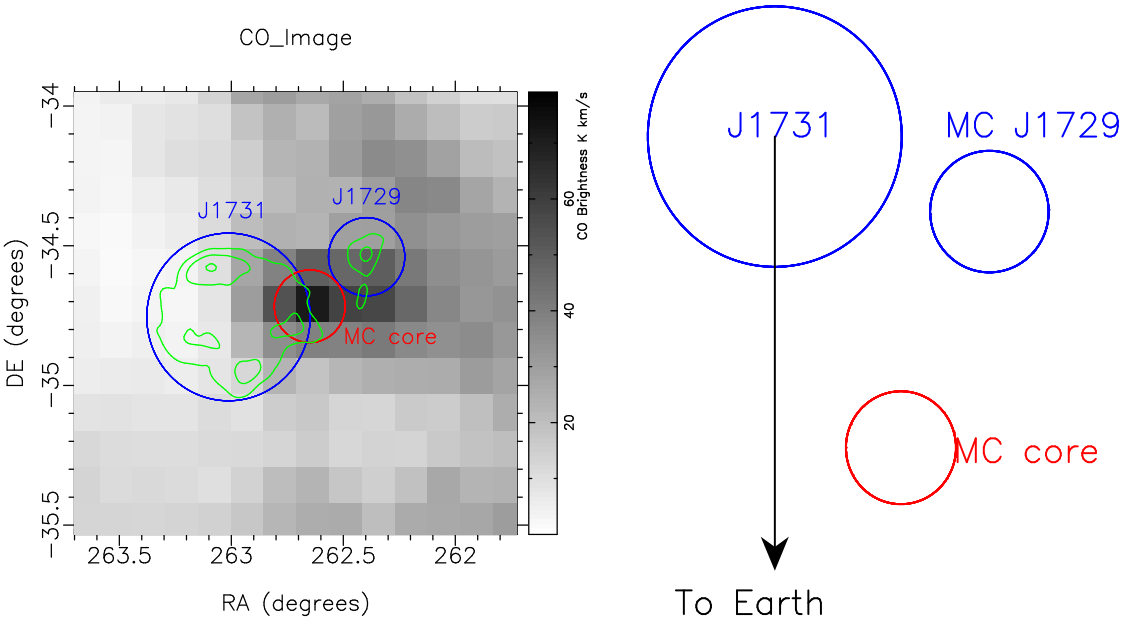

Figure 4.6: *The left panel* is the ^{12}CO image from the CfA ^{12}CO survey, which is integrated from $-13\,\mathrm{km\,s^{-1}}$ to $-25\,\mathrm{km\,s^{-1}}$ as same as used in H.E.S.S. Collaboration et al. (2011). The big blue circle is centered at the CCO of SNR J1731-347 with a radius of 0.3° . The small blue circle is centered at HESS J1729-345(RA 17h29m35s, Dec -34°32'22") with a radius of 0.14°. The red circle represent the densest core of MC (RA 17h30m36s, Dec -34°43'0")with a radius of 0.13°. The TeV significance image from H.E.S.S. Collaboration et al. (2011) is also shown in green contour, with 3 levels $(4\sigma, 6\sigma, 8\sigma)$. *The right panel* is an imaginary scratch showing the same three-dimensional structure as left panel, only seen from different viewing angle. Figure is from Cui et al. (2016).

The ^{12}CO image in Fig. 4.6 is obtained using the CO data from CfA survey (Dame et al., 2001). The CO cube data of the whole Galactic survey can be downloaded from `https://www.cfa.harvard.edu/rtdc/CO/CompositeSurveys/`. In the cube data, the x, y, and z axis represents velocity, longitude, and latitude, respectively.

The gas of the molecular clouds shown in Fig. 4.6 is likely concentrated in relatively dense clumps and filaments with sizes $\lesssim 10\,\mathrm{pc}$. The most simplified representation of the overall molecular cloud structure that satisfies our goal consists of two spherical, homogeneously filled

clumps: one corresponding to the HESS J1729-345 region (MC-J1729) with radius 7.8 pc (see the small blue circle in Fig. 4.6) and a second corresponding to the densest molecular cloud core region (MC-core) which is centered at R.A. 17h30m36s, Dec -34°43'0" with an ad-hoc set radius of 7.2 pc (see the red circle in Fig. 4.6). To translate the measured CO intensity of these two clumps into corresponding gas density, we adopt the CO-to-H_2 mass conversion factor $1.8 \times 10^{20}\,\mathrm{cm^{-2}K^{-1}km^{-1}s}$ (Dame et al., 2001), and obtain mean densities of $367\,\mathrm{H_2\,cm^{-3}}$ (MC-core, total mass 2.84×10^4 $M_\odot$) and $240\,\mathrm{H_2\,cm^{-3}}$ (MC-J1729, 2.36×10^4 $M_\odot$).

As can be seen in the left panel of Fig. 4.6, the gas density and the TeV observational image are not a very good match. In our setup, this is a consequence of the nonuniform density of the CRs injected by the SNR, following the injection and diffusion history over the lifetime of the SNR. Putting MC-J1729 closer in space to the SNR than the bulk of the gas material (represented in our setup by MC-core) will result in a TeV emissivity dominated by MC-J1729. As shown in the imaginary scratch of Fig. 4.6, MC-J1729 is set to be at the minimum possible distance, i.e., the projected 30.7 pc distance to the SNR, while MC-core is placed at a distance of 100 pc in the foreground of the SNR.

In our work, we simplify the hadronic collisions between CRs and target atoms (e.g., in the MC) to pp collisions only. The cross-section table of the pp collision was obtained from Kachelrieß & Ostapchenko (2012).

5

Explaining the observational data from HESS J1731&J1729

The main work in this chapter is to explain the TeV emission from HESS J1729-345 with a feasible scenario, in which the runaway super-TeV CRs from SNR HESS J1731-347 are interacting with local molecular clouds. Following Chapt. 3 and Chapt. 4, we have successfully setup the CR acceleration, CR diffusion, SNR evolution and three-dimension MC models:

- In the SNR evolution model, the shock velocity $v_{\rm SNR}(t)$, SNR radius $R_{\rm SNR}(t)$ and the density of the material $n_0(R_{\rm SNR})$ that the shock is sweeping into are provided at any time t.
- In the CR acceleration model, the CR density N_0 at the shock and the escaping flux $J(v_{\rm SNR}, n_0)$ from the absorption boundary $R_{\rm Abs}(R_{\rm SNR}, t)$ are given at any time t.
- In the CR diffusion model, we can obtain the final CR density at any target position outside the SNR (e.g. MC clumps) at time $t_{\rm end}$.
- In the three-dimension MC model, we delivered the densities, sizes, and distances of the MC clumps – MC-J1729 and MC-core.

As discussed in Sect. 4.1, we present the SNR evolution histories of five CC SN scenarios and find out that SNR HESS J1731-347 should be still evolving inside the MS bubble (scenario $17\,{\rm M}_\odot$, $20\,{\rm M}_\odot$, $25\,{\rm M}_\odot$). In section Sect. 5.1 we explain the TeV spectrum and morphology of HESS J1729-345 using only SNR scenario $20\,{\rm M}_\odot$, and $25\,{\rm M}_\odot$, meanwhile, we assume a leptonic dominated TeV emission of SNR HESS J1731-347. In section Sect. 5.2, assuming the shock is already encountering with the MS bubble shell, we further build the scenario $20\,{\rm M}_\odot$ in-shell, and $25\,{\rm M}_\odot$ in-shell to test the hadronic explanation for the TeV emission from the SNR itself.

5.1 SNR still inside the main-sequence bubble

5.1.1 The CR diffusion results with analytical diffusion method

In this subsection, we explore the the CR releasing and CR diffusion histories in different SNR evolution scenarios. For simplicity, we use the analytical diffusion method with a homogeneous diffusion environment covering the entire space. Following the SNR evolution

histories of the five SNR scenarios mentioned above, we have calculated their total released CRs into the space, their CR spectrum at target distance (30 pc and 100 pc), and their hadronic γ-ray spectrum at target distance, as shown in Fig. 5.1, 5.2.

During the calculations in this subsection, each SNR history is evenly divided into hundreds of small time intervals along the logarithm of time. At each time interval, we release $J(E)$ CRs from the surface of the absorption boundary of the SNR. Adopting a homogeneously diffusion coefficient ($D_{10} = 10^{28}\,\mathrm{cm}^2/\mathrm{s},\ \delta = 0.3$) in the entire space, we use the analytical diffusion method described in Sect. 3.1.2 and Sect. 3.2 to calculate the CR density n_{target} at target distance D_{MC} and time t_{age}. As shown in Fig. 5.1, 5.2, the CR spectrum are evenly divided into 120 bands along the logarithm of energy, ranging from 1GeV to 1000TeV. Hence, the expected hadronic TeV spectrum received on Earth can be written as

$$F(E_\gamma)/dE_\gamma = \int_{1\,\mathrm{GeV}}^{1000\,\mathrm{TeV}} dE_{\mathrm{CR}} \cdot n_{\mathrm{target}}(E_{\mathrm{CR}}, D_{\mathrm{MC}}, t_{\mathrm{age}}) \cdot M_{\mathrm{MC}} \cdot \sigma_{\mathrm{pp}}(E_{\mathrm{CR}}, E_\gamma) \cdot c \cdot \frac{1}{4\pi D_{\mathrm{J1731}}^2}, \quad (5.1)$$

where M_{MC} is the total mass of a MC clump, the $\sigma_{\mathrm{pp}}(E_{\mathrm{CR}}, E_\gamma)$ is the derivative of the pp cross section of generating E_γ γ-rays by E_{CR} protons, and the energy of γ-rays and CRs are shown as E_γ and E_{CR}, respectively.

Despite the fact that scenario $8\,\mathrm{M}_\odot$ and scenario $15\,\mathrm{M}_\odot$ fail to explain the high shock velocity at present time t_{age}, the CR releasing and diffusion results of all five scenarios are shown for a better comparison:

1. *Scenario SNe IIP* $8\,\mathrm{M}_\odot$: The SNR in scenario $8\,\mathrm{M}_\odot$ has released much more CRs ($\mathcal{E}_{\mathrm{CR,end}} \approx 0.23\,\mathcal{E}_{51}$) than ones in other scenarios have done, mostly due to that its shock has swept much more material during its long evolution history. The higher-energy CRs, as shown as the higher-energy peak in the spectrum of total released CR in Fig. 5.1, is mostly attributed to the high shock velocity during the first 1000 years of the SNR history. At the end of the SNR history (~ 1.5 kyr), most of these higher-energy CRs have already propagated into outer-space ($\gtrsim 100$ pc). Hence, in contrast to the spectrum of total released CRs, the CR spectrum at 30 pc has shown a significant drop of the higher-energy peak.

2. *Scenario SNe IIP* $15\,\mathrm{M}_\odot$: Right before the SNR encounters with the MS bubble shell (~ 2000 years), it has only released $\mathcal{E}_{\mathrm{CR}} \approx 0.02\,\mathcal{E}_{51}$ CRs with energy from ~ 20 TeV to ~ 150 TeV. Right after the SNR enter the MS bubble shell, for merely $\lesssim 100$ years the high shock velocity together with the high density of target gas allow $\mathcal{E}_{\mathrm{CR}} \approx 0.04\,\mathcal{E}_{51}$ CRs to be released with energy up to hundreds of TeV (~ 100 TeV to ~ 300 TeV). Same like the situation in scenario $8\,\mathrm{M}_\odot$, the higher-energy peak of the CR spectrum at 30 pc in scenario $15\,\mathrm{M}_\odot$ also shows a more severe decline than the lower-energy part does.

3. *Scenario SNe IIL/b* $20\,\mathrm{M}_\odot$: When the SNR is still expanding inside the dense RSG bubble (the first 1500 years), as a result of the coexistence of the high density gas and the high shock velocity, it has released $\mathcal{E}_{\mathrm{CR}} \approx 0.04\,\mathcal{E}_{51}$ CRs with energy from ~ 40 TeV to ~ 170 TeV into the space. Here one should notice that the η_{esc} in scenario $17\,\mathrm{M}_\odot$, $20\,\mathrm{M}_\odot$, and $25\,\mathrm{M}_\odot$ are 5 or 10 times lower than ones in scenario $8\,\mathrm{M}_\odot$, and $15\,\mathrm{M}_\odot$. These early released CRs (the first 1500 years) are responsible for $\sim 80\%$ of the total released CRs ($0.05\,\mathcal{E}_{51}$) in the entire SNR history (6100 years). Due to the relative short SNR evolution history (6100 years), the decline of the higher-energy peak described in scenario $8\,\mathrm{M}_\odot$ and $15\,\mathrm{M}_\odot$ is not very obvious in scenario $20\,\mathrm{M}_\odot$.

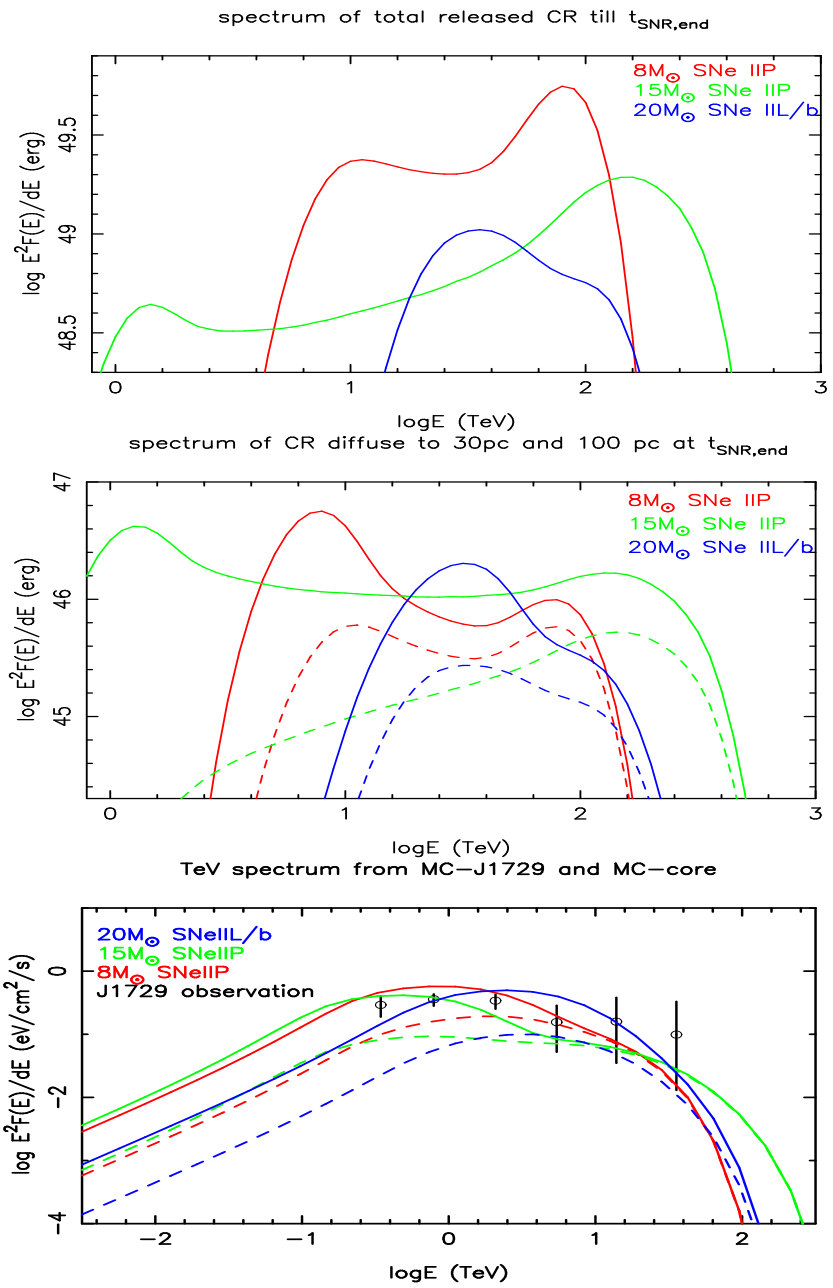

Figure 5.1: Here we present the CR releasing and diffusing results in SNR scenario $8\,M_\odot$ SNe IIP(red), $15\,M_\odot$ SNe IIP(green), $20\,M_\odot$ SNe IIL/b(blue). The detail parameters of these SNR scenarios are shown in Fig. 4.4,4.5 and Table 4.2. *The top panel*: The spectra of total released CRs integrated from $t = 0$ (SN explosion) to $t = t_{\rm SNR,\,end}$. *The middle panel*: The spectra of CRs at 30 pc(solid lines) and 100 pc(dashed lines) when $t = t_{\rm SNR,\,end}$. These spectra is obtained through multiplying the CR density at 30 pc and 100 pc with the volume of MC-J1729 ($4/3\pi R^3$, $R = 7.8$ pc) and the volume of MC-core ($R = 7.2$ pc) separately. *The bottom panel*: The hadronic γ-ray spectra of MC-J1729 and MC-core, the mass of MC clumps follow the setup described in Sect. 4.4. Observational data of HESS J1729-345 reduced by H.E.S.S. Collaboration et al. (2011) is shown in black circles. Figures are taken from Cui et al. (2016).

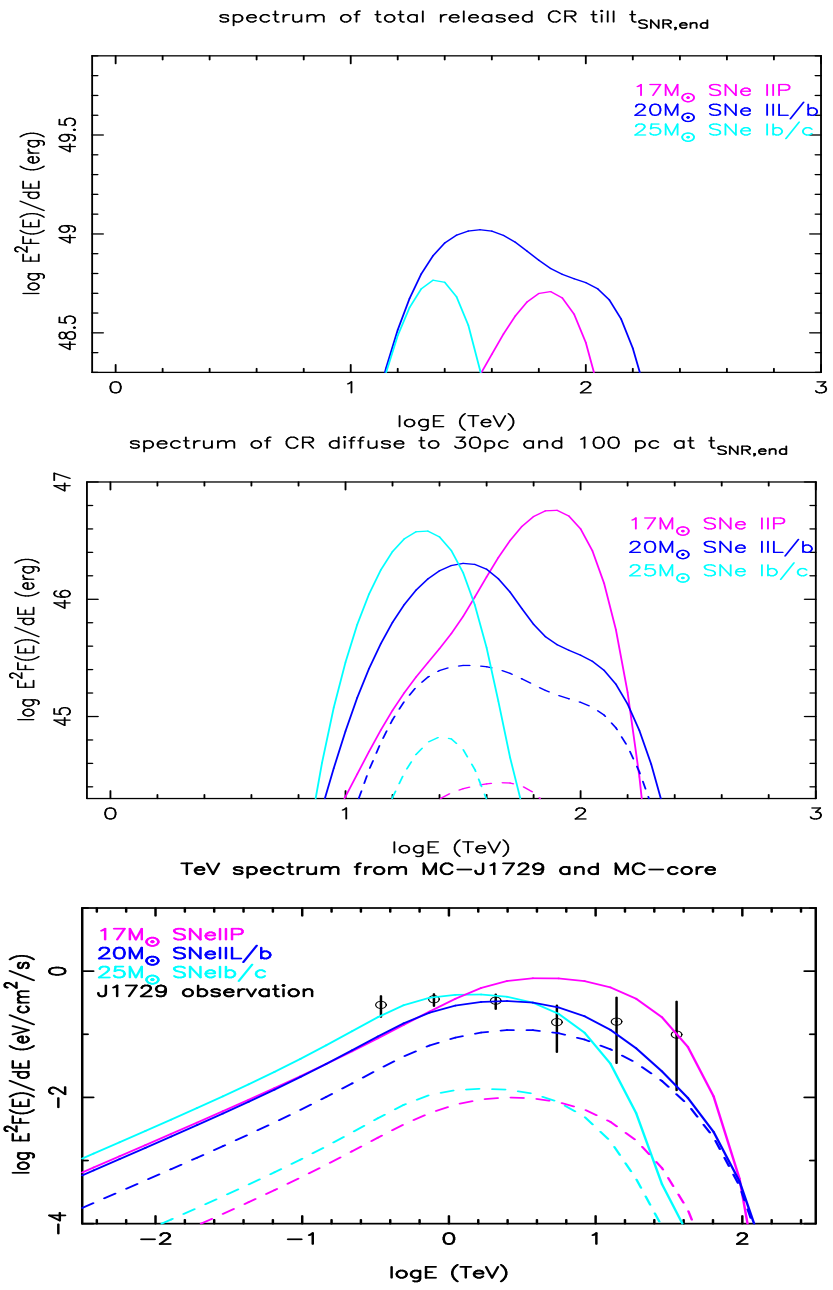

Figure 5.2: Here we present the CR releasing and diffusing results in the SNR scenario 25 $M_\odot$ SNe Ib/c(cyan), 17 $M_\odot$ SNe IIP(purple), 20 $M_\odot$ SNe IIL/b(blue). The detail parameters of these SNR scenarios are shown in Fig. 4.5 and Table 4.2. Same figure setup used in Fig. 5.1 are used here. We show the results in SNR scenario 20 $M_\odot$ again for better comparison. Figures are taken from Cui et al. (2016).

4. *Scenario SNe IIP* 17 $M_\odot$ *and SNe Ib/c* 25 $M_\odot$: The SNRs in these two scenarios are basically expanding inside the empty MS bubble during their entire SNR history (before $t_{\rm SNR,end}$). Due to the lack of significant changes in the shock velocity or the density of encountered circumstellar gas, the spectra of total released CRs clearly show narrow features.

Once we obtain the CR density at the target MC clumps, we can calculate the TeV

spectrum by multiply the CR density with the mass of the MC clumps The $\eta_{\rm esc}$ of all five scenarios, as seen in Table 4.2, are based on the spectrum fitting shown in Fig. 5.1, 5.2. In the following work, we only focus on the spectrum fitting in SNR scenario $17\,M_\odot$, $20\,M_\odot$, and $25\,M_\odot$. Adopting the Galactic diffusion coefficient ($D_{10} = 10^{28}\,{\rm cm^2/s},\ \delta = 0.3$), both scenario $20\,M_\odot$ and $25\,M_\odot$ can very well reproduce the TeV spectrum of HESS J1729-345, while scenario $17\,M_\odot$ has shown a much harder spectrum with exponential cutoff up to 10s of TeV, which is due to its higher average shock velocity. Meanwhile, the TeV emissions from MC-core are well suppressed in all three SNR scenarios.

5.1.2 The CR diffusion results with Monte Carlo diffusion method

With the Monte Carlo diffusion method, we are able to record the CR spatial distribution outside the SNR at any time in an inhomogeneous diffusion environment. Same like the methods discussed above (Sect. 5.1.1), the SNR history is evenly divided into hundreds of small time intervals along the logarithm of time, and the CR spectrum is evenly divided into 120 bands along the logarithm of energy. Different from the analytical diffusion method, here the released CR number is an integer and we simulate and record the trajectory of each CR released from the SNR. At each time interval ($\Delta t_{\rm SNR} \approx 1 - 100\,{\rm years}$) of the SNR evolution, we release certain number of CRs $\Delta n(E_{\rm CR})$ with the given energy $E_{\rm CR}$ from the surface of the absorption boundary. The CR number $\Delta n(E_{\rm CR})$ follows a energy distribution ($E_{\rm CR}$ distribution) as described below,

$$\Delta n(E_{\rm CR}) = \int_{E_{\rm CR}+\Delta E_{\rm CR}}^{E_{\rm CR}} \frac{J(E_{\rm CR})\Delta t_{\rm SNR}}{C_{\rm J}} dE_{\rm CR} \approx \Delta E_{\rm CR} \cdot \frac{J(E_{\rm CR})\Delta t_{\rm SNR}}{C_{\rm J}} = E_{\rm CR} \cdot \frac{J(E_{\rm CR})\Delta t_{\rm SNR}}{C'_{\rm J}}, \tag{5.2}$$

where $J(E_{\rm CR})$ is the spectrum of runaway CR flux defined in Sect. 3.1, and $C_{\rm J}$, $C'_{\rm J}$ are the normalization factors. The value of $C'_{\rm J}$ is carefully chosen with the concern of our limited computing power and that at each energy band between 100 GeV and 1000 TeV, statistically sufficient CRs ($\Delta n(E_{\rm CR}) \gtrsim 10$) should be able to be released. Obviously, in order to have sufficient higher-energy CRs released during each time interval ($\Delta n(E_{\rm CR} \gtrsim 100\,{\rm TeV}) \gtrsim 10$), one often has to release too many lower-energy CRs ($\Delta n(E_{\rm CR} \lesssim 1\,{\rm TeV}) \gtrsim 10^5$). Therefore, to reduce the computing time in our simulation, we use a slightly different energy distribution ($E^2_{\rm CR}$ distribution) which can increase the ratio between higher-energy CRs and the total released CRs:

$$\Delta n(E_{\rm CR}) = E^2_{\rm CR} \cdot \frac{J(E_{\rm CR})\Delta t_{\rm SNR}}{C'_{\rm J}}. \tag{5.3}$$

An even better solution which can be applied in the future coding is to make $C'_{\rm J}(E_{\rm CR})$ energy dependent, in such a way the number of released CRs in each time interval becomes energy independent ($\Delta n(E_{\rm CR}) = \Delta n_{\rm const}$). Nevertheless, the computing time of a higher-energy CR is much longer than that of a lower-energy CR. This is due to that the time step (Δt) of a higher-energy CR in the Monte Carlo diffusion is much shorter than the one of a lower-energy CR, with regard to a constant step length $\Delta r = 1\,{\rm pc}$ used in our simulation and mentioned in Sect. 3.2.2.

The starting position of each CR is set randomly on the absorption boundary surface, the diffusion steps are described in Sect. 3.2.2. After calculating the trajectory of every CR, we

can obtain the spectrum of CRs in any confined spatial volume $V_{\rm MC}$ at any given time $t_{\rm diff}$. To represent the diffusion results in the figures shown below, we record the physical position of each CR at several given times, for example, $t_{\rm diff} = 300\,\text{years}$ or $t_{\rm diff} = 1500\,\text{years}$. As described in last paragraph, each group of released CRs ($\Delta n(E_{\rm CR}, t_{\rm r})$) has their own $C'_{\rm J}$ and $\Delta t_{\rm SNR}$, where $t_{\rm r}$ is the time when these CRs are released. After the Monte Carlo diffusion process, some of the CRs released at time $t_{\rm r}$ ($\Delta n_{\rm diff}$) have been found inside the given volume $V_{\rm MC}$ and at time $t_{\rm diff}$. Thus the final CR spectrum $N_{\rm CR}(E_{\rm CR})$ inside $V_{\rm MC}$ can be written as

$$N_{\rm CR}(E_{\rm CR}, V_{\rm MC}, t_{\rm diff}) = \sum_{t_{\rm r}=t_0}^{t_{\rm r}=t_{\rm diff}} \frac{\Delta n_{\rm diff}(E_{\rm CR}, t_{\rm r}) \cdot C'_{\rm J}(E_{\rm CR}, t_{\rm r})}{E_{\rm CR}^2}. \tag{5.4}$$

As introduced in Sect. 4.4, we place MC-J1729 at the shortest possible distance to the SNR (30.7 pc), while MC-core is located at the foreground of the SNR, 100 pc away. The simulated TeV sky maps in the following subsections illustrates that the expected TeV emission from MC-core is substantially suppressed with respect to the MC-J1729 emission, and thus remains undetectable in the measured TeV sky map due to the dominance of the emission from the SNR itself. This suppression of TeV emission from MCs other than MC-J1729 was indeed one main boundary condition for the choice of the model setup parameters in this work. The emission from the SNR itself is likely dominated by IC emission from VHE electrons, given the low gas density inside the wind bubble in which the forward shock still resides. The target gas density inside the entire MS wind bubble is assumed as $n_{\rm ISM} = 0.01\,\text{cm}^{-3}$ and $n_{\rm ISM} = 0.02\,\text{cm}^{-3}$ for scenario $20\,\text{M}_\odot$ and $25\,\text{M}_\odot$, respectively. The dense gas in the RSG bubble region and the downstream region of the forward shock are ignored in our Monte Carlo simulation, since our study mainly focus on the hadronic TeV emissions outside the SNR, i.e. at MC-J1729 and MC-core in our models. However, the density of target gas at MS wind bubble shell is considered in our simulation and follows the pre-SN environments mentioned in Sect. 4.1.

In the following subsections, we study the evolution of CR spatial distribution in different SNR scenarios and in different diffusion scenarios, the CR diffusion results are shown as 1 TeV γ-ray sky maps and TeV spectra below. In Sect. 5.1.2.1, we only focus on the differences of the CR diffusion results between two SNR scenarios, thus a homogeneous diffusion coefficient in the entire space is adopted for both SNR scenarios. While in Sect. 5.1.2.2, we only focus on the differences of the CR diffusion results among three diffusion scenarios, therefore, the SNR scenario $20\,\text{M}_\odot$ is adopted for all diffusion scenarios.

5.1.2.1 Compare the CR diffusion results in different SNR scenarios

In this subsection, we explore the CR diffusion histories of SNR scenario $20\,\text{M}_\odot$ and $25\,\text{M}_\odot$ using the Monte Carlo diffusion method described in Sect. 3.2.2. The $t_{\rm SNR,\,end}$ in scenario $20\,\text{M}_\odot$ and $25\,\text{M}_\odot$ are $\sim$6 kyr and $\sim$3 kyr, respectively. To better compare these two scenarios, we only show the diffusion results at time frames 300 years, 900 years, 1500 years, and 3000 years.

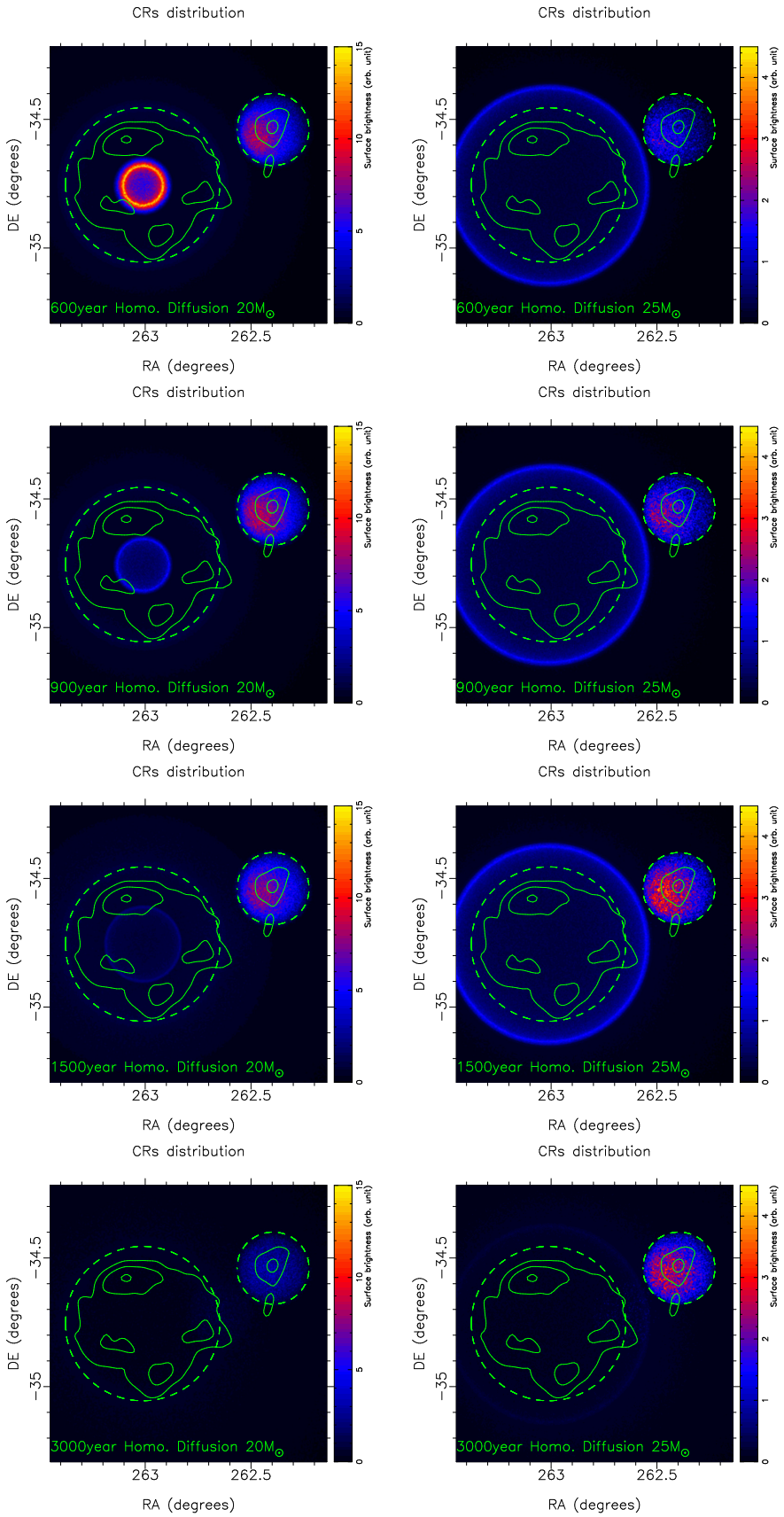

Figure 5.3: The 1 TeV images of different SNR evolution scenarios(from left to right) at different ages(from top to bottom) are shown. Green contour in solid lines is the observation TeV data from H.E.S.S. Collaboration et al. (2011), the big/small dashed circles represent the location of HESS J1731-345/HESS J1729-347.

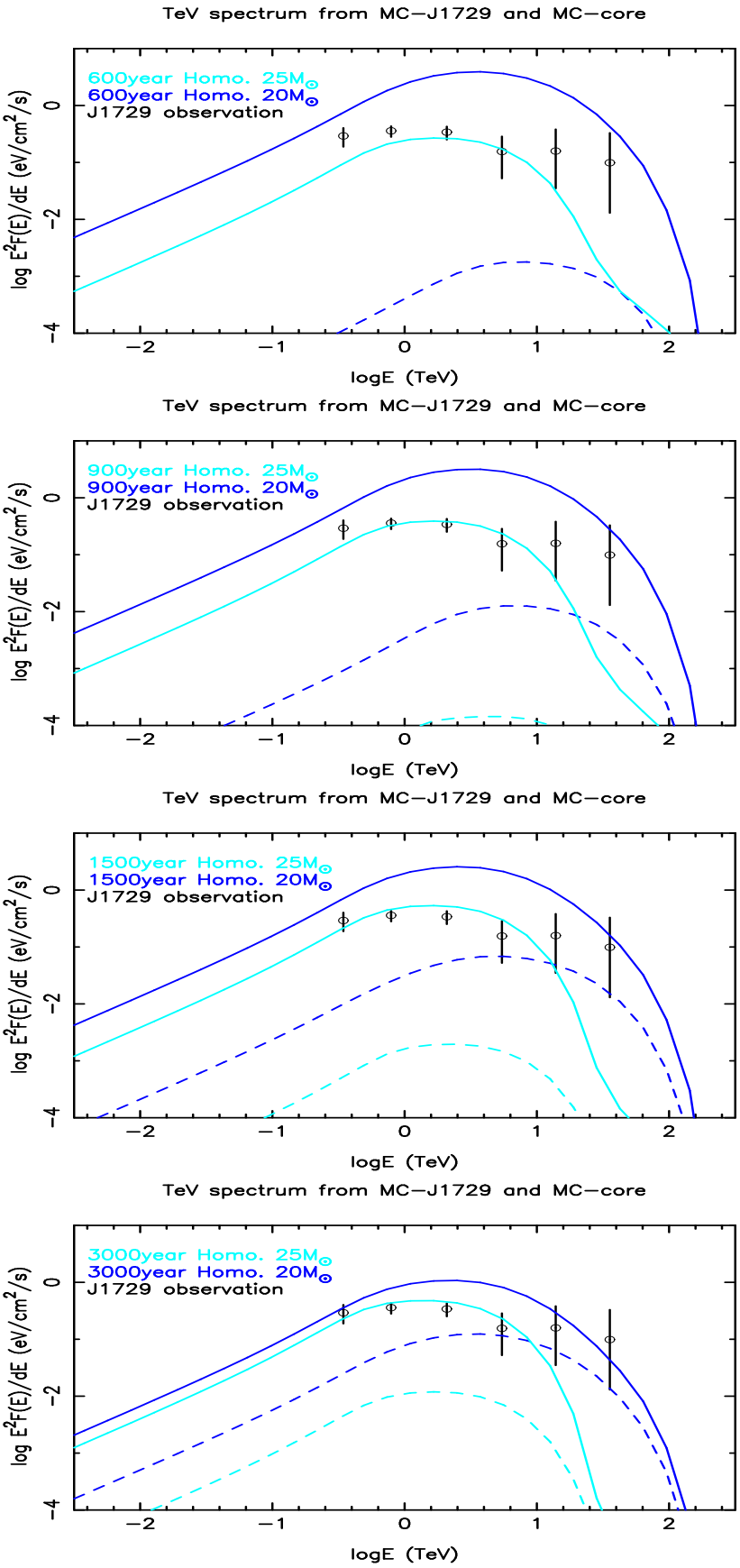

Figure 5.4: The reproduced TeV spectrum from MC-J1729(solid lines) and MC-core(dashed lines) of different SNR evolution scenarios at different ages(from top to bottom) are shown. Observation data of HESS J1729-345 shown in black circles are taken from H.E.S.S. Collaboration et al. (2011).

Since we mainly focus on a comparison of the diffusion results in two different SNR scenarios, here we adopt a homogeneous diffusion environment in both scenario $20\,M_\odot$ and $25\,M_\odot$ ($D_{10} = 10^{28}\,cm^2/s,\ \delta = 0.3$).

In Fig. 5.3, we show the 1 TeV γ-rays sky maps which are generated by runaway CRs colliding with target gas at different time frames. In Fig. 5.4, the corresponding TeV spectra from MC-J1729 and MC-core are also shown. In conclusion, with the Galactic diffusion coefficient, both scenario $20\,M_\odot$ and $25\,M_\odot$ have successfully explain the TeV emission from HESS J1729-345 while keep the TeV emission from MC-core suppressed. More details about the diffusion results in these two SNR scenarios are presented below.

In scenario $20\,M_\odot$, most of the higher-energy CRs ($E > 10$ TeV) are released in a very early stage ($t \lesssim 1000$year) when the SNR is still expanding inside the dense RSG bubble. This group of higher-energy CRs slowly spread outwards and form an expanding shell, which can be seen as the bright expanding ring in the left panels of Fig. 5.3. The TeV emission from MC-J1729 reaches its peak at $t \lesssim 1000$ years, and then gradually fades away. The distant MC-core also starts to show comparable TeV emission (10% of that from MC-J1729) in the later period ($t \gtrsim 2000$ years). To further test this SNR scenario that the SNR is expanding inside the dense RSG bubble, we look forward to future TeV observational evidences for a scenario that a very young SNR (a few hundreds years old) is capable of showing bright TeV emission from the SNR (leptonic or hadronic) as well as illuminating nearby MCs with runaway CRs.

In scenario $25\,M_\odot$, until present time, the SNR is only expanding inside the MS wind bubble without any density changes, as a consequence of that, the released CRs are quite evenly distributed along the SNR evolution history. At ~ 1000 years, the TeV emission from MC-J1729 reaches its peak and remains at this peak in the following 2000 years. In contrast to the early released CRs in scenario $20\,M_\odot$, the CRs in scenario $25\,M_\odot$ are released much later and face a difficulty of reaching MC-core at $t = 3000$ years. As seen in Fig. 5.3 and Fig. 5.4, TeV emission from MC-core is significantly lower than that from MC-J1729 ($F_{\rm core} < 1\%\,F_{\rm J1729}$) in each time frame. The bright ring larger than the SNR in Fig. 5.3 is caused by the high gas density at the MS bubble shell. This ring is especially bright in the TeV sky maps of scenario $25\,M_\odot$, owing to the fact that in scenario $25\,M_\odot$ the density of the MS bubble shell is higher and the upper-limit of the color bars is lower.

5.1.2.2 Compare the CR diffusion results in different diffusion scenarios

In this subsection, we explore the impact of the physical parameters – mostly the diffusion coefficients on our Monte Carlo diffusion results. Therefore, here we adopt the SNR evolution history of SNR scenario $20\,M_\odot$ in different diffusion scenarios. After separating the diffusion environment into three regions – the MS bubble, ICM, and MC clumps, we setup three different diffusion scenarios as shown in Table 5.1. Our modification of the diffusion coefficient in Table 5.1 are still in the range of Galactic standard ($D_{10} = 10^{28}\,cm^2/s,\ \delta = 0.3 - 0.6$).

Following the three diffusion scenarios in Table 5.1, we presented their 1 TeV sky maps at given time frames (600, 1500, 3000, 6000 years) in Fig. 5.5. The corresponding spectra from MC-J1729 and MC-core are also shown in Fig. 5.6. In scenario "homogeneous diffusion", the TeV emissions from MC-J1729 and MC-core reach their peaks at ~ 1000 years and ~ 3000 years, respectively. In both scenario "slow diffusion in MC" and scenario "fast

Table 5.1: Diffusion index (δ) in different regions for Monte Carlo simulation in Fig. 5.7.

Diffusion(Dif.) regions	MS bubble	ICM	MC clumps
Density $1\,\mathrm{cm}^{-3}$	0.01	5	480/734 (J1729/Core)
Homogeneous Dif.	0.3	0.3	0.3
Fast Dif. in MC clumps	0.3	0.5	0.5
Slow Dif. in MC clumps	0.3	0.5	0.3

In this work we only modify the energy index δ of the diffusion coefficient $D(E) = D_{10}(E/10\,\mathrm{GeV})^{\delta}$, while $D_{10} = 10^{28}\,\mathrm{cm}^2/\mathrm{s}$ is fixed in each scenario. From $\delta = 0.3$ to $\delta = 0.5$, diffusion coefficient of 10 TeV CR has increased ~ 3 times.

diffusion in MC", due to their higher diffusion coefficient in the ICM than that of scenario "homogeneous diffusion", the TeV emissions from MC-J1729 and MC-core reach their peaks at only ~ 500 years and ~ 1500 years, respectively. All panels in Fig. 5.5 share the same color bar, thus it is clearly seen that the TeV emission from MC clumps in scenario "slow diffusion in MC" is much brighter than that in scenario "fast diffusion in MC". Ultimately, both scenario "slow diffusion in MC" and "homogeneous diffusion" have successfully reproduced the TeV spectrum of HESS J1729-345 and suppressed the TeV emission from MC-core at present time (~ 6000 years). More discussions about the impact of the diffusion coefficients on our results are presented below.

As shown in Fig. 5.6 and Fig. 5.4, the spectra show sharper cutoff at higher energy band than the analytical spectra do in Fig. 5.2, this is due to the lack of higher-energy CRs ($E \gg 10$TeV) in our Monte Carlo simulation. At each time interval Δt_{SNR}, due to the limited computing power, the number of released higher-energy CRs Δn is often normalised to less than 1 and saved in a double variable. This double variable is then transferred into the integer "0" in the actual simulation. In Fig. 5.7, we avoid this problem by releasing 10 times more CRs at each time interval than that in Fig. 5.6 as well as by adopting $E^2 \cdot J(E)$ instead of $E \cdot J(E)$ as the energy distribution of released CRs.

In this subsection, diffusion coefficient is the only free parameter. However, in Table 5.2, we list the impacts of all five key parameters on our simulation results. The explanations for these impacts are presented below.

1. *When the SN explosion energy increases*: The averaged shock velocity increases and the age of the SNR is shortened. A higher shock velocity leads to a higher escape energy E_{max} and a higher CR escaping flux, while the shortened SNR age causes the difficulty for CRs to reach the distant MC-core.

2. *When the SN ejecta mass increases*: Although the shock velocity is smaller at the very beginning of SNR evolution, the deceleration of the shock velocity is also lowered and the shock can keep higher speed in a long run (see e.g. equation 4.4).

3. *When the acceleration coefficient increases*: More kinetic energy from the incoming plasma are transferred into the CR energy. Therefore, the escape energy and the CR escaping flux are also boosted.

4. *When the diffusion coefficient inside ICM increases*: More released CRs are able to reach distant targets. The advantages of MC-J1729 and the higher-energy CRs, as being closer to the SNR and being diffusing faster, respectively, are jeopardized.

5. *When the diffusion coefficient inside MC-clumps increases*: The average time for a CR walking inside the MC-clumps decreases. As a result of that, less CRs are accumulated inside the MCs.

Table 5.2: Parameter tuning to fit the TeV data from HESS J1729-345.

When increasing	$\mathcal{E}_{\rm ej}$	$M_{\rm ej}$	$\eta_{\rm esc}$	$D_{\rm ICM}$	$D_{\rm MC}$
Flux [a]	increasing	increasing	increasing	increasing	decreasing
Spectrum index [b]	harder	harder	harder	softer	softer
MC-J1729 vs MC-core [c]	increasing	increasing	-	decreasing	-

[a] The TeV flux from MC-J1729.
[b] The spectrum index of the TeV spectrum from MC-J1729.
[c] The flux ratio between from MC-J1729 and from MC-core $x_{\rm MC} = F_{\rm J1729}/F_{\rm core}$, a higher $x_{\rm MC}$ represents a better matching with the TeV image of HESS J1729-345.

Several of the free parameters of our model are obviously correlated. First, the difference between the CR density at MC-core and MC-J1729 can be increased by lowering the ICM diffusion coefficient at the relevant high energies. In turn, if we use a higher ICM diffusion coefficient than the galactic standard value ($\delta > 0.5$), we would have to put MC-core even further away from the SNR. Second, with a lower diffusion coefficient in MC clumps like MC-J1729, more CRs will be trapped there, while the CR density at MC-J1729 is not sensitive to the diffusion coefficient in the ICM. For our scenario, the lower diffusion coefficient inside the MC clumps (by choosing $\delta = 0.3$ as in "homogeneous diffusion" or "slow diffusion in MC") matches the measured TeV spectrum reasonably well; see Fig. 5.7. Nevertheless, the "fast diffusion in MC" setup could be modified to match the TeV data as well, either by increasing $\mathcal{E}_{\rm ej}$ or $\eta_{\rm esc}$ to generate more CRs from the SNR. And third, the CRs that have diffused to the MC clumps have a particle energy spectrum that peaks near the average $E_{\rm max}$. To move the peak (and thus also the corresponding TeV γ-ray peak) to lower energies, the acceleration efficiency can be lowered or the diffusion coefficient in the ICM can be increased. The distance between MC-J1729 and the SNR cannot be lowered below 30.7 pc, since this already corresponds to the minimum possible distance.

In summary, the model is in general sensitive to the choice of diffusion coefficients in the medium. However, the TeV brightness contrast between MC-J1729 and MC-core (in the foreground of the SNR) can be kept such that it does not violate the TeV data by adjusting several parameters that are not strongly constrained. Therefore, no conclusion on the actual diffusion coefficients in the different media can be drawn in the framework of the presented model.

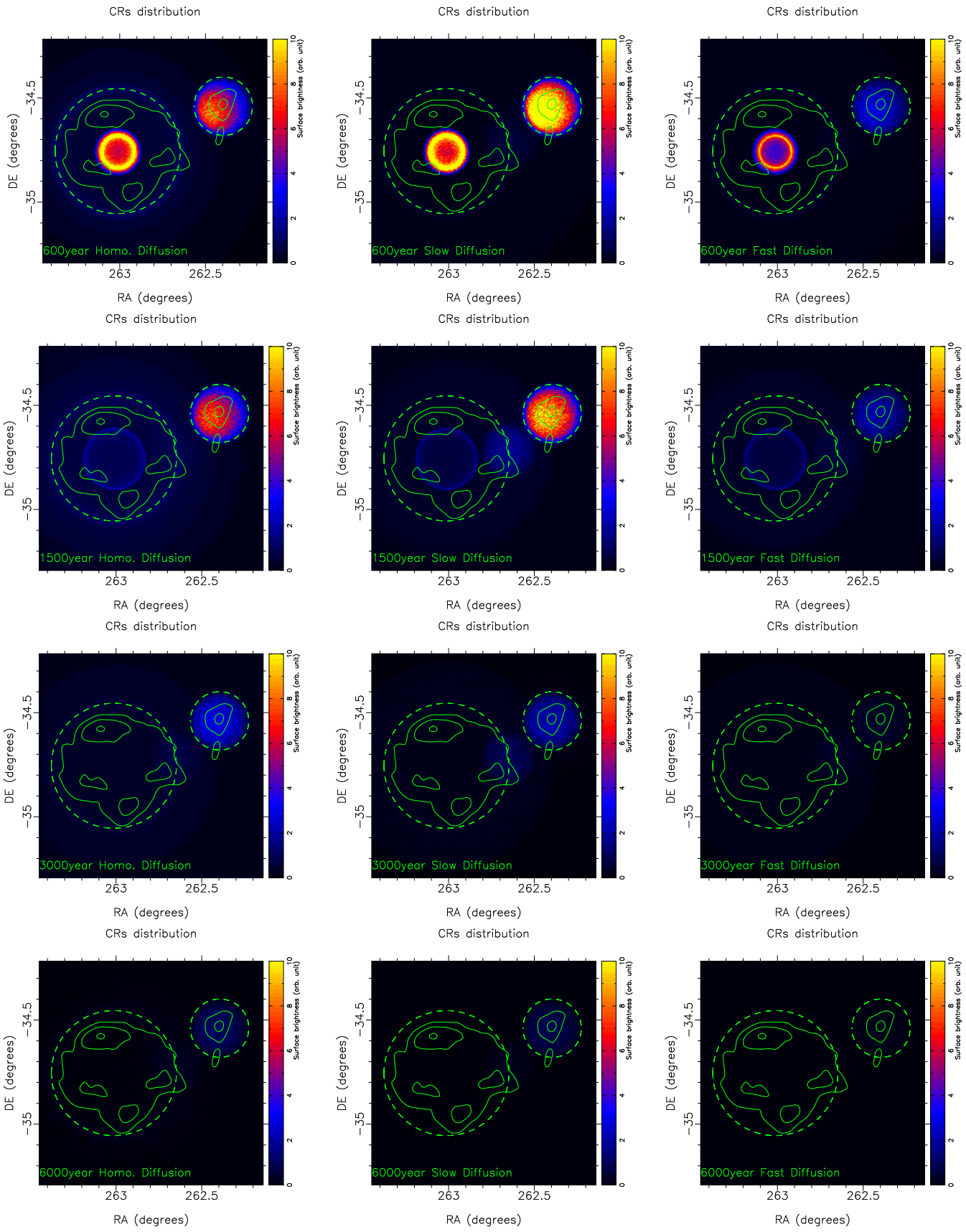

Figure 5.5: The 1 TeV images of different diffusion scenarios(from left to right) at different ages(from top to bottom) are shown. Green contour in solid lines is the observation TeV data from H.E.S.S. Collaboration et al. (2011), the big/small dashed circles represent the location of HESS J1731-345/HESS J1729-347. All figures share the same color bar.

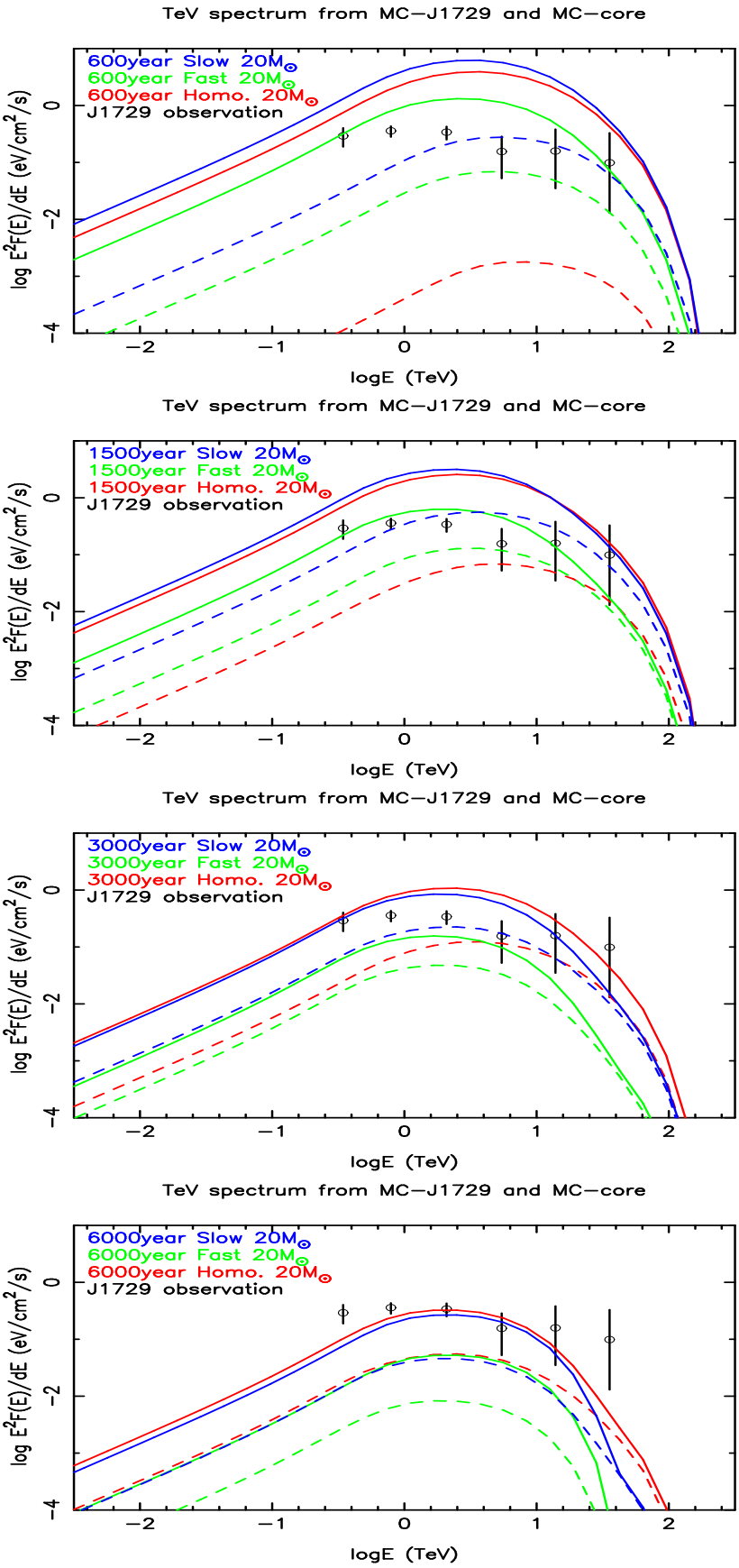

Figure 5.6: The reproduced TeV spectrum from MC-J1729(solid lines) and MC-core(dashed lines) of different diffusion scenarios at different ages(from top to bottom) are shown. Observation data of HESS J1729-345 shown in black circles are taken from H.E.S.S. Collaboration et al. (2011).

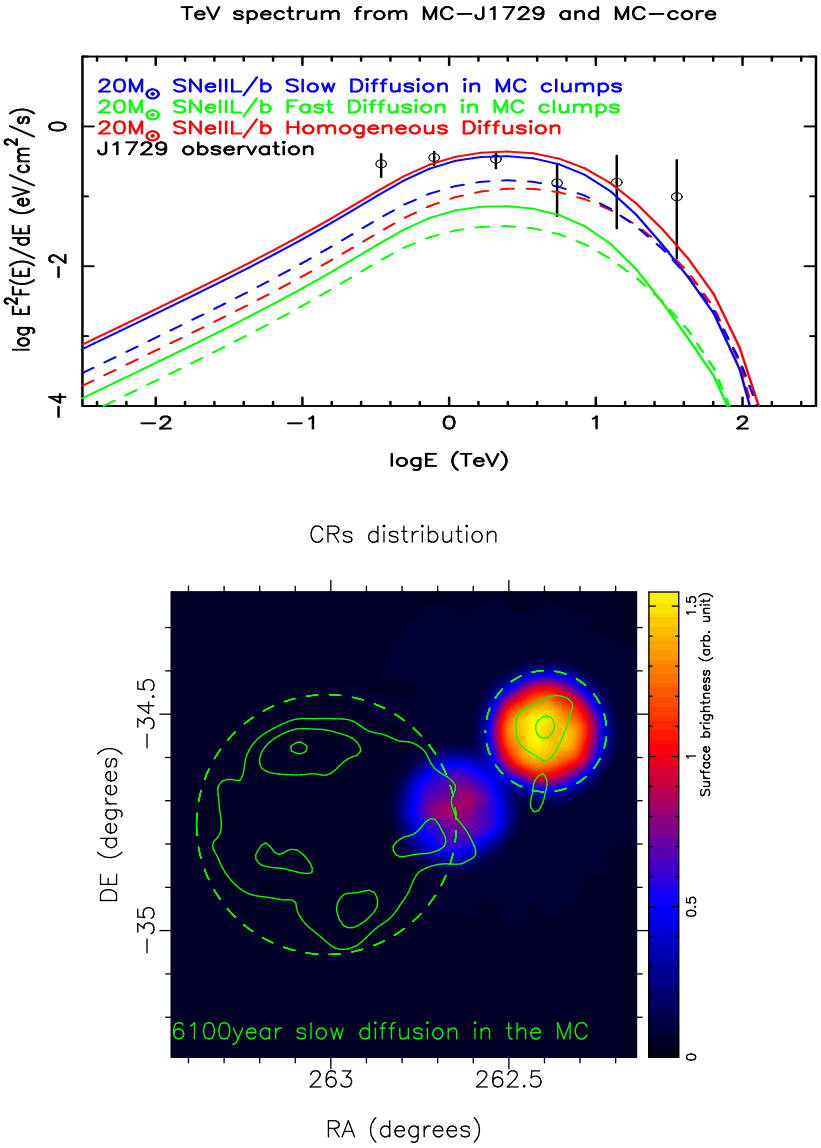

Figure 5.7: Diffusion results in 20 $M_\odot$ scenario with Monte Carlo diffusion method. *The top panel*: the TeV spectra of hadronic process by the CRs inside MC-J1729(solid lines) and MC-core(dashed lines) are shown. Red, green and blue lines represent different diffusion scenarios shown in Table 5.1. *The bottom panel*: The smoothed 1 TeV image are shown which correspond to the blue lines(slow diffusion in MC) in the left panel. Green contour in solid lines is the observation TeV data from H.E.S.S. Collaboration et al. (2011), the big/small dashed circles represent the location of HESS J1731-345/HESS J1729-347. Figures are from Cui et al. (2016).

5.1.2.3 Using the diffusion coefficient from a purely turbulent magnetic field $\sim 10\,\mu$G

In this subsection, adopting the diffusion coefficients derived from a purely turbulent magnetic field, we deliver the corresponding CR diffusion results with SNR scenario $20\,M_\odot$. As discussed in Sect.3.2, assuming a Kolmogorov's B-turbulence with magnetic field strength $|\vec{B}| = 10\,\mu$G and maximum wavelength $L_{\rm max} = 1\,pc$, the derived diffusion coefficients are much lower than the Galactic standard. These diffusion coefficients also face a difficulty of describing the statistical behavior of CRs in short diffusion time $t \lesssim 10^3 - 10^4$years. Hence, we choose scenario $20\,M_\odot$ as our SNR evolution model, because of its long SNR age (6100 years) at present time.

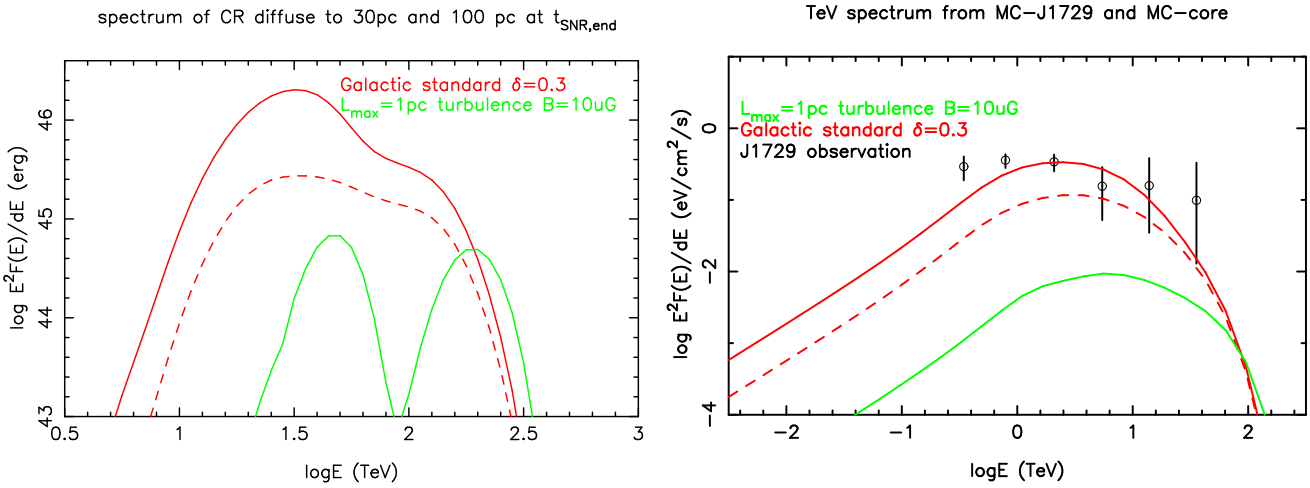

Figure 5.8: Here we present the CR density (left panel) and TeV spectrum (right panel) at the MC clumps based on the SNR scenario $20\,M_\odot$. Same setup used in Fig. 5.1 are used here. Diffusion coefficients following Galactic standard (red) and Fig. 3.9 (green) are adopted in the entire space.

As seen in Fig. 5.8, we present the reproduced CR density and TeV spectrum at the MC clumps while adopting the diffusion coefficients from Fig. 3.9 in the entire space. Additionally, the diffusion results using a Galactic diffusion coefficient are also shown in Fig. 5.8 for comparison. There are mainly two components in the CR spectrum at MC-J1729 (two green peaks in the left panel): a) the higher-energy component which is generated when SNR is still inside dense RSG wind bubble; b) the lower-energy component which is generated when SNR is inside MS wind bubble. In contrast to the Galactic diffusion coefficient, as seen in Fig. 3.9, the diffusion coefficients of Kolmogorov's B-turbulence are significantly low in the lower-energy band, while in the higher-energy band $E_{\rm CR} \gg 10$TeV the diffusion coefficients of Kolmogorov's B-turbulence starts to catch up with the Galactic one. This leads to that only those higher-energy CRs in a relative narrower band could travel to distant targets. Ultimately, the overall low diffusion coefficients of the Kolmogorov's B-turbulence fail to explain the TeV emission of HESS J1729-345. As discussed in Sect. 3.2.6, a more realistic diffusion model of the B-turbulence would consider the magnetic tubes, which can help the fast transporting of CRs into certain distant targets.

5.2 SNR evolving into the main-sequence bubble shell

5.2.1 The "in-shell" scenarios

In the $17\,M_\odot, 20\,M_\odot, 25\,M_\odot$ scenarios described in the previous section, the shock front is still located inside the MS progenitor wind bubble. With such a low density of target gas material for π^0-induced γ-ray production, the TeV emission from the SNR itself cannot be explained in a hadronic emission scenario. As shown in H.E.S.S. Collaboration et al. (2011), the target gas density has to be of order $1\,cm^{-3}$ to reach the observed γ-ray emissivity in a hadronic scenario with a still reasonable fraction of SN energy ($\sim 0.5 \times 10^{51}$erg) going into cosmic rays.

Table 5.3: SNR evolution when SNR evolving into the MS bubble shell.

Scenarios [a]	$R_{b,MS}$	$\mathcal{E}_{ej}$	M_{ej}	$R_{SNR,end}$	$t_{SNR,end}$	$v_{SNR,end}$	n_{end} [b]	η_{esc}	$E_{max,end}$	$\mathcal{E}_{CR,end}$	$\mathcal{E}_{CR,sh}$ [c]
$20\,M_\odot$ in-shell	20.5 pc	$2\,\mathcal{E}_{51}$	$2\,M_\odot$	15 pc	4.9 kyr	$1150\,km\,s^{-1}$	$0.58\,cm^{-3}$	0.02	15.6 TeV	$0.13\,\mathcal{E}_{51}$	$0.12\,\mathcal{E}_{51}$
$25\,M_\odot$ in-shell	21.5 pc	$2\,\mathcal{E}_{51}$	$2\,M_\odot$	15 pc	2.4 kyr	$1170\,km\,s^{-1}$	$0.35\,cm^{-3}$	0.02	6.6 TeV	$0.08\,\mathcal{E}_{51}$	$0.07\,\mathcal{E}_{51}$
$20\,M_\odot$ in-shell* [d]	20.5 pc	$2\,\mathcal{E}_{51}$	$2\,M_\odot$	15 pc	4.9 kyr	$1150\,km\,s^{-1}$	$0.58\,cm^{-3}$	0.05	29 TeV	$0.29\,\mathcal{E}_{51}$	$0.27\,\mathcal{E}_{51}$
$25\,M_\odot$ in-shell*	21.5 pc	$2\,\mathcal{E}_{51}$	$2\,M_\odot$	15 pc	2.4 kyr	$1170\,km\,s^{-1}$	$0.35\,cm^{-3}$	0.14	28 TeV	$0.54\,\mathcal{E}_{51}$	$0.46\,\mathcal{E}_{51}$

[a] For both first two scenarios, the same initial progenitor star (scenario $20\,M_\odot$, SNe IIL/b and scenario $25\,M_\odot$, SNe Ib/c) and the same RSG bubble structure as shown in Table 1 are assumed. They only differ in MS bubble shell structure and SN energy.
[b] The gas density in the upstream of the shock at $t_{SNR,end}$.
[c] The total CR energy trapped inside the downstream of the shock at $t_{SNR,end}$. Here we roughly assume that the total CR number $N \approx N_0 \cdot 4\pi R_{SNR}^2 \cdot 0.1 R_{SNR}$.
[d] The last two scenarios which shows "*" at the end are test scenarios with increased η_{esc}. They are used to fit the spectrum of the SNR itself, as seen in the bottom panel of Fig. 5.10.

It is however possible, also in a similar $\sim 20\,M_\odot$ ($\sim 25\,M_\odot$) progenitor star scenario like the one above, that the shock has just recently entered the dense shell swept up by the MS wind. This would permit to maintain a high shock velocity $v_{SNR} > 1000\,km\,s^{-1}$ and at the same the shock is right now embedded in high circumstellar medium density with $n \gg 0.1\,cm^{-3}$, providing thus dense target material for hadronic γ-rays. Under these well-adjusted conditions, the GeV-TeV spectrum may contain a sizeable fraction of π^0-induced γ-rays. To explore such a scenario, we introduced two further scenarios as shown in Table 5.3 and Fig. 5.9, a $20\,M_\odot$ in-shell and a $25\,M_\odot$ in-shell scenario. We use the same configuration for these two scenarios as used in the $20\,M_\odot$ and $25\,M_\odot$ scenarios above except adopting a different initial SN energy and a different MS bubble size with an exponential gas density profile at the shell. This density profile has been used by Berezhko Völk (2006); Berezhko et al. (2009) for the case of RX J1713.7-3946 and Vela Jr., with $n(r) = n_b + (r/R_b)^{3(\sigma_{sh}-1)} n_{sh}$, where $n_{sh} = \sigma_{sh} n_{ICM}$ is the maximum density of the shell at the outer boundary of the shell. In our work, we set $\sigma_{sh} = 5$.

As shown in Fig. 5.10, we try to fit the spectrum of both HESS J1731-347 and HESS J1729-345 assuming as in Sect. 5.1 that MC-J1729 is located 30 pc away from the CCO. The total

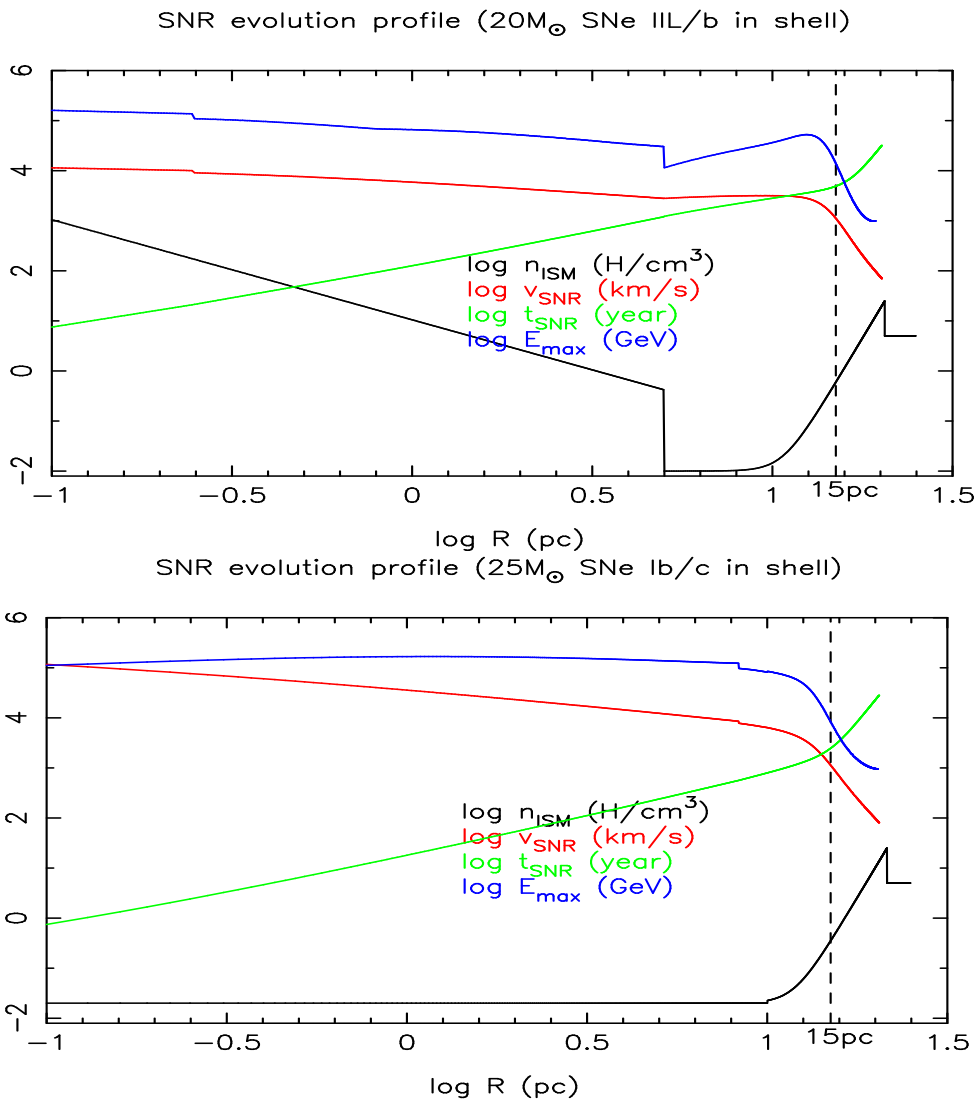

Figure 5.9: The SNR evolution profile of two different scenarios : $20\,M_\odot$ SNe IIL/b in-shell and $25\,M_\odot$ SNe Ib/c in-shell. Same figure setup from Fig. 4.4 is used here.

SN energy for both scenarios are set higher than in Sect. 5.1 (to 2×10^{51}erg) in order to obtain a higher shock velocity when the SNR shock hits the MS bubble shell. As shown in Table 5.3, in scenario $20\,M_\odot$ in-shell ($25\,M_\odot$ in-shell), the MS bubble size is set just such that the SNR keeps a fast enough shock velocity of 1150 (1170) km/s at present time.

Compared to the $25\,M_\odot$ in-shell scenario, the $20\,M_\odot$ in-shell scenario have more mass swept up at an early phase of the SNR evolution because of the dense RSG wind bubble. This is equivalent to the SNR having a much higher ejecta mass. Consequently, the shock can enter deeper into the MS bubble shell with high velocity, with a density at the present shock position of $n_{\rm end} = 0.58\,{\rm cm}^{-3}$, compared to only $n_{\rm end} = 0.35\,{\rm cm}^{-3}$ for the $25\,M_\odot$ in-shell scenario. Most of the CRs inside the SNR are confined at the acceleration region downstream of the shock. Zirakashvili & Ptuskin (2008) provide the CR density $N_0(E)$ at the shock front as discussed in Sect. 3.1. Here, we roughly assume $0.1R_{\rm SNR}$ (Zirakashvili & Ptuskin, 2012) as the size of the acceleration region downstream of the shock. The CRs (with density N_0) are assumed

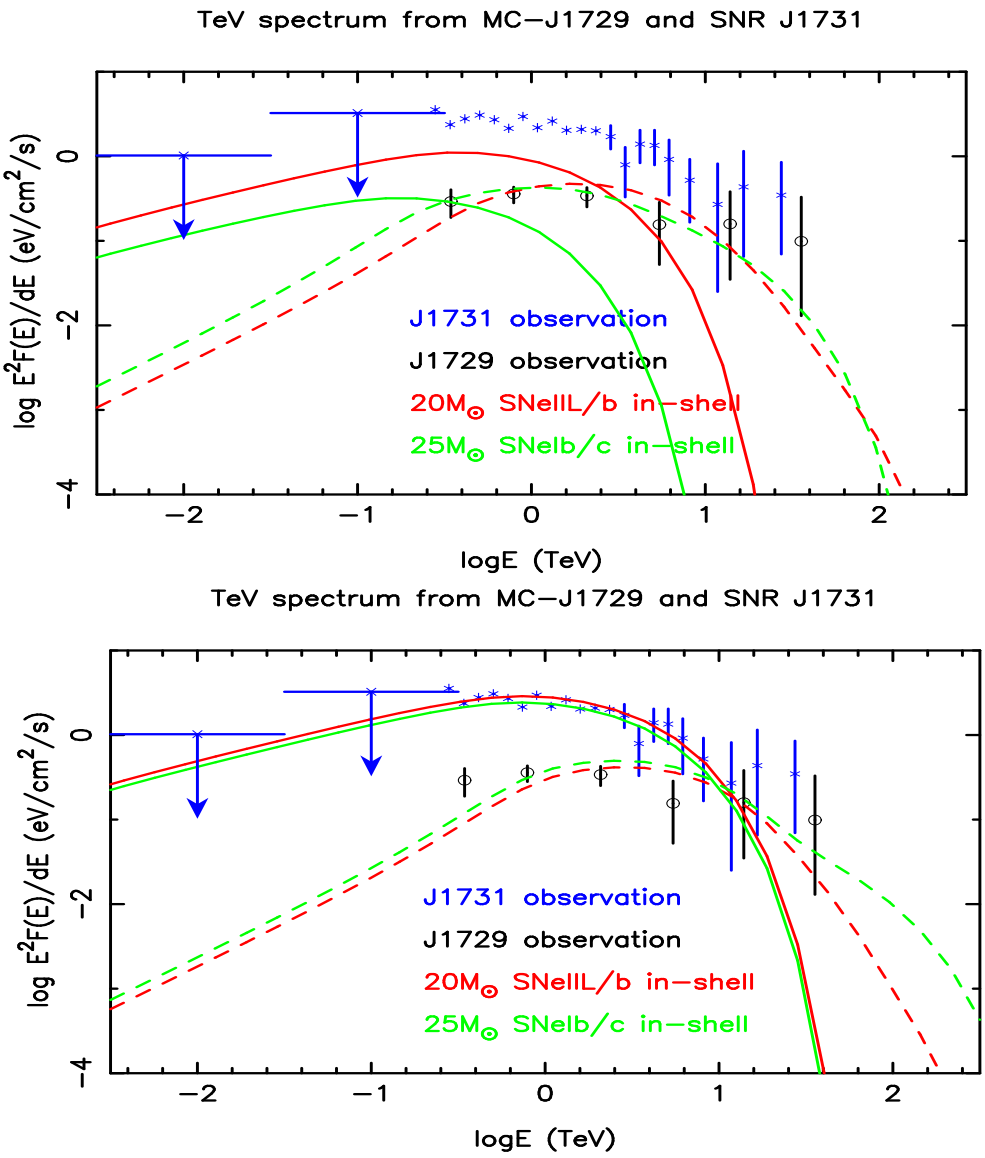

Figure 5.10: *The top panel*: The TeV spectra through hadronic process by CRs trapped inside the downstream of SNR HESS J1731-347(solid lines) and MC-J1729(dashed lines) are shown. Red/green lines represent $20\,M_\odot$ in-shell/$25\,M_\odot$ in-shell scenarios shown in Table 5.3. Assuming Galactic standard diffusion coefficient $D_{10} = 10^{28}\,\mathrm{cm^2 s^{-1}}$, $\delta = 0.5$ in the entire space, we fitted the spectrum of MC-J1729 (at 30 pc). Observation data from H.E.S.S. Collaboration et al. (2011); Acero et al. (2015) for HESS J1731-347 and HESS J1729-345 are shown as blue stars and black circles. *The bottom panel*: With the same setup used in top panel, the fitting results from testing scenarios $20\,M_\odot$ in-shell*/$25\,M_\odot$ in-shell* are shown. The diffusion coefficient in the MCs is set as $D_{10} = 10^{28}\,\mathrm{cm^2 s^{-1}}$, $\delta = 0.6(0.65)$ in the entire space for scenario $20(25)\,M_\odot$ in-shell* respectively. Figures are from Cui et al. (2016).

to be evenly distributed in this region. The total CR energy trapped in this downstream acceleration region can be calculated with $\mathcal{E}_{\mathrm{CR,sh}} = \int dE \cdot E \cdot N_0(E) \cdot 4\pi R_{\mathrm{SNR}}^2 \cdot 0.1 R_{\mathrm{SNR}}$. The total swept-up gas at present time can be assumed to be confined inside this region as well,

with $\sim 60\,M_\odot$ / $30\,M_\odot$ for scenario $20\,M_\odot$ in-shell / $25\,M_\odot$ in-shell. Upstream of the shock, the CRs are mainly confined inside the acceleration region with size $\sim 0.05\,R_{\rm SNR}$, where the magnetic turbulence is amplified by the CRs. This region has a much lower CR pressure ($\sim$10 times lower) than the downstream region (Zirakashvili & Ptuskin, 2012). For the γ-ray spectrum, we therefore did not include the upstream contribution from hadronic interactions, although the total target gas mass here is higher ($\sim$2 times higher in our scenarios) than in the downstream area.

Table 5.3 lists the parameters for our optimised model scenarios. In order to be compliant with the Fermi-LAT upper-limit of the SNR (Acero et al., 2015), we introduce a very hard CR spectrum at the shock, $N_0 \propto E^{-1.5}$. In Fig. 5.10, the resulting γ-ray spectra are compared to the observational data from HESS J1731&J1729. The spectrum of HESS J1729-345 is fitted well in both scenarios with a diffusion coefficient $D_{10} = 10^{28}\,{\rm cm^2 s^{-1}}$, $\delta = 0.5$ set in the entire space. But the $20\,M_\odot$ in-shell/$25\,M_\odot$ in-shell scenarios would need about 3/8 times higher CRs density or swept-up mass in order to fit the spectrum of the SNR itself, respectively. For these scenarios, the swept-up gas mass is constrained by the requirement of maintaining a high shock velocity, and the downstream CR density is constrained mainly by the total CR energy content generated by the SNR, $\mathcal{E}_{\rm CR,end} + \mathcal{E}_{\rm CR,sh} \lesssim 0.1\,\mathcal{E}_{\rm ej}$. Only when substantially violating these limits and in addition increasing the diffusion coefficient above Galactic standard, an acceptable fit to the data both for HESS J1731-347 and for MC-J1729 could be achieved as shown as two test scenarios, $20\,M_\odot$ in-shell* and $25\,M_\odot$ in-shell* in Table 5.3 and Fig. 5.10. In conclusion, mostly due to the limitation of total CR energy, both our shock-"in shell" scenarios fail to dominate the TeV emission from the SNR. However, there are some alternatives which are discussed in the following subsection.

5.2.2 More discussions about the hadronic TeV emission in the SNR

To summarize the presented shock-"in shell" scenarios, with the approximate estimates of the CR population and gas densities downstream and upstream of the shock, the corresponding hadronic γ-ray emission is well below the measured TeV emission from HESS J1731-347. This is in agreement with the conclusions by Acero et al. (2015) concerning the dominant leptonic nature of the γ-ray emission from ths SNR. There are however additional processes which still may contribute significantly to the γ-ray emission in direction of HESS J1731-347:

- Some of the observed TeV emission inside SNR region can be caused by hadronic γ-ray emission in molecular clouds located far from the SNR but still along the line of sight of the SNR. The corresponding spectral component would resemble the one expected from MC-J1729 (cf. Fig.5.7), with a peak at high energies. Since the measured TeV morphology of HESS J1731-347 is shell-like, a dominant contribution of this effect is not very likely.

- Molecular cloud clumps may have survived the MS wind. Being embedded inside the MS bubble, the forward shock of SNR could have passed around them. Such molecular cloud clumps can easily provide $10^{2\sim4}\,M_\odot$ target material for hadronic CR-induced γ-ray emission inside the SNR. Observational evidence may come from the detection of molecular clumps with strong velocity dispersion within the SNR with more detailed

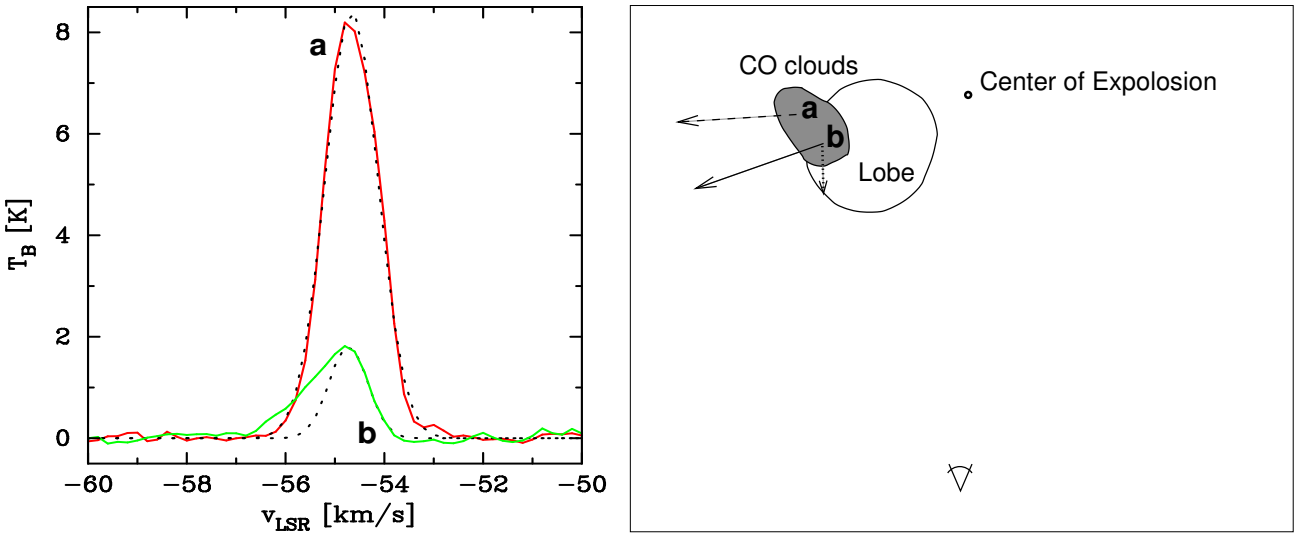

Figure 5.11: *The left panel*: Velocity profiles of the eastern CO cloud (which is believed to be encountering with SNR CTB 109) at the position of IRAS 23004+5841 (a) and in the Lobe (b). The Lobe represents an X-ray bright interior feature found near the SNR and is suggested to be the result of an interaction of the SNR shock wave with a molecular cloud complex. Solid lines show the data, dotted lines the Gaussian fits. *The right panel*: Schematic view of SNR CTB 109 showing the Lobe and the eastern cloud. The solid arrow shows the directions to which the part of the cloud at position b has been accelerated. The velocity component directed towards us is shown with a dotted line. As it is not certain how the cloud component at position a is moving in reality, the possible movement of position a is shown with a dashed arrow. Figures are from Sasaki et al. (2006).

^{12}CO or CS data, cf. e.g. to the SNR CTB 109 (Sasaki et al., 2006). In Fig. 5.11, the velocity dispersion and a schematic view of MC clump a and b are shown, where MC clump a and b represent two CO clouds discovered near the SNR CTB 109. This hypothesis is also consistent with the partial interaction theory discussed in Sect. 1.5.

As seen in Fig. 5.12, Fukuda et al. (2014) suggested that HESS J1731&J1729 could be associated with gas located in the 3 kpc arm of our Galaxy, using ^{12}CO data from NANTEN and HI data at $-90\,\mathrm{km\,s^{-1}}$ to $-75\,\mathrm{km\,s^{-1}}$. In this scenario, the SNR would have a distance to Earth of ~ 5.2 kpc and a radius of ~ 25 pc. A hadronic origin of the TeV γ-ray emission was argued to be likely under these circumstances. Here, we note that such a setting could also be accommodated for in our model scenarios, if we artificially increase the MS bubble to a size $R_\mathrm{b} > 25$ pc. Then, a SNR with $20\,\mathrm{M}_\odot$ progegenitor mass and a SN kinetic energy of 2×10^{51} erg can maintain a shock velocity $\sim 2000\,\mathrm{km\,s^{-1}}$ after ~ 8000 years when the SNR shock expands to 25 pc.

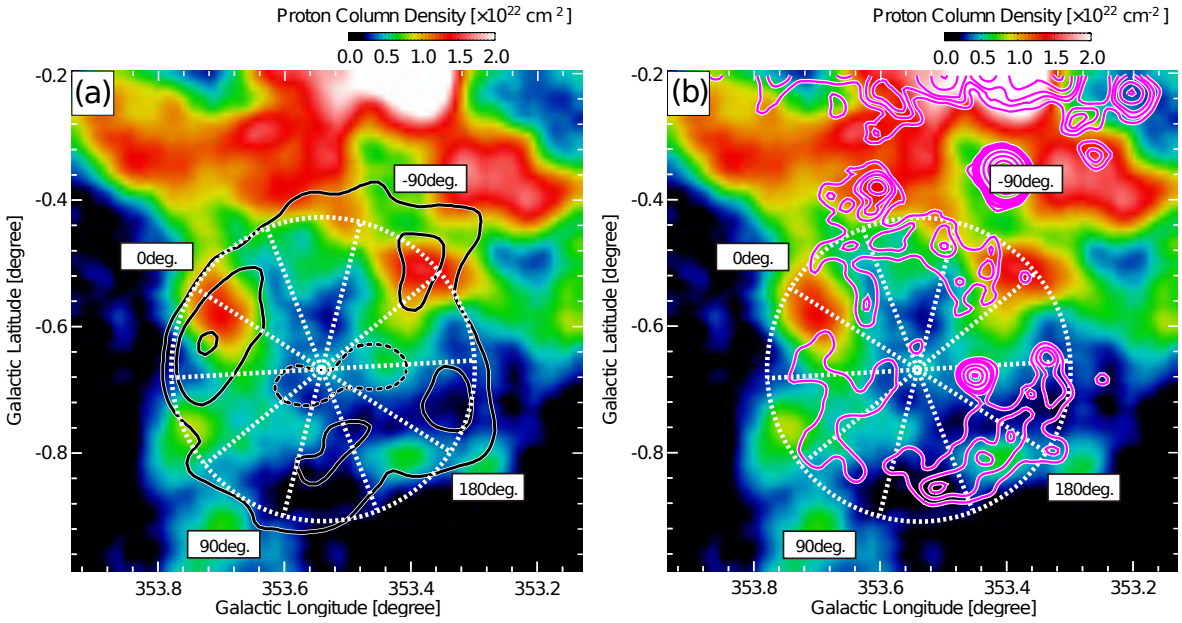

Figure 5.12: Distributions of column density of the total ISM protons $N_{\rm p}({\rm H_2{+}HI})$ in a velocity range from $-90\,{\rm km\,s^{-1}}$ to $-75\,{\rm km\,s^{-1}}$. Contours are (left) the TeV γ-rays and (right) 1.4 GHz continuum distribution, respectively. The dashed white circle shows the position angle in azimuthal distribution and 0° corresponds to North and 90° to East in the equatorial coordinate. Figures are from Fukuda et al. (2014).

6

The stars near/behind SNR HESS J1731-347

6.1 The motivations behind star searching

As discussed in Chapt. 2, the discovery of the CCO in SNR HESS J1731-347 indicates a massive progenitor star. Massive stars (OB stars) are normally born in clusters or associations at roughly the same time (e.g. Kroupa & Weidner, 2003; Portegies Zwart et al., 2010). Unlike the SNR, a star with detailed spectral information could provide us direct evidences for its mass, age, and distance. Thus, if any stars are found to be associated with SNR HESS J1731-347, they could provide constraints at least on the lifespan of the progenitor of the SNR. From the lifespan of the progenitor, the mass and pre-SN environments of the progenitor can then be derived via theoretical star evolution model. However, it is very difficult to link the new found OB star clusters (if we could find) to SNR HESS J1731-347, since SNR HESS J1731-347 lies in the Galactic plane. In this chapter, we adopt 3.2 kpc as the distance of the SNR, and any stars with distances to Earth from 3 kpc to 3.4 kpc would become our potential candidates.

Another more feasible motivation behind star searching is using the stars as the infrared background sources. Low-energy cosmic rays are a fundamental source of ionization of molecular clouds (the cross section of CR colliding with atoms/moleculars in MCs is peaked at $E_{\rm CR} \sim 70\,{\rm keV}$), influencing their chemical, thermal and dynamical evolution. If the SNR have already encountered with some MCs, then some of the very low energy CRs trapped by the shock could be released into these MCs and ionize the atoms/moleculars there. One of the most direct observational features of the ionization inside the MCs is the H_3^+ absorption lines (from 3.5 to 4.0 μm), which requires a background source (stars, AGNs) with known spectrum at infrared band (Goto et al., 2002; Padovani et al., 2009; Indriolo et al., 2010). Considering that AGNs are normally extremely faint along the Galaxy plane, we focus on searching bright stars that are behind the SNR.

To identify whether the stars are near or behind the SNR, we need to first constrain the location of the SNR and the interstellar medium structures along the line of sight to the SNR. As discussed in Chapt. 2, according to the CfA mm telescope survey data, there are mainly two giant MCs along the line of sight of SNR J1731-347:

- MCs (MC-3kpc) inside the Scutum-Crux arm is located at a distance of $\sim 3.2\,{\rm kpc}$ from Earth, see Fig. 6.1 and the left bottom panel of Fig. 2.9.
- MCs (MC-5kpc) near the Norma-Cyg arm is located at a distance of $\sim 5-6\,{\rm kpc}$ from Earth, see Fig. 6.1 and the left top panel of Fig. 2.9.

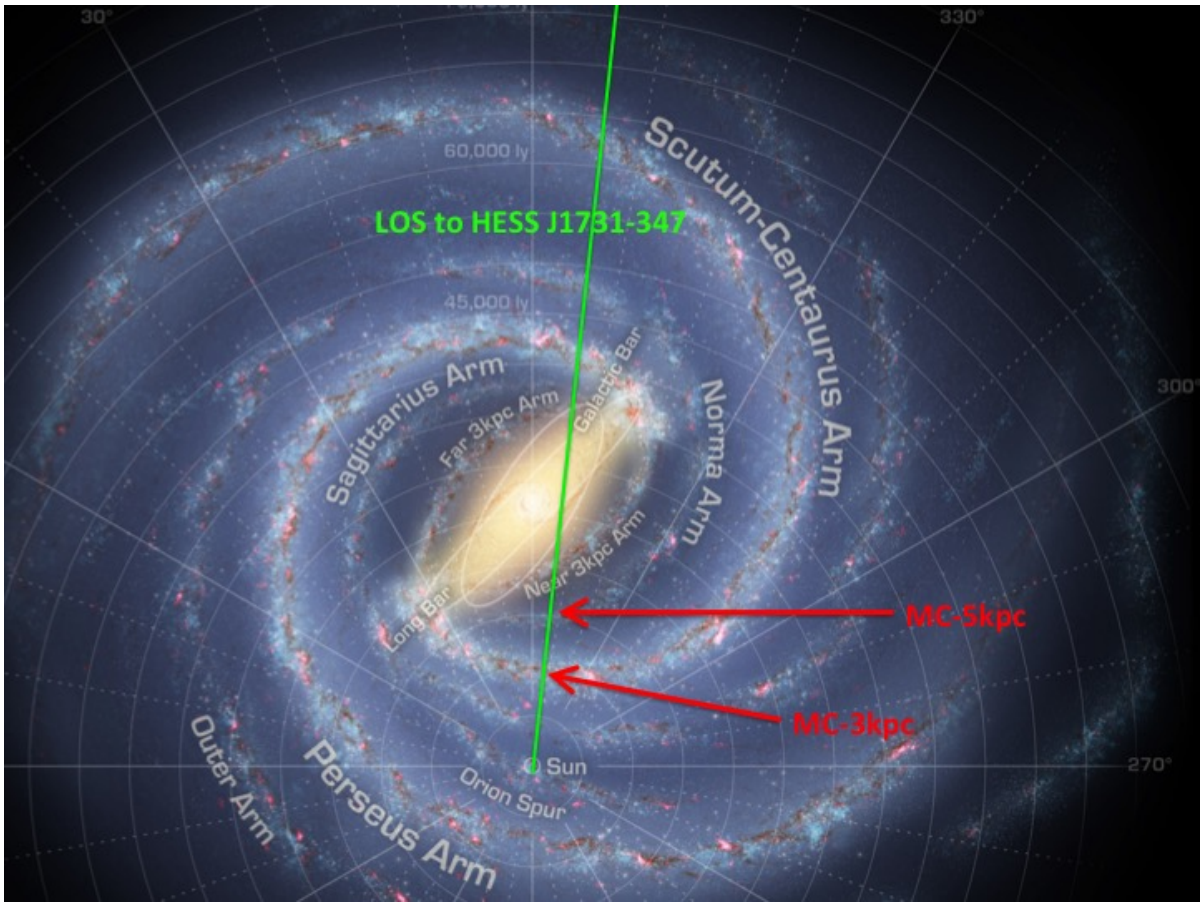

Figure 6.1: The locations of the MC-3kpc and the MC-5kpc are pointed out on the Galactic plane by red arrows. Sun and Galactic arms are shown as well. The line of sight (LOS) toward SNR HESS J1731-347 is marked in green line. The background Galactic plane is from Robert Hurt's Artist's Conception of the Milky Way, the original image can be found at "A Roadmap to the Milky Way".

Through matching the X-ray absorption map with the ^{12}CO map, the SNR is believed located between these two MCs. Actually, we expect that the SNR is right behind MC-3kpc, since our main goal in this chapter is finding proofs for a plausible scenario that the SNR is encountering with MC-3kpc and the released low energy CRs are ionizing it. Although most of the observed stars along the line of sight toward the SNR would be actually located in front of MC-3kpc due to their much less extinction, the stars we are looking for are either between MC-3kpc and MC-5kpc, or between MC-5kpc and the Sagittarius arm (~ 12 pc). In the following sections, because of some uncertainties of the locations of MC-3kpc and MC-5kpc, our expectations of the location of stars between MC-3kpc and MC-5kpc (behind MC-5kpc) are roughly set as $\sim$3 kpc to $\sim$6 kpc ($\sim$5 kpc to $\sim$10 kpc). For simplicity, we ignore the possible scenario that some stars may be just inside MC-3kpc or MC-5kpc.

Given the distance of a star (behind MC-3kpc or MC-5kpc), we could derive its extinction according to the CO and HI data. For stars behind MC-5kpc, we ignore the column density of gas beyond the MC-5kpc, which is very low in the SNR region. Through fitting the extinction reduced spectrum, we could find the best fitting parameters of each star including its distance, its mass, and its age. Detailed optical data (e.g. spectrum in V band) of the

stars in the region of HESS J1731&J1729 are very rare, may due to the heavy extinction. Before planing further deep observations on this region, in the next sections, we first screen our star candidates within the public catalogs, where the magnitudes in certain wavebands are provided.

6.2 Searching stars within WISE Catalog and SIMBAD Catalog

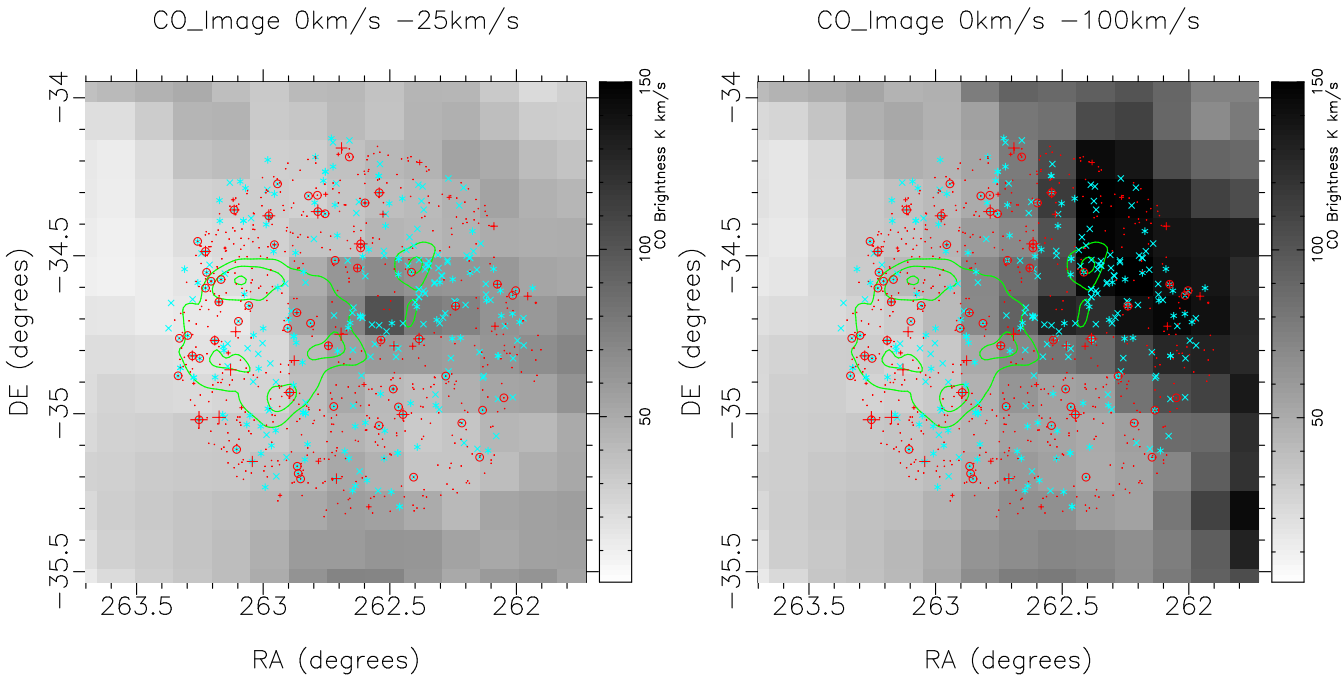

Figure 6.2: ^{12}CO images integrated from 0 km/s to -25 km/s (left) and 0 km/s to -100 km/s (right) using data from CfA survey are shown. TeV morphology from H.E.S.S. Collaboration et al. (2011) are shown in green contour. The small red crosses indicate the infrared sources obtained from WISE, their sizes represent the observational luminosity in w1 band. The light blue "*"("x") shape symbols represent the stars(star candidates) found in SIMBAD catalog. When any source (including sources other than the stars and star candidates) in SIMBAD catalog can find a good spatial match in WISE catalog (distance smaller than 2 arcseconds), we draw a small red circle on it.

In this section, we search stars in the public catalogs of Wide-field Infrared Survey Explorer (WISE) and SIMBAD. The WISE has four detectors – w1(3.368 μm), w2(4.618 μm), w3(12.082 μm) and w4(22.194 μm), clearly w1 is the key band for detecting the absorption features of H_3^+. We obtain the WISE data from the NASA/IPAC infrared science archive which also contain data in J, H, K bands. SIMBAD is a database of sources beyond our solar system, it provides data of bands from infrared to UV. Considering that the H_3^+ absorption feature from MC-3kpc is our main interests, as seen in Fig. 6.2, we select our potential star sources within a circle region which is centered at the MC-core (RA 17h30m36s, Dec -34°32'22") with a radius of 0.6°.

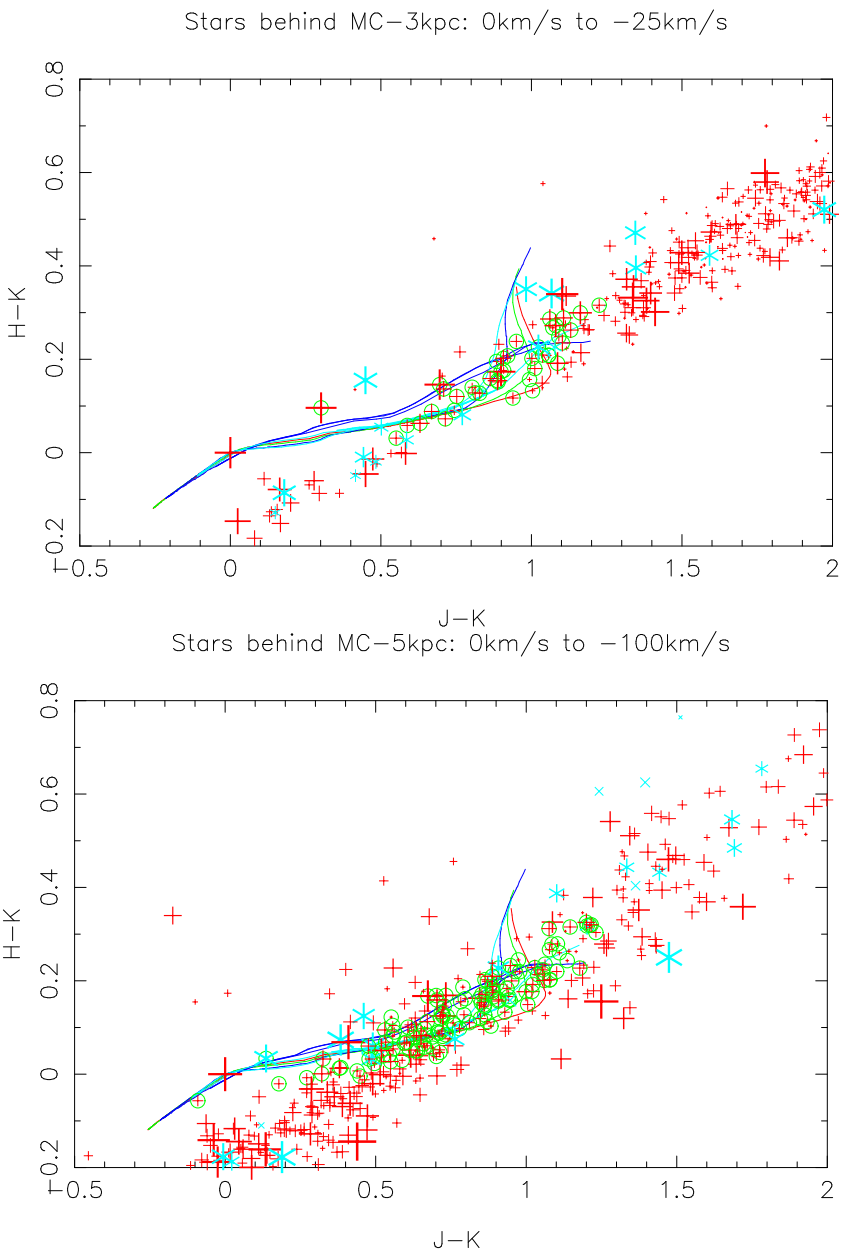

Figure 6.3: Infrared color diagrams of selected sources satisfying the first two selection criteria. Sources between MC-3kpc and MC-5kpc (behind MC-5kpc) are shown in the top (bottom) panel. Light blue "*" and "x" symbols are the stars and candidate stars from SIMBAD catalog, red crosses are WISE sources with no match to the SIMBAD catalog. All of these symbols have their sizes representing the observation luminosity in w1 band. The sources satisfying the third selection criteria ($\chi^2 < 0.001\,\mathrm{mag}^2$) are marked with green circles. The lines with color red, green, blue, light blue, purple represent the theoretical star evolution profiles at $10^5, 10^6, 4\times10^6, 10^7, 10^8$ year, respectively. From left bottom to right top, these theoretical lines follow the star masses from $0.1\,\mathrm{M}_\odot$ to about $100\,\mathrm{M}_\odot$.

Assuming that all the stars are behind either MC-3kpc or MC-5kpc, we can calculate the corresponding extinctions of each star based on the gas column density at the location of the star. Stars between MC-3kpc and MC-5kpc are blocked only by MC-3kpc (0km/s to

-25km/s, as seen in the left panel of Fig. 6.2), while stars behind MC-5kpc are blocked by both MC-3kpc and MC-5kpc (0km/s to -100km/s; as seen in the right panel of Fig. 6.2). The extinctions rely on the dust density which correlate well with the cold gas density. In reality, the extinctions in our Galaxy varies with different gas components (e.g. MCs, HI region) and different viewing angle towards the Galaxy. However, in our study we adopt the averaged Galactic extinction coefficient of each waveband (U, B, V, R, I, J, H, K band) and $R_V = A_V/(A_B - A_V) = 3.1$ from Cardelli et al. (1989); O'Donnell (1994), where A_V and A_B are the extinctions in V and B band. Through utilizing the X-ray absorption and optical extinction studies on 22 supernova remnants, a linear relationship between the hydrogen column density (N_H) and optical extinction (A_V) in our Galaxy are found by Güver & Özel (2009):

$$N_H = (2.21 \pm 0.09) \times 10^{21} \frac{A_V}{1\,\mathrm{mag}}\ \mathrm{cm}^{-2}. \tag{6.1}$$

Using this linear relation, we can calculate the extinctions with only the total hydrogen column density (H_2 and HI), regardless of the complex dust-to-gas ratio in different regions. The total hydrogen column density can be obtained via the CO-to-H_2 mass conversion factor $1.8 \times 10^{20}\,\mathrm{cm}^{-2}\mathrm{K}^{-1}\mathrm{km}^{-1}\mathrm{s}$ (Dame et al., 2001) and the conversion factor of HI brightness temperature to column density $1.82 \times 10^{18}\,\mathrm{cm}^{-2}\mathrm{K}^{-1}\mathrm{km}^{-1}\mathrm{s}$ (Dickey & Lockman, 1990). Knowing the location of each source on the sky map, we derive its corresponding hydrogen (H_2 molecular) column density with the CO data. However, considering that the HI region (neutral H atoms) is far less clumpy than the MCs, we adopt the HI cumulative density from Fig. 2.9 for all sources regardless of their locations on the sky map. Ultimately, we simply choose $0.5 \times 10^{22}\mathrm{cm}^{-2}$ ($1 \times 10^{22}\mathrm{cm}^{-2}$) as the HI column density for stars behind MC-3kpc (MC-5kpc), due to that most of the HI gas is concentrated on the Galactic spiral arms.

Once the extinction and the corresponding distances for each source are established, we can derive its absolute magnitude in every waveband which is then used to match with the database of theoretical star evolution. The theoretical database at certain star ages (1×10^5, 2×10^5, 4×10^5, 8×10^5, 1×10^6, 2×10^6, 4×10^6, 8×10^6, 1×10^7, 2×10^7, 4×10^7, 8×10^7, 1×10^8 years) are downloaded from the CMD 2.8 website, and following the studies by Bressan et al. (2012); Chen et al. (2014, 2015); Tang et al. (2014). As shown in Fig. 6.2 and Fig.6.3, we try to find the possible stars behind either MC-3kpc or MC-5kpc by following three selection criteria:

1. Sources from SIMBAD catalog which can not find any matches (within 2 arc second) in WISE catalog are excluded, as seen in Fig 6.3. The well matched sources are shown as red circles in Fig 6.2.

2. Every source shown in Fig.6.2 has observational data in J, H, K, w1, w2, w3, w4 band, some sources from SIMBAD catalog (the light blue"*" or"x") also have optical data. The w1 band is the key band to detect the H_3^+ absorption features, thus any sources with $w1 > 8\,\mathrm{mag}$[1] are excluded, as seen in Fig. 6.2.

3. Given the extinction and distance (distance is also a free parameter with certain confines discussed above), the extinction reduced data of each source can be compared to the theoretical star evolution table. The best fitting of the observational data in

[1]This criteria is suggested by Miwa Goto through private conversation.

U, B, V, R, I, J, H, K bands of each source is obtained through finding the minimum $\chi^2 = (\sum_1^n \Delta L^2)/n$, where ΔL is the magnitude difference between the observational data and the theoretical data in each band. Sources with minimum $\chi^2 > 0.001\,\mathrm{mag}^2$ are excluded, as seen in Fig. 6.4.

For better comparison, as seen in Fig 6.3, both the theoretical star evolution profiles and the sources that satisfying the first two selection criteria (data after the extinction and distance reduction) are shown in the infrared color diagrams. The sources that agree with all three selection criteria are marked in green circles in Fig 6.3.

6.3 Results and discussions

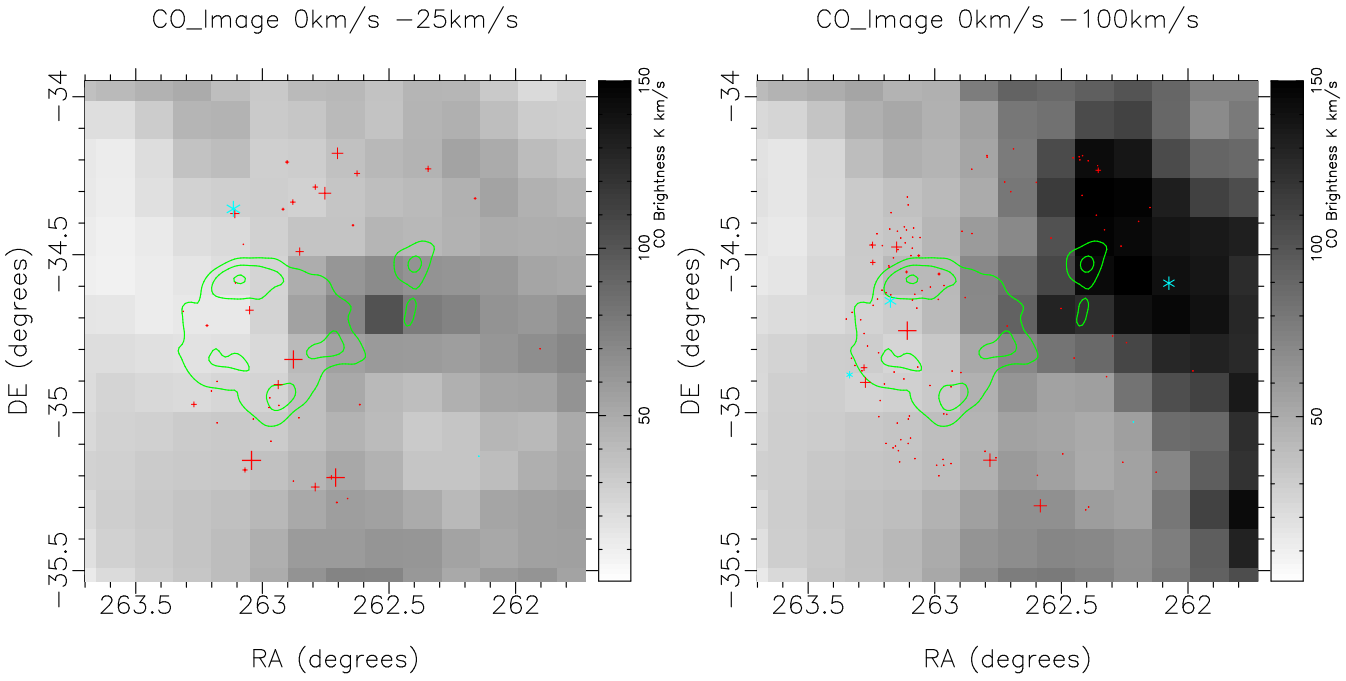

Figure 6.4: ^{12}CO images integrated from 0 km/s to -25 km/s (left) and 0 km/s to -100 km/s (right) using data from CfA survey are shown. TeV morphology from H.E.S.S. Collaboration et al. (2011) are shown in green contour. The sources behind MC-3kpc (MC-5kpc) satisfying all three selection criteria are shown in the left (right) panel. All sources are represented (e.g. red cross, light blue "*") in the same way mentioned in Fig. 6.3.

Following the three selection criteria mentioned above, we find 41 (125) potential infrared sources between MC-3kpc and MC-5kpc (behind MC-5kpc), as seen in Fig. 6.4 and Table 6.1. In the first group (41 sources), only two sources have shown counterparts in SIMBAD (2MASS J17283488-3508161 as an asymptotic giant branch star candidate; 2MASS J17322747-3421182 as a star). In the second group (125 sources), four sources with counterparts in SIMBAD are found (IRAS 17300-3450, IRAS 17249-3433, and 2MASS J17324197-3438459 as stars; 2MASS J17285172-3501465 as an Asymptotic Giant Branch Star candidate). An ideal observational

data of our selected sources should contain the optical data, owing to that a detailed optical spectrum is often the smoking gun to determine the properties of a star. Unfortunately, none of these (41+125) sources has optical data. Furthermore, for most of the sources satisfying the first two selection criteria, the observational data used for the spectrum fitting only contain data in J, H, K bands. The error-bars of the observational data in J, H, K bands (around $\pm 0.02 \sim \pm 0.05$ mag) are not shown in Table 6.1. Additionally, our ideal sources should be located close to both the SNR and the MC-3kpc, i.e. where the MC-core is. Obviously, as seen in Fig. 6.4, due to the heavy extinction, very few selected sources are found there. We look forward to improvements of our star searching study in the future, which include the access to better CO data (e.g. the NANTEN data), and proposals for deep optical observations of some selected sources in the first group.

Table 6.1: Results of star searching

[a] Classes of sources. This depends on whether the sources are between MC-3kpc and MC-5kpc (class A) or behind MC-5kpc (class B). This also depends on whether the sources have counterparts in SIMBAD (all marked in blue color; class 1 for identified stars; class 2 for star candidates) or not (class 0) .

[b] RA and Dec represents the equatorial coordinates of the sources found in WISE catalog.

[c] The ages of the stars that best fit the theoretical model.

[d] The masses of the stars that best fit the theoretical model.

[e] The distances of the stars that best fit the theoretical model.

[f] The observational luminosities of sources in J, H, K, w1, w2 bands, non of the sources in this table have data in U, V, B, R, I bands.

S[a]	RA[b]	Dec[b]	t (Myr)[c]	M ($M_\odot$)[d]	d (kpc)[e]	J (mag)[f]	H (mag)	K (mag)	w1 (mag)	w2 (mag)
A0	263.270386	-34.973900	200	4.0	4.0	8.584000	7.052000	6.390000	5.886000	6.068000
A0	263.178375	-35.032257	80	5.8	3.2	9.228000	7.529000	6.759000	6.439000	6.372000
A0	263.201141	-34.931389	800	2.5	4.2	10.938000	8.890000	7.910000	7.454000	7.169000
A0	262.973572	-34.983627	40	7.8	4.8	10.812000	8.599000	7.427000	6.812000	6.659000
A0	262.934937	-34.977062	40	7.7	6.0	11.546000	9.358000	8.198000	7.594000	7.081000
A0	262.970520	-34.953156	100	5.3	5.5	11.397000	9.186000	7.983000	6.786000	6.155000
A0	262.937317	-34.911087	200	4.0	3.0	9.768000	7.373000	6.217000	5.456000	5.148000
A0	262.877350	-34.831749	10	19.0	3.8	7.951000	6.300000	5.274000	4.289000	3.360000
A0	263.178406	-34.901081	800	2.5	4.2	10.908000	8.905000	7.866000	7.364000	6.786000
A0	263.311951	-34.679474	80	5.8	5.2	9.686000	8.230000	7.588000	7.092000	7.160000
A0	263.218567	-34.724297	40	7.9	3.6	8.269000	7.025000	6.528000	6.238000	6.412000
A0	263.035767	-35.020332	400	3.2	6.0	11.676000	9.629000	8.694000	7.645000	7.481000
A2	262.145386	-35.137814	800	2.5	5.8	11.600000	9.555000	8.577000	7.459000	6.634000
A0	262.705963	-35.284245	20	11.2	6.0	8.986000	7.491000	6.853000	6.372000	6.525000
A0	263.042847	-35.151234	10	18.3	5.0	7.140000	5.457000	4.582000	4.176000	3.978000
A0	262.615387	-34.974434	20	11.2	3.6	10.197000	7.974000	6.830000	6.393000	6.163000
A0	262.727264	-35.204735	40	8.0	3.6	8.606000	7.045000	6.381000	6.029000	6.203000
A0	262.966217	-35.090492	400	3.2	5.0	11.419000	9.338000	8.427000	7.509000	7.317000
A0	262.710632	-35.205578	10	18.3	5.8	6.956000	5.311000	4.546000	4.263000	3.640000
A0	262.791077	-35.235386	40	7.8	3.5	8.790000	7.083000	6.302000	5.506000	5.862000
A0	262.877319	-35.216888	40	7.8	4.0	9.101000	7.598000	6.913000	6.513000	6.665000
A0	262.663605	-35.271820	40	7.8	5.8	9.456000	7.999000	7.348000	6.839000	6.890000
A0	263.068604	-35.181469	40	7.8	3.0	8.356000	6.870000	6.199000	5.962000	5.736000
A0	262.855713	-35.016300	200	4.0	5.5	10.528000	8.391000	7.310000	7.036000	6.547000
A0	261.903076	-34.797722	80	5.8	3.6	10.941000	8.576000	7.466000	6.917000	6.863000

Continued on next page

Table 6.1 – *Continued from previous page*

S	RA	Dec	t (Myr)	M ($M_\odot$)	d (kpc)	J (mag)	H (mag)	K (mag)	w1 (mag)	w2 (mag)
A0	262.753143	-34.305412	100	5.3	4.6	7.762000	6.031000	5.173000	4.984000	4.316000
A0	262.879791	-34.333668	20	11.2	3.8	8.270000	6.830000	6.135000	5.908000	5.864000
A0	262.852570	-34.490128	20	11.5	4.8	8.231000	6.678000	5.981000	5.559000	5.542000
A0	263.108826	-34.369816	40	8.0	6.0	8.148000	6.539000	5.716000	5.420000	4.845000
A0	262.918182	-34.356163	20	11.2	4.8	9.134000	7.487000	6.740000	6.233000	6.296000
A0	262.626007	-34.242794	200	4.0	3.6	8.892000	7.017000	6.134000	5.851000	5.341000
A0	262.703369	-34.179043	40	8.0	5.0	8.196000	6.380000	5.460000	5.126000	4.308000
A0	263.074860	-34.467365	40	7.7	4.0	9.421000	8.004000	7.422000	6.739000	6.960000
A0	263.050446	-34.675789	200	4.0	3.2	8.162000	6.490000	5.652000	5.552000	5.029000
A0	262.642029	-34.406860	200	4.0	3.5	9.482000	7.627000	6.788000	6.300000	6.261000
A0	263.106140	-34.588970	80	5.8	6.0	9.136000	7.612000	6.944000	6.525000	6.687000
A0	262.790863	-34.285843	400	3.2	5.0	9.064000	7.328000	6.507000	5.918000	5.860000
A0	262.902374	-34.206928	20	11.2	5.0	8.997000	7.304000	6.509000	6.091000	6.175000
A1	263.114502	-34.354939	40	8.0	3.0	7.121000	5.490000	4.727000	4.263000	3.586000
A0	262.345306	-34.228424	40	8.0	5.0	8.949000	7.436000	6.714000	5.810000	6.005000
A0	262.159790	-34.321823	400	3.2	5.2	8.953000	7.268000	6.453000	6.267000	5.925000
B0	263.121948	-34.893284	40	8.0	5.2	11.690000	9.547000	8.439000	7.278000	6.961000
B0	262.896912	-34.873173	4	50.2	7.6	12.428000	10.085000	8.613000	7.444000	6.836000
B0	263.292664	-34.705910	200	4.0	8.7	11.370000	9.275000	8.214000	7.586000	7.421000
B0	263.265625	-34.789154	40	7.8	5.8	10.556000	8.733000	7.816000	7.262000	7.191000
B1	263.336060	-34.880051	100	5.3	5.0	8.903000	6.807000	5.710000	5.516000	4.552000
B0	263.215088	-34.961788	20	11.2	9.1	10.783000	8.862000	7.903000	7.216000	7.224000
B0	263.315369	-34.850792	20	11.2	7.2	10.644000	8.783000	7.938000	7.528000	7.438000
B0	263.192596	-35.097420	20	11.2	6.0	10.121000	8.029000	6.947000	6.462000	6.202000
B0	263.143402	-35.120312	100	5.3	10.0	11.444000	9.317000	8.200000	7.466000	7.069000
B0	263.147919	-35.033131	40	7.8	6.3	11.185000	9.199000	8.123000	7.720000	7.303000
B0	263.164459	-35.111416	20	11.2	8.7	11.430000	9.561000	8.632000	7.855000	7.612000
B0	263.278473	-34.749550	40	8.0	7.2	11.000000	9.114000	8.232000	7.764000	7.568000
B0	263.279266	-34.857616	10	19.1	9.5	8.875000	7.105000	6.223000	5.776000	5.667000
B0	263.198608	-34.909012	40	7.8	6.0	12.029000	9.752000	8.554000	7.769000	7.066000
B0	263.287476	-34.867588	40	8.0	9.1	11.254000	9.301000	8.346000	7.854000	7.731000
B0	263.221069	-35.012608	400	3.2	8.3	10.764000	8.770000	7.781000	6.854000	6.828000
B0	262.964539	-35.003864	20	11.2	5.8	11.461000	9.285000	8.180000	7.480000	7.201000
B0	263.160461	-34.871391	20	11.2	7.2	12.027000	9.643000	8.332000	7.307000	6.742000
B0	263.274017	-34.904362	10	19.2	8.7	8.487000	6.593000	5.651000	5.213000	4.569000
B0	263.067169	-34.855747	400	3.2	6.6	11.999000	9.445000	8.021000	6.795000	6.270000
B0	263.328888	-34.828156	100	5.3	8.3	10.756000	8.722000	7.654000	7.021000	6.637000
B0	263.104553	-35.097626	20	11.2	6.9	10.910000	8.995000	7.937000	7.811000	7.234000
B0	263.221985	-34.810299	20	11.2	9.5	11.283000	9.443000	8.529000	7.935000	7.836000
B0	262.931274	-34.868431	40	8.0	6.6	12.406000	9.672000	8.197000	7.031000	6.473000
B0	262.935455	-34.918133	10	18.0	9.1	11.794000	9.230000	7.840000	7.370000	6.805000
B0	263.134338	-35.085377	40	8.0	6.3	11.045000	9.014000	8.040000	7.369000	6.855000
B0	263.104279	-35.020241	40	8.0	7.9	11.617000	9.526000	8.457000	7.902000	7.786000
B0	263.325958	-34.682739	100	5.3	5.5	11.073000	9.046000	8.086000	7.582000	7.440000
B0	263.095581	-35.080822	20	11.2	7.6	11.161000	9.162000	8.182000	7.700000	7.514000
B0	263.349304	-34.703716	40	7.7	6.6	11.210000	9.230000	8.302000	7.844000	7.870000
B0	263.108490	-34.740471	10	18.3	6.0	8.647000	6.618000	5.471000	4.265000	3.346000
B0	263.100220	-35.010372	40	7.7	5.8	10.546000	8.388000	7.332000	6.664000	6.516000
B0	263.155029	-35.105923	20	11.2	7.9	11.321000	9.311000	8.329000	7.594000	7.517000
B0	263.018951	-34.914017	20	11.2	5.8	12.643000	10.257000	8.909000	7.531000	6.966000
B0	262.714020	-34.725677	8	22.0	6.0	12.977000	9.533000	7.541000	6.616000	5.610000
B0	262.392517	-35.298599	40	7.9	6.3	13.022000	10.512000	9.181000	7.746000	7.108000
B0	262.242859	-34.778309	200	4.0	5.8	15.102000	11.338000	9.264000	7.801000	6.969000

Continued on next page

Table 6.1 – *Continued from previous page*

S	RA	Dec	t (Myr)	M ($M_\odot$)	d (kpc)	J (mag)	H (mag)	K (mag)	w1 (mag)	w2 (mag)
B0	262.321777	-34.885956	20	11.7	8.7	14.415000	10.585000	8.408000	7.121000	6.018000
B0	262.257629	-35.157188	10	19.0	8.7	12.693000	10.068000	8.528000	7.582000	6.850000
B0	262.494415	-35.130535	40	8.0	5.2	12.148000	9.555000	8.276000	7.500000	7.348000
B0	262.449738	-34.827206	20	11.2	6.6	14.920000	10.784000	8.476000	6.872000	5.806000
B0	262.403961	-35.307705	20	11.2	5.0	11.862000	9.353000	8.009000	7.269000	6.753000
B0	261.980438	-34.867908	80	5.9	5.8	14.539000	10.660000	8.526000	7.170000	6.338000
B2	262.215546	-35.029598	40	7.7	5.8	14.283000	10.735000	8.801000	6.802000	5.933000
B0	262.125702	-35.188671	20	11.2	6.3	14.715000	11.484000	9.629000	7.602000	6.963000
B0	262.583069	-35.294662	10	18.0	7.9	9.791000	7.742000	6.618000	4.896000	3.795000
B0	262.935577	-35.161182	20	11.2	7.2	11.603000	9.414000	8.318000	7.629000	7.141000
B0	262.781860	-35.150459	10	19.2	6.6	8.545000	6.500000	5.445000	4.864000	3.965000
B0	262.801422	-35.122383	20	11.2	6.0	10.424000	8.227000	7.140000	6.419000	6.175000
B0	262.992737	-35.166649	40	7.8	5.5	11.367000	8.991000	7.842000	7.166000	6.942000
B0	262.967163	-35.148018	40	8.0	5.2	11.241000	9.103000	8.057000	7.575000	7.345000
B0	262.758209	-35.142803	40	8.0	9.5	11.502000	9.312000	8.162000	7.755000	7.006000
B0	262.594574	-35.198616	20	11.2	6.0	12.100000	9.698000	8.434000	7.484000	7.031000
B0	262.964844	-35.166565	40	7.8	5.2	11.370000	9.201000	8.135000	7.572000	7.356000
B0	263.138763	-35.155830	40	7.8	5.0	10.541000	8.644000	7.741000	7.258000	7.104000
B0	262.952820	-35.005524	40	7.8	5.5	11.878000	9.550000	8.383000	7.741000	7.443000
B0	262.983643	-35.199669	40	8.0	5.2	11.243000	9.081000	7.919000	7.311000	6.975000
B0	263.078522	-35.145393	20	11.2	5.2	10.218000	8.187000	7.230000	6.762000	6.749000
B0	262.297699	-34.757061	20	11.2	5.2	14.639000	11.034000	9.097000	7.877000	6.978000
B1	262.075409	-34.590233	4	53.3	6.9	9.704000	7.277000	5.748000	4.615000	3.570000
B0	263.088318	-34.643574	20	11.2	5.8	10.984000	8.760000	7.670000	7.065000	6.742000
B0	263.249664	-34.468323	40	8.0	7.6	11.132000	9.214000	8.297000	7.841000	7.594000
B1	263.174896	-34.646210	10	19.2	5.2	8.234000	6.031000	4.824000	4.560000	3.091000
B0	262.983215	-34.561195	200	4.0	6.6	11.777000	9.014000	7.474000	6.225000	5.777000
B0	263.094238	-34.502960	400	3.2	8.7	11.793000	9.481000	8.249000	7.747000	7.323000
B0	263.049805	-34.613556	20	11.2	6.3	11.937000	9.337000	7.974000	6.805000	6.336000
B0	263.180054	-34.539478	20	11.2	7.9	10.887000	8.848000	7.770000	6.869000	6.176000
B0	263.181793	-34.534866	20	11.2	7.9	10.901000	8.818000	7.794000	7.177000	7.170000
B0	263.057709	-34.445820	20	11.2	7.2	11.218000	9.151000	8.128000	7.574000	7.166000
B0	263.145203	-34.483929	40	8.0	6.9	11.382000	9.379000	8.416000	7.895000	7.751000
B0	263.150543	-34.475792	10	19.1	5.8	8.409000	6.521000	5.557000	5.204000	4.779000
B0	263.243134	-34.660511	100	5.3	6.0	10.305000	8.221000	7.204000	6.588000	6.379000
B0	263.206818	-34.471172	40	7.8	6.0	10.857000	8.960000	7.987000	7.479000	7.340000
B0	263.063293	-34.502773	10	18.0	9.1	9.968000	7.853000	6.770000	6.258000	6.023000
B0	263.017273	-34.602272	40	8.0	6.6	12.537000	10.177000	8.872000	7.336000	6.833000
B0	263.244781	-34.524574	10	19.1	9.5	8.825000	7.071000	6.215000	5.920000	5.714000
B0	263.245728	-34.469631	10	18.0	7.9	9.116000	7.177000	6.156000	5.746000	5.216000
B0	262.879272	-34.635597	20	11.2	10.0	13.581000	10.546000	8.894000	7.717000	7.318000
B0	262.700012	-34.300514	20	11.5	5.2	12.117000	9.213000	7.654000	6.588000	5.795000
B0	263.163208	-34.509842	20	11.5	6.9	10.037000	8.142000	7.196000	6.543000	6.501000
B0	263.111755	-34.421383	40	8.0	5.2	10.809000	8.794000	7.761000	7.017000	6.864000
B0	263.119904	-34.411678	80	5.9	9.5	11.340000	9.110000	7.930000	7.180000	7.093000
B0	263.070587	-34.669018	20	11.2	5.8	11.026000	8.837000	7.730000	7.239000	6.975000
B0	262.892303	-34.425907	8	22.0	9.5	11.885000	9.124000	7.555000	6.763000	5.534000
B0	263.088470	-34.479588	40	7.8	5.0	10.822000	8.868000	7.886000	7.306000	7.094000
B0	263.087219	-34.444695	20	11.2	7.2	11.151000	9.146000	8.100000	7.553000	7.411000
B0	263.079010	-34.625416	200	4.0	5.8	11.083000	8.840000	7.759000	7.069000	6.966000
B0	263.116455	-34.462353	20	11.2	7.2	11.201000	9.159000	8.158000	7.608000	7.326000
B0	262.723755	-34.269775	20	11.2	5.8	13.076000	10.226000	8.618000	7.304000	6.638000
B0	263.225861	-34.640682	200	4.0	9.1	11.557000	9.419000	8.375000	7.825000	7.543000

Continued on next page

Table 6.1 – *Continued from previous page*

S	RA	Dec	t (Myr)	M ($M_\odot$)	d (kpc)	J (mag)	H (mag)	K (mag)	w1 (mag)	w2 (mag)
B0	263.111359	-34.554882	20	11.7	10.0	10.013000	7.882000	6.691000	6.247000	5.559000
B0	262.985657	-34.641647	80	5.8	9.1	12.266000	9.727000	8.390000	7.272000	6.815000
B0	263.173859	-34.626839	200	4.0	5.5	11.499000	9.151000	7.958000	6.973000	6.493000
B0	262.853058	-34.433128	20	11.6	7.9	12.874000	9.901000	8.237000	7.543000	6.543000
B0	262.963409	-34.597530	80	5.9	10.0	11.967000	9.128000	7.686000	6.796000	6.495000
B0	263.208313	-34.612366	40	7.7	9.5	11.010000	9.044000	8.048000	7.519000	7.271000
B0	262.793915	-34.186737	10	19.0	10.0	11.622000	9.286000	7.939000	6.395000	5.395000
B0	262.853760	-34.229553	200	4.0	6.0	13.110000	10.235000	8.697000	7.354000	7.075000
B0	262.689178	-34.164711	10	18.3	8.7	11.305000	8.728000	7.256000	6.443000	5.490000
B0	263.083649	-34.415577	20	11.2	6.9	10.749000	8.630000	7.529000	6.973000	6.750000
B0	263.177490	-34.418797	40	7.7	9.5	11.731000	9.582000	8.424000	7.865000	7.621000
B0	263.147217	-34.426044	20	11.2	7.9	11.330000	9.435000	8.440000	7.804000	7.294000
B0	263.134155	-34.447041	20	11.2	6.0	10.657000	8.773000	7.791000	7.084000	6.678000
B0	263.192047	-34.620224	40	7.7	5.5	11.147000	9.023000	8.031000	7.540000	7.357000
B0	262.792755	-34.191666	20	11.2	5.2	12.099000	9.610000	8.263000	7.553000	7.098000
B0	263.108246	-34.317280	20	11.2	6.6	11.037000	9.124000	8.080000	7.282000	6.766000
B0	263.104736	-34.342377	20	11.2	7.6	11.348000	9.304000	8.280000	7.686000	7.659000
B0	263.172394	-34.366840	20	11.2	7.2	11.171000	9.281000	8.219000	7.986000	7.523000
B0	263.228149	-34.433876	40	7.8	5.2	10.518000	8.576000	7.667000	7.031000	6.782000
B0	262.264496	-34.472942	40	8.0	6.3	11.974000	9.055000	7.542000	6.976000	6.500000
B0	262.354523	-34.232876	10	19.2	7.9	10.632000	8.023000	6.536000	5.903000	4.702000
B0	262.393707	-34.202549	200	4.0	6.6	12.306000	9.346000	7.698000	6.825000	6.231000
B0	262.329742	-34.421062	100	5.3	5.8	13.296000	10.118000	8.415000	7.157000	6.259000
B0	262.417908	-34.312328	20	11.2	6.3	12.270000	9.510000	8.018000	6.944000	6.197000
B0	262.453491	-34.193279	20	11.4	5.8	11.999000	9.042000	7.367000	7.236000	6.250000
B0	262.541016	-34.447487	10	19.0	5.8	12.671000	9.476000	7.626000	6.715000	5.948000
B0	262.416443	-34.186333	20	11.2	7.2	12.579000	9.833000	8.334000	7.629000	6.914000
B0	262.598785	-34.271187	20	11.5	8.3	13.133000	10.231000	8.611000	6.710000	5.839000
B0	262.356873	-34.218018	10	19.1	9.1	11.116000	8.529000	7.174000	6.489000	6.114000
B0	262.426971	-34.199677	40	7.7	6.0	13.091000	10.247000	8.816000	7.959000	7.690000
B0	262.361908	-34.375317	20	11.2	6.9	12.357000	9.561000	8.085000	7.574000	7.049000
B0	262.429626	-34.190060	80	5.8	5.5	12.481000	9.561000	8.084000	7.324000	7.036000
B0	262.501160	-34.670143	10	18.0	9.1	14.226000	10.634000	8.606000	6.686000	5.940000
B0	262.195160	-34.394718	100	5.3	5.0	12.165000	9.229000	7.692000	6.575000	6.114000
B0	262.150299	-34.350651	40	8.0	5.8	11.701000	9.318000	8.081000	7.152000	6.706000

7

Explaining the TeV and GeV emission from SNR W28

7.1 Introduction

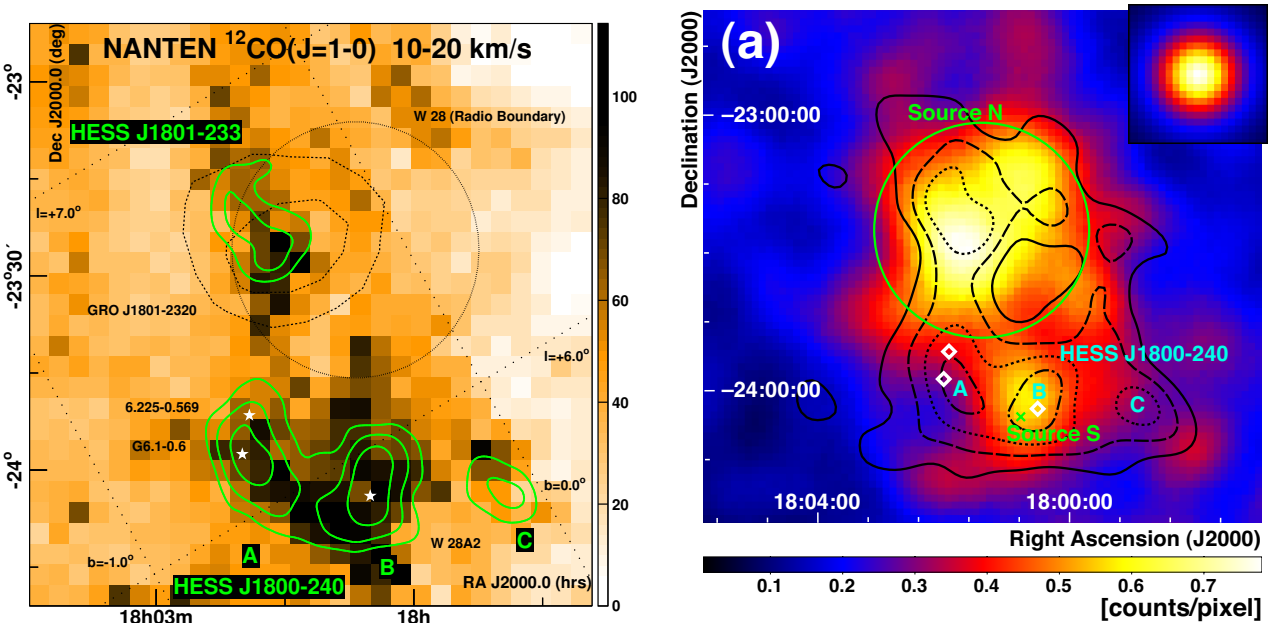

Figure 7.1: *Left panel*: NANTEN ^{12}CO(J=1-0) image of the W28 region (linear scale in K km s^{-1}) for $V_{\rm LSR}$=10 to 20 km s^{-1} with H.E.S.S. significance contours overlaid (green) — levels 4,5,6σ. The radio boundary of W28, The 68% and 95% location contours of GRO J1801-2320 and the location of the HII region W28A2 (white stars) are indicated. *Right panel*: Close-up views of the LAT 2–10 GeV count map around W28. A green circle in the north of each figure indicates the best-fit disk size for the GeV source at north. A green cross indicates the position of the GeV source at south. White diamonds indicate HII regions. Black contours in show the H.E.S.S. significance map for TeV gamma rays at 20, 40, 60 and 80% of the peak value. The figure on the left and right are taken from Aharonian et al. (2008a) and Abdo et al. (2010), respectively.

As mentioned in Sect. 1.5, SNR W28 is known as one of the best cases among the ones in which the CRs released from the SNR are illuminating nearby MCs. For old SNRs, the released TeV CRs which are mostly the runaway CRs at the early stage of the SNR are expected filling the nearby environment homogeneously at present time. This hypothesis has

been well testified by SNR W28, as seen in the left panel of Fig. 7.1, the TeV data along with the NANTEN ^{12}CO data has indicated that the MC at North of the SNR (MC-N) and the three MCs to the South of the SNR (MC-A, MC-B, and MC-C) morphologically match well with the TeV features – HESS J1801-233 and HESS J1800-240 (A,B,C), respectively. Further GeV observation of SNR W28 indicates that this old SNR is releasing its GeV CRs into nearby MCs as well, especially into MC-N, as seen in the right panel of Fig. 7.1. Before we build our models to explain the GeV-TeV emission from SNR W28, we first introduce the multi-wavelength observational data of SNR W28 in the following paragraphs.

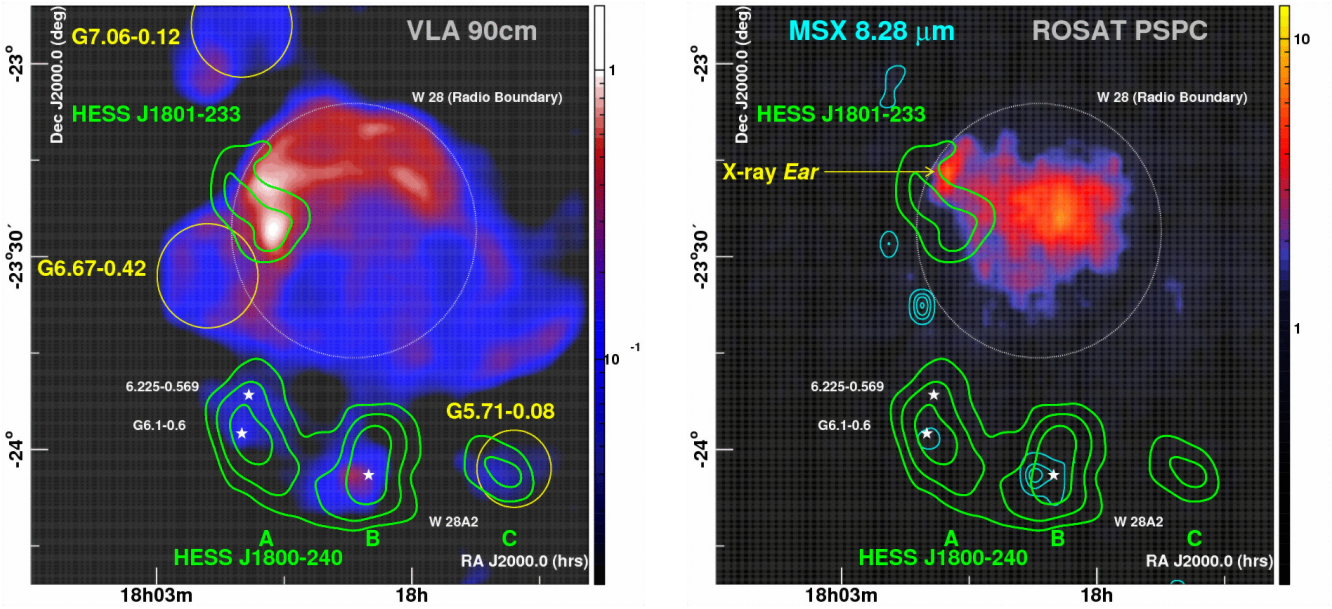

Figure 7.2: *Left Panel*: VLA 90cm radio image from Brogan et al. (2006) in Jy beam^{-1}. The VHE significance contours (green) are overlaid along with the HII regions (white stars) and the additional SNRs and SNR candidates (with yellow circles indicating their location and approximate dimensions). *Left Panel* ROSAT PSPC image — 0.5 to 2.4 keV from Rho & Borkowski (2002). Overlaid are contours (cyan — 10 linear levels up to 5×10^{-4} W m^{-2} sr^{-1}) from the MSX 8.28 μm image. Other contours and objects are as for the left panel. The X-ray *Ear* representing a peak at the northeastern edge is indicated. Both figures are taken from Aharonian et al. (2008a)

The radio data as seen from the left panel of Fig. 7.2 has shown a clear shell structure, which provides us the location (RA 18h01m42.2s, Dec -23°20'6.0") and the radius (0.34°) of SNR W28. In the right panel of Fig. 7.2, one can see the thermal X-ray emission from the heated gas remaining inside the SNR, the estimated X-ray mass is only $20-25\,M_\odot$ (Rho & Borkowski, 2002). The lack of nonthermal X-ray emission suggests that this SNR is very old and can no longer accelerate fresh TeV electrons. Interestingly, there is a bright region at northeast (NE) of the SNR which is shown in both radio and X-ray images. This NE feature indicates that SNR W28 has already encountered with nearby MCs, i.e. the MC-N, and shocked the gas there. This is also consistent with other observational evidences, as seen in Fig. 7.3: The NE region of SNR W28 contains a rich concentration of 1720-MHz OH masers (Frail et al., 1994; Claussen et al., 1999) (with VLSR in the range of $5-15$km s^{-1}), and nearIR rovibrational H_2 emission (Reach & Rho, 2000; Neufeld et al., 2007; Marquez-Lugo &

Phillips, 2010); the velocity dispersion distribution of the NH_3 emission line at this NE region suggests an external disruption from the W28 SNR direction (Nicholas et al., 2011, 2012).

The Fermi data of SNR W28 (Abdo et al., 2010), as seen in the right panel of Fig. 7.1, has presented the GeV counterparts of MC-N and MC-B only. At present time, SNR W28 can no longer accelerate particles up to TeV band. Therefore, both the TeV and GeV emissions from the SNR and nearby regions are believed to be hadronic dominated, assuming that the SNR W28 is the only power source. The GeV emission from MC-N can be naturally explained by the GeV CRs which are mostly released when the SNR is encountering with the MC-N. Compared to the GeV emission from MC-N, the GeV emission from MC-B is weaker and its spectrum is harder, this could be the result of the long distance between MC-B and the SNR. Additionally, some GeV CRs may be released from regions other than the MC-N region, and they could contribute significantly to the CR density at MC-B. The lack of detection of GeV emission from MC-A or MC-C could be that they are even further away from the SNR than MC-B is. Ultimately, the GeV-TeV data naturally fits in a scenario that the GeV CRs are released much later and propagating much slower than those super-TeV CRs are, and can only illuminate MCs in the vicinity of the SNR.

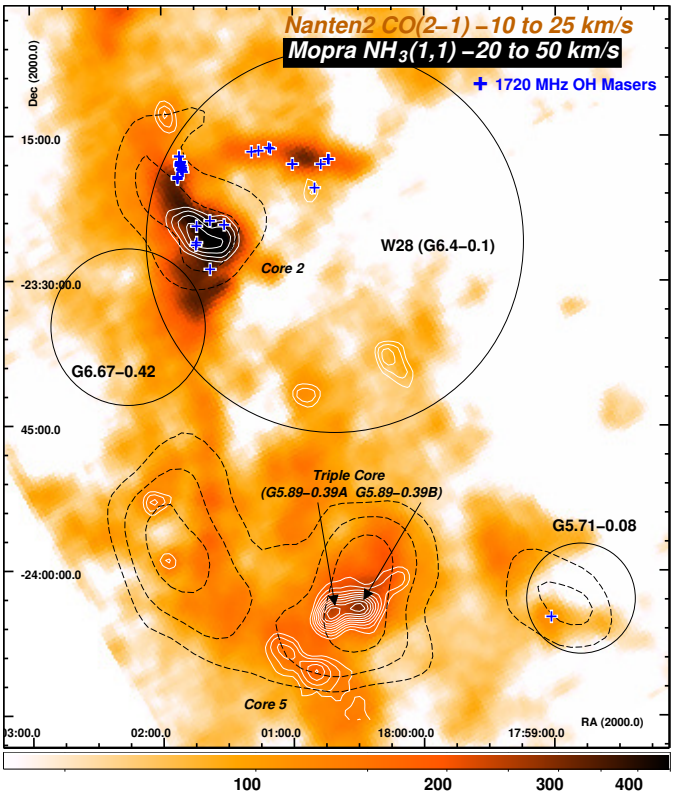

Figure 7.3: NANTEN ^{12}CO $(2-1)$ image ($K\,km\,s^{-1}$) (Fukui, 2008) in log scale, with contours of Mopra NH_3 (1,1) (white) and HESS TeV gamma-ray significance (black-dashed). 1720 MHz OH masers from (Claussen et al., 1999) and (Hewitt & Yusef-Zadeh, 2009) are also indicated in blue/white +. Figure is taken from Nicholas et al. (2011).

Based on the observational data introduced above, we are certain that SNR W28 is quite old and can no longer accelerate fresh CRs or electrons. Furthermore, we believe that SNR W28 has already encountered with MC-N, maybe with other MCs as well, therefore, the

SNR has been releasing its GeV CRs. To construct our W28 model to explain the GeV-TeV emissions of SNR W28, we adopt some physical parameters of SNR W28 as shown in the following lists.

- Distance to Earth as 2 kpc and SNR radius as 12 pc. SNR W28 is located inside complex star-forming region, where HII region M 20 (d $\sim$ 1.7 kpc Lynds & Oneil 1985) and M 8 (d $\sim$ 2 kpc Tothill et al. 2002) are seen, nonetheless, there is no solid evidence to link these HII regions with SNR W28. Owing to the perfect match between the gas density and the TeV morphology inside/around SNR W28, we believe that the MCs (MC-N, MC-A, MC-B, MC-C) are indeed associated with the SNR W28, with distances to the SNR no more than 100 pc. However, with the CO (J = 1-0) data from NANTEN, most components of these MCs are found covering a broad velocity range from 10 km s^{-1} to 20 km s^{-1} which corresponds to a kinematic distance of approximately 2 to 4 kpc (Aharonian et al., 2008a). Additionally, Velázquez et al. (2002) suggested the distance of W28 as $\sim$ 1.9 kpc when associated it with a 70M$_\odot$ HI feature detected at the SNR region, this HI feature is also seen as the evidence of the interaction between W28 and its surrounding gas.

- The ICM density as 5 cm^{-3}. Through the near-infrared and millimeter-wave observation, Reach et al. (2005) argued that the different morphologies of W28 at different wavelengths are explained by the highly nonuniform structure of giant molecular clouds, with low-density gas ($\sim$ 5 cm^{-3}) occupying most (90%) of the volume, moderate-density gas ($\sim 10^3$ cm^{-3}) occupying most of the rest of the volume, and dense gas in the cores. Velázquez et al. (2002) also derive a similar ICM density $\sim 1.5 - 2$ cm^{-3}, assuming that observed mass (HI around the SNR) are evenly distributed inside a sphere with radius 20 pc.

- Ejecta Mass, 1.4 M$_\odot$. Considering the old age of W28, it is not surprising that no CCO is found so far. The small X-ray mass found in the center of the SNR could be due to the empty pre-SN wind bubble or other processes, such like evaporation (Rho & Borkowski, 2002). So far, we can not conclude the type of SN. Thus for simplicity of the pre-SN environment, we assume a type Ia SN with the standard ejecta mass, which is consistent with Gabici et al. (2010).

- Ejecta Energy, 0.4 $\mathcal{E}_{51}$. Following the requirements of the observed shock velocity at present time and the measured circumstellar gas density, we adopt this value in our SNR evolution model as seen in next section.

- Shock velocity at present time, $60 - 100$ km s^{-1}. Through observing the neutral hydrogen around the SNR, a HI cloud is detected by Velázquez et al. (2002) near $V_{\rm LSR} = +37$ km s^{-1}, overlapping the center of W28. This expanding HI cloud is likely to be a swept thick HI shell by the shock, hence, the velocity dispersion of this HI cloud is expected to be lower than the intrinsic shock velocity. A more accurate method is through directly measuring the forbidden lines at the shock, Bohigas et al. (1983) estimate shock velocities of W28 between 60 km s^{-1} and 90 km s^{-1} using the line strength ratio of OIII λ5007/H$_\alpha$, while Long et al. (1991) derive velocities larger than 70 km s^{-1} from line strength ratio of NII/H$_\alpha$ and SII/H$_\alpha$.

- Diffusion coefficient is set as 10% of the Galactic diffusion coefficient ($D(E) = 10^{27}(E/10\,\mathrm{GeV})^{\delta}\mathrm{cm}^2/\mathrm{s},\ \delta = 0.5$) for the entire space. This is consistent with Gabici et al. (2010) who used a point CR source approximation to explain the GeV-TeV emission from W28.

- The mass of MC-N is $5 \times 10^4\,\mathrm{M}_\odot$ when integrating the $0 - 25\,\mathrm{km\,s^{-1}}$ NANTEN ^{12}CO data (Aharonian et al., 2008a). The masses of MC A, B are $6 \times 10^4\,\mathrm{M}_\odot$, $4 \times 10^4\mathrm{M}_\odot$, respectively, when integrating the 0-20km/s NANTEN ^{12}CO data (Gabici et al., 2010).

- The project distances of MC A, B, C are at ∼20 pc from the center of the SNR(Aharonian et al., 2008a), assuming the distance of the SNR as 2 kpc.

7.2 Models

In this chapter, our main goal is to provide a hadronic explanation for the GeV-TeV emission of SNR W28. Similarly, we adopt the SNR evolution model and the CR acceleration model developed for HESS J1731-347, which are described in Chapt. 3 and Chapt. 4, into our W28 study. Nonetheless, different from the HESS J1731-347 models, our W28 model would need to introduce an additional system for the later released GeV CRs. So far, the releasing process of the GeV CRs from old SNRs is still an open question. In contrast to the previous works on W28, see e.g. Li & Chen (2010); Ohira et al. (2011), in which the E_{max} are gradually reduced to 1 GeV at the end of SNR history (12 pc) and CRs with energy E_{max} are released from the whole SNR surface, we assume that most of the GeV CRs are released when certain parts of the shock has encountered with the MC clumps and can no longer confine the GeV CRs. Ultimately, in our model the released CRs are divided into two parts – the super-TeV CRs and the GeV CRs. At early stage of the SNR evolution, we adopt the acceleration model from Zirakashvili & Ptuskin (2008), and the SNR only release super-TeV CRs ($E > E_{\mathrm{max}}$). Once certain parts of the shock start to encounter with the MC clumps($n > 10^2\,\mathrm{H\,cm^{-3}}$), their velocity drop significantly in a few years, and eventually, those parts of the shock are disassembled and dissipated into the local medium. At this moment, all the CRs (mostly GeV CRs) used be trapped inside those parts of the shock are totally released.

Addition to the basic parameters mentioned above, to better reproduce the observational data, we introduce the following setups into our W28 model:

- In this chapter, we only focus on the γ-ray emission from MC-N, MC-A, and MC-B, owing to the low TeV emission from MC-C. Since the SNR is encountering with MC-N, the three-dimensional distance of MC-N to the center of SNR is set similar to the R_{SNR} as 11.5 pc. The three-dimensional distances of MC-B is set as the projected distance 20 pc. Due to the lack of GeV emission, MC-A is set much further, with a distance to the SNR center 35 pc.

- We use the analytical solutions described in Sect. 4.2 to calculate the ejecta-dominated stage and the Sedov-Taylor stage of W28. When the shock is further slowed and the SNR enters the pressure-driven snowplow (PDS) stage, we adopt the analytical solution

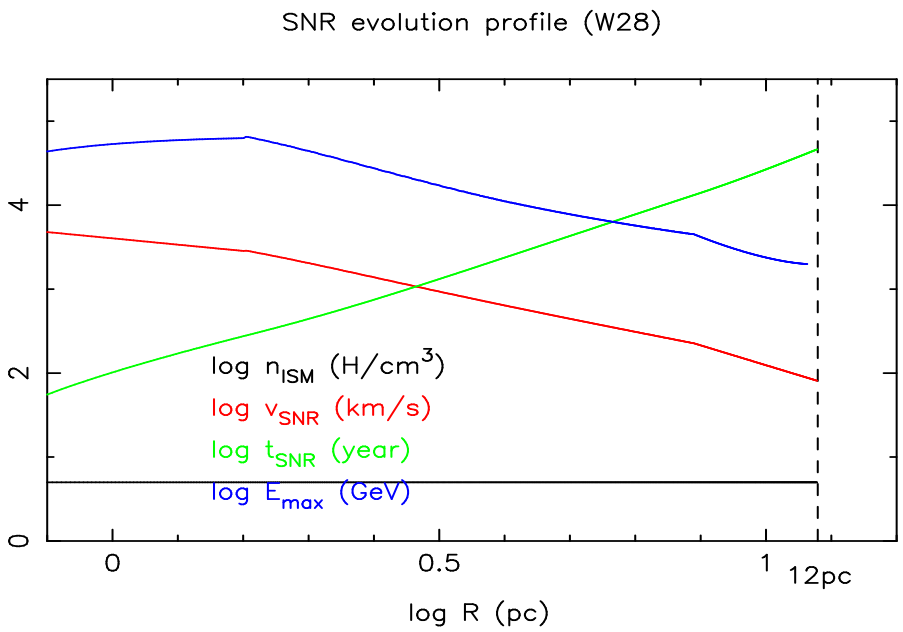

Figure 7.4: The SNR evolution profile in our W28 model. Same figure setup from Fig. 4.4 is used here.

by Cioffi et al. (1988) which is described as follows.

$$R_{\rm SNR} = R_{\rm PDS}\left(\frac{4\,t_{\rm SNR}}{3\,t_{\rm PDS}} - \frac{1}{3}\right)^{3/10}, \quad v_{\rm SNR} = v_{\rm PDS}\left(\frac{4\,t_{\rm SNR}}{3\,t_{\rm PDS}} - \frac{1}{3}\right)^{-7/10}, \tag{7.1}$$

where the $R_{\rm PDS}$, $v_{\rm PDS}$, and $t_{\rm PDS}$ are the radius, velocity, and age of the SNR at the beginning of PDS stage, and they can be written as

$$\begin{aligned} R_{\rm PDS} &= 14.0\left(\frac{\mathcal{E}_{\rm ej}}{\mathcal{E}_{51}}\right)^{2/7}\left(\frac{n_{\rm ISM}}{1\,{\rm cm^{-3}}}\right)^{-3/7}\left(\frac{\zeta_{\rm m}}{1}\right)^{-1/7}\ {\rm pc}, \\ v_{\rm PDS} &= 413\left(\frac{\mathcal{E}_{\rm ej}}{\mathcal{E}_{51}}\right)^{1/14}\left(\frac{n_{\rm ISM}}{1\,{\rm cm^{-3}}}\right)^{1/7}\left(\frac{\zeta_{\rm m}}{1}\right)^{3/14}\ {\rm km\,s^{-1}}, \end{aligned} \tag{7.2}$$

the metallically factor $\zeta_{\rm m} = 1$ for solar abundances is adopted in our work. As shown in Fig. 7.4, using a homogeneously ICM density $n_{\rm ISM} = 5\,{\rm H\,cm^{-3}}$, the SNR spends its first ~ 200 years (~ 1.5 pc) in the ejecta-dominated stage, after the Sedov-Taylor stage it enters the PDS stage at ~ 13 kyr (~ 7.7 pc), at the end it reaches 12 pc at 46 kyr and the present shock velocity is $81\,{\rm km\,s^{-1}}$.

- As shown in the left panel of Fig. 7.1, the north part of the MC-B has shown a filament-like feature connecting the MC-B and the south pole of the SNR on the sky map. Assuming this filament-like MC is indeed swept by the shock, we introduce another GeV CR source – MC at south pole in addition to the existing GeV CR source – MC-N. Ultimately, in our model the SNR starts to encounter with MC-N (assuming 20% of the total SNR surface) and the MC at the south pole (assuming 6% of the total SNR surface) when it reaches 11.5 pc radius (∼40 kyr). Once enter the MC clumps, these 20% and 6% parts of the shock are quickly disassembled and release all the CRs in them.

- The released GeV CRs from a disassembled shock follow a power-law distribution of energy, and can be written as

$$N_{\rm GeV} = N_0 \cdot 0.1 R_{\rm SNR} \cdot 4\pi R_{\rm SNR}^2 \cdot X_{\rm s}, \tag{7.3}$$

where the $N_0 \propto E^2$ is the CR density at the shock with cutoff energy at $E_{\rm max}$ (Zirakashvili & Ptuskin, 2008), $X_{\rm s} = 20\%(6\%)$ represents the percentage of the SNR shock that are encountering with the MC-N(MC at south pole). In the realization of this scenario, most of the CRs ($N_{\rm GeV}$) used to be trapped in the shock are set free ($\sim$40 kyr) from two instantaneous point sources(Source-N, Source-S) on the surface of the SNR (11.5 pc). Source-N is set at where the MC-N is, while Source-S is located at the south pole of the SNR in the RA-Dec coordinates. During the calculation of the γ-ray spectrum, all MC clumps are considered as point targets for the pp collision. The diffusion distances between the GeV CR sources and the MC clumps, as shown in table 7.1, are used to calculate the final CR density at each MC clump at present time.

Table 7.1: Diffusion distances between the MC clumps and the GeV CR sources.

Diffusion distances	MC-N	MC-A	MC-B
Source-N	0.1 pc	33.9 pc	22.4 pc
Source-S	16.2 pc	30.8 pc	8.0 pc

7.3 Results and discussions

As seen in Fig.5.7, we successfully reproduced the GeV-TeV spectrum of MC-N, MC-A, and MC-B. The key strategy in our model is realized by using runaway TeV CRs from early stage of the SNR to explain the H.E.S.S. data, and using the lately released GeV CRs from the shocks that are hitting the MCs to explain the Fermi data.

In our SNR evolution model of W28, we have only explored a type Ia scenario which delivers a homogeneous pre-SN environment. This type Ia scenario has successfully explained the observed shock velocity (81 km s^{-1}) at present time and the measured gas density 5 cm^{-3} near the SNR. Obviously, SNR W28 is unlikely still evolving inside the MS bubble, if a new SNR scenario with a more massive progenitor star is adopted in our SNR evolution model of W28, then the SNR is expected to have already swept the MS bubble shell and entered the ICM before it reaches 12 pc. In this new SNR scenario, adopting the same SN energy $\mathcal{E}_{\rm ej}$ used in the type Ia scenario, similar shock velocity (81 km s^{-1}) at present time is expected. This is due to that the final shock velocity is mostly sensitive to the total swept mass, see

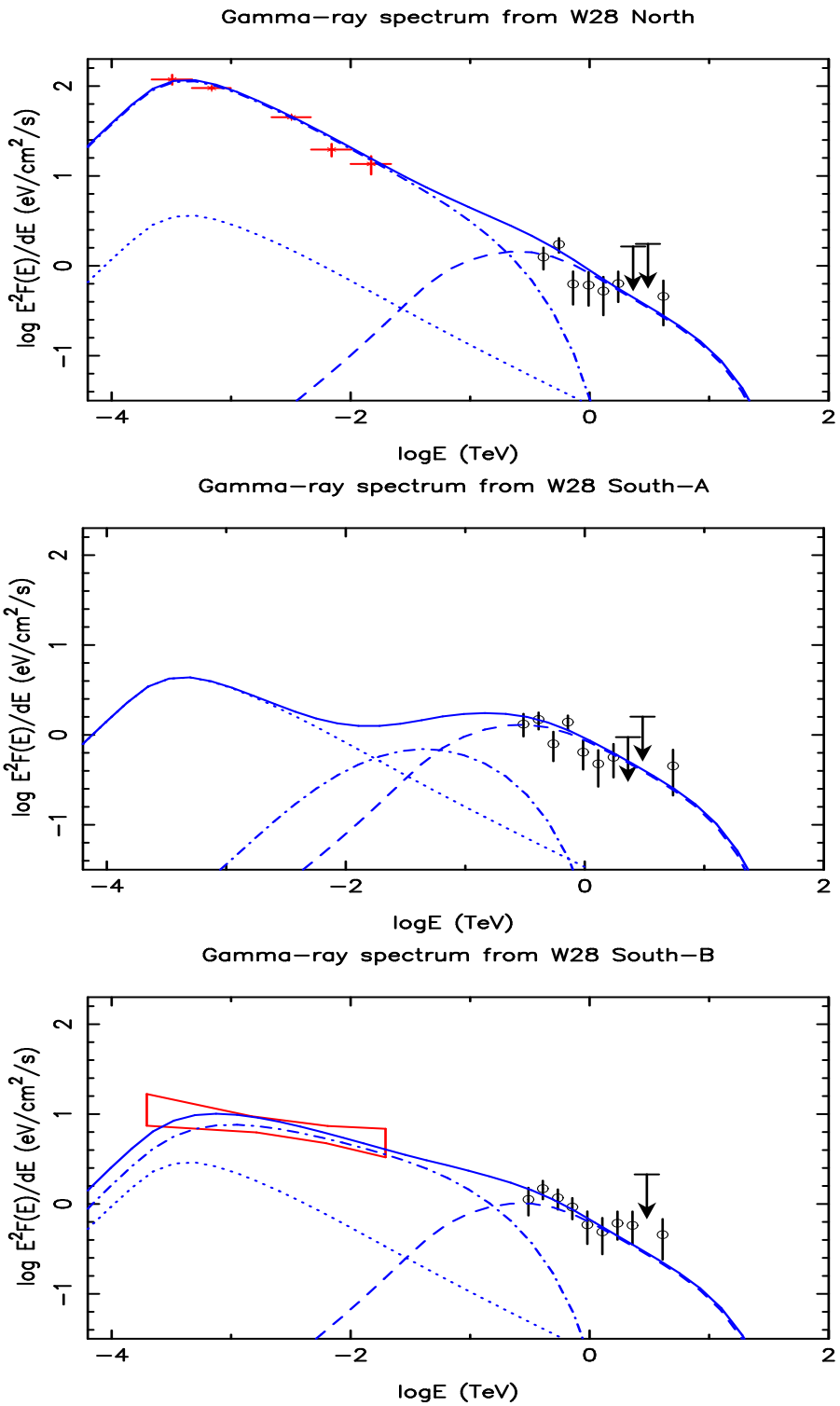

Figure 7.5: Broad band fit to the γ ray emission detected by Fermi telescope and H.E.S.S. from the sources HESS J1801-233 (W28 north), HESS J1800-240 A and B (top to bottom). In each panel, the hadronic γ-ray emission calculated using only runaway super-TeV CRs, using only the GeV CRs, using only the Galactic CR background, and using all three components are shown in dashed lines, dash-dotted lines, dotted lines, and solid lines, respectively. Fermi (Abdo et al., 2010) and H.E.S.S. (Aharonian et al., 2008a) data points are plotted in red and black, respectively. No GeV emission has been detected from HESS J1800-240 A.

e.g. the scenario $8M_\odot$ and scenario $15M_\odot$ in Chapt. 4. Furthermore, the GeV CR releasing process which happens after the MS bubble shell sweeping is expected to be similar to that in the type Ia scenario as well. However, the super-TeV CR releasing which happens mostly in the early stage of the SNR evolution will be affected in this new SNR scenario.

In the reproduction of the TeV data from MC-N, MC-A, and MC-B, the diffusion coefficient for the entire space is fixed as $D(E) = 10^{27}(E/10\,\mathrm{GeV})^{\delta}\mathrm{cm}^2/\mathrm{s},\ \delta = 0.5$. Thus the fine tune of other parameters in our model is needed to explain the GeV data from MC-B and MC-N. To reproduce the Fermi data from MC-N, we need the SNR to release GeV CRs at quite late time $\sim 40\,\mathrm{kyr}$ from Source-N. In fact, the SNR has already reached 10 pc at $\sim 25\,\mathrm{kyr}$ and it may start to encounter with the MC-N at a much earlier time than $\sim 40\,\mathrm{kyr}$. Due to this late releasing time of Source-N ($\sim 40\,\mathrm{kyr}$) as well as its long distance to MC-B ($\sim 23\,\mathrm{pc}$), GeV CRs released from Source-N are not able to reach the MC-B at present time. Therefore, we introduce Source-S which is much closer to the MC-B than Source-N is. If this scenario, that GeV CRs of Source-S are transported through the filament-like MCs at the south pole of the SNR, is true, the detection of a bridge feature connecting the MC-B and the SNR in GeV band is expected.

Adapting the $\eta_{\mathrm{esc}} = 0.1$ in our model, at the end of Sedov-Taylor stage ($\sim 13\,\mathrm{kyr}$), the SNR has already released most of the super-TeV CRs with total energy about $0.1\,\mathcal{E}_{51}$. After parts (20%+6%) of the SNR have encountered with MCs ($\sim 40\,\mathrm{kyr}$), about $0.01\,\mathcal{E}_{51}$ CRs are released from the Source-N and Source-S. Hence, the SNR has totally released about $0.11\,\mathcal{E}_{51}$ CRs into the surrounding space at present time. The energy of the total accelerated CRs including both the released CRs and the trapped CRs inside the SNR is $\mathcal{E}_{\mathrm{CR,end}} + \mathcal{E}_{\mathrm{CR,sh}} \approx 0.13\,\mathcal{E}_{51} \approx 30\%\mathcal{E}_{\mathrm{ej}}$ at present time. This ratio (30%) is marginally larger than the expected CR acceleration efficiency inside SNRs $\sim 10\%\mathcal{E}_{\mathrm{ej}}$. The total SN energy $\mathcal{E}_{\mathrm{ej}}$ in our model is limited by the observational requirements as described in last section. If a lower η_{esc} is adopted in our model, we need to decrease the diffusion coefficient as well in order to trap more super-TeV CRs near the SNR. In such a scenario, in order to illuminate MC-B in GeV band at present time, the GeV CRs from Source-S need to be released much earlier than 40 kyr, or a magnetic tube can be introduced to build a fast transportation between the SNR and MC-B.

In summary, our model explains the GeV-TeV emission of W28 very well, but within quite narrow parameter space. The most bold assumption in our model is the introduction of Source-S, which lacks of direct observational evidences, e.g. masers. In future study, we would like to explore a scenario using only Source-N as the GeV CR source as well as adopting a more complex diffusion environment (e.g. the magnetic tube connecting MC-B with SNR) to explain the GeV emission from MC-B. In our present model, we choose two instantaneous point sources as the GeV CR sources. However, in reality, the releasing of the GeV CRs could be a more continuous and complex procedure, which varies along the time and location. Hence, we look forward to improved CR releasing mechanism as well as more observational constraints on the timing and positioning of the interaction between MCs and the SNR in the future study.

8

Conclusions

8.1 TeV data analysis of HESS J1731&J1729

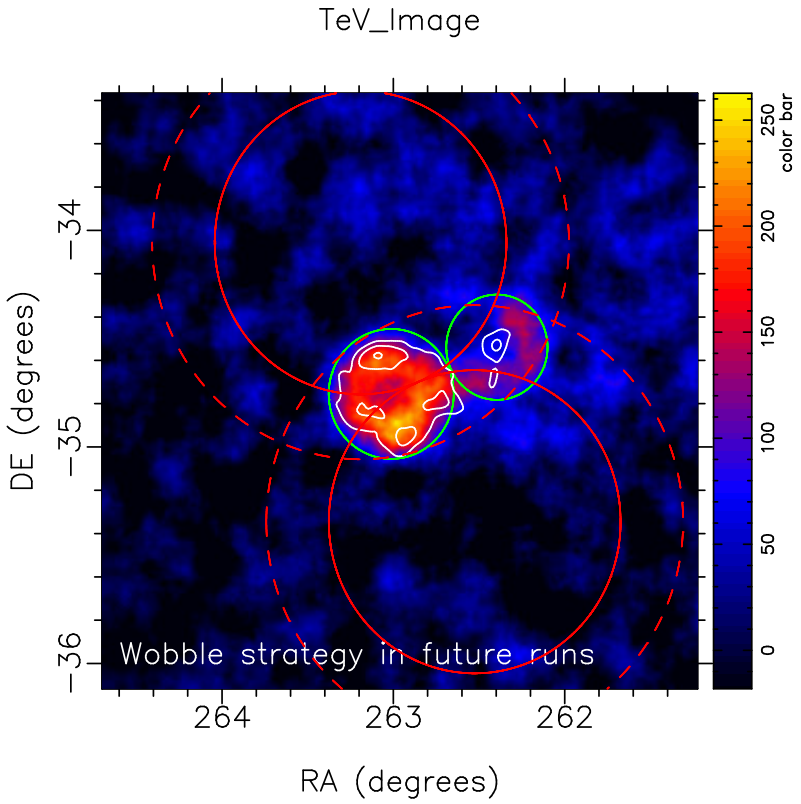

Figure 8.1: The proposed new viewing centers are set as RA=262.5254 Dec=-35.34533 (southwest circle) and RA=263.1913 Dec= -34.05689 (northeast circle). The dashed red circles with radius of 1° are meant to represent the flat field of view area for H.E.S.S. II. SNR HESS J1731-347/HESS J1729-345 are marked as big/small green circles. The white contours show the TeV morphology reproduced by H.E.S.S. Collaboration et al. (2011), while the colored image represent the TeV morphology reproduced with ImPACT and new data sets (see more details in Sect. 2.1).

Our TeV data analysis has mainly focused on two extended TeV sources – SNR HESS J1731-347 (detection 22σ, radius 0.3°) and HESS J1729-345 (8σ, 0.14°), which are first identified by H.E.S.S. Collaboration et al. (2011). Using ImPACT/TMVA (analysis tools) and the H.E.S.S. data taken from 2004 to 2013, we present the morphological and spectral analysis results of SNR HESS J1731-347 and HESS J1729-345:

- Our morphological structures of SNR HESS J1731-347 and HESS J1729-345 are slightly

different from the ones published in H.E.S.S. Collaboration et al. (2011), who used the analysis tool Model++ and H.E.S.S. data taken from 2004 to 2009. Particularly, we found a bridge structure connecting these two sources, as seen in Sect. 2.1 and Fig. 8.1. Considering the relative low TeV flux and the small size of HESS J1731&J1729, the differences of the analysis results between these two analysis tools are within the statistical fluctuation. However, our new morphological results obtained with ImPACT can be better matched with the CS and CO data (cold gas density) at $\sim 3.2\,\mathrm{kpc}$ in our preliminary studies. Unfortunately, our proposals which suggested a deep observation of this bridge, as seen in Fig. 8.1, for both 2015 (Galactic center year) and 2016 (HESS-I upgrading) had been delayed.

- Despite the fact that some minor morphological differences are found inside the SNR when using different analysis tools, our spectral analysis results of SNR HESS J1731-347 match perfectly with the one published in H.E.S.S. Collaboration et al. (2011). The same on-region of SNR HESS J1731-347 used in H.E.S.S. Collaboration et al. (2011) (a circle region with a radius of 0.3° marked as the left green circle in Fig. 8.1) is adopted in our spectral analysis as well. Based on our morphological analysis results of HESS J1729-345, two other on-regions of HESS J1729-345 than the one in H.E.S.S. Collaboration et al. (2011) are adopted in our spectral analysis. Therefore, it is not surprising that we obtain quite different spectral analysis results of HESS J1729-345 when compared to the ones in H.E.S.S. Collaboration et al. (2011).

8.2 The hadronic TeV emission of HESS J1729-345

Through exploring the SNR evolution history with different scenarios ($8\,\mathrm{M}_\odot$, $15\,\mathrm{M}_\odot$, $17\,\mathrm{M}_\odot$, $20\,\mathrm{M}_\odot$, and $25\,\mathrm{M}_\odot$ progenitor masses), we found that the SNR HESS J1731-347 is most likely still expanding inside its progenitor main-sequence wind bubble. With $17\,\mathrm{M}_\odot$, $20\,\mathrm{M}_\odot$ and $25\,\mathrm{M}_\odot$ progenitor mass scenarios, we successfully reproduce relatively fast shocks of $> 2000\,\mathrm{km/s}$ at present time ($\sim 3\,\mathrm{kyr}$, $\sim 6\,\mathrm{kyr}$ and $\sim 3\,\mathrm{kyr}$ after the SN explosion), which is required by the nonthermal X-ray emission detected from the SNR.

One of our main goals in my Ph.D study was to verify whether the TeV emission from the nearby source HESS J1729-345 can be explained by γ-ray emission from runaway CRs that have been accelerated in SNR HESS J1731-347 and presently illuminate molecular clouds near the SNR. To this extent, a simplified three-dimensional molecular cloud geometry near the SNR was constructed in accordance with existing ^{12}CO data. Adopting the CR acceleration model of nonresonant streaming instability from Zirakashvili & Ptuskin (2008), the CR injection into the surroundings of the SNR was calculated throughout the different simulated SNR evolutions. Diffusion of the CR particles into the inhomogeneous surrounding medium was simulated by means of a Monte Carlo transport code. By placing HESS J1729-345 30 pc away from the center of the SNR, its spectrum can be reproduced in scenarios with $20\,\mathrm{M}_\odot$ and $25\,\mathrm{M}_\odot$ progenitor masses, with a diffusion coefficient of $D_{10} = 10^{28}\,\mathrm{cm^2 s^{-1}}$, $\delta = 0.3$, inside the molecular cloud clumps.

The following key features of our simulations are basically driven by the young age of the SNR in our model scenario:

- The escaped CRs concentrate in one energy band at relatively high energies. The simulated TeV γ-ray spectrum of HESS J1729-347 peaks at ~ 1 TeV. Thus no detection from Fermi is expected in our model. Future HESS-II or CTA observations with high sensitivity around 100 GeV may also provide key evidence for our model.

- The CR density drops very fast with increasing distance from the SNR. Inside the $20\,M_\odot$ progenitor mass scenario, we also explored the parameter space by adopting different diffusion coefficients at the ICM or inside MC clumps. The observed TeV image can be explained well assuming a Galactic diffusion coefficient in the ICM ($D_{10} = 10^{28}\,\mathrm{cm^2 s^{-1}},\ \delta = 0.3 - 0.5$). Assuming that HESS J1729-345 (MC-J1729) is ~ 30 pc away from the center of the SNR, γ-rays from hadronic interactions from the corresponding molecular cloud can very well dominate the TeV emission outside the SNR, when the densest MC region (MC-core) is placed at a larger distance ~ 100 pc from the SNR.

Additionally, some interesting comparison results are also found when we adopt different SNR evolution scenarios and different diffusion scenarios into our simulation.

- The SNR in scenario $25M_\odot$ spends all its life inside the empty MS wind bubble, which is filled with the approximated homogeneous wind material. Hence, the runaway CRs are released quite evenly during the entire SNR evolution history (~ 3 kyr). As the results of this constantly CR releasing scenario, the TeV flux of MC-J1729 first increases gradually to the peak at ~ 1 kyr, then it follows a plateau shaped light curve for the next 2 kyr. On the other hand, the SNR in scenario $20M_\odot$ has released most of the higher-energy CRs (E>10 TeV) in the early stage (t<1 kyr) when the SNR is still expanding inside the dense RSG bubble. Therefore, the released CRs are forming an expanding spherical thin-shell, and the light curve of HESS J1729-345 displays a spike when the thin-shell is passing by.

- Our diffusion environments can mainly be separated into two regions – target gas region (i.e. the MC clumps) and the space connecting the CR source to the target gas region (i.e. the ICM). When the diffusion coefficient inside the MC clumps is lowered, the average walking time of CRs inside the MC increases. As the result of that, more CRs are accumulated inside the MC clumps and the TeV emissions of the MC clumps finally increase. When the diffusion coefficient inside the ICM is increased, the CRs (especially the lower-energy CRs) are able to reach further targets, i.e. the MC-core in our simulation. Thus the diffusion coefficient in the ICM becomes the dominating factor in adjusting the ratio between the TeV flux of MC-J1729 and that of MC-core (x_{MC}), a higher x_{MC} represents a better matching with the TeV image of HESS J1729-345.

8.3 The hadronic TeV emission of SNR HESS J1731-347 ?

Although the GeV upper-limits from Fermi-LAT favor a leptonic nature of the γ-ray emission from the SNR, we introduced two additional scenarios ($20\,M_\odot$ in-shell and $25\,M_\odot$ in-shell) in which the SNR has at present started to evolve into the progenitor MS bubble shell. Also in

these scenarios, the TeV γ-ray spectrum of HESS J1729-345 can be reproduced with hadronic emission from runaway CRs, when adopting a diffusion coefficient $D_{10} = 10^{28}\,\mathrm{cm^2 s^{-1}}$, $\delta = 0.5$ everywhere. Still, it seems that the hadronic contribution to the SNR γ-ray emission does not dominate also under such conditions either; the expected emission from the downstream region of the shock only provides $\sim 30\%$ and $\sim 12\%$ of the observed TeV emission for the two in-shell scenarios, respectively. The shortage of hadronic emission in our models is mainly attributed to two limited factors.

- One of the key constraints on our models is from the total accelerated CRs throughout the SNR history, which includes both the released super-TeV CRs and the CRs trapped inside SNR ($\mathcal{E}_{\mathrm{CR,end}} + \mathcal{E}_{\mathrm{CR,sh}} \lesssim 0.1\,\mathcal{E}_{\mathrm{ej}}$). To explain the CR density observed on Earth, with a kinetic energy output of 10^{51} erg per explosion and a rate of 2–3 per 100 years, an average of 10% of the supernova kinetic energy needs to be converted into CR energy (Hinton & Hofmann, 2009). And both the $20\,\mathrm{M_\odot}$ in-shell and $25\,\mathrm{M_\odot}$ in-shell scenarios have already adopted a quite high SN explosion energy as $\mathcal{E}_{\mathrm{ej}} = 2\,\mathcal{E}_{51}$.

- The other key constraint on our models comes from the accumulated gas at the shock, which is also limited by the explosion energy. Higher explosion energy allows the shock to sweep deeper into the MS bubble shell, in which the gas density increases very rapidly ($n_{\mathrm{ISM}} \propto r^{12}$ in our models).

8.4 The cosmic ray propagation near the SNR

Understanding the diffusion process of CRs near the SNR (<100 pc) is one of our most important tasks from the beginning of my PHD study. In the CR diffusion models of our earlier work (see Chapt. 5 and Cui et al., 2016), for simplicity we used the diffusion coefficient, which is, in fact, not a very good parameter to describe the statistical behaviour of the CRs in relative small diffusion environment ($\lesssim 100$ pc). Therefore, a purely numerical code that describes CR propagating inside a given magnetic turbulence is builded in later 2015, and it delivers results consistent with the conclusions of previous works (e.g. Casse et al., 2002; Fatuzzo et al., 2010). Some interesting findings from our numerical simulation are presented in the following lists.

- A strong background magnetic field can behave like a “magnetic tube”, inside which the particles are confined and propagating semi-ballistically.

- The CRs only starts to behave diffusively when the mean propagating distance is larger than the maximum wavelength of the magnetic turbulence. This is due to that the large magnetic eddies behave more like “magnetic tubes” when CRs are propagating in an environment smaller than the size of the eddies.

- The CRs show ballistic movement unless the mean propagating distance is much larger than the CR Gyro-radius and the CRs are able to be scattered multiple times.

- Through simulating the propagating trajectories of hundreds of thousands of CRs inside random Kolmogorov's turbulences, we derive the corresponding diffusion coefficients of CRs with certain energies. The energy spectrum of the derived diffusion coefficients has clearly shown three power-law slopes, which were explained in Sect. 3.2.5 and Casse et al. (2002). Overall, our results are sensitive to the maximum length scale of the magnetic turbulence, but insensitive to the minimum length scale.

This purely numerical code naturally leads to more free parameters, such like the power spectrum of the magnetic turbulence, the structure of background magnetic field. It is very difficult to obtain the direct observational data of the magnetic fields in the vicinity of the SNRs, therefore, a more feasible plan in our future study is to constrain these magnetic parameters through matching the results of our numerical code with the TeV observations.

8.5 Star searching near/behind the SNR HESS J1731-347

Our star searching project is based on two possible scenarios: one in which SNR HESS J1731-347 is born within an OB star cluster; and a second scenario in which SNR HESS J1731-347 has already encountered with nearby MCs and ionized the MCs through releasing its low energy CRs into them, while the ionization features of the MCs can be observed through the H_+^3 absorption lines with infrared background sources.

We choose our stars within the WISE catalog and SIMBAD catalog. Assuming that our potential star candidates are either between MC-A (MC clump at $\sim 3.2\,\mathrm{kpc}$) and MC-B (MC clump at $\sim 5.2\,\mathrm{kpc}$) or behind MC-B, we can obtain the corresponding extinction of each star. Through comparing the observational data (after the reduction of the extinction and distance) with the theoretical star evolution model, we find 41 (125) potential infrared sources between MC-A and MC-B (behind MC-B). Unfortunately, non of these star candidates has optical data so far, which is often the smoking gun for identifying the physical characters of a star. Therefore, we look forward to future optical observations on these star candidates, particularly, the 41 stars candidates located roughly between the Scutum-Crux arm and the Norma-Cyg arm (3–5 kpc).

8.6 The TeV and GeV emission of SNR W28

We successfully explained the GeV-TeV emission around SNR W28 (HESS J1801-233 and HESS J1800-240 A, B) using the SNR evolution model and the CR acceleration/diffusion model developed for HESS J1731-347. Following the assumption that the GeV CRs are only released when the shock has encountered with the MC clumps and dissipated into the local medium, two GeV CR releasing sources – Source-N and Source-S are introduced in our W28 model. Here the releasing processes of both GeV CRs and super-TeV CRs are consistent with the acceleration theory in Zirakashvili & Ptuskin (2008).

Source-N is located at HESS J1801-233, where a MC clump (MC-N) is found being swept by the shock (supported by multiple observational evidences). However, Source-S which is located at the south pole of the SNR is artificially introduced into our model, due to that the GeV CRs released from Source-N face a difficulty of reaching HESS J1800-240 B. Instead of introducing Source-S, a different approach – introducing an anisotropic diffusion environment near the SNR will be adopted in our future study.

Bibliography

H.E.S.S. Collaboration, Abramowski, A., Acero, F., et al. 2011, A&A, 531, A81

Abdo, A. A., Ackermann, M., Ajello, M., et al. 2010, ApJ, 718, 348

Abdo, A. A., Ackermann, M., Ajello, M., et al. 2011, ApJ, 734, 28

Acero, F., Ballet, J., Decourchelle, A., et al. 2009, A&A, 505, 157

Acero, F., Aharonian, F., Akhperjanian, A. G., et al. 2010, A&A, 516, A62

Acero, F., Lemoine-Goumard, M., Renaud, M., et al. 2015, arXiv:1506.02307

Aharonian, F. A., & Atoyan, A. M. 1996, A&A, 309, 917

Aharonian, F. A., & Atoyan, A. M. 1999, A&A, 351, 330

Aharonian, F. 2004, 22nd Texas Symposium on Relativistic Astrophysics, 43

Aharonian, F., Akhperjanian, A. G., Bazer-Bachi, A. R., et al. 2006, A&A, 449, 223

Aharonian, F., Akhperjanian, A. G., Bazer-Bachi, A. R., et al. 2007, ApJ, 661, 236

Aharonian, F., Akhperjanian, A. G., Bazer-Bachi, A. R., et al. 2008, A&A, 481, 401

Aharonian, F., Akhperjanian, A. G., Barres de Almeida, U., et al. 2008, A&A, 477, 353

Aharonian, F., Buckley, J., Kifune, T., & Sinnis, G. 2008, Reports on Progress in Physics, 71, 096901

Aharonian, F., Akhperjanian, A. G., Barres de Almeida, U., et al. 2008, A&A, 488, 219

Albert, J., Aliu, E., Anderhub, H., et al. 2007, ApJ, 664, L87

Asaoka, I., & Aschenbach, B. 1994, A&A, 284, 573

Arthur, S. J. 2007, Astrophysics and Space Science Proceedings, 1, 183

Bamba, A., Pühlhofer, G., Acero, F., et al. 2012, ApJ, 756, 149

Bell, A. R. 1978, MNRAS, 182, 147

Bell, A. R. 2004, MNRAS, 353, 550

Berezinskii, V. S., Bulanov, S. V., Dogiel, V. A., & Ptuskin, V. S. 1990, Amsterdam: North-Holland, 1990, edited by Ginzburg, V.L.,

Berezhko, E. G., Völk, H. J. 2000, A&A, 357, 283

Berezhko, E. G., Pühlhofer, G., Völk, H. J. 2003, A&A, 400, 971

Berezhko, E. G., Völk, H. J. 2006, A&A, 451, 981

Berezhko, E. G., Pühlhofer, G., Völk, H. J. 2008, International Cosmic Ray Conference, 2, 255

Berezhko, E. G., Pühlhofer, G., Völk, H. J. 2009, A&A, 505, 641

Berge, D., Funk, S., & Hinton, J. 2007, A&A, 466, 1219

Bisnovatyi-Kogan, G. S., & Silich, S. A. 1995, Reviews of Modern Physics, 67, 661

Bohigas, J., Ruiz, M. T., Carrasco, L., Salas, L., & Herrera, M. A. 1983, Revista Mexicana de Astronomia y Astrofisica, 8, 155

Bressan, A., Marigo, P., Girardi, L., et al. 2012, MNRAS, 427, 127

Brogan, C. L., Gelfand, J. D., Gaensler, B. M., Kassim, N. E., & Lazio, T. J. W. 2006, ApJ, 639, L25

Cardelli, J. A., Clayton, G. C., & Mathis, J. S. 1989, ApJ, 345, 245

Casse, F., Lemoine, M., & Pelletier, G. 2002, Phys. Rev. D, 65, 023002

Cioffi, D. F., McKee, C. F., & Bertschinger, E. 1988, ApJ, 334, 252

Chen, Y., Zhou, P., & Chu, Y.-H. 2013, ApJ, 769, L16

Chen, Y., Girardi, L., Bressan, A., et al. 2014, MNRAS, 444, 2525

Chen, Y., Bressan, A., Girardi, L., et al. 2015, MNRAS, 452, 1068

Chevalier, R. A. 1982, ApJ, 259, 302

Chevalier, R. A. 1999, ApJ, 511, 798

Chevalier, R. A. 2005, ApJ, 619, 839

Claussen, M. J., Goss, W. M., Frail, D. A., & Desai, K. 1999, ApJ, 522, 349

Crutcher, R. M. 2012, ARA&A, 50, 29

Cui, Y.-D., Yuan, Y.-F., Li, Y.-R., & Wang, J.-M. 2012, ApJ, 746, 177

Cui, Y., Pühlhofer, G., & Santangelo, A. 2016, A&A, 591, A68

Dame, T. M., Hartmann, D., & Thaddeus, P. 2001, ApJ, 547, 792

Daum, A., Hermann, G., Heß, M., et al. 1997, Astroparticle Physics, 8, 1

de Naurois, M., & Rolland, L. 2009, Astroparticle Physics, 32, 231

Dickey, J. M., & Lockman, F. J. 1990, ARA&A, 28, 215

Doroshenko, V., Puehlhofer, G., Kavanagh, P., et al. 2015, arXiv:1508.03557

Drury, L. O. 1983, Reports on Progress in Physics, 46, 973

Dwarkadas, V. V. 2008, Physica Scripta Volume T, 132, 014024

Fatuzzo, M., Melia, F., Todd, E., & Adams, F. C. 2010, ApJ, 725, 515

Filippenko, A. V. 1997, ARA&A, 35, 309

Frail, D. A., Goss, W. M., & Slysh, V. I. 1994, ApJ, 424, L111

Fraschetti, F., & Melia, F. 2008, MNRAS, 391, 1100

Fukuda, T., Yoshiike, S., Sano, H., et al. 2014, ApJ, 788, 94

Fukui, Y. 2008, American Institute of Physics Conference Series, 1085, 104

Funk, S., Hermann, G., Hinton, J., et al. 2004, Astroparticle Physics, 22, 285

Funk, S. 2005, The PHD thesis of Funk Stefan: A new population of very high-energy γ-ray sources detected with H.E.S.S. in the inner part of the Milky Way

Gabici, S., Aharonian, F. A., & Casanova, S. 2009, MNRAS, 396, 1629

Gabici, S., Casanova, S., Aharonian, F. A., & Rowell, G. 2010, SF2A-2010: Proceedings of the Annual meeting of the French Society of Astronomy and Astrophysics, 313

Gabici, S., & Aharonian, F. A. 2014, MNRAS, 445, L70

Gaensler, B. M., & Slane, P. O. 2006, ARA&A, 44, 17

Giacalone, J., & Jokipii, J. R. 1994, ApJ, 430, L137

Giacinti, G., Kachelrieß, M., Semikoz, D. V., & Sigl, G. 2012, J. Cosmology Astropart. Phys., 7, 031

Giacinti, G., Kachelrieß, M., & Semikoz, D. V. 2013, Phys. Rev. D, 88, 023010

Ghiotto, A., & for The VERITAS Collaboration 2015, arXiv:1511.00309

Güver, T., & Özel, F. 2009, MNRAS, 400, 2050

Goto, M., McCall, B. J., Geballe, T. R., et al. 2002, PASJ, 54, 951

Han, J. L., Ferriere, K., & Manchester, R. N. 2004, ApJ, 610, 820

Hewitt, J. W., & Yusef-Zadeh, F. 2009, ApJ, 694, L16

Hillas, A. M. 1985, International Cosmic Ray Conference, 3, 445

Hinton, J. A., & Hofmann, W. 2009, ARA&A, 47, 523

Hou, L. G., Han, J. L., & Shi, W. B. 2009, A&A, 499, 473

Indriolo, N., Blake, G. A., Goto, M., et al. 2010, ApJ, 724, 1357

Janka, H.-T. 2012, Annual Review of Nuclear and Particle Science, 62, 407

Jokipii, J. R. 1966, ApJ, 146, 480

Jokipii, J. R. 1971, Reviews of Geophysics and Space Physics, 9, 27

Jones, F. C., & Ellison, D. C. 1991, Space Sci. Rev., 58, 259

Kachelrieß, M., & Ostapchenko, S. 2012, Phys. Rev. D, 86, 043004

Katarzyński, K., Sol, H., & Kus, A. 2001, A&A, 367, 809

Kennel, C. F., & Coroniti, F. V. 1984, ApJ, 283, 710

Klochkov, D., Pühlhofer, G., Suleimanov, V., et al. 2013, A&A, 556, AA41

Klochkov, D., Suleimanov, V., Pühlhofer, G., et al. 2015, A&A, 573, AA53

Kroupa, P., & Weidner, C. 2003, ApJ, 598, 1076

Krymskii, G. F. 1977, Akademiia Nauk SSSR Doklady, 234, 1306

Kusunose, M., & Takahara, F. 2008, ApJ, 682, 784

Li, H., & Chen, Y. 2010, MNRAS, 409, L35

Long, K. S., Blair, W. P., Matsui, Y., & White, R. L. 1991, ApJ, 373, 567

Lorenz, E., & The MAGIC Collaboration 2004, New Astronomy Reviews, 48, 339

Lozinskaya, T. A. 1974, Soviet Astronomy, 17, 603

Lynds, B. T., & Oneil, E. J., Jr. 1985, ApJ, 294, 578

Malkov, M. A., Diamond, P. H., Sagdeev, R. Z., Aharonian, F. A., & Moskalenko, I. V. 2013, ApJ, 768, 73

van Marle, A. J., Langer, N., & García-Segura, G. 2004, Revista Mexicana de Astronomia y Astrofisica Conference Series, 22, 136

van Marle, A. J., Langer, N., & García-Segura, G. 2007, A&A, 469, 941

Marquez-Lugo, R. A., & Phillips, J. P. 2010, MNRAS, 407, 94

Mazzali, P. A., Röpke, F. K., Benetti, S., & Hillebrandt, W. 2007, Science, 315, 825

Meyer, M., Horns, D., & Zechlin, H.-S. 2010, A&A, 523, A2

Nadezhin, D. K. 1985, Ap&SS, 112, 225

Narayan, R., & Piran, T. 2012, MNRAS, 420, 604

Nava, L., & Gabici, S. 2013, MNRAS, 429, 1643

Neufeld, D. A., Hollenbach, D. J., Kaufman, M. J., et al. 2007, ApJ, 664, 890

Nicholas, B., Rowell, G., Burton, M. G., et al. 2011, MNRAS, 411, 1367

Nicholas, B. P., Rowell, G., Burton, M. G., et al. 2012, MNRAS, 419, 251

Ohira, Y., Murase, K., & Yamazaki, R. 2011, MNRAS, 410, 1577

Ostriker, J. P., & McKee, C. F. 1988, Reviews of Modern Physics, 60, 1

O'Donnell, J. E. 1994, ApJ, 422, 158

Parker, E. N. 1958, ApJ, 128, 664

Padovani, M., Galli, D., & Glassgold, A. E. 2009, A&A, 501, 619

Parsons, R. D., & Hinton, J. A. 2014, Astroparticle Physics, 56, 26

Parsons, R. D., Balzer, A., Füssling, M., et al. 2015, arXiv:1509.05191

Prosekin, A. Y., Kelner, S. R., & Aharonian, F. A. 2015, Phys. Rev. D, 92, 083003

Ptuskin, V. 2006, Journal of Physics Conference Series, 47, 113

Rho, J., & Borkowski, K. J. 2002, ApJ, 575, 201

Reach, W. T., Rho, J., & Jarrett, T. H. 2005, ApJ, 618, 297

Reach, W. T., & Rho, J. 2000, ApJ, 544, 843

Rees, M. J., & Gunn, J. E. 1974, MNRAS, 167, 1

Sasaki, M., Kothes, R., Plucinsky, P. P., Gaetz, T. J., & Brunt, C. M. 2006, ApJ, 642, L149

Smartt, S. J. 2009, ARA&A, 47, 63

Smartt, S. J., Eldridge, J. J., Crockett, R. M., & Maund, J. R. 2009, MNRAS, 395, 1409

Tanaka, T., Allafort, A., Ballet, J., et al. 2011, ApJ, 740, L51

Tang, J., Bressan, A., Rosenfield, P., et al. 2014, MNRAS, 445, 4287

Tian, W. W., Leahy, D. A., Haverkorn, M., & Jiang, B. 2008, ApJ, 679, L85

TOTEM Collaboration, Antchev, G., Aspell, P., et al. 2011, EPL (Europhysics Letters), 96, 21002

Tothill, N. F. H., White, G. J., Matthews, H. E., et al. 2002, ApJ, 580, 285

Truelove, J. K. & McKee, C. F. 1999, ApJS, 120, 299

Treumann, R. A., & Jaroschek, C. H. 2008, arXiv:0806.4046

Velázquez, P. F., Dubner, G. M., Goss, W. M., & Green, A. J. 2002, AJ, 124, 2145

Vink, J. 2006, The X-ray Universe 2005, 604, 319

Vink, J. 2008, ApJ, 689, 231

Vink, J. 2012, A&A Rev., 20, 49

Vink, J. 2013, 370 Years of Astronomy in Utrecht, 470, 269

Völk, H. J., & Bernlöhr, K. 2009, Experimental Astronomy, 25, 173

Weaver, R., McCray, R., Castor, J., Shapiro, P., & Moore, R. 1977, ApJ, 218, 377

Weekes, T. C., Cawley, M. F., Fegan, D. J., et al. 1989, ApJ, 342, 379

Weekes, T. C., Badran, H., Biller, S. D., et al. 2002, Astroparticle Physics, 17, 221

Winkler, P. F., Williams, B. J., Reynolds, S. P., et al. 2014, ApJ, 781, 65

Park, N., & for the VERITAS Collaboration 2015, arXiv:1508.07068

Portegies Zwart, S. F., McMillan, S. L. W., & Gieles, M. 2010, ARA&A, 48, 431

Ptuskin, V. 2006, Journal of Physics Conference Series, 47, 113

Ptuskin, V. S., & Zirakashvili, V. N. 2005, A&A, 429, 755

Yang, R.-z., Zhang, X., Yuan, Q., & Liu, S. 2014, A&A, 567, A23

Yuan, Q., Liu, S., & Bi, X. 2012, ApJ, 761, 133

Zirakashvili, V. N., & Ptuskin, V. S. 2008, ApJ, 678, 939

Zirakashvili, V. N., & Ptuskin, V. S. 2012, Astroparticle Physics, 39, 12

Acknowledgements

I would like to express my sincere gratitude to the people who have helped me accomplishing this Ph.D work.

- Professor Andrea Santangelo is the first I like to thank. As my supervisor, he has led me to become an independent researcher with his uncompromising attitude to the quality of scientific works, and he has always boosted my motivations on science with his optimism and humor.

- I am very grateful to my second supervisor Gerd Pühlhofer, who is always available to help and guide my work in all ways with his precise and inclusive scientific minds.

- I am greatly honored to have the opportunity to be involved in the H.E.S.S. team and ISM-SPP team during my Ph.D study. Many people in these teams have provided valuable opinions on my study.

- I like to give a special thank to Professor Heinrich Völk and Professor Vladimir Zirakashvili in MPIK for their important suggestions on the physics models in my study.

- I feel very lucky to have my wonderful colleagues and teachers in IAAT as well as some best friends in Astrophysics: Victor Doroshenko, Dmitry Klochkov, Manami Sasaki, Lorenzo, Emma, Patrick, Sara, Gabi, Christian, Daniel (who has translated my abstract into German), Yang, Guangxing, et al.. I have received professional helps from them covering a wide range from the fundamental physics to technical details. Additionally, I deeply appreciate the countless helps from Chris Tenzer, which has smoothed my everyday life and work in Tübingen.

- At last, my deepest thanks are for my parents (in-law), my wife Iina, and my son Atte, without their support, I will not dare to drown myself into this dream career – Astrophysics.

Curriculum Vitae

University of Science and Technology of China 2007-2012
Master student with Prof. Yefei Yuan

- Within a fully General Relativistic framework, we builded the mini-jets model to explain the TeV emissions in the vicinity of the black hole of M87. 2009-2011
- Taught experimental physics to undergraduate students. 2008

University of Tübingen(Germany) 2012-present
Ph.D student with Dr. Gerd Pühlhofer and Prof. Andrea Santangelo

- HESS-I data analysis with HAP, mostly on HESS J1731-347 and HESS J1729-345. 2012-2014
- Following H.E.S.S. Collaboration et al. (2011) who identified a young TeV SNR HESS J1731-347 along with an extended TeV source HESS J1729-345 next to it, we explained the TeV emission from HESS J1729-345 using runaway cosmic rays that are interacting with nearby molecular clouds. 2012-2015
- Searching stars behind/near SNR HESS J1731-347; 18 (66) candidates are found right behind the molecular clouds located at $\sim$3 kpc ($\sim$5 kpc) using the CfA ^{12}CO data, the WISE catalog, and the SIMBAD catalog. 2014
- Builded a purely numerical code for cosmic rays propagating in magnetic turbulence. 2015
- Taught 10th and 12th grade students about the Astrophysics basics, at Pyhäjärvi, Finland. Sep/2015.